Impurity Asymmetries in the Pedestal Region of the Alcator C-Mod Tokamak

by
Randy Michael Churchill
B.S. Electrical Engineering and Computer Science
Brigham Young University (2006)

Submitted to the Department of Nuclear Science and Engineering
in partial fulfillment of the requirements for the degree of
Doctor of Philosophy in Nuclear Science & Engineering
at the
MASSACHUSETTS INSTITUTE OF TECHNOLOGY
June 2014

Signature redacted

Author .....
Department of Nuclear Science and Engineering
May 1, 2014

Certified by ..... Signature redacted .....
Bruce Lipschultz
Senior Research Scientist
Thesis Supervisor

Certified by ..... Signature redacted
Ian Hutchinson
Professor of Nuclear Science & Engineering
Thesis Supervisor

Certified by ..... Signature redacted .....
Dennis Whyte
Professor of Nuclear Science & Engineering
Thesis Reader

Accepted by ..... Signature redacted ...
Mujid S. Kazimi
TEPCO Professor of Nuclear Engineering
Chairman, Department Committee on Graduate Theses

Impurity Asymmetries in the Pedestal Region of the Alcator C-Mod Tokamak

by

Randy Michael Churchill

Submitted to the Department of Nuclear Science and Engineering
on May 1, 2014, in partial fulfillment of the
requirements for the degree of
Doctor of Philosophy in Nuclear Science & Engineering

Abstract

In an effort to illuminate the effects of the strong plasma gradients in the pedestal region on impurity transport, research was conducted to measure complete sets of impurity density, poloidal and parallel velocity, and temperature at two separate poloidal locations in the pedestal region of the Alcator C-Mod tokamak. To this end, the diagnostic technique gas puff-CXRS was refined and expanded on, allowing for the first time in a tokamak complete measurements of impurities at the high-field side (HFS).

Large in-out B^{5+} impurity density asymmetries were measured in H-mode plasmas with strong boundary electron density gradients, with a build-up of impurity density at the HFS. Impurity temperatures were also found to be asymmetric in the pedestal region, with larger temperatures at the low-field side (LFS). Such temperature asymmetries suggest a significant asymmetry in electron density near the separatrix. In contrast to these H-mode results, plasmas with low boundary electron density gradients, such as L-mode and I-mode, exhibit constant impurity density on a flux surface, even if strong electron temperature gradients are present.

Mechanisms which could drive such poloidal asymmetries are explored. Experiments provide evidence against localized impurity sources and fluctuation-induced transport as primary causes. Particle transport timescales are compared, showing that the radial transport becomes comparable to or faster than the parallel transport in the pedestal region. Additionally, modelling of impurity transport using conventional, one-dimensional neoclassical physics fails to correctly reproduce the measured flux-surface averaged impurity density, suggesting along with the timescale estimates that a more complete two-dimensional treatment of impurity particle transport is required.

The measured impurity velocities at the LFS and HFS are compared to the canonical form for particle flow velocity within the flux surface of a tokamak. Within the error bars of the measurement, agreement is found with the canonical form. The implications of exact matches to the canonical form are low radial transport, and the $\mathbf{E} \times \mathbf{B}$ drift dominating the perpendicular impurity flow. Further work is motivated

into more precise velocity measurements to determine if the velocities exactly match this canonical form.

Thesis Supervisor: Bruce Lipschultz
Title: Senior Research Scientist

Thesis Supervisor: Ian Hutchinson
Title: Professor of Nuclear Science & Engineering

Thesis Supervisor: Dennis Whyte
Title: Professor of Nuclear Science & Engineering

Acknowledgments

Reflecting back on the 6 years of research and learning that went into this thesis, I'm struck by the many influences and contributions others have made to allow me to finally complete such a document. I would be remiss to not show my appreciation to those people here.

First, a special thanks goes to Dr. Bruce Lipschultz, who acted as my direct advisor and mentor for the majority of my time at MIT. It was his vision and persistence that created and guided the edge CXRS system on Alcator C-Mod, which I was able use and improve on in this thesis. He has been very helpful in answering my questions, and guiding my efforts. He was a perfect combination of expectation and understanding when it came to my work/life balance. I enjoyed learning how to think like an applied physicist from him, and can only hope to one day emulate his ability to quickly grasp the big picture and important aspects of a problem.

Next, I thank Professor Ian Hutchinson who, besides giving crucial advice in development of the GP-CXRS diagnostic, also pinch-hit as my advisor for the last year of this thesis work. His deep understanding of plasma and tokamak physics were very useful in making sense of the measurements made in this thesis, and I learned quite a lot from our discussions.

Professor Dennis Whyte also deserves thanks for giving his time both as a member of my thesis committee and as the reader for this thesis. His critical reading and insight lead to multiple improvements in this thesis.

While not directly part of my thesis committee, two people made considerable contributions to this thesis. Dr. Christian Theiler's work as a postdoc, while only covering two too short years, helped tremendously in all aspects of the GP-CXRS system: hardware, analysis software, daily operation, and physics interpretations. He has been a thorough reviewer and contributor to the various papers I've prepared and this thesis, always striving for perfection. Also, Dr. Matt Reinke gave considerable time and interest into the measurements and results. His constant encouragement and in-depth knowledge of impurity density asymmetries were invaluable. His tireless

work and multitude of interests have contributed greatly to this thesis and Alcator C-Mod in general. In addition to these two, I should recognize Dr. Rachael McDermott and Dr. Ken Marr, who initially developed the edge CXRS system on C-Mod. It was an incredible help to have an operational system on which to build on. They also both gave of their time to teach me the ins and outs of the diagnostic and C-Mod.

Several members of the PSFC theory department deserve special mention. Professor Peter Catto and Professor Felix Parra-Diaz were excellent professors in the subject of plasma transport, and were generous in their time explaining concepts to me. Dr. Matt Landreman was also happy to discuss and explain transport physics to me, and I benefitted from his thorough and clear explanations. I learned from and appreciated various conversations with Dr. Darin Ernst.

A special thanks also goes to Thomas Pütterich from IPP-Garching, who spent time at MIT, and from whom I learned quite a bit about spectroscopy, diagnostics, and plasma physics. Dr. Steve Lisgo at ITER gave a lot of his time to get things going with the neutral transport code OSM-EIRENE. Dr. Daren Stotler at PPPL contributed DEGAS2 simulations. Felix Reimold and Jordan Goldstein also contributed to setting OSM-EIRENE for Alcator C-Mod.

Many staff scientists, engineers, and technicians in the Alcator project have given of their time and expertise in making the work contained herein a reality. Dr. Jerry Hughes helped with all things pedestal related, and didn't hesitate to answer my questions on pedestal physics and C-Mod operation. Dr. Amanda Hubbard also imparted of her broad knowledge of pedestal and tokamak physics. Dr. Brian LaBombard helped with NINJA control, KN1D simulations, and discussions on various edge physics topics. Rui Vieira helped with the engineering and design of in-vessel components such as the gas puff capillary holder and LFS toroidal periscope. Sam Pierson helped with in-vessel installation and work. Henry Savelli provided CAD design of various components. Tommy Toland and Ronnie Rosati did wonderful vacuum vessel work, and weren't too angry when I forgot to tighten a vacuum mini-conflat. Bill Parkins and Willy Burke helped with PCB layout and other electronics. Josh Stillerman and Tom Fredian helped with tree data access and storage in MDSplus. In gen-

eral, the entire Alcator C-Mod team was very useful in carrying forward the research in this thesis. The project's contribution to the fusion community is paramount, as it provides a reactor-relavent machine, while allowing the freedom for a graduate student to learn and make significant contributions.

I benefitted greatly from the friendship and help from several fellow grad students. Bob Mumgaard in particular was a great source of diagnostic knowledge and clear thinking, along with interesting conversations. Geoff Olynyk, Jungpyo Lee, Mike Garrett, Dan Brunner, Ted Golfinopolous, John Walk, Chi Gao, Ian Faust, Paul Ennever, Evan Davis, Choon-gki Sung, and many others greatly enhanced my learning and my time as a graduate student.

I also want to thank those from before my days at MIT that gave me the opportunity to be involved in fusion research, even when I couldn't contribute much. Specifically Dr. Aaron Redd and Dr. Brian Nelson at the University of Washington, and John Ellsworth at Brigham Young University.

Many people gave non-scientific contributions to this research. My parents, Randy and Camille Churchill, taught me to wonder at the world, and instilled in me the work ethic and principles that have enabled me to accomplish my goals. My many siblings and extended family, who gave encouragement throughout my Ph.D career. The many church and Westgate friends we've made while here, who gave me and my family their friendship and care, and a supportive community. My two girls, Lily and Cali, who always made me smile and laugh. Daddy had to spend some long hours working, but you were never far from my heart. Finally, to my wife Danielle. I owe so much to you for your love, support, sacrifice, and belief in me. These past 6 years have been a burden for both of us at times, but it has been made light by having you by my side.

Contents

List of Figures

List of Tables

Glossary

Symbol	Description	Units
$\mathbf{b}$	Magnetic field direction vector, $\mathbf{b} = \mathbf{B}/B$	
$\mathbf{B}$	Magnetic field vector	T
$\mathbf{E}$	Electric field vector	V/m
$\mathbf{F}$	Arbitrary force vector	kg m / s^2
$K_j(\psi)$	Velocity flux function (see Appendix A)	m^{-2} s^{-1} T^{-1}
m	Particle mass	kg
I	Radiance	photons/s/m^2/ster
I^λ	Spectral radiance	photons/s/m^2/ster/Å
LOS	Optical line-of-sight	
m_j	Particle mass of species j	kg
n_j	Density of species j	particles / m^3
n^D	Principal quantum number of a deuterium atom	
n_D	Deuterium neutral density	m^{-3}
p_j	Pressure of species j	Pa
q	Particle charge	Coulomb
q	Safety Factor, the average number of toroidal turns the magnetic field makes in one complete turn around the poloidal direction $q = \oint \frac{\mathbf{B}\cdot\nabla\zeta}{\mathbf{B}\cdot\nabla\theta}$	
q_{95}	Edge safety factor, at the 95% flux surface	
$q_{eff,i}$	Effective CX rate coefficient	photons m^3/s
q_j	Heat flux vector of species j	W/m^2

Q_j	Energy exchange between species j and other species	W/m^3
R	Major radius	m
$\mathbf{R}_j$	Friction force	N
S_j^n	Particle source	m^{-3}/s
$\mathbf{S}_j^M$	Momentum source	N/m^3
S_j^E	Energy source	W/m^3
t	Time	s
T_j	Temperature of species j	eV
$\mathbf{v}$	Particle velocity vector	m/s
$\mathbf{V}_j$	Fluid velocity vector of species j	m/s
Z	Atomic charge	
Z'	Atomic charge of CX receiver species	
Z^D	Nuclear charge of CX donor species	
ε	Emissivity	$photons/s/m^3$
ε^λ	Spectral emissivity	$photons/s/m^3/\mathring{A}$
∇	Gradient operator ($\nabla f = \hat{x}_j \frac{\partial f}{\partial x_j}$)	
$\nabla\cdot$	Divergence operator ($\nabla \cdot \mathbf{f} = \frac{\partial f_j}{\partial x_j}$)	
$\overleftrightarrow{\pi}_j$	Pressure anisotropy tensor	N/m
ψ	Poloidal magnetic flux, $\psi = \int \mathbf{B} \cdot d\mathbf{A}$	$T \cdot m^2$
θ	Poloidal coordinate	
$\omega_j(\psi)$	Velocity flux function (see Appendix A)	s^{-1}
σ_{cx}	Charge exchange cross-section	m^2
ζ	Toroidal coordinate	
$\langle\rangle$	Flux surface average, $\langle f \rangle = \oint f d\ell / \oint d\ell$	
$\langle\rangle_t$	Time average, $\langle f \rangle_t = 1/T \int_0^T f dt$	
$\perp$	In a direction perpendicular to the magnetic field	
$\parallel$	In a direction parallel to the magnetic field	

Chapter 1

Introduction

Fusion is an enticing method of producing baseload electrical energy to meet the increasing worldwide demand for energy. Among the potential benefits of fusion are an abundant and accessible fuel supply (deuterium, an isotope of hydrogen, which is easily separated from seawater, and lithium), minimal radioactive waste, and zero carbon emissions. Despite enormous progress made over the past decades, many challenges in engineering and physics still need to be overcome before a fusion reactor can be useable, let alone economical, as an electrical power plant.[1].

From the knowledge and experience gained over decades of research, an international coalition of countries has designed and is in the process of building a large experimental thermonuclear fusion machine, named ITER, located in the south of France. In these types of devices, nuclear fusion reactions are made possible by confining a plasma (ionized gas) to extreme temperatures and pressures, allowing ions to overcome their natural repulsion and come in close enough proximity for the strong nuclear force to fuse the two ionic nuclei, releasing energy in the process. The primary goal of ITER will be to produce fusion power that is at least ten times larger than the required input power, while furthering the technological and scientific capabilities needed to construct a commercial fusion power plant.

Modelling and extrapolations from current experiments indicate that ITER can achieve this power gain goal by operating in an enhanced confinement regime, known as H-mode (short for high confinement mode). The H-mode is characterized by a

large increase in plasma density and temperature in a narrow region at the edge of the plasma, known as the pedestal region since it raises the core density and temperature also. The height of the pedestal is projected to determine the overall fusion power generated, since the core profiles are dominated by turbulent processes which limit the gradient scale lengths in this region[2].

Obviously a deep understanding (or at the least, robust empirical scalings) of the physics governing this pedestal region is crucial to the success of next-step fusion devices. Unfortunately, the sharp gradients in the pedestal region make analytical theories and computational codes intractable, and there isn't currently a commonly accepted theory explaining all of the transport effects in the pedestal region. Progress is being made[3], driven by a mutually beneficial relationship between theory, simulation, and experiment, with the ultimate goal of producing a validated predictive model for the pedestal.

Understanding the physics of the pedestal region will be particularly important for understanding the levels of impurity ions which will be present in the plasma. Impurities are non-fuel ions that are present in the plasma due to sputtering of material surfaces, production of helium ash from fusion reactions, or deliberately seeded into the plasma for diagnostic use or performance enhancement. Impurity levels must be controlled, as high-Z impurities can radiate energy away from the plasma, causing the plasma to cool and possibly destabilize, and low-Z impurities effectively dilute the main ion fuel available for fusion reactions.

In this thesis, experimental observations are made on the MIT Alcator C-Mod tokamak to further the understanding of impurity transport in the pedestal region, by measuring impurity density, temperature, velocity, and the radial electric field at two separate poloidal locations and comparing these measurements with theoretical models. Beyond impurity transport, these observations also give insights into the physics governing the pedestal region.

1.1 Tokamak

From the beginning of fusion research with magnetic confinement devices, several machine configurations have been experimented with, but none have matched the stored energy performance of the tokamak, a Russian acronym meaning "toroidal chamber with axial magnetic field". Starting with the 1968 announcement of record setting plasma temperatures in the T-3 tokamak at Novosibirsk, Russia[4], the worldwide effort to develop fusion for peaceful purposes has been dominated by the tokamak design.

The principal components of a the tokamak is a vacuum chamber in the shape of a torus, surrounded by magnetic coils, and a solenoid transformer in the core of the torus to drive current in the plasma by magnetic induction. The main magnetic coils establish a magnetic field in the toroidal direction (B_ζ in figure 1-1), and the inductive current (I_p) driven in the plasma by the solenoid establishes a poloidal field (B_θ in figure 1-1).

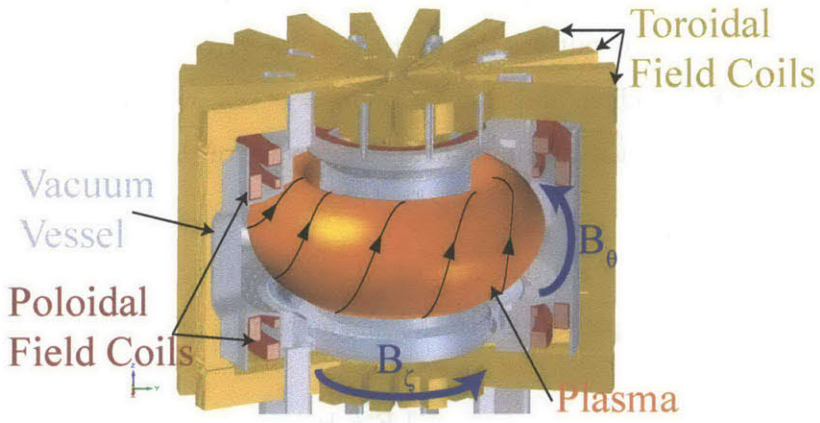

Figure 1-1: Basic layout of a tokamak fusion device. Toroidal magnetic field coils wrap around transverse to the magnetic axis, poloidal magnetic field coils wrap around parallel to the magnetic axis. Base CAD model courtesy of Rick Leccacorvi.

The magnetic fields in a tokamak are used to confine the charged particles (electrons and ions) that make up a plasma. Charged particles tend to follow magnetic field lines, due to the Lorentz force:

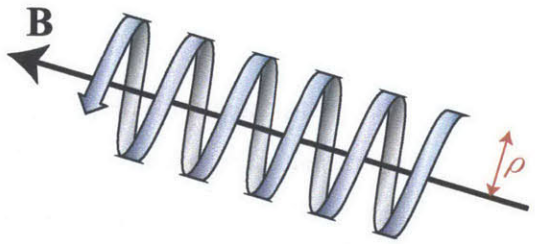

Figure 1-2: Motion of a charged particle in a magnetic field. The gyro-radius, or Larmor radius, is labelled ρ.

$$\mathbf{F}_{Lorentz} = \frac{d}{dt} m\mathbf{v} = q\mathbf{E} + q\mathbf{v} \times \mathbf{B} \tag{1.1}$$

In a straight, homogeneous magnetic field, with no electric field ($\mathbf{E} = 0$), this equation can be solved directly for the particle position $\mathbf{x}$ to show that a particle of charge q will stream along a magnetic field, while executing a circular motion, or gyro-motion, perpendicular to the magnetic field, shown in figure 1-2. The frequency of this gyro-motion, known as the gyro-frequency, is $\omega_c = qB/m$, where q is the charge of the particle, B is the total magnetic field, and m is the particle mass. The radius of the circle traced out by the particle in its gyro-motion is known as the gyro-radius or Larmor radius, and is given by $\rho_L = v_\perp/\omega_c$, where $v_\perp$ is the particle's velocity perpendicular to the magnetic field. The center of the circle is known as the particle's guiding center.

If other external forces $\mathbf{F}$ act on the charged particle, they will cause the particle's guiding center to drift perpendicular to the magnetic field line, with a velocity:

$$\mathbf{v}_{\perp,\mathbf{D}} = \frac{1}{q} \frac{\mathbf{F} \times \mathbf{B}}{B^2} \tag{1.2}$$

Due to the spatial non-uniformity of the magnetic field, and the centrifugal force felt by a streaming particle on a curved magnetic field, charged particles develop a vertical ∇B-curvature drift:

$$\mathbf{v}_{\perp,\nabla\mathbf{B}-\kappa} = \mathbf{v}_{\nabla\mathbf{B}} + \mathbf{v}_\kappa = -\frac{\frac{1}{2}mv_\perp^2}{qB} \frac{\nabla B \times \mathbf{B}}{B^2} - \frac{mv_\parallel^2}{q} \frac{[\mathbf{b} \cdot \nabla \mathbf{b}] \times \mathbf{B}}{B^2} \tag{1.3}$$

where $\mathbf{b}$ is the unit vector in the direction of the magnetic field, $\mathbf{b} = \mathbf{B}/B$, and $v_{\|}$ is the particle velocity parallel to the magnetic field, $\mathbf{v} = v_{\|}\mathbf{b} + \mathbf{v}_{\perp}$. Because electrons and ions have ∇B-curvature drifts in opposite directions, a charge imbalance occurs, leading to a vertical pointing electric field. The resulting electric field force $\mathbf{F_E} = q\mathbf{E}$ causes an additional charged particle drift, the $\mathbf{E} \times \mathbf{B}$ drift:

$$\mathbf{v}_{\perp,\mathbf{ExB}} = \frac{\mathbf{E} \times \mathbf{B}}{B^2} \tag{1.4}$$

The $\mathbf{E} \times \mathbf{B}$ drift is the same for electrons and ions; radially outwards. Therefore, if the tokamak consisted of a toroidal magnetic field alone, the plasma would be unstable, quickly forced to the outer wall. The addition of the poloidal magnetic field averages out the vertical drifts, preventing the development of a vertical electric field. External poloidal magnetic coils add additional vertical magnetic field to the plasma current generated poloidal magnetic field to ensure the plasma is stable.

A simple calculation of the magnetic flux from the toroidal field coils through a toroidal ring reveals that the vacuum toroidal magnetic field has the form $B_\zeta \propto 1/R$, where R is the major radius; the distance from the center of the solenoid. Accordingly, the outboard side of the plasma is referred to as the low-field side (LFS) and the inboard side the high-field side (HFS). A picture of the magnetic flux surfaces is shown in figure 1-3. If particles simply followed their orbits along these field lines, with the drifts as described above completely cancelled, they would be confined in the plasma indefinitely. Unfortunately, there are several ways for particles to be knocked off their orbits, known as cross-field transport, which causes plasma particles, and the energy associated with such particles, to be lost from the plasma. The first such cross-field transport mechanism is through particle collisions, which are Coulomb collisions due to plasma particles having electric charge. In general tokamak plasmas, many small angle deflections of a particle through collisions cause a significant change in its velocity vector, leading to a physical displacement in its guiding center position. Second, turbulent fluctuations of electric and magnetic fields can cause radially outward motion of particles. The turbulent fluctuations are due to micro-instabilities

that form in the plasma, which are driven by free energy in the plasma, e.g. density and temperature gradients. In most regions of a tokamak plasma, the cross-field transport of particles and heat is dominated by turbulent transport.

Because of collisions and turbulence transporting particles and energy out of the plasmas, a method to protect the vacuum vessel walls was needed. Early research focused on using a dedicated sacrificial material structure, known as a limiter, to intercept the outward flux of particles and heat. However, an improved method known as a divertor was devised to further reduce the interaction of the plasma with material surfaces, and has become the most often used configuration of tokamak plasmas. The magnetic geometry shown in 1-3 is a divertor configuration. As shown, magnetic field lines form closed surfaces in the central regions of the vessel, but outside of the red contour, which is known as the separatrix, the magnetic field lines are open, intercepting material surfaces. This is made possible by a poloidal magnetic field null (X-point), created using external poloidal field coils with current flowing in the same direction as the plasma current. The region of open magnetic field lines surrounding the confined plasma region is called the scrape-off layer (SOL), since plasma particles lost from the confined plasma by cross-field transport are "scraped-off"; quickly transported parallel to the open magnetic field lines into the divertor region. The main benefit of the divertor configuration is that it moves the plasma-material interface far from the confined plasma region, reducing impurity content in the plasma. In D-T reactors, the divertor will also serve to remove helium ash, a byproduct of D-T fusion reactions.

1.2 Pedestal Region

As mentioned above, the pedestal region is a narrow region of the plasma located just inside the separatrix, with sharply increasing density and/or temperature during high performance discharges. An example of a pedestal is shown in Figure 1-4. For the purposes of this thesis, we will refer to a large gradient in density/temperature near the separatrix as "a pedestal". However, we will refer to this region near the

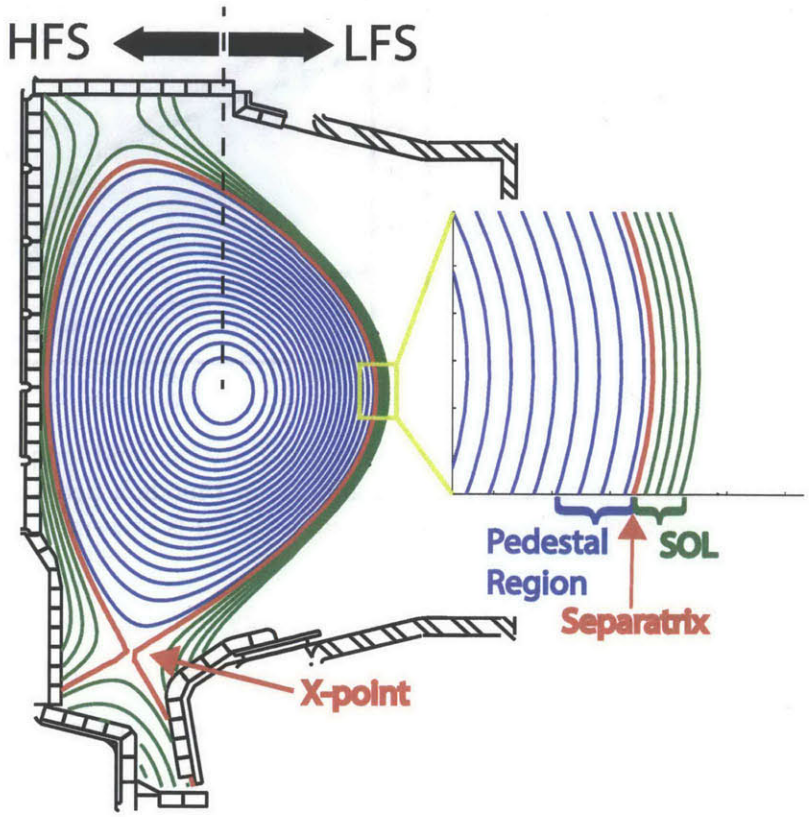

Figure 1-3: Magnetic flux surfaces in the divertor configuration. The yellow box shows the zoomed in area. The scrape-off layer (SOL) area has open field lines, intercepting material surfaces. Inside of the separatrix, magnetic field lines form closed flux surfaces.

separatrix as "the pedestal region" even in the absence of large density/temperature gradients, such as in L-mode plasmas.

A pedestal was first observed in 1982 on ASDEX[5], with the discovery of the H-mode[6]. This was a direct result of running a divertor configuration. While there have been pedestals observed in limited plasmas, they are almost always observed in diverted configurations. This is usually attributed to the reduced impurity content, with resulting reduced radiation power loss. However there are good indications that the X-point plays a strong role[5, 7].

The formation of a density and/or temperature pedestal marks a reduction of

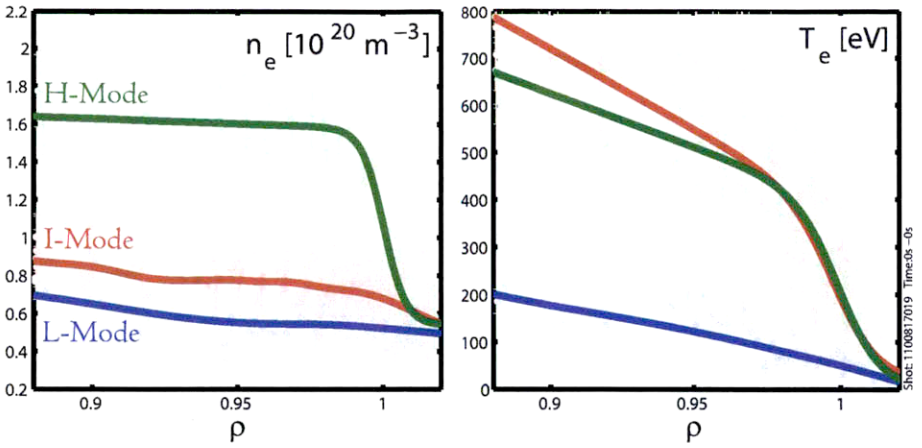

Figure 1-4: Example pedestal structure in electron density (n_e) and temperature (T_e). In H-mode, a pedestal is present in both n_e and T_e, in I-mode a pedestal is present only in the energy channel, T_e, and in L-mode no pedestal is present.

the local outward transport of particles and/or energy from the plasma, and so is often referred to as a transport barrier. The general theory of how a pedestal is sustained[8] is based on the presence of a strongly spatially varying radial electric field (E_r), which produces a mean $E \times B$ flow. When there is a strong enough radial gradient in the $E \times B$ flow (commonly referred to as "shear"[9]), this flow will stretch and distort turbulent eddies, until they are broken up (i.e. decorrelated)[8, 10]. This reduces the turbulent transport, which is normally the dominant transport mechanism in tokamak plasmas. It is then expected that, in these regions of strongly sheared $E \times B$ flow, the transport levels are reduced to near the minimum level, known as neoclassical transport. With these lower transport levels, larger gradients in density and/or temperature can be realized at the same levels of heat and particle transport.

Why a radial electric field develops in the first place is an open question, with several existing theories. These are generally grouped under the topic of L-H mode transitions. Among the most prominent theories are non-ambipolar transport (ion orbit losses)[11], increased main ion pressure gradients[12], and fluctuating $E \times B$ flows (zonal flow), driven by fluctuating Reynolds stress[13], the latter theory having gained the most traction and experimental support[14] in recent times. Regardless of the initial mechanism which forms the radial electric field, the resulting increased

pressure will take over to sustain the E_r, as long as the external plasma heating is sufficient to maintain the pressure pedestal.

Although the pedestal region only covers a small fraction of the plasma, the enhanced density and temperature has a disproportionately larger effect on the total plasma confinement. In core regions of the plasma inside of the pedestal, turbulent transport dominates. This is observed to follow a critical gradient model[2], which means that at a threshold gradient in temperature, the turbulent driven heat flux increases substantially. In turn, this increased heat flux reduces the temperature, reducing the gradient, and the cycle repeats. For sufficient heating, this essentially clamps the temperature profile at a specific gradient, making it rather insensitive to heating, i.e. a "stiff" profile. To access higher temperatures, a fusion device would have to be made larger, as the gradient is fixed. This is unfavorable, as the cost of a fusion reactor will to a large extent be set by its volumetric size. The pedestal greatly ameliorates the situation, raising the temperature profile across the entire plasma.

The pedestals that form in improved confinement regimes, such as H-mode, can be significantly different for the particle and energy channels, and also for the various plasma particle species. In plasmas referred to as I-mode[15], the electron/ion density stays flat (at L-mode gradient levels), while the electron/ion temperature develops a strong pedestal (see Figure 1-4). Also, in most tokamak H-modes, the ion temperature T_i develops a notably wider pedestal than the electron temperature T_e, usually by 30-40% [16]. This has been variously attributed to low collisionality[17] or preferential ion heating by neutral beams[18]. Additionally, in H-mode plasmas generally the width of the electron density pedestal is typically smaller than that of the electron temperature profile[19].

These variations hint at the possibility of several physical mechanisms playing a role in determining the pedestal structure. For example, atomic physics effects such as neutrals that can act as a particle source through ionization and an energy sink through charge exchange[20, 19]. Another mechanism involves ideal and resistive MHD instabilities (peeling-ballooning and kinetic ballooning modes), which set limits on the attainable pedestal height and width[21]. In many tokamaks, these

instabilities are manifest in a fast expulsion of plasma at the edge, known as Edge Localized Modes (ELMs), which transiently reduces both the density and temperature pedestals. While ELMs do serve to remove unwanted impurities from the plasma, they threaten damage to material surfaces, and so their effects must be mitigated. Several confinement regimes have been developed that are ELM-less, with varying degrees of utility[3]. Almost always these ELM-less regimes involve a naturally occurring plasma mode (broadly and respectfully grouped under the title "benevolent" modes), which is believed to enhance particle transport to a level which allows a pedestal, but flushes out impurities.

Unfortunately, the gradient scale lengths ($L_a = a/|\nabla a|$) in density and temperature in the pedestal region are often the size of the main ion poloidal gyro-radius, L_{n_i}, $L_{T_i} \sim \rho_{\theta,i}$, which violates the orderings used in conventional plasma transport theories. This leads to the main ions sampling a wide range of densities and temperatures during their gyro-orbit, requiring a global treatment of transport in the pedestal region. Simulation and theory work in this direction is moving forward[22, 23, 7], but to date there isn't a commonly accepted theory of transport in the pedestal region.

1.3 Alcator C-Mod Tokamak

Tokamak research at the Massachusetts Institute of Technology, Cambridge, USA, began in the early 1970's, leading to the design and construction of the Alcator C-Mod tokamak, in operation since 1993. A CAD drawing of the structure is shown in Figure 1-5. Also shown in Figure 1-6 is a picture of inside the C-Mod vacuum vessel.

Alcator C-Mod has many salient features which make it unique in the tokamak community. C-Mod is a compact tokamak with the largest magnetic field of any tokamak in the world. This combination of small size and high field allows studies of reactor relevant conditions, while staying within a university level research program. A comparison chart of key operational and plasma characteristics of Alcator C-Mod and ITER are shown in table 1.1.

Due to the high magnetic field and compact size combination, high plasma density

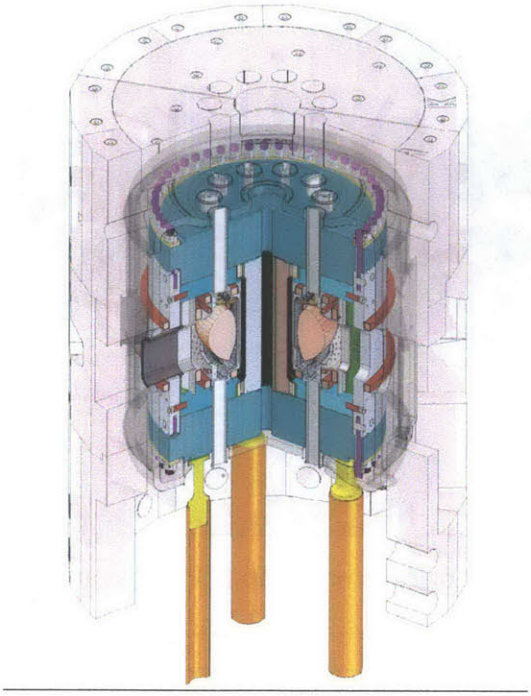

Figure 1-5: CAD drawing of Alcator C-Mod. Courtesy of Rick Leccacorvi.

discharges are achieved, leading to high divertor heat fluxes similar to those expected on ITER. The plasma facing components (PFC's) are all made out of molybdenum, a high-Z metal. Metal PFCs will be critical in a fusion reactor to avoid tritium retention, and avoid material melting. The all-metal walls have, as a necessity, led to in depth research on impurity transport and plasma-material interactions, in particular how to prevent metal impurities from coming into the plasma. To this end, a thin layer of boron is routinely (~every 2 weeks) deposited onto material surfaces to prevent heavy metal erosion, a process dubbed boronization. Highest performing plasmas are often achieved after boronizations.

External heating of the plasma is done primarily with Ion Cyclotron Radio Frequency (ICRF) waves, which damp on minority ions, usually hydrogen. The minority ions then collisionally transfer their energy preferentially to the electrons, but also to background main deuterium ions, raising the plasma temperature. The ICRF technique of plasma heating imparts no significant torque or particle source, in contrast to high energy neutral beams, currently the most popular heating method in fusion

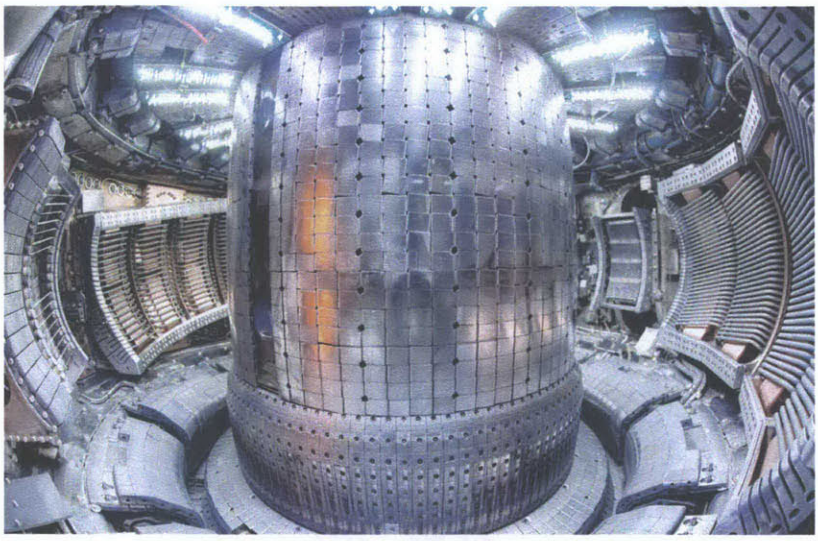

Figure 1-6: In-vessel view of Alcator C-Mod. Photo courtesy of Bob Mumguuard.

Quantity	Alcator C-Mod	ITER
Plasma Major Radius (R_0)	0.67	6.2
Plasma Minor Radius (a)	0.21	2.0
Toroidal Field (B_ζ)	5.4	5.3
Plasma Current (I_p)	1.2	15
Elongation	1.7	1.85
Triangularity	0.45	0.2
External Heating Power [MW]	5	50
Fusion Power	60 W	500 MW
Average Electron Density [$10^{20}m^{-3}$]	1.0	1.0
Average Electron Temperature [keV]	2.0	8.8
β_n	0.5 - 1.2	1.8
ρ^*	0.005 - 0.008	0.0015

Table 1.1: Comparison of Alcator C-Mod parameters and parameters expected in ITER

devices. Reactors will also not have significant external torque or particle sources, owing to the large size required for an economical reactor. The major radius where the wave damps is typically in the core of the plasma, but can be varied by changing the source frequency or the applied toroidal magnetic field. The ICRF waves are launched into the plasma through three separate antennas, the D and E antennas, which are two strap antennas, and the J antenna, which is a 4-strap antenna. Straps

are phased for optimal heating. The total ICRF power available to inject into the plasma is 5 MW.

1.3.1 C-Mod Operating Regimes

Alcator C-Mod has several different operating regimes, each with unique characteristics that will be used in this study of impurity transport through the pedestal region.

L-Mode

L-mode, or "low confinement mode", is the plasma operation when there is insufficient power to transition to improved confinement regimes. As mentioned above, L-mode plasmas exhibit very little gradient in density and temperature in the pedestal region. In L-mode plasmas without ICRF, known as Ohmic L-mode since all heating is from plasma current, very little boron is found in the plasma. This is because core impurity levels are correlated with ICRF source power[24], thought to be due to enhanced sputtering from material surfaces due to fast wave rectification[25]. Most L-mode plasmas have very low impurity particle confinement time, making measurements of impurities difficult. L-mode plasmas can be obtained with higher impurity densities by inputting limited amounts of RF power to avoid transitioning to an higher confinement plasma. In particular, operating with the ion ∇B drift direction pointing *away* from the active X-point almost doubles the allowed input power before a transition to an improved confinement regime occurs[26].

H-mode

Several varieties of H-mode plasmas can be run on Alcator C-Mod. Perhaps the most commonly run is the Enhanced D_α (EDA) H-mode, so named because of an increase in emitted D_α light. This is significant since in most tokamak H-modes, the D_α light is decreased for the duration of the H-mode. The enhanced D_α is indicative of an enhanced particle recycling at the edge, allowing EDA H-modes to be a steady, ELM-less H-mode. The particle transport is thought to be regulated by

a "benevolent" mode in the edge known as the Quasi-Coherent(QC) mode. The QC mode is poloidally localized on the LFS, and radially localized to near the separatrix, with an extent of about 3 mm. It has a characteristic frequency of around 100 kHz, with a bandwidth of 20 kHZ. At the pedestal top, typical electron densities range from 1×10^{20} to 5×10^{20} m^{-3}, and electron temperatures from 400 eV to 700 eV. To obtain EDA H-modes, the edge safety factor must meet the criterion $q_{95} > 3.5$, otherwise the plasma generally transitions into an ELM-free H-mode.

ELM-free H-modes are, as the name implies, also ELM-less plasmas, but unlike EDA H-mode they are transient in nature. The particle confinement time is long, leading to an increase in plasma density, but also accompanied by an accumulation of impurities in the core. At a critical density, these impurities will radiate enough power from the plasma to cause a radiative collapse of the plasma back into L-mode. Since the external input power is usually still above the L-H threshold, this cycle of ELM-free H-mode buildup followed by radiative collapse can occur several times through a plasma discharge. ELM-free H-modes exhibit very little fluctuations in the pedestal region.

H-mode discharges with ELMs are generally difficult to obtain on C-Mod. However, an H-mode known as ELMy H-mode, can be run on C-Mod which has small ELM's thought to be type I. These ELMy H-modes are run using a non-standard magnetic configuration, combined with reduced fueling[27]. This is a useful regime in pedestal structure comparisons with other machines[28]. In between ELMs, after the T_e pedestal has recovered from the ELM crash, there is a strong coherent mode that develops in the pedestal, with a central frequency of 300 kHz. This coherent mode may regulate the pedestal, much like the QCM in EDA H-mode[29]. However, the pedestal steadily builds until it reaches a stability boundary, after which an ELM is triggered. ELMy H-modes tend to have a wider density pedestal than EDA H-modes, but a larger achieved pedestal temperature, with $T_{e,ped}$ ranging from 600 - 900 eV.

All three of these H-mode regimes give unique pedestal parameters, that will allow testing of the variation of impurity transport in different regimes.

I-mode

The I-mode regime is also a high performance plasma, with a temperature pedestal typically higher than most H-mode plasmas. However, the I-mode is markedly different from the H-mode in that it lacks an electron density pedestal[15], as mentioned above. This leads to lower electron densities throughout the plasmas. I-mode plasmas are almost always obtained by running with the X-point in the unfavourable ion ∇B-drift direction setup. At a certain level of external input power, the plasma will make a sudden transition to the I-mode, usually triggered by a sawtooth crash in the core plasma. These sawteeth crashes are thought to drive a heat pulse from the core to the plasma edge, helping trigger the L-I transition. T_e and T_z are generally at the same level at the top of the pedestal, and typically range 600 - 1000 eV. The pedestal top temperature varies during the I-mode due to heat pulses from core sawteeth crashes, though the temperature in the pedestal region remains fixed. Temperature gradient scale lengths are larger in I-mode vs H-mode. I-mode is an ELM-less regime, as could be expected from the low density gradients. There is a benevolent mode in the pedestal region, with a central frequency of $\sim$200 kHz and bandwidth of $\sim$75 kHz, known as the Weakly Coherent Mode (WCM). Like the QCM, it is thought to regulate densities in the pedestal region through enhancing particle transport[30], perhaps even more so than the QCM since a density pedestal never forms. Although the I-mode on C-Mod was only discovered around 2008, much research has been dedicated to it in recent years. The I-mode is seen as an attractive operating regime for a fusion reactor since the L-mode-like particle transport gives little impurity accumulation, while the H-mode-like energy transport gives higher pressure, leading to higher performance.

1.4 Thesis Goals and Outline

By the end of this thesis, the reader will better understand the mechanisms controlling impurity transport in the presence of strong radial gradients in density and temperature, such as in the pedestal region.

Chapter 2 gives background information on previous research investigating poloidal variation of impurities on a flux surface, focusing on velocity measurements which revealed a discrepancy between measured and expected HFS parallel flow.

Chapter 3 introduces the Gas Puff Charge Exchange Recombination Spectroscopy (GP-CXRS) diagnostic used in making the impurity measurements in the pedestal region. The physics basis for the diagnostic is explained, drawing contrasts to high-energy neutral beam CXRS diagnostics. The implementation of the GP-CXRS diagnostic on Alcator C-Mod is presented, for both the LFS and HFS system. Finally, the method of analyzing collected spectra is presented.

Chapter 4 presents measurements of impurity density, temperature, poloidal and parallel velocity, and derived radial electric field at two separate poloidal locations. The registration of profiles to flux surfaces is discussed, and a method of aligning LFS to HFS profiles is presented which seeks to satisfy the total parallel momentum equation.

Chapter 5 discusses asymmetries in the impurity density and temperature, and explores the variation with respect to plasma parameters and operating regimes. Mechanisms which can drive such asymmetries are explored, and most likely causes are ascertained. Additionally, asymmetries in background electron and ion density are explored.

Chapter 6 further explores the impurity velocity measurements, and compares them to the expected flux surface variation of flows in a tokamak. The implications of these measurements on the radial transport of impurities in the pedestal region is assessed for H-mode.

Chapter 7 concludes with a discussion and summary of the research conducted and main conclusions. It also lists several topics and issues for future work on the subject of impurity transport in the pedestal region, poloidal variation of impurities and main plasma quantities in the pedestal, and diagnostic upgrades for the Alcator C-Mod GP-CXRS system.

Chapter 2

Background

Here we review previous results investigating the flows of impurities in the pedestal region, which gave initial motivation for the work accomplished in this thesis. We outline several issues and subjects to address, all towards the final goal of understanding how impurity transport is affected by the pedestal region.

2.1 Transport

We begin with a brief review of transport in a tokamak plasma, leaving most details to more in depth treatments[31, 32].

A plasma is composed of a number of particles of various species. Particles of a particular species j can be described by a particle velocity distribution function, $f_j(\mathbf{x}, \mathbf{v}, t)$, which details the number of particles per unit volume at location $\mathbf{x}$ with velocity $\mathbf{v}$ (both $\mathbf{x}$ and $\mathbf{v}$ are vectors). The particle velocity distribution function is normally assumed to follow the Boltzmann equation:

$$\frac{\partial f_j}{\partial t} + \mathbf{v} \cdot \nabla f_j + \frac{Z_j e}{m_j} (\mathbf{E} + \mathbf{v} \times \mathbf{B}) \cdot \nabla_{\mathbf{v}} f_j = C_j (f_j) \tag{2.1}$$

where most terms have been described previously, except $C_j(f_j)$, which is a collision operator detailing how self-collisions and collisions with other particle species affects the particle velocity distribution f_j. $\nabla_{\mathbf{v}}$ is the gradient operator with respect

to velocity, $\nabla_{\mathbf{v}} = \frac{\mathbf{v}}{v}\frac{\partial}{\partial \mathbf{v}}$.

By taking various velocity moments of Equation 2.1, we can derive equations governing the bulk quantities of the particle j (i.e. "fluid" equations):

Continuity

$$\frac{\partial n_j}{\partial t} + \nabla \cdot (n_j \mathbf{V}_j) = \quad S_j^n \tag{2.2}$$

Momentum

$$m_j n_j \left(\frac{\partial \mathbf{V}_j}{\partial t} + \mathbf{V}_j \cdot \nabla \mathbf{V}_j \right) = \quad -\nabla p_j - \nabla \cdot \overleftrightarrow{\pi}_j + Z_j e n_j \left(\mathbf{E} + \mathbf{V}_j \times \mathbf{B} \right) + \mathbf{R}_j + \mathbf{S}_j^M \tag{2.3}$$

Energy

$$\frac{3}{2} n_j \left(\frac{\partial T_j}{\partial t} + \mathbf{V}_j \cdot \nabla T_j \right) = \quad -\nabla \cdot \mathbf{q}_j - p_j \nabla \cdot \mathbf{V}_j - \overleftrightarrow{\pi}_j : \nabla \mathbf{V}_j + Q_j + S_j^E \tag{2.4}$$

where n_j is the particle density of species j, $\mathbf{V}_j$ is the particle bulk fluid velocity, T_j the species temperature, m_j the particle mass, $p_j = n_j T_j$ the pressure, $\overleftrightarrow{\pi}_j$ the pressure anisotropy tensor, Z_j the particle charge, $\mathbf{R}_j$ the friction force of species j with all other species, $\mathbf{q}_j$ the heat flux vector, and Q_j the energy exchange between species term. Here we also include source terms (S_j^n, $\mathbf{S}_j^M$, and S_j^E), which account for any external sources.

These fluid equations are valid when the plasma species j is in a short mean-free path regime, i.e. that particles undergo several "effective collisions" as they stream along field lines before completing a trip around a flux surface. If particles do not experience frequent collisions, kinetic effects must be treated through the Vlasov equation (or its reduced variants, such as the drift kinetic equation[31]).

When there are inhomogeneities in the magnetic field, such as in a tokamak, the

particle and heat transport is enhanced, known as neoclassical transport. In high collisionality regimes, i.e. short mean-free path regimes, this is caused by the Pfirsch-Schluter flow, which arises to cancel guiding-center drifts that aren't completely cancelled by rotational transform. The increased parallel flow leads to larger parallel friction, which is turn drives radial transport. In low collisionality regimes, when particles can complete a full poloidal circuit without experiencing collisions, the effect of magnetic field inhomogeneities on transport is through particle trapping. Particles with a velocity vector nearly perpendicular to the magnetic field, $|v_\parallel|/v_\perp \lesssim \varepsilon^{1/2}$, will be trapped to the LFS, and so will experience unbalanced guiding center drifts which will enhance their radial transport.

A normalized collisionality parameter, ν^*, is typically used to denote the various transport regimes. This parameter is a measure of the effective collision frequency to the bounce frequency:

$$\nu^* \equiv \frac{\nu_i/\varepsilon}{\omega_b} = \frac{qR_0}{\varepsilon^{3/2} v_{th,i}} \nu_i \tag{2.5}$$

where $\omega_b = \sqrt{\varepsilon} v_{th,i}/qR_0$ is the bounce frequency, $\nu_i = \sum_j \nu_{ij}$ is the ion collision frequency incorporating collisions with all other species, $\varepsilon = r/R_0$ is the inverse aspect ratio, with R_0 the major radius of the magnetic axis, r the minor radius (distance from the magnetic axis), and q is the safety factor. The collision frequency of a particle a with particle b is defined as[32, 33, 34]:

$$\nu_{ab} = \frac{1}{\tau_{ab}} = \frac{4\sqrt{2\pi}}{3} \frac{1}{m_a} \sqrt{\frac{m_a m_b}{m_a + m_b}} \frac{n_b Z_a^2 Z_b^2 \ln\Lambda}{T_a T_>^{\frac{1}{2}}} \left(\frac{e^2}{4\pi\epsilon_0}\right)^2 \tag{2.6}$$

m is the particle mass, Z the particle charge, e is the Coulomb charge, n the density, $\ln\Lambda$ is the Coulomb logarithm, T is the temperature, $T_>$ the temperature of the species with the faster thermal velocity ($v_{th} = \sqrt{2T/m}$), and ε_0 is the vacuum permittivity. Although we defined ν^* with respect to the main ions, we could equally use electrons since $\nu_i/v_{th,i} \sim \nu_e/v_{th,e}$ The various transport regimes are defined in terms of ν^* as:

$$
\begin{array}{rll}
 & \nu^* > \varepsilon^{-3/2} & \text{Pfirsch-Schluter regime} \\
1 \leq & \nu^* \leq \varepsilon^{-3/2} & \text{Plateau regime} \\
 & \nu^* < 1 & \text{Banana regime}
\end{array} \tag{2.7}
$$

The Pfirsch-Schluter regime is the highly collisional, short-mean free path regime mentioned previously, where particle collisions occur before the particle can complete a full poloidal turn. The banana regime is the lowest collisionality regime, where both trapped and passing particles complete poloidal turns without experiencing collisions. The plateau regime is an intermediate regime, where passing particles complete poloidal turns, but trapped particles are interrupted by collisions before completing their orbit. These boundaries between collisionality regimes will be used as strict limits throughout this thesis, while in actuality the boundaries between such regimes are not as clearly defined.

In Alcator C-Mod, H-mode pedestal regions typically span these three collisionality regimes, with the portions far inward of the pedestal top in the banana regime, then the plateau regime up to near the foot of the pedestal, with the remaining portion out into the SOL in the Pfirsch-Schluter regime. The I-mode pedestal region is much lower collisionality (since n_i decreases and T_i increases, and $\nu^* \propto n_i/T_i^2$), with significant portions of the pedestal being in the banana regime.

Most impurities which have a significant density will tend to be highly collisional (i.e. in the Pfirsch-Schluter regime) in the pedestal region, due to the strong Z^2 scaling of the collision frequency. This means that in general for impurities the fluid equations 2.2-2.4 will be valid.

2.2 HFS Parallel Flow Discrepancy

The spatial inhomogeneity of the magnetic field has a direct effect on the form of bulk particle flows on a flux surface, which, under certain common assumptions, can be shown to be (see Appendix A):

$$\mathbf{V}_j = \frac{K_j(\psi)}{n_j}\mathbf{B} + \omega_j(\psi)R\hat{\zeta} \tag{2.8}$$

This equation is applicable for any species: electrons, main ions, and impurity ions. Here $K_j(\psi)$ and $\omega_j(\psi)$ are as of yet unspecified functions which are constant on a flux surface (i.e. flux functions). $\mathbf{V}_j$ is the bulk velocity vector of the particle species j, n_j is the particle density, and other quantities have been defined previously.

Initial investigations[35] into the impurity flow structure in the pedestal region on Alcator C-Mod discovered a significant discrepancy in a commonly used model, as shown in Figure 2-1: the measured parallel flow at the HFS (in red) was more than 3x smaller than the expected (in blue). This expected HFS flow was calculated from Equation 2.8 using LFS measurements of impurity density, poloidal flow, and toroidal flow, and assuming constant impurity density on a flux surface. LFS/HFS comparisons were accomplished by registering the measurement spatial position to its corresponding flux surface, then aligning profiles by enforcing impurity temperature (T_z) constancy on a flux surface[35].

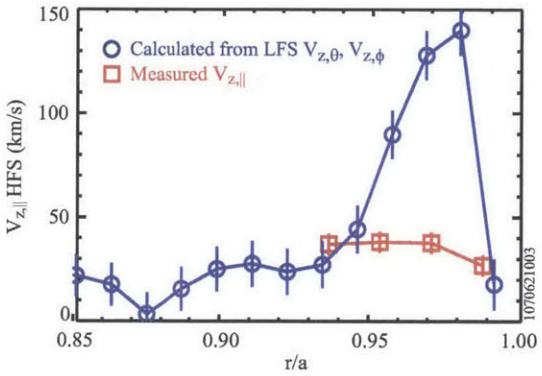

Figure 2-1: Measured and expected HFS parallel flows

An explanation had to be found for this HFS parallel flow discrepancy. Marr et. al. [35] hypothesized that the impurity density was in fact not constant on a flux surface. If the HFS impurity density was larger than the LFS impurity density by a factor of 3-4, the expected HFS parallel flow would be in agreement with the measured flow. While this conjecture can be made directly based on Equation 2.8, there was

also experimental and theoretical evidence, starting back in 1977, that a significant impurity density asymmetry could exist from the HFS to the LFS. A thorough review of past impurity density asymmetry measurements and theory can be found in Ref [36].

Similar HFS parallel flows on ASDEX Upgrade corroborated the existence of the HFS parallel flow discrepancy [37]. However, the authors correctly identified that a density asymmetry isn't the only plausible explanation. Specifically, any physical mechanism which creates a non-negligible radial flux would invalidate the flow equation (Equation 2.8), with the added complication that enhanced radial transport could introduce impurity sources to specific poloidal locations.

Such a discrepancy could be an indication of a significant change in impurity transport behavior, as the impurity transport is directly connected to impurity flows. In order to untangle the various pieces that can be at the cause of the HFS parallel flow discrepancy, we first need to understand in detail the assumptions made in the derivation of the flow equation (Equation 2.8), then inspect the assumptions made in the calculation of the expected HFS parallel flow, which deviates significantly from the measurement. We can then identify further measurements and experiments which will allow an identification of the physics responsible for the HFS parallel flow discrepancy.

2.3 Flows in a Tokamak

The equation for flows in a tokamak (Equation 2.8) is derived making two principal assumptions (see Appendix A):

1. Source-free, steady state continuity equation: $\nabla \cdot n_j \mathbf{V}_j = 0$
2. All flows are directed along a flux surface (i.e. flows normal to the flux surface are negligible, $\mathbf{V}_j \cdot \nabla\psi = 0$)

In the first statement, densities and flows are assumed to be steady-state. This is typically a good assumption in modern day tokamaks, with steady-state conditions

maintained for several energy confinement times. Additionally, the level of density fluctuations is low enough to ignore RMS contributions: $\nabla \cdot \langle \tilde{n}_j \tilde{V}_j \rangle_t \approx 0$.

The more important assumption in the first statement, especially for impurities, is that of source-free region. In the pedestal region, temperatures range between 50 eV to 1000 eV. Impurities have several ionization states, and require more energy to fully ionize. The ionization energy for single-electron impurities is $E = Z^2 E_{Ry}$, where the ionization energy $E_{Ry} = 13.6eV$ is that for a deuterium atom. The study by Marr[35] which discovered the HFS parallel flow discrepancy was done by measuring the flow of full-stripped boron ions (Z=5). The source atoms (B^{4+}) have an ionization energy of ~340 eV, well within the pedestal region. Although impurity transport modelling is required to give more quantitative results, these ionization energies give qualitative evidence that it may be important to retain the source terms in the impurity continuity equation, which in turn would affect the final form of the equation for the impurity bulk flow.

The second statement, that radial flows can be neglected, is an assumption that can be understood by remembering the tendency of particles to stream along field lines, with slow radial movements due to collisions or turbulent motion. However, in regions of strong background plasma gradients, such as the pedestal region, radial velocities increase dramatically, $V_{zr} \propto a_1 \frac{1}{L_{n_i}} + a_2 \frac{1}{L_{T_i}}$ (here a_1 and a_2 are as of yet unspecified constants, see Section 5.3). Even still, the absolute levels of radial velocity will typically remain small (< 1 km/s). However, due to the narrow width of pedestal density and temperature profiles, there can be a non-negligible radial flux, so that $\nabla \cdot (n V_r \hat{r})$ is not negligible in the continuity equation. Recent simulations with the PERFECT code[22], which retains certain pedestal effects (strong L_{n_i}, weak L_{T_i}), showed that indeed the radial flux can become important in the pedestal region, and lead to a breaking of the main ion flux function $K_i(\psi)$. While these simulations aren't specifically applicable to Alcator C-Mod orderings (strong L_{T_i}), they are suggestive that in the pedestal region, radial velocity (or more appropriately divergence of radial flux) can not necessarily be neglected, as is done in the derivation of the flow equation (Equation 2.8).

As shown in Appendix A, the second assumption above can be written in terms of the velocity perpendicular to the magnetic field (but still within the flux surface!):

$$\mathbf{V}_{\mathbf{j}\perp} = -\omega_j(\psi,\theta)\frac{\mathbf{B}\times\nabla\psi}{B^2} \tag{2.9}$$

This ω_j is the same ω_j that appears in the final flow equation (Eq. 2.8). However, the flow equation derivation still holds if we let $\omega_j = \omega_j(\psi,\theta)$, i.e. that ω_j need not be a flux function. The reason it is normally assumed to be a flux function is that the perpendicular velocity is assumed to be to lowest order a combination of the $E\times B$ drift and the diamagnetic drift, which result in $\mathbf{B}\times\nabla\Phi$ and $\mathbf{B}\times\nabla p_j$ terms respectively. If our assumption of small radial velocity is to be satisfied, Φ and p_j must be flux functions, or else the $\mathbf{B}\times\nabla$ terms will produce a radial velocity. As a consequence of Φ and p_j being flux functions, ω_j will be also.

2.4 HFS Parallel Flow Calculation

We now review the method of calculating the HFS parallel flow, which indicated a discrepancy with measurement, as shown in Figure 2-1. The steps to calculate the expected HFS parallel flow are:

1. Measure at the LFS $n_{z,L}$, $V_{z\theta,L}$, and $V_{z\zeta,L}$ using a beam-based diagnostic ('L' indicates a LFS quantity, 'H' indicates a HFS quantity).

2. Calculate the flux function $K_z(\psi)$ and $\omega_z(\psi)$, using Equation 2.8:

$$\begin{aligned} K_z(\psi) &= \frac{n_{z,L}V_{z\theta,L}}{B_{\theta,L}} \\ \omega_z(\psi) &= \frac{1}{R_L}\left[V_{z\zeta,L} - \frac{B_{\zeta,L}}{B_{\theta,L}}V_{z\theta,L}\right] \end{aligned} \tag{2.10}$$

3. Align the LFS and HFS impurity profiles by aligning the measured impurity temperature, T_z.

4. Calculate the expected HFS parallel flow, assuming that $n_{z,H} = n_{z,L}$:

$$V_{z\|,H}^{exp} = \frac{K_z(\psi)}{n_{z,L}} B_H + \omega_z(\psi) R_H \frac{B_{\zeta,H}}{B_H} \tag{2.11}$$

5. Compare $V_{z\|,H}^{exp}$ to the HFS parallel flow measured using a gas-puff based diagnostic

With the knowledge gained from the derivation of the flow Equation 2.8 in the previous section, we can now identify several potential issues with the above method which could explain the observed HFS parallel flow discrepancy.

First, as seen in item 1 and 5, the measurements of impurity parameters at the LFS are made with a diagnostic technique which is different than that of the HFS. As will be discussed in Section 3.5, these two techniques probe the impurity ions using neutral atoms of very different energies, which can potentially give erroneous impurity measurements. A comparison of the two diagnostic techniques was needed to validate the techniques.

Second, item 2 shows that this method relies on K_z and ω_z being flux functions, which can be violated through strong radial transport, or non-conservative forces.

Third, item 3 assumes that temperature is constant on a flux surface. This was based on various estimates of the energy transport time scales, showing that the parallel energy transport was faster than any local radial energy transport, forcing the LFS and HFS T_z profiles to match. As with the particle transport, the relative role of radial energy transport can be significantly increased in the presence of strong gradients.

Fourth, item 4 again points out the need to assume that impurity density is constant on a flux surface, as the diagnostic and knowledge to calculate the HFS impurity density hadn't been developed. However, various evidence from experiment and theory indicate that impurities can vary significantly in the edge of the plasma, especially in the presence of strong background plasma gradients, as is found in the pedestal region.

2.5 Outline of Thesis Research

Clearly from the list of assumptions and their potential pitfalls above, a broader suite of impurity measurements was desired in order to better understand the origins of the HFS parallel flow discrepancy, and in turn understand how the pedestal region affects impurity transport. Research and diagnostic upgrades were conducted to address each of these concerns, and further probe the physics of impurity transport in the pedestal region:

1. A LFS gas-puff based diagnostic was installed and operated, allowing impurity measurements which were redundant of the LFS beam-based diagnostic measurements, allowing an 'apples-to-apples' comparison of the two different diagnostic techniques.

2. A HFS poloidal viewing diagnostic was installed and operated, enabling a direct measurement of the constancy of K_z on a flux surface:

$$K_z = \frac{n_{z,L} V_{z\theta,L}}{B_{\theta,L}} = \frac{n_{z,H} V_{z\theta,H}}{B_{\theta,H}} \tag{2.12}$$

   Along with the poloidal and parallel periscopes installed for the LFS GP-CXRS system, and the already installed HFS parallel periscope, this provided a means to fully measure the velocity vector at the LFS and HFS midplanes, and compare the poloidal variation to the expected form of Equation 2.8.

3. Diagnostic upgrades to measure D_α emission and extensive neutral transport modelling were undertaken to measure the impurity density at the HFS, since the impurity emission depends on the magnitude of the local excited deuterium atoms as a function of distance into the plasma.

4. Experiments were done in plasmas of varying gradient scale lengths in background plasma density and temperature to understand their role in impurity density asymmetries and radial impurity transport.

5. Experiments were done to determine the effect, if any, of a strong, poloidally localized source on the impurity density and flows in the pedestal region.

With these upgrades and experiments, a more complete picture was formed of the transport of boron, the main impurity in C-Mod plasmas, in the pedestal region, and how large background plasma gradients affect this transport.

Chapter 3

Gas Puff Charge Exchange Recombination Spectroscopy Diagnostic

Charge eXchange Recombination Spectroscopy (CXRS, also known as CHERS, CERS, or CXS) is a well-known, mature plasma diagnostic technique used to derive information about ion species in a plasma, such as ion density, ion temperature, and ion bulk velocity[38, 39]. The basic idea behind CXRS is to inject neutral atoms (D^0) into the plasma, which will then undergo charge-exchange (CX) reactions with plasma ions (A^{Z+}):

$$A^{Z+} + D^0 \rightarrow A^{(Z-1)+*} + D^{1+} \tag{3.1}$$

The newly formed excited atoms ($A^{(Z-1+)*}$) radiatively decay, emitting photons which are then collected by optics. Injecting neutrals into the plasma allows localization of the CX reactions to the intersection of the optics line-of-sight and the injected neutral's path. Most CXRS diagnostic systems utilize a high energy (50-100keV range) neutral beam to localize CX reactions. Here we present a novel, alternative CXRS system which uses a simple thermal gas puff to inject neutrals into the plasma.[40]

This alternate system, which we will refer to as GP-CXRS (gas puff CXRS), offers many advantages over a conventional CXRS system which uses high energy neutral

beams. First, the apparatus to inject room-temperature gas is simple, inexpensive, and easy to maintain, whereas high energy neutral beams are large devices which are expensive both in terms of initial cost and maintenance. Second, gas delivery tubes can be placed almost anywhere around the plasma containment vessel, allowing ion measurements at plasma locations not normally accessible to high energy neutral beams, such as the inboard (high-field side or HFS) of a tokamak. This opens up studies of previously inaccessible physics, such as variations in impurity ion density and velocity on a flux-surface[35, 41, 42]. Third, the emission region is narrower, since the gas puff produces a neutral cloud that is smaller in width than a typical high energy neutral beam. This helps avoid smearing effects on the profile measurements[38]. Fourth, compared to some high-energy beam-based CXRS systems, the signal-background ratio is much larger in the GP-CXRS system (typically 10x or more, dependent on beam current and size) in the edge/pedestal region, due mainly to the increased neutral density. This can be especially beneficial in the steep gradient regions of the pedestal[43].

The main disadvantage of the GP-CXRS system compared to a high-energy beam CXRS system is the rapid decay of signal further into the core of the plasma, due to the decreased penetration depth of the slow neutrals produced by the gas puff. In tokamaks, the GP-CXRS system is therefore effectively limited to making measurements in the edge region ($r/a > 0.85$). However, this covers the pedestal region, which is critical to the overall performance of tokamak plasmas through profile stiffness[2] and turbulence reduction by sheared $E \times B$ flow[44]. CXRS diagnostics are one of the principal diagnostics for measuring the radial electric field (E_r) used in calculating the $E \times B$ flow. Extending the predictive capabilities and physics understanding of the pedestal region is an active area of research[45].

Several machines have used results from GP-CXRS systems in published physics papers, among them Alcator C-Mod[35], ASDEX Upgrade[41], and MAST[46], though none have described the diagnostic technique in detail. The focus of this chapter will be to provide the physics basis for the GP-CXRS system, including related diagnostic issues, and describe the analysis process.

3.1 Transport of Neutrals Produced by a Gas Puff

The transport into the plasma of neutrals produced from a gas puff is different from that of neutrals produced by a high-energy beam, mainly due to differences in the energy distribution. The gas puff neutrals have a thermal distribution of energies, which approaches the plasma temperature ($E \sim T_i$). This is in contrast to high-energy beam neutrals, which have fairly discrete energies that are typically much larger than the plasma temperature ($E \gg T_i$). In this section we will develop a picture of the transport of the gas puff neutrals, and show simulation results of the shape and particle density of the gas puff neutral cloud, which is important for GP-CXRS. In the following discussion, we will assume the gas species used is molecular deuterium (D_2), although in practice other gas types can be used with varying benefits (see Section 3.6.1 on spectral contamination by molecular lines).

A simple picture of the production of a neutral from a gas puff and its subsequent transport into the plasma is as follows: a room temperature D_2 gas molecule travels into the edge of the plasma, where it quickly undergoes Franck-Condon dissociation into two separate deuterium (D) neutral atoms, each with kinetic energy of ~3 eV. These neutrals dissociate isotropically, so generally one neutral will continue further into the plasma, and the other will return towards the wall. The neutrals continuing into the plasma will penetrate until being ionized by electron-impact, or charge-exchanging with a background plasma deuterium ion:

$$\begin{aligned} D^0 + e^- &\rightarrow D^{1+} + 2e^- \quad \text{electron impact ionization} \\ D^0 + D^{1+} &\rightarrow D^{1+} + D^0 \quad \text{deuterium charge-exchange} \end{aligned} \tag{3.2}$$

Even in the scrape-off layer (SOL), a region of low temperature and density, these Franck-Condon neutrals have a mean-free path only on the order of the distance to the separatrix[47], clearly an undesirable situation given that we need a significant population of neutrals penetrating beyond the pedestal region. However, the charge-exchange process produces additional generations of neutrals which can then penetrate further into the plasma[48]. These neutrals produced by charge-exchange

retain the energy of the background plasma ions from which they came, so that with sufficient charge-exchange reactions, the neutral population takes on an energy distribution approaching that of the background plasma ion distribution.

To give quantitative results of the neutral penetration, fluid approximations could be used, as is often done in neutral transport problems. Neutrals are treated as either diffusive[49] , which leads to a neutral penetration depth of $\delta \sim (\lambda_{ion}\lambda_{cx})^{\frac{1}{2}} \sim \frac{v_{th}}{n_e(\langle\sigma v\rangle_{ion}\cdot\langle\sigma v\rangle_{cx})^{\frac{1}{2}}}$, or free-streaming[50], leading to a neutral penetration depth of $\delta \sim \lambda_{ion} \sim \frac{V_n}{n_e\langle\sigma v\rangle_{ion}}$. The diffusive nature makes sense when charge-exchange reactions dominate over ionization, as the CX reactions act as a randomizing event, leading to a random walk problem with a step size of λ_{cx}. The free-streaming would be more appropriate if the ionization rate were much larger than the CX rate.

Unfortunately these fluid approximations are too simple for most cases involving neutral transport in the edge/pedestal region. To properly give a more detailed, quantitative treatment of the production and transport of the gas puff neutrals requires the use of numerical, kinetic neutral transport codes. The reasons requiring a kinetic treatment over the simpler fluid treatments are (1) the gradient scale lengths in the pedestal region are often smaller than the neutral mean-free path, violating the fluid approximation and (2) the CX and ionization rate coefficients, $\langle\sigma v\rangle$, are of the same order for a significant temperature range[51], as seen in Fig. 3-1. This range of temperatures basically covers the range of temperatures seen in the pedestal region in most current tokamak devices.

Several kinetic codes exist to simulate neutral transport, the most popular being full 3D Monte Carlo codes such as DEGAS2[53] and EIRENE[54], which are often coupled to 2D fluid codes such as UEDGE, OSM, and B2, to provide full simulation of neutral transport in a background plasma. These codes can offer a complete picture of the gas puff neutral transport at the expense of long code execution times, in order to have good statistics. A simpler code that treats the neutral transport problem analytically is KN1D[55], though it uses a simplified 1D slab geometry.

To study the shape and particle density of the gas puff neutral cloud, OSM-EIRENE simulations were undertaken for a number of different plasma conditions,

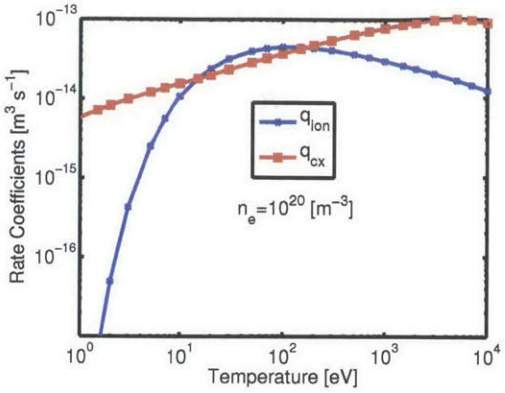

Figure 3-1: Electron-impact ionization and deuterium-deuterium charge-exchange rate coefficients. Taken from the Atomic Data and Analysis Structure (ADAS) code adf11 files[52]

ranging from L-mode plasmas with low T_e and n_e to H-mode and I-mode plasmas with large gradients in the pedestal region. As inputs into the code, measured electron density and temperature profiles are input, covering the entire simulation domain (pedestal region and SOL). As the SOL n_e and T_e aren't measured routinely in H-mode plasmas, a simple model was used typical of SOL profiles[47], with an exponential fall-off in the near SOL followed by a much smaller decay in the far SOL. For these simulations it was assumed $T_i = T_e$.

The results from the OSM-EIRENE simulations are shown in Fig. 3-2 for simulations with gas injected from a gas tube extending from the outer-wall, with Fig. 3-2(a) showing the neutral density along the center-line of the gas puff, $n_{D0}(R)$, where R is the major radius, and Fig.3-2(b) showing the gas puff spread (here the $1/e$ point of the neutral density, $n_D(R,\eta)$), from the gas puff center-line value, in the transverse direction η. As seen, despite the wide range of plasma parameters, the resulting gas puff shape is very similar for all simulations, and can be described by the following diverging Gaussian beam-like formula:

$$n_D(R,\eta) = n_{D0}(R)\exp\left[-\left(\frac{\eta}{W(R)}\right)^2\right] \tag{3.3}$$

where W(R) describes the diverging width of the Gaussian beam:

$$W(R) = w_0 \left(1 + \frac{|R - R_{puff}|}{w_0} tan(\theta_0)\right) \tag{3.3b}$$

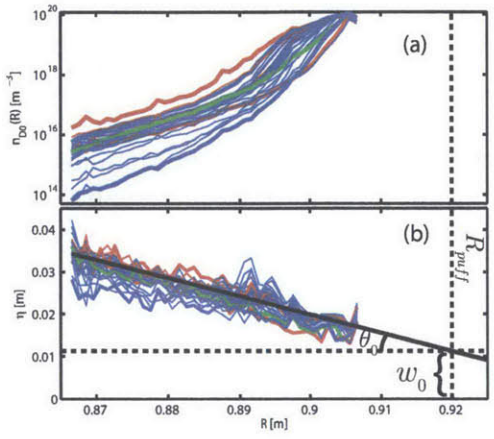

Figure 3-2: OSM-EIRENE simulation results over a wide range of input n_e and T_e profiles: H-modes (blue), I-modes (red), and L-modes (green). Bold lines show the high and low n_{D0} from each group. In (a) is shown the center-line D^0 density from the puff, $n_{D0}(R)$ and in (b) the 1/e point in the transverse direction of n_D from the center line value n_{D0}, showing the puff shape stays the same over a wide range of parameters.

where R_{puff} is the major radius where the gas exits the delivery tube and enters the vacuum chamber, w_0 represents what the beam width *would* be (not actually *is*) at R_{puff} if the gas puff was a pure truncated cone, and θ_0 is the divergence half-angle of the gas puff (see Fig. 3-2(b) for a picture of these parameters). Note that this doesn't necessarily describe the gas puff cloud outside of the separatrix, as the simulation grid was sparse outside of the separatrix. For a gas puff at the outer-midplane, with $R_{puff} - R_{separatrix} \sim 2$ cm, and assuming a cosine distribution of gas molecules entering the plasma, the parameters were fit to be $w_0 \approx 1.1$ cm, and $\theta_0 \approx 23°$. Note also from Fig.3-2 that while a single angle θ_0 parameter describes all of the simulations, the $n_{D0}(R)$ profile varied over several orders of magnitude. No simple scaling was found for the $n_{D0}(R)$ profile shape with n_e or T_e, nor was the $n_{D0}(R)$ profile shape adequately explained by simple neutral penetration models,

like $\text{sech}^2(\frac{|R-R_{puff}|}{\sqrt{\lambda_{cx}\lambda_{ion}}})$ or $exp(-\frac{\langle\sigma_{ion}v\rangle}{V_n}\int n_e dR)$, showing the importance of treating the neutral transport problem kinetically.

These simulations also resolve the velocity distribution of the neutrals, allowing calculation of the neutral temperature, $T_D = \frac{2}{3}\langle E\rangle$. T_D is consistently lower than the background plasma temperature, as shown in Fig. 3-3. This is expected, as the charge-exchanged neutrals can travel to regions of temperature different from that of their local birth location[56]. Other numerical simulations have shown this as well[57]. This difference will introduce an error in the CX rate coefficient if not accounted for, as will be shown in Section 3.2.

Simulated gas puff shape similar for various plasma conditions. Neutral temperature lower than T_i

While relying solely on simulations to deduce the gas puff densities requires further validation studies, these simulation results show two important features of the transport of the gas puff neutrals: (1) the neutral cloud resulting from the gas puff has a small-angle spread and (2) the neutral temperature, T_D, is consistently lower, but approaches the background plasma temperature T_e. From multiple simulations, the ratio of T_D/T_e inside the separatrix and towards the core is usually in a range of $0.3 < T_D/T_e < 0.8$. This range of T_D/T_e holds true for simulations using parameters from either Alcator C-Mod, or ASDEX Upgrade.

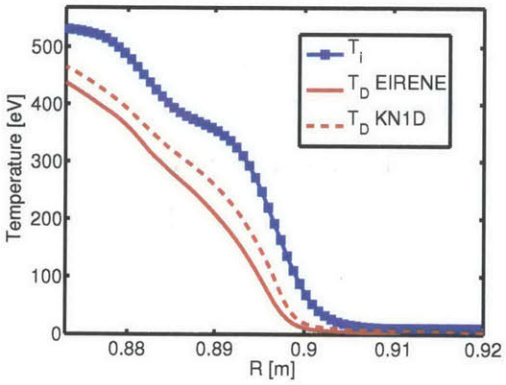

Figure 3-3: Simulated neutral temperature (T_D, in red) vs input measured ion temperature (T_i, in blue. Recall for these simulations $T_e = T_i$.), showing the neutral temperature is generally lower than the electron temperature. Separatrix location is near 0.898 [m].

3.2 Charge Exchange of Impurities with Neutrals from a Gas Puff

The charge-exchange process is also affected by the lower energy and thermal distribution of the gas puff neutrals. This is due to a number of peculiarities of the CX process which will be reviewed and discussed here in the context of GP-CXRS. Depending on the impurity species and the transition used, excited states of the neutral can have a much larger, even dominant, contribution to the CXRS signal.

Charge-exchange is a resonant process, and as a result the donor electron will preferentially populate excited states of the receiver ion that conserve the electron's orbital energy and radius[58]. The prefered, resonant excited state of the impurity ion is:

$$n'_{res} = n^D \left(\frac{Z'}{Z^D}\right)^{\frac{3}{4}} \tag{3.4}$$

where n^D and Z^D are the principal quantum number and nuclear charge of the donor species (the D neutral atom), and n' and Z' are the principal quantum number and charge of the receiver species (the impurity A^{Z+}). This equation is valid for a large range of interacting energies [58, 59]. At low collision velocities, the resonant character is pronounced, leading to large partial CX cross-sections $\sigma_{cx}(n')$ only at or near the excited state n'_{res}. As the interaction energy increases to intermediate energy levels typical of neutral beams, different mechanisms start contributing to the resonant reactions, leading to a broadened n'-distribution of the partial CX cross-sections, as shown in Fig. 3-4. Additionally, in the low collision energy regime the total CX cross-section scales like $\sigma_{cx,tot,lowE} \propto \left(n^D\right)^4$, while the intermediate collision energy regime scales oppositely[60], $\sigma_{cx,tot,intE} \propto \frac{1}{(n^D)^3}$.

These three charge-exchange attributes at low collision energy (preferential excited state n'_{res} of receiver, narrow n'-distribution of partial CX cross-section, and increasing total CX cross-section with n^D) lead to the excited neutrals playing a much more significant photon generating role in GP-CXRS than in high-energy beam CXRS. Figure 3-4 illustrates this point and shows all three CX attributes, for a low

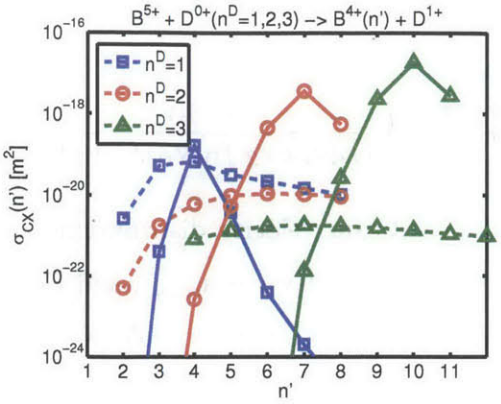

Figure 3-4: Partial cross-sections for electron-capture into the n' excited state of B^{5+} with D^0. Solid lines (_) are for collision energies of 0.25 keV/amu, dotted lines(- - -) are for 50 keV/amu. The $n^D = 3$ cross-sections at low energy are not available[61], and so were scaled from the $n^D = 2$ cross-sections.

energy (0.25keV/amu, solid lines) and an intermediate energy (50keV/amu, dotted lines), using as an example the $B^{5+} + D^0(n^D = 1, 2, 3) \rightarrow B^{4+}(n') + D^{1+}$ reaction. For the diagnostically relevant $n' = 7$ reaction (used for the Alcator C-Mod GP-CXRS system), the $D(n^D = 2)$ cross-section is over 4 orders of magnitude larger than the $D(n^D = 3)$ cross-section, and over 6 orders of magnitude larger than the $D(n^D = 1)$. Despite the small fraction of excited neutrals (typically $\frac{n_D(n^D=2)}{n_D(n^D=1)} \sim 1\%$), they will almost always make the dominant contribution to the GP-CXRS signal. It should be noted that $A^{Z+} + D(n^D = 2)$ being the dominant reaction is a general result for most common applications of GP-CXRS. This is due to a combination of the facts that pedestal CXRS systems typically use low-Z impurities ($Z \leq 10$) with low ionization energies, which guarantee a large population of fully-ionized impurities in the pedestal, and atomic transitions that emit photons in the visible region (400nm-700nm), as the optics are simpler.

Signal from CX with excited state neutrals dominant in GP-CXRS

Of course, the above are simply guidelines; for quantitative results, such as for accurate ion density measurements or GP-CXRS signal estimation, the effective CX rate coefficients must be calculated. In its general form, the rate coefficient for CX into a particular level n' is calculated integrating over the distributions of the interacting

ion and the neutral:

$$\langle \sigma_{cx}(n')v \rangle = \frac{\iint d\mathbf{v}_D d\mathbf{v}_Z \, \sigma_{cx}(n', |\mathbf{v}_D - \mathbf{v}_Z|)|\mathbf{v}_D - \mathbf{v}_Z| f_D(\mathbf{v}_D) f_Z(\mathbf{v}_Z)}{\iint d\mathbf{v}_D d\mathbf{v}_Z \, f_D(\mathbf{v}_D) f_Z(\mathbf{v}_Z)} \tag{3.5}$$

For neutral beam systems, the beam velocity distributions are mono-energetic, i.e. discrete delta-functions, $f_D(\mathbf{v}_D) = n_D \delta(\mathbf{v}_D - \mathbf{u}_{beam})$, and Eq. (3.5) reduces to a 1D integral if the impurity ion species is Maxwellian. For GP-CXRS, the thermal distribution of the neutrals requires averaging over both species velocity distributions. If we assume both the impurity ions and the neutrals have Maxwellian velocity distributions, while allowing them to have different temperatures, Eq. (3.5) reduces to:

$$\langle \sigma_{cx} v \rangle = \sqrt{\frac{8}{\pi m_r}} \frac{1}{T_{eff}^{\frac{3}{2}}} \int_0^\infty dE \, \sigma_{cx}(E) E e^{-\frac{E}{T_{eff}}} \tag{3.6}$$

where

m_r	Reduced mass, $\frac{m_Z m_D}{m_Z + m_D}$ [kg]
T_{eff}	Effective temperature, $\frac{m_D T_Z + m_Z T_D}{m_D + m_Z}$ [J]
E	Center-of-mass energy, $\frac{1}{2} m_r \lvert \mathbf{v}_Z - \mathbf{v}_D \rvert^2$

Here bulk-velocity has been neglected in both species, since it was found that large differences between the bulk velocity of the neutrals and that of the impurity ions of > 60 km/s were needed to make a 10% difference in $\langle \sigma_{cx} v \rangle$. The thermal-thermal averaged rate coefficient in Eq. (3.6), which uses different temperatures ($T_Z \neq T_D$), has the same form of the thermal-thermal rate coefficient using equal temperatures [62], ($T_Z = T_D$), except that the equal temperature is replaced by the effective temperature, T_{eff}. Using this thermal-thermal rate coefficient, the effective CX rate coefficient, $q_{eff}(n' \rightarrow n'')$, is then formed by taking into account the branching ratio of the specific atomic transition, $n' \rightarrow n''$, cascades from states above n', and l-mixing of the states[38]. The effective thermal-thermal CX rate coefficient can be calculated using a combination of the ADAS314 and ADAS308 codes[52], creating a lookup table of q_{eff} values depending on the plasma parameters of n_e, T_e, and Z_{eff}. While these codes only treat same temperature receiver and donor, the effective

temperature T_{eff} (see Eq. (3.6)) can be used for the temperature in the lookup tables of q_{eff} for the case of unequal temperatures.

As shown from neutral transport simulations in Section 3.1, the neutral temperature can be different from the background plasma temperature. In principle, measurements of the temperature of the gas puff neutrals can be made spectroscopically[63]. However, if the neutral temperature is unknown or uncertain, the relative error in the CX rate coefficient can be calculated by using a value in the middle of the expected range, i.e $T_D = 0.5T_Z$. Since the CX cross-section of interest for GP-CXRS systems are relatively independent of energy at low energies, a simple analytical upper bound on the relative error can be found. Taking σ_{cx} to be constant reduces Eq. (3.6) to $\langle \sigma_{cx} v \rangle \approx \sigma_{cx} v_{th}$, producing a relative error, $\epsilon_{\langle \sigma v \rangle}$:

$$\begin{aligned} \epsilon_{\langle \sigma v \rangle} &= \frac{\left| \sqrt{T_{eff}|_{T_D = 0.5T_Z}} - \sqrt{T_{eff}} \right|}{\sqrt{T_{eff}}} \\ &= \left| 1 - \sqrt{\frac{m_D + 0.5 m_Z}{m_D + m_Z \cdot \frac{T_D}{T_Z}}} \right| \end{aligned} \tag{3.7}$$

This upper-bound on the relative error (Eq.(3.7)) is shown in green on Figure 3-5, along with relative errors using the actual CX cross-section in the integral of Eq.(3.6). Of course, neutral simulations can be used to determine the neutral temperature, T_D, and reduce this error $\epsilon_{\langle \sigma v \rangle}$ considerably, but this upper bound error shows that, in the expected T_D/T_Z range, the maximum relative error of $\langle \sigma v \rangle$ assuming $T_D = 0.5T_Z$ is less than 20%. This is near the level of the cross-section error also. Note that while this affects the absolute level of the impurity density, in the comparison of impurity density at the LFS and HFS this error drops out.

Assume $T_D = 0.5T_i$, giving maximum error of 20% in CX rate coefficient

An example of the ADAS calculated thermal-thermal effective CX rate coefficient, q_{eff}, appropriate for use with GP-CXRS is shown in Fig. 3-6, for the $B^{5+} + D(n^D = 1, 2) \rightarrow B^{4+}(n' = 7) + D^{1+} \rightarrow B^{4+}(n'' = 6) + D^{1+} + h\nu$ reaction. Also shown is q_{eff} multiplied by the excited state fraction, which shows the relative amount of CXRS signal photons each neutral fraction is producing. Excited state fractions were determined

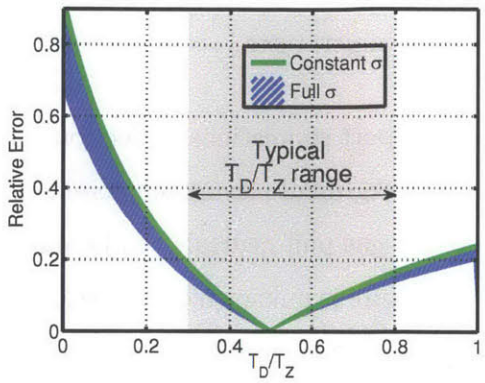

Figure 3-5: Error made in the thermal-thermal CX rate coefficient when assuming a scaled neutral temperature of $T_D = 0.5T_Z$. Typical range of T_D/T_Z from simulation is 0.3 to 0.8

by the ADAS photon emissivity coefficients (PEC)[52]:

$$\frac{n_D(n^D = 2)}{n_D(n^D = 1)} = \frac{PEC_{21}^{EXC}}{A_{21}} n_e \tag{3.8}$$

where A_{21} is the Einstein coefficient for the $n^D = 2 \rightarrow 1$ transition, and PEC_{21}^{EXC} are the ADAS photon emissivity coefficients (PEC) due to excitation. The PEC coefficients are obtained using a full collisonal-radiative model. Here and elsewhere in this thesis, the recombination PEC is neglected, as it is negligible at temperatures above a few eV. The charge-exchange PEC is also neglected, as the deuterium-deuterium charge-exchange process will dominantly produce products that are the same as reactants, giving no net change in excited state populations. As seen in Fig. 3-6(b), for densities larger than $n_e \sim 10^{19}[m^{-3}]$, the $D(n^D = 2)$ excited state fraction will make the dominant contribution to the total emitted CXRS light.

3.3 Energy Dependent Rate-Coefficient Effects

Energy dependent rate coefficients can also have an influence on the apparent temperature and flow of the impurity ions. For CXRS with a high-energy neutral beam, such energy dependent cross-section effects have been investigated extensively [64, 65, 66].

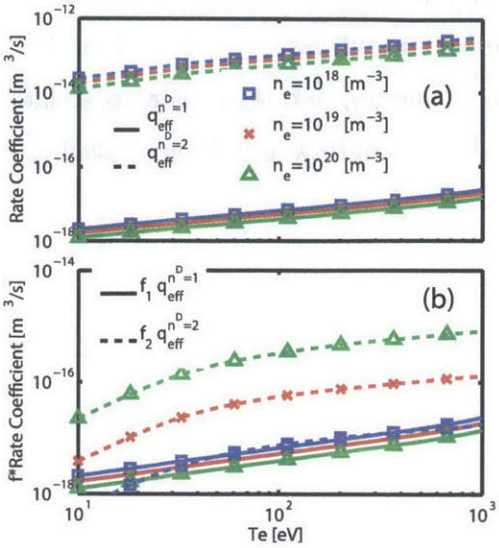

Figure 3-6: (a) $BV(7 \rightarrow 6)$ effective CX rate coefficient, $q_{eff}^{n^D=1,2}$ and (b) $q_{eff}^{n^D=1,2}$ multiplied by the neutral density excited state fraction, $f_i = n_D(n^D = i)/n_D(n^D = 1)$. This represents the amount of light each excited neutral species contributes to the total CX signal.

Here, we treat this problem for GP-CXRS, where the situation is qualitatively different in the sense that the velocity of the donor particles is of the same order as that of the impurity ions.

To quantitatively evaluate measurement errors associated with energy dependent rate coefficients, we need the general expression for the emitted number of photons per unit of time, volume, and wavelength induced by charge exchange (CX) reactions between the donor particles D and the receiver particles A^{Z+} (the impurity ions). We indicate this quantity, the spectral emissivity, with ε^λ, such that

$$\varepsilon^\lambda \mathrm{d}\lambda = \left[\iint \mathrm{d}\mathbf{v}_D \cdot \mathrm{d}\mathbf{v}_{\perp Z} \cdot f_D(\mathbf{v}_D) \cdot f_Z(\mathbf{v}_Z) \cdot |\mathbf{v}_Z - \mathbf{v}_D| \cdot \sigma_{cx,eff}(|\mathbf{v}_Z - \mathbf{v}_D|) \right] \cdot \mathrm{d}v_{\parallel Z}. \tag{3.9}$$

Here, $\mathbf{v}_D$ ($\mathbf{v}_Z$) and f_D (f_Z) are the velocity and velocity distribution function of the donor (receiver) particles, $\perp$ and $\parallel$ indicate the velocity components with respect to

the line of sight, and $\sigma_{cx,eff}$ is the effective emission charge exchange cross section for the transition of interest, in our case $n = 7 \rightarrow 6$ of B^{4+}. The integral is five dimensional and performed over $\mathbf{v}_D$ and $\mathbf{v}_{\perp Z}$. For non-relativistic velocities of the impurity ions, the emitted wavelength λ and $\mathrm{d}\lambda$ are linked to $v_{\parallel Z}$ and $\mathrm{d}v_{\parallel Z}$ by

$$\lambda - \lambda_0 = \frac{\lambda_0}{c} \cdot v_{\parallel Z}, \quad \mathrm{d}\lambda = \frac{\lambda_0}{c} \mathrm{d}v_{\parallel Z}, \tag{3.10}$$

with λ_0 the rest wavelength of the transition and c the speed of light.

Before solving Eqs. (3.9) and (3.10) for realistic cases, we first consider a simplified situation for illustration. We assume that the neutrals in the gas puff are cold and have zero drift, thus $\mathbf{v}_D = 0$. We further assume Maxwellian impurity ions with an arbitrary drift $\mathbf{u}_Z = \langle \mathbf{v}_Z \rangle$ (here, brackets indicate an average over the velocity distribution function). Eqs. (3.9) and (3.10) then simplify to

$$\begin{aligned} \varepsilon^{\lambda} \quad \propto \quad & \int \mathrm{d}\mathbf{v}_{\perp Z} \cdot f^{M}_{\perp Z}(\mathbf{v}_{\perp Z} - \mathbf{u}_{\perp Z}) \cdot |\mathbf{v}_Z| \cdot \sigma_{cx,eff}\left(|\mathbf{v}_Z|\right) \\ & \cdot \quad \exp\left(\frac{-(\lambda - \lambda_1)^2}{2\left(\sqrt{\frac{T_Z}{m_Z}}\frac{\lambda_0}{c}\right)^2} \right) \end{aligned} \tag{3.11}$$

where $f^{M}_{\perp Z}$ is a two-dimensional Maxwellian with temperature T_Z and mass m_Z, and we have defined λ_1 as

$$\lambda_1 = \lambda_0 \cdot (1 + u_{\parallel Z}/c). \tag{3.12}$$

The variable $|\mathbf{v}_Z|$ is expressed as a function of $\mathbf{v}_{\perp Z}$ and λ:

$$|\mathbf{v}_Z| = \sqrt{\mathbf{v}^2_{\perp Z} + \left(\frac{c}{\lambda_0}(\lambda - \lambda_0)\right)^2}, \tag{3.13}$$

Ideally, if the rate coefficient $|\mathbf{v}_Z| \cdot \sigma_{cx,eff}\left(|\mathbf{v}_Z|\right)$ in Eq. (3.11) was constant, the λ−dependence would only appear in the exponential term of Eq. (3.11). In this case, fitting a Gaussian to the measured spectrum allows to extract the accurate

temperature and fluid velocity along the line of sight. However, as will be shown below, the rate coefficient increases with $|\mathbf{v}_Z|$ over most of the energy range of interest here. This means that faster impurity ions are more likely to emit a CX photon and the observed spectrum broadens. Ignoring this effect results in an overestimation of the impurity temperature. The special case with $\sigma_{cx,eff}(|\mathbf{v}_Z|) = const.$ and with no drifts, $\mathbf{u}_Z = 0$, can easily be treated analytically and fitting the obtained spectrum with a Gaussian would then result in an overestimation of the temperature by $\approx 50\%$ (note that these effects could in principle result in non-Gaussian spectral shapes). Besides a line broadening, our simplified treatment also shows that a rate coefficient increasing with $|\mathbf{v}_Z|$ leads to an overestimation of the line shift. To see this, let us assume a drifting Maxwellian for the impurity ions with a drift velocity along the line of sight, away from the observer, such that the central wavelength shows a red shift. The particles moving away at a velocity higher than the drift velocity then have, on average, a larger $|\mathbf{v}_Z|$ and emit more CX photons than the other half of the particles which have a velocity along the line of sight smaller than the drift. This leads to an increase of the apparent line shift.

After these simplified cases, we now quantitatively treat more realistic situations to estimate errors in the measured values of T_Z and $u_{\|Z}$ caused by energy dependent rate coefficients. In particular, we relax the condition of static neutrals. Assuming Maxwellian velocity distributions for the impurity ions and donor particles and using effective emission cross-sections from ADAS[52], we solve Eqs. (3.9) and (3.10) with a Monte-Carlo scheme. We then fit the calculated spectra assuming a simple Gaussian shape to extract the apparent temperatures and flows and compare these with the true values.

For the effective emission cross-sections, we consider Boron charge exchange with $D(n^D = 2)$ neutrals with a subsequent transition from $n = 7 \rightarrow 6$ of B^{4+}. These cross-sections include direct CX into the $n = 7$ level, as well as CX into higher n-levels with subsequent cascades into the $n = 7$ level, the branching ratio for the $n = 7 \rightarrow 6$ transition, l-mixing, and collisional excitations. In Fig. 3-7, we plot the rate coeffi-

cient $v_{col} \cdot \sigma_{cx,eff}(v_{col})$ as a function of $v_{col} = |\mathbf{v}_Z - \mathbf{v}_D|$, which now also depends on the velocity of the neutrals. The data in Fig. 3-7 is plotted up to v_{col} value that is $\sim 3 \cdot (v_{th,D} + v_{th,B})$, with the thermal velocities evaluated at $T_i = 1000$ eV. Cross-sections are plotted for an electron density n_e of 5×10^{18} m^{-3} (green), 5×10^{19} m^{-3} (blue), and 5×10^{20} m^{-3} (red). For each value of n_e, the ion temperature has been varied in the range $100 - 1000$ eV. Increasing ion temperature increases the cross-section, but this is a small effect. Fig. 3-7 shows that the rate coefficients increase approximately linearly with v_{col} over most of the energy range of interest here.

In a first step, we now evaluate errors in the apparent impurity temperature and

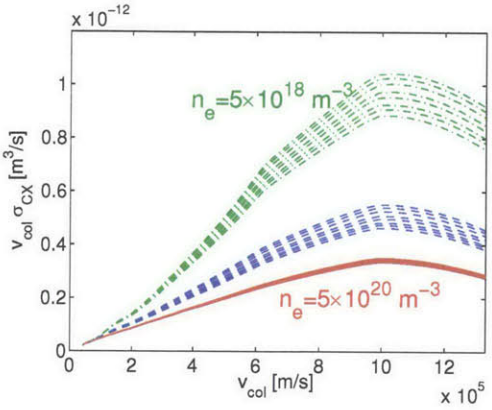

Figure 3-7: Product of v_{col} and the effective emission cross-section for CX reactions between $D(n^D = 2)$ and B^{5+} with subsequent $n = 7 \rightarrow 6$ transition. Red solid, blue dashed, and green dash-dotted curves are obtained with data from ADAS for an electron density of 5×10^{20} m^{-3}, 5×10^{19} m^{-3}, and 5×10^{18} m^{-3}, respectively. Different curves of each color correspond to different values of T_i in the range 100 eV to 1000 eV.

flow for different values of T_Z, T_D, and $u_{\|Z}$, while setting $\mathbf{u}_D = 0$, $\mathbf{u}_{\perp Z} = 0$, and $n_e = 5 \times 10^{19}$ m^{-3}. Fig. 3-8 shows the relative error in T_Z for $u_{\|Z} = 0$ (solid blue) and $u_{\|Z} = 50$ km/s (dashed red), plotted as a function of T_D/T_Z. Curves of the same color correspond to different values of T_Z in the range 100 eV to 1000 eV. At zero flow, the different T_Z curves lie on top of each other. As expected from the analytic solution discussed above, the error in T_Z is approximately 50% for $T_D/T_Z = 0$. This error quickly reduces for finite T_D, reaching values $\lesssim 15\%$ for typical values of $0.3 < T_D/T_Z < 0.8$ (see Section 3.1). Finite parallel flows reduce the error in T_Z,

more importantly for lower values of T_Z.

Fig. 3-9 shows the plot analogous to Fig. 3-8 for the relative error in $u_{\|Z}$, revealing a similar behavior. While errors also become smaller for larger parallel flows, especially for low impurity temperatures, this effect is weaker than for the temperature. Thus, both temperature and flows tend to be overestimated, in agreement with the qualitative discussion above.

In a next step, we have varied the electron density n_e. The results in Figs. 3-8 and 3-9 are found to be relatively weakly dependent on this quantity. Relative errors increase (decrease) by about 20% (10%) when n_e is decreased (increased) by an order of magnitude.

We have further looked at the effect of perpendicular flows, $\mathbf{u}_{\perp Z} \neq 0$. We find that the relative error in the apparent $u_{\|Z}$ decreases with increasing perpendicular flow in a similar way as it does with increasing parallel flow. Perpendicular flows also reduce the error in T_Z, but to a considerable smaller extent than parallel flows observed in Fig. 3-8.

Finally, the effect of a finite drift of the neutrals, $\mathbf{u}_D \neq 0$, can be estimated by applying Galilean transforms to the results above. Drifts of the neutrals can be expected in case of main ion flows, such that the main ions transfer not only their individual velocity, but also their macroscopic flow to the neutrals via CX reactions. This could cause large relative errors in $u_{\|Z}$ in situations where the drift of the impurities is low, while that of the neutrals is not. Let us assume for example that $u_{\|Z} = 0$ and that the drift of the neutrals (and that of the main ions) is $u_{\|D} = -50$ km/s. Transferring to a frame that moves at -50 km/s w.r.t. the lab frame, the neutrals and main ions have no drift and the impurities have $u'_{\|Z} = 50$ km/s. This is the situation solved in Fig. 3-9. For $T_D/T_Z = 0.5$, the measured impurity flow is then overestimated by $\approx 10\%$ or about 5 km/s. Back in the lab frame, we would thus measure an apparent impurity flow of $u_{\|Z} \approx 5$ km/s, directed opposite to the movement of the neutrals.

Overall, we find that for experimentally relevant parameters, cross-section effects associated with GP-CXRS lead to an overestimation of impurity temperatures and

flows of $\lesssim 15\%$. Currently, such errors are neglected in the analysis. However, we stress that GP-CXRS results at both the LFS and HFS will be affected equally to lowest order, so that comparisons between the two locations should be robust. Finally, we note that larger relative errors in the impurity flows could be expected in cases where the main ions have a large flow, particularly if it is opposite to that of the impurities, and if the main ions transfer that velocity to the neutrals.

CX cross-section effects overestimate T_z and V_z by less than 15%

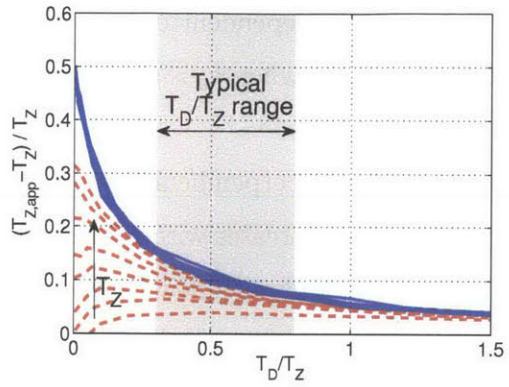

Figure 3-8: Relative errors in the apparent temperature as a function of T_D/T_Z obtained by solving Eqs. (3.9) and (3.10) with the cross-section data of Fig. 3-7 for $n_e = 5 \times 10^{19}$, $\mathbf{u}_{\perp Z} = 0$, and $u_{\parallel Z} = 0$ (blue), and $u_{\parallel Z} = 50$ km/s (dashed red). Different curves for a given color are obtained for different value of T_Z in the range 100 eV to 1000 eV. The arrow indicates increasing T_Z within dashed red curves. The shaded area highlights the experimentally relevant range of T_D/T_Z.

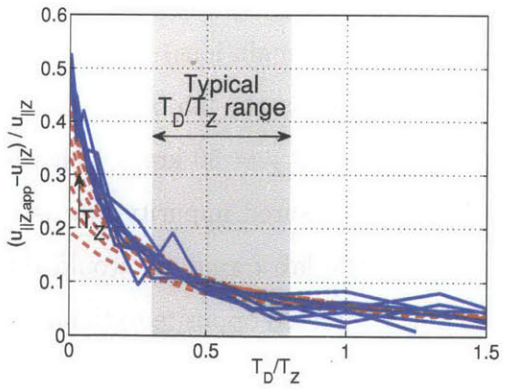

Figure 3-9: The same as in Fig. 3-8 for relative errors in the apparent parallel flow. Here, blue curves correspond to a parallel flow of $u_{\parallel Z} = 5$ km/s.

3.4 Estimates of Expected GP-CXRS Signal

With the information on neutral penetration and effective CX rate coefficients given above, and an approximate impurity concentration in the plasma, estimates can be made to determine the GP-CXRS generated signal. Then, if the background emission (i.e. from bremsstrahlung, CX with naturally occurring neutrals, and electron excitation of the hydrogen-like impurity, $A^{(Z-1)+}$) is known previously from measurement or modelling[67, 68], the amount of injected gas needed for a particular signal/background ratio can be calculated.

The CXRS radiance (sometimes referred to as brightness[1]) is given by the usual equation:

$$I_{cx}(n' \rightarrow n'') = \frac{1}{4\pi} \sum_i \int_{LOS} dl \, q_{eff,i}(n', n'') n_{D,i} n_{A^{z+}} \tag{3.14}$$

where

I_{cx}	CXRS radiance of the atomic transition from upper level n' to lower level n'' $[photons/s/m^2/ster]$
$\sum_i$	Sum over the excited states of the neutral, i=1,2,3,...
$\int_{LOS} dl$	Integral over the optical line-of-sight (LOS)
$q_{eff,i}$	Effective CX rate coefficient $[photons \cdot m^3/s]$
$n_{D,i}$	Neutral density $[m^{-3}]$
$n_{A^{z+}}$	Impurity density $[m^{-3}]$

Simplifying (but accurate) assumptions can be made. First, if the optics are properly aligned to be tangent to flux surfaces at the point of emission, $q_{eff,i}$ and $n_{A^{z+}}$ can assumed to be constant over the LOS integral. Second, based on the discussion in Section 3.2, the $D(n^D = 2)$ reaction will dominate. Using the expression for the $D(n^D = 2)$ density (Eq. (3.8) combined with Eq.(3.3), the equation for the $n^D = 1$ neutral density cloud) and plugging into Eq.(3.14), we arrive at the approximate

[1] 'Brightness' has been used variously to denote the quantity of 'radiance', i.e. both have the units of [photons/s/m^2/ster]. However, the technical definition of brightness is radiance but weighted for the perception of the human eye. As these are absolute radiometric measurements, we will use radiance throughout this thesis.

signal:

$$I_{cx} \simeq \frac{1}{4\pi} q_{eff,2}\, n_{A^{z+}} \frac{PEC_{21}^{EXC}}{A_{21}} n_e n_{D0}(R) \sqrt{\pi} W(R) \tag{3.15}$$

A simple and quick procedure for calculating the neutral density profile, $n_{D0}(R)$, for use in estimating the GP-CXRS signal, is to use KN1D to simulate the $n_{D0}(R)$ profile, as the shape was found to match well with the OSM-EIRENE $n_{D0}(R)$ profile. To match the KN1D molecular pressure input (given in mTorr) to the diagnostically relevant gas flow rate (which will match the absolute values of $n_{D0}(R)$), an effective area of the gas puff cloud must be used, since KN1D is a 1D code. This was found to be empirically $A_{eff} \simeq 2.7 \cdot 10^{-3}\,\mathrm{m}^2$. This corresponds to a radius of $r \simeq 2.9$ cm, which is characteristic of the gas puff extent. The conversion then from gas flow rate to KN1D input molecular pressure is[55]:

$$P_{KN1D} = \frac{u_{D_2}}{\frac{1}{4} \cdot 0.1333 \cdot \frac{1}{k_B T} \bar{v}\, A_{eff}} \tag{3.16}$$

where

P_{KN1D}	KN1D input molecular pressure $[mTorr]$
u_{D_2}	Gas flow rate $[D_2\, particles/s]$
0.1333	Conversion factor $[m^{-3} \cdot J/mTorr]$
k_B	Boltzmann constant, $1.38 \cdot 10^{23}$ [J/K]
T	Gas temperature (usually room temperature, $\sim 293[K]$)
$\bar{v}$	Molecular average speed, $\sqrt{\frac{8k_BT}{\pi m_{D_2}}}$

An example of using Eq. (3.15) to estimate the GP-CXRS signal is shown in Fig. 3-10, compared to actual measured GP-CXRS signal. A constant impurity fraction $n_{B^{5}+} = 0.01 \cdot n_e$ was assumed over the entire profile, which is a typical level for these types of plasmas past the pedestal top. On Alcator C-Mod, the LFS impurity density pedestal location can be significantly shifted inward with respect to the electron density pedestal location, due to the ionization energy of the impurity, and the possible presence of an inward pinch[69]. This constant impurity fraction case is then only expected to match beyond the impurity density pedestal top, which in this case is $R < 0.883$ cm. Of course, if the actual impurity density profile is known

from other diagnostics, much better estimates can be obtained. After doing such an analysis, a user can adjust the input gas flow rate into KN1D to arrive at a desired signal level, I_{cx}, for the GP-CXRS system. This will give a simple, first estimate for the gas puff flow rate needed to generate a usable signal level. For more detailed estimates, full 3D modelling of the gas puff should be used.

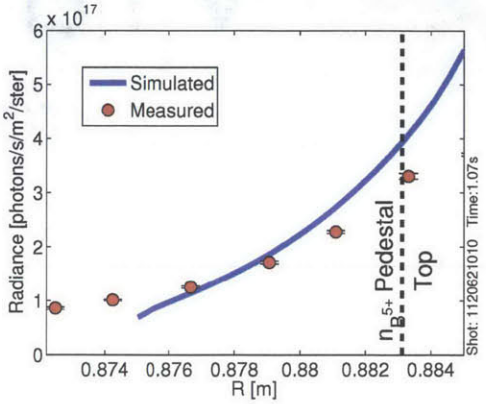

Figure 3-10: Simulated CXRS radiance for views at the top of the pedestal, calculated from Eq. (3.15), assuming a constant $n_Z = 0.01 \cdot n_e$, using B^{5+} for the receiving ion. Agreement with measurement is within 20%

3.5 Alcator C-Mod GP-CXRS System

The Alcator C-Mod GP-CXRS system was initially developed by B. Lipschultz and K. Marr in 2005[70] to measure HFS parallel flows[35]. The system has steadily expanded since then. The spectrometers used are the same as those for the beam-based edge CXRS diagnostic[71]. At the time of this writing, the GP-CXRS system consists of two separate gas puff nozzles, located respectively at the low-field side (LFS) midplane and the high-field side (HFS) midplane. Each gas puff location has its own separate set of in-vessel optical periscopes, one viewing poloidally (vertical at the midplane) and one viewing mainly toroidally (at the location of the gas puff, these views are parallel to the magnetic field). A summary table of these periscopes is given in Table 3.1 and Fig. 3-11.

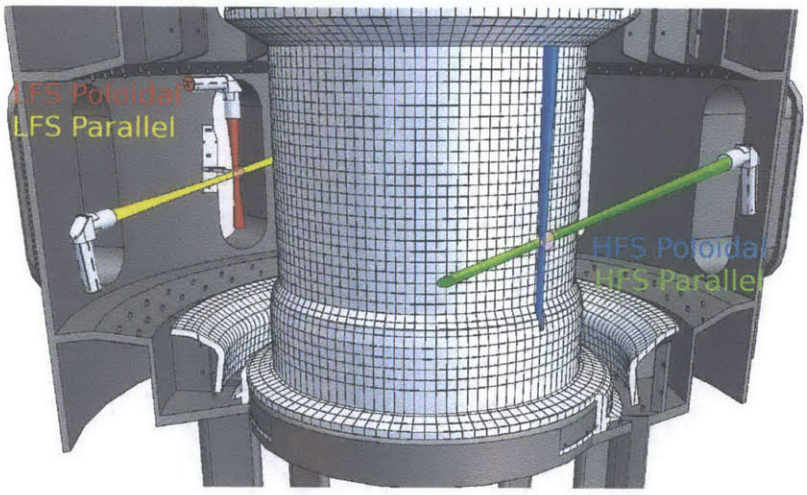

Figure 3-11: Drawing of the in-vessel periscope setup for the Alcator C-Mod GP-CXRS system. Background periscopes are not shown.

Location	Angle of LOS w.r.t $\hat{\phi}$ [deg]	Spot Size [mm]	Typical r/a range	Typical # Views CXRS	Typical # Views D_α
Active (gas-puff viewing)					
LFS	-90	2.0	0.87 - 1.01	14	14
LFS	7	2.7	0.76 - 0.99	14	-
HFS	90	4.0	0.89 - 1.01	9	-
HFS	-10	4.0	0.89 - 1.01	9	9
Background/DNB					
LFS	-90	2.0	0.83 - 1.01	18	1
LFS	173	2.7	0.82 - 1.03	17	-
HFS	90	4.0	0.89 - 1.01	9	-
HFS	-10	4.0	0.89 - 1.01	9	-

Table 3.1: Optical periscope information.

The gas puff nozzles are not nozzles at all, but simple gas capillary tubes, of 1mm inner-diameter and approximate length of 3 m. The outer-wall capillary is held in place by a dedicated structure made of Inconel, at a position of $R \simeq 0.92$ m (the limiter is at $R_{lim} = 0.905$ m). The inner-wall capillary is held in place by the wall-protection tiles, so is positioned at $R \simeq 0.44$ m. These capillary tubes are fed D_2 gas by the C-

Mod Neutral INJection Apparatus (NINJA) system[72]. The NINJA system consists of a gas plenum of volume $1.26 \cdot 10^{-3}\,\mathrm{m}^3$, connected to several capillaries, with each individual capillary controlled by a pneumatic-actuated valve. There are two separate plenums which allow controlling the LFS and HFS gas capillaries with independent gas sources, though they can also be operated from a single plenum, as the volume is large enough to supply both capillaries. Typical input gas quantities for a gas puff used during a shot with the GP-CXRS system are ~4 Torr·L, with a valve opening of 0.1 sec and a plenum pressure of 500 Torr. Because of trapped volumes and long tube lengths, the gas enters the vacuum chamber over a longer period of time[72]. Estimated peak flow rates are $\sim 1.36 \cdot 10^{21}$ D^0atoms / s. An in-vessel image of the LFS gas puff is shown in Fig. 3-12, along with the normalized vertical line outs through the puff from various discharges, showing the gas puff shape is fairly constant for varying plasma parameters, in agreement with the OSM-EIRENE simulations (see Fig. 3-12).

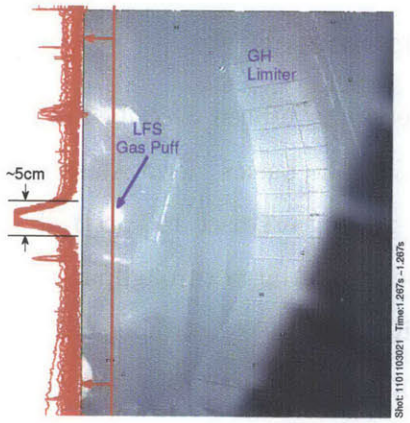

Figure 3-12: In-vessel image of the LFS gas puff. Red lines to the left of the image are vertical line outs from 40+ shots (H-modes, I-modes, L-modes), showing the gas puff shape is similar for varying plasma parameters. The gas puff extent is about 5cm, in rough agreement with OSM-EIRENE simulations.

Optical periscopes are placed in-vessel, as the C-Mod port structure doesn't easily allow external views focused on the pedestal region. Optics focus the light onto 400 μm core diameter multimode fibers, which exit the vessel and are relayed to the

spectrometer/CCD setup. Most periscopes are designed with two doublet achromat lenses, and a front surface mirror to prevent line-of-sight damage to the lenses. A snout measuring 9 cm extends from the mirror, and provides protection from gas films forming during the frequent wall-conditioning boronizations[73]. The exception to this general periscope design is the HFS poloidal periscope, which is embedded in the lower wall-protection tiles of the center stack. Due to the space constraints, this is a smaller periscope, with a single doublet achromat lens, and no mirror. The LFS poloidal and the HFS parallel periscopes have an extra row of fibers co-linear with the normal GP-CXRS fibers, but separated by a small transverse distance (at the spot of best focus, 3mm). These extra fibers are used to measure neutral emission of the gas puff species (usually $D_\alpha, \lambda = 656.10$ nm). The neutral emission measurements are used in the calculation of impurity density, as will be shown in Section 3.6. Additionally, optical periscopes are installed that don't intersect the gas puff, for use as effective background views, to remove passive light contribution to the GP-CXRS signal[67].

3.5.1 CXRS Spectrometers

The edge CXRS spectrometers have been described in detail by McDermott[74] and Marr[75]. Here we will review the basics. Two Kaiser spectrometers with a Volume Phase Holographic (VPH) grating are used to spectrally resolve the CXRS light[76]. These gratings have the benefit of large throughput, allowing 54 views (3 columns, 18 rows) to be imaged with a single spectrometer/CCD setup, but at the cost of a fixed wavelength grating. Three of these views are sacrificed to image a neon lamp, for spectral calibration during an experiment. A flat bandpass (high-cavity), 3 nm bandpass interference filter is used at the entrance of the spectrometer to allow 3 columns of fibers. Because of the fixed gratings, the C-Mod GP-CXRS system monitors exclusively the $BV(n' = 7 \rightarrow 6, \lambda = 494.467$ nm) transition. The CCD used is a Princeton Instruments Photonmax, which has high quantum efficiency ($> 90\%$) and low readout noise (3 e-rms). A mechanical chopper is used to cover the CCD during frame transfer, since otherwise light from all other views in a column would add to each view, effectively smearing the spectra[77]. Integration times are typically 5 ms.

Because the 54 views imaged on the CCD camera can have large differences in light levels (whether it's a background, beam, or gas puff view), its desired to attenuate certain high light level views to prevent saturation, without having to reduce the signal levels globally, through the gain of the CCD, or the F-stop of the spectrometer input lens. For saturating views, short 1 m attenuator fibers with smaller core diameters (100, 200, or 300 μm) than the relay fiber are connected before the spectrometer fiber patch panel. These give an attenuation factor of $f \simeq D^2_{atten}/D^2_{relay}$, where D represents the fiber core diameter.

3.5.2 D_α Photodetectors

The D_α neutral emission is not spectrally resolved since it is the brightest line in the boundary, and so should not have any significant intruding lines. The D_α radiance is measured using Hamamatsu S8746-01 photodiodes. These photodiode packages have a built-in pre-amp, with a specific gain setting ($1\,G\Omega$), allowing for excellent low-noise light collection. Additional parallel feedback resistance can be added to the circuit to reduce the gain setting, and decrease the response time ($t_{rise} = 0.35 \cdot 2\pi \cdot R_f C_f$). Individual $H_\alpha(\lambda = 656.3\,\text{nm}, \Delta\lambda = 3\,\text{nm})$ interference filters were used on each photodiode to measure $D_\alpha(\lambda = 656.1\,\text{nm})$, with an optical collimator before the filter to prevent wavelength shifts of the filter central wavelength.

3.6 CXRS Spectrum Analysis

Spectra obtained from the Alcator C-Mod GP-CXRS system are shown in Fig 3-14. As seen, the signal-to-background ratio is large, even at this spatial location, which is near the pedestal top. Deriving Doppler spectrometry quantities of radiance, velocity, and temperature from the GP-CXRS signal proceeds as in any other CXRS system: remove passive light contributions from the spectra, use a computational nonlinear regression analysis to derive the moments of the spectra (taking care to remove instrument function and Zeeman effects[78]), then relate these moments with their physical quantities[60]. Here we describe these steps in more detail.

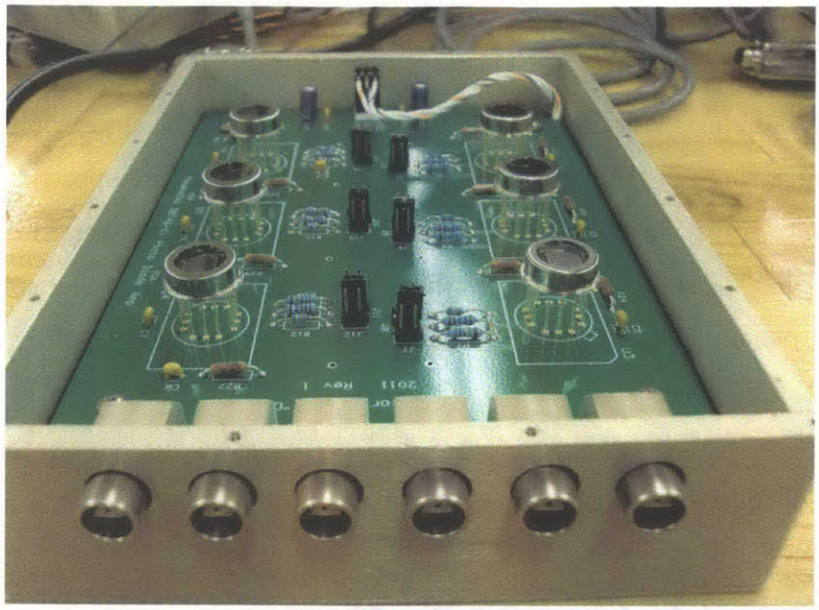

Figure 3-13: D_α photodetectors, in the enclosure for the circuit board. Not shown is the lid, which holds the D_α filter and collimator optics

3.6.1 Passive Light

The light emitted as the result of charge-exchange with gas puff neutrals is known as active CXRS spectrum. There are a number other processes which can produce light in the same wavelength region, and must be removed in order to isolate the active spectrum[67].

First, continuum light, I^{λ}_{Brem}, emitted by the slowing down of free electrons interacting with ions, known as bremsstrahlung, contributes an overall background across the entire wavelength spectrum. While bremsstrahlung light does have a wavelength dependence, it is essentially constant over the 3 nm bandpass of the CXRS system. It is removed from the active spectrum by simply removing the constant offset to the spectrum.

Second, fully-stipped boron ions (B^{5+}) can charge-exchange with naturally occurring neutral atoms, usually in the periphery of the plasma, emitting light I^{λ}_{pass}.

Third, B^{4+} atoms, which generally exist in a thin radial shell around the plasma near the separatrix, can be excited by collisions with electrons, and subsequently emit light (I^{λ}_{exc}) from the same $n = 7{-}6$ transition used for active CXRS. Both I^{λ}_{pass} and I^{λ}_{exc}

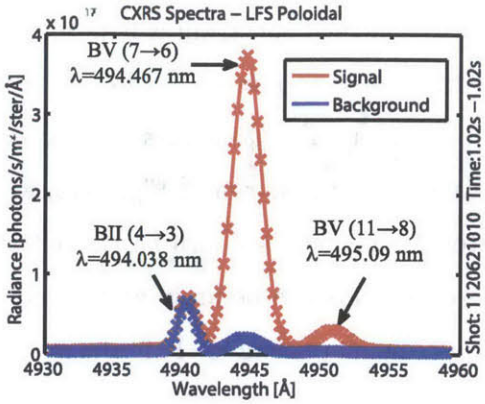

Figure 3-14: Spectra from the GP-CXRS LFS poloidal periscope, showing signal enhancement over the background passive emission. Taken from a view in the pedestal top region.

are emitted at exactly the same wavelength as the active BV spectrum, but generally emit at regions of lower density and temperature, and so affect the spatial resolution. These contributions need to be removed, either by modelling[67, 68] or monitoring a similar spatial region which does not view the gas puff. The latter method is used on Alcator C-Mod, with various background periscopes, as detailed in Table 3.1. For the LFS system, the DNB periscopes are used as background periscopes, interpolating the background from beam off phases (if the beam is on). A time window of about 50-100ms is used before a gas puff to compare the moments of the spectrum from the active periscope to the background periscope. Using these spectrum moment comparison, the background spectrum during the gas puff is then scaled, so that an effective background spectrum is created, and removed from the spectrum collected by the gas puff viewing periscope, leaving the active gas puff CXRS spectrum.

Fourth, there is a neighboring line, BII ($n = 4 - 3$, $\lambda_0 = 494.0376$ nm) to the BV $n = 7 - 6$ line, shown in Figure 3-14), which is from electron excitation of a low ionization stage of boron . While this BII line is well separated from the BV $n = 7-6$ line, it can bleed into the fitting region of the BV line when the temperature and/or magnetic field are high. Generally I^{λ}_{BII} is accounted for by narrowing the fitting region for BV to 494.3nm $< \lambda <$ 494.6nm, though in rare cases (i.e. for HFS toroidal spectrum in reversed field) the BII line is fitted and removed.

The final contribution to collected spectrum is light emitted from molecular deuterium, D_2. Because of the many degrees of freedom in a molecule (translational, rotational, vibrational), molecular light has several closely spaced lines, producing a complicated spectrum. An example is shown in Fig. 3-15, where the measured spectrum right before and after the gas puff is shown for the outermost view ($\rho \approx 1.04$) of the LFS poloidal periscope. As this can be an important contribution near the bottom of the pedestal, we describe more completely in the following section the method to remove the D_2 contribution from the GP-CXRS spectrum.

D_2 Passive Light

The position of tabulated molecular deuterium lines[79] is indicated with green vertical lines. The tabulated lines which are plotted are only the lines from Ref. [79] which have an assigned intensity in the I_2 column of that paper. These tabulated lines agree well with measured emission from a D_2 spectral lamp.

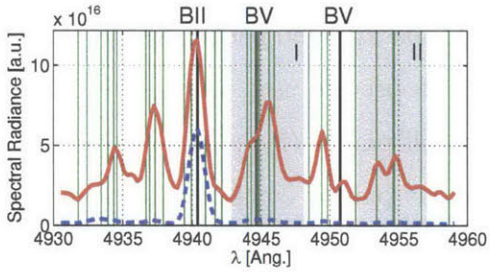

Figure 3-15: Pre (blue dashed) and post (red solid) puff spectrum on the outermost view of the LFS poloidal periscope. The position of D_2 lines as tabulated in Ref. [79] are indicated by vertical green lines.

The parts of the spectra outside the wavelength region of the boron lines can be used to detect the presence of D_2 lines. One can then exclude these spectra in the analysis. Alternatively, one can try to estimate the D_2 contribution to the spectra in order to extract information on the B^{5+} population. In the following, we present a heuristic technique to achieve this. We then validate it using He puffs instead of D_2 puffs, which avoids the problem of contaminating lines in the spectra. He puffs are not used on all shots since this produces a CX signal which is much lower and reaches

less far into the plasma compared to D_2 puffs[80]. Also, the CXRS system is not set up to measure the helium density necessary to calculate $n_{B^{5+}}$ (optical interference filters at a He emission wavelength would need to be purchased).

The technique presented here to estimate the D_2 contribution to the spectrum around the BV line is based on two assumptions. First, we assume that far out in the SOL, the spectrum is entirely due to D_2 emission, i.e., we assume that the contribution of the BV line in the shaded region I in Fig. 3-15 is negligible with respect to the contribution from D_2. Second, we assume that all D_2 lines in the shaded areas I and II of Fig. 3-15 scale with the same factor as we move further into the plasma. To analyze a given spectrum, we then take the active spectrum in Fig. 3-15, scale it such that the amplitude of the lines in region II match those of the spectrum we want to analyze, and subtract the scaled spectrum over the spectral range of interest (region I). Region II is used as it is free from other spectroscopic lines that occasionally appear in other regions. The remaining spectrum is then fitted as usual, using a three Gaussian, Blom-Jupin function[78], to extract intensity, central wavelength, and width of the BV line.

Fig. 3-16 shows an example spectrum and the contributions of D_2 and BV emission obtained with the described method. In order to see how sensitive the result is on the scale factor we apply to the D_2 spectrum, we vary it by $\pm 10\%$ and include the variation of the final fit parameters in the error bars of the deduced plasma parameters.

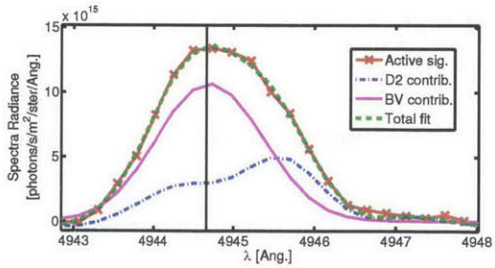

Figure 3-16: Example of a fit to a spectrum where both the BV and D_2 lines contribute.

Fig. 3-17 shows profiles of radiance, ion temperature, and ion poloidal flow of B^{5+} for two similar shots, where D_2 and He was used for the gas puff, respectively. The

profiles in green are obtained by analyzing data from the shot with the D_2 puff and ignoring the presence of molecular lines. The blue data points are obtained for the same data, applying the D_2 subtraction technique described above. We can see that these fit results agree rather well with the data in red, obtained from the discharge with the He puff.

This analysis also clearly shows that a radially increasing ion temperature in the SOL, which one could infer from data with D_2 puffs, is not correct.

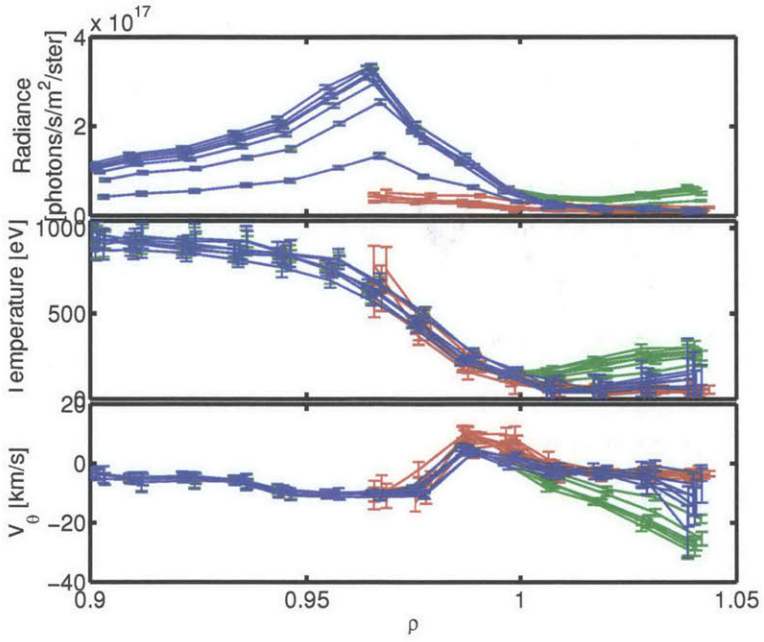

Figure 3-17: A test of the D_2 subtraction method for an I-mode plasma (shots 1120828025/26). Green profiles are obtained from an analysis where the D_2 lines in the spectrum have been ignored. The blue profiles are obtained when the D_2 subtraction technique is applied. Red profiles are obtained from a similar shot where He was puffed instead of D_2.

3.6.2 Zeeman Effect

In the presence of an external magnetic field, the energy levels of an atom split, which is known as the Zeeman effect. With the increased number of energy levels available, the emitted light is made up of several Zeeman components. In practice,

these components are not spectrally resolved, since the plasma temperature is usually high enough that the Doppler broadening effectively smears together the individual contributions. However, at low temperatures and high magnetic field, the splitting caused by the Zeeman effect can result in a spectrum which is much wider than the Doppler broadened spectrum would be in the absence of a magnetic field. If this effect isn't accounted for, erroneously high temperatures would be interpreted from the spectrum.

In determining the Zeeman spectra, generally approximations are made as to whether the perturbation due to the magnetic field is small or large compared to the spin-orbit interaction of the atom ("strong" or "weak" field approximations). However, in many tokamak plasmas, including C-Mod, an intermediate region can be expected, where the perturbation to the atomic energy levels due to the magnetic field and the spin-orbit interaction need to be treated simultaneously. The energy level splitting can be solved exactly for single electron systems[81]:

$$\Delta E_m^{\pm} = \frac{W}{2}\left[2m\beta - 1 \pm \sqrt{\beta^2(g_s-1)^2 + 4m\beta(g_s-1) + (2l+1)^2}\right] \tag{3.17}$$

where $W = \dfrac{m_e c^2}{4}\dfrac{(Z\alpha)^4}{n^3 l(l+)(l+1)}$ and $\beta = \mu_B B/W$, with μ_B the Bohr magneton, $\mu_B = \dfrac{e\hbar}{2m_e}$. Note that the dominant term, the first on the RHS, is proportional to the magnetic field strength, B, and so the energy splitting ΔE and hence wavelength splitting ($\Delta\lambda = \lambda\Delta E/E$) will be larger at the HFS.

Although the most accurate treatment of fitting measured spectra would include each individual Zeeman component as a separate line to fit, in practice this is cumbersome and time consuming. A simple parametrization of the spectra[78] can be used to group the Zeeman pattern according to their polarization, σ^-, π, and σ^+. This parameterization consists of three parameters, α, β, and γ, which are tabulated for a number of atoms and transitions[78]. Below are the constraints found in this parametrization:

$$\frac{I_\pi}{I_\sigma} = \frac{2\sin^2\theta}{1+\cos^2\theta}$$
$$\Delta\lambda_\sigma = \alpha B \tag{3.18}$$
$$W_{fit} = \lambda\sqrt{\frac{T_z}{mc^2}}\sqrt{1+(\beta T_z^\gamma)^2}$$

W_{fit} represents the measured width, which results from the quadrature addition of the Doppler broadening and Zeeman broadening (see Figure 3-18).

Figure 3-18 gives a graphical representation of these quantities. The intensity of the central polarization group (π) compared to either σ^- or σ^+ is given by the first equation, which is dependent on the angle the optics line-of-sight makes with the magnetic field (θ). The wavelength split between the σ^- and σ^+ components is given by the second equation, and as seen is linear in magnetic field strength. The third equation gives the fitted width of each polarization component. The Blom-Jupin parameters for the BV $n = 7 - 6$ line are:

$$\alpha = 0.228379$$
$$\beta = 1.6546 \tag{3.19}$$
$$\gamma = -0.2941$$

From the third equation, what is really desired is the temperature for a given width, $T_z = T_z(W_{fit})$. As γ is in general a non-rational number, the easiest way to calculate $T_z(W_{fit})$ is to calculate W_{fit} for a range of temperature, then fit a function for $T_z(W_{fit})$ that can be used in data analysis. For the BV line, over a temperature range of 10 to 1000 eV this gives a function:

$$T_z(W_{fit}) = -0.01511W_{fit}^5 + 0.2528W_{fit}^4 - 1.716W_{fit}^3 + 416.4W_{fit}^2 - 36.22W_{fit} - 0.3558 \tag{3.20}$$

On Alcator C-Mod, the magnetic field is generally low enough and the temperature high enough that the two Zeeman polarization groups, I_π and $I_{\sigma^\pm}$, are not resolved. On the HFS, however, the periscope viewing parallel to the magnetic field can collect spectra in which I_{σ^+} and I_{σ^-} are resolved, if the temperature is low enough ($T_z < 200$

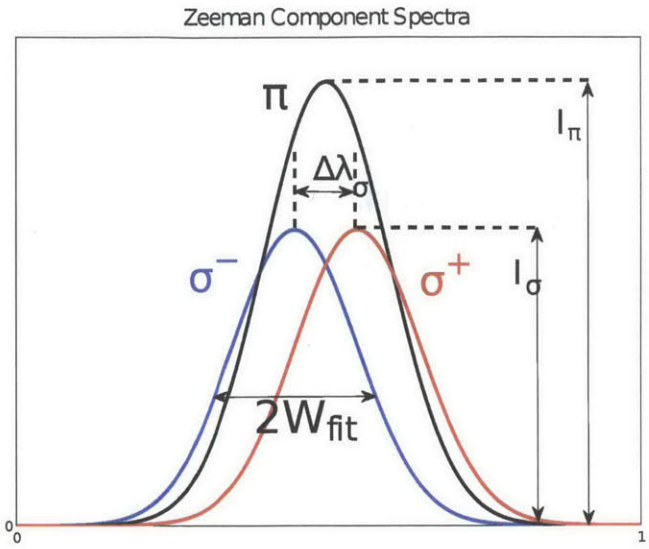

Figure 3-18: Description of the Zeeman parameterization, which groups components into 3 groups determined by polarization: σ^-, π, σ^+.

eV). This is due to the I_π component not being present when viewing parallel to the magnetic field, and because the magnetic field is $\sim R_L/R_H \sim$ 2x larger on the HFS than on the LFS. An example spectrum from the HFS parallel periscope is shown in Figure 3-19.

While the Blom-Jupin parameterization assumes equal heights of the $\sigma^\pm$ components, $I_{\sigma+} = I_{\sigma-}$, the complete Zeeman spectrum has asymmetric components[78], which can become more apparent at low temperatures. This is caused by the the small quantum number ℓ transitions at shorter wavelengths contributing more to the total spectral shape. This has the effect of making $I_{\sigma-} > I_{\sigma+}$. However, as seen in Figure 3-19, the opposite is true for HFS C-Mod spectra. The resolution of this difference appears to be in the spatial resolution of the HFS parallel periscope[82]. In high performance plasmas, such as the H-mode during which the data of Figure 3-19 was collected, the HFS parallel velocity is strongly decreasing, and so a smeared spectrum is collected, leading to the observed asymmetric peaks. In low temperature, low rotation plasmas, the HFS parallel spectra is symmetric.

As the Zeeman effect produces polarized light, care must be taken to ensure that

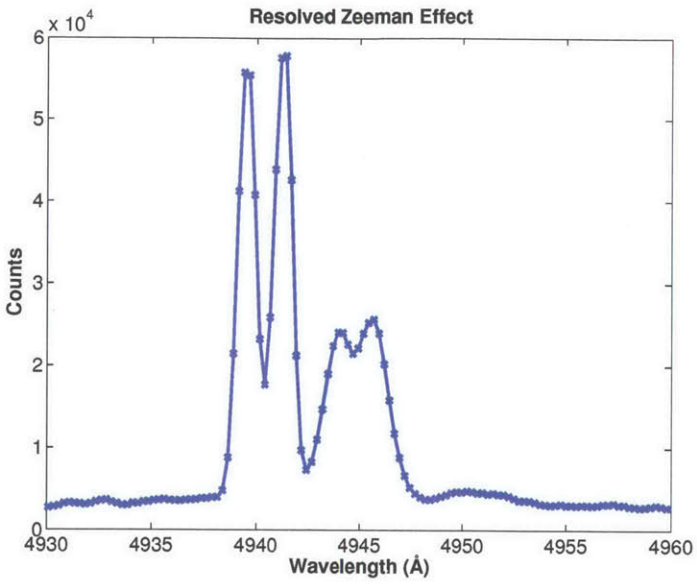

Figure 3-19: Spectrum from the HFS parallel system, showing resolved Zeeman structure.

the light gathering diagnostic is not polarization sensitive, otherwise the ratio I_π/I_σ will not be as parameterized. This incorrect ratio would mainly affect poloidal measurements, since the parallel viewing periscopes have a small I_π, and therefore the ratio is small. The polarization effect is especially a concern for the CXRS periscopes with mirrors, as an apparent blue-ish film develops after being exposed to plasma operations (see before/after comparison in Figure 3-20). This film appears to be due to the interaction of the mirror's enhanced-reflection coating and the plasma. Measurements were made to determine the sensitivity of optical periscopes to linearly polarized light, and found that mirrors with the film had a higher sensitivity, with decreased reflectivity of 15% for light polarized in the plane of the direction of light propagation.

To determine how this polarization sensitive component would affect the measured temperature, synthetic spectra were generated with a code[83] which included the complete Zeeman pattern, and allowed inserting arbitrary linear polarizers in the optical path. Spectra were generated with a 15% polarization effect, and then fit with the typical Blom-Jupin parameterized function used during plasma operations.

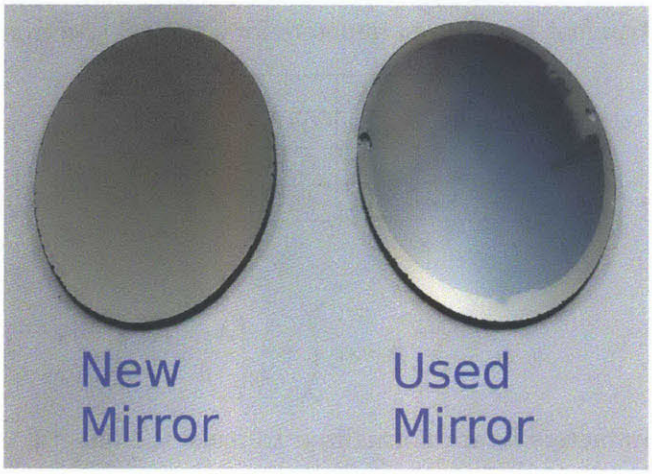

Figure 3-20: In-vessel CXRS periscope mirror before and after a plasma operation campaign.

The difference between the input and fitted temperature was small,, < 15 eV, so we conclude that the polarization of the CXRS optical system has a negligible effect on the derived temperature.

3.6.3 Instrument Function

The spectrometer introduces spectral spreading into any measured light. For an infinitely thin spectral line, the resulting measured spectrum is known as the instrument function (identical to the response function used in signal processing). This instrument function must, like the Zeeman effect, be accounted for in order to derive correct temperatures (and velocities) from the measured spectrum. Instrument functions are measured for the CXRS spectrometers using two Ne I neon lines (λ = 4939.043Å and 4944.987Å) from a neon spectral calibration lamp. These are low temperature lamps, and so the width of the spectral lines should be dominated by the instrumental broadening (the fine structure will give a minor contribution). In terms of the instrument function, the second neon line is redundant, but gives more constraints in the fitting to data (the second line also allows determining the linear dispersion, and so the wavelength at each pixel). The fitting function used for the instrument function is a sum of three Gaussians:

Table 3.2: Instrument function parameters for a typical spectrometer channel.

	h_i	l_i	w_i
$i=1$	0.068	0.214	0.624
$i=2$	0.953	0.048	0.316
$i=3$	0.232	-0.427	0.238

$$y_{inst} = \sum_{i=1}^{3} h_i \exp\left(-\frac{1}{2}\left[\frac{\lambda - l_i}{w_i}\right]^2\right) \tag{3.21}$$

The height parameters h_i are normalized to make the integral of the instrument function unity (attenuation by the measuring instrument are determined in a separate calibration). The three Gaussian form is used because the instrument functions for the CXRS spectrometers can, in general, be asymmetric. A table of instrument function parameters for a typical spectrometer channel are shown in Table 3.2.

3.6.4 Spectrum Fitting

After removing the passive light from measured spectrum as described in Section 3.6, we can now fit the resulting active spectrum to a function encompassing the Zeeman effect, instrument function, and of course Doppler broadening, which is ultimately the effect we are interested in measuring. The emitted light in the Blom-Jupin form will be:

$$I_{cx}^{\lambda} = \frac{B_z}{2 + \frac{I_\pi}{I_\sigma}} \sum_{j=\sigma^-,\pi,\sigma^+} \frac{R_j}{\sqrt{2\pi W_z^2}} \exp\left(-\frac{1}{2}\left[\frac{\lambda - L_z - s_j}{W_z}\right]^2\right) \tag{3.22}$$

$$R_j = \begin{cases} 1, & j = \sigma^- \\ I_\pi / I_\sigma, & j = \pi \\ 1, & j = \sigma^+ \end{cases} \qquad s_j = \begin{cases} -\frac{\alpha B}{2}, & j = \sigma^- \\ 0, & j = \pi \\ \frac{\alpha B}{2}, & j = \sigma^+ \end{cases} \tag{3.23}$$

where B_z is the total radiance, L_z is the line position, and W_z is the half-width of each Zeeman polarization group.

After passing through the optical measuring system, the light will be attenuated by the various transmission components, and spread due to the instrument function. Convolving the emitted light I_{cx}^{λ} with the instrument function we arrive at the measured signal:

$$I_{cx}^{\lambda,meas} = \frac{B_z/B_0}{2+\frac{I_\pi}{I_\sigma}} \sum_i \sum_j \frac{R_j h_i w_i}{\sqrt{W_z^2+w_i^2}} \exp\left(-\frac{1}{2}\left[\frac{\lambda - L_z - s_j - l_i}{\sqrt{W_z^2+w_i^2}}\right]^2\right) \tag{3.24}$$

Here B_0 is the brightness factor, which represents the total transmission and normalized brightness response of the system:

$$B_0 = \frac{R_{spectrometer}^{\lambda}}{T_{peri}T_{relay}T_{filter}^{\lambda}} \tag{3.25}$$

where $R_{spectrometer}^{\lambda}$ is the normalized brightness response of the spectrometers (whitefield image).

The equation for the measured active CXRS spectra, Equation 3.24, is used in a non-linear regression code, MATLAB's `fit`, which derives the best fitting parameters B_z, L_z, and W_z in order to minimize the error between the measured and functional form of $I_{cx}^{\lambda,meas}$. The parameters R_j and s_j, which are functions of the angle of the optical LOS with the magnetic field and the total magnetic field strength, are determined using magnetic fields reconstructed from normal EFIT, and are considered fixed in the non-linear regression.

With the fitted parameters B_z, L_z, and W_z, the measurements of interest, B_z, V_z, and T_z can be extracted. The radiance B_z is the same as the fitted parameter. The velocity V_z follows from the Doppler shift relationship:

$$V_z = c\left(\frac{L_z}{\lambda_0} - 1\right) \tag{3.26}$$

where c is the speed of light, and λ_0 the rest wavelength of the BV transition. The temperature T_z is determined by the Doppler broadening, modified by the Zeeman effect, which is given in the Blom-Jupin parameterization (see Equation 3.20 and

Equation 3.18).

Example radiance, velocity and temperature profiles from the poloidal and parallel LFS systems are shown in Fig 3-21 for an EDA H-mode[84]. The match in temperature validates the expectation from Section 3.3 that the background drift velocity in the direction of viewing does not have a large effect on the measured temperature.

With the profiles of impurity density, temperature, and poloidal and parallel velocities, we can calculate the radial electric field, based on lowest order radial force balance:

$$E_r = \frac{1}{Zn_z}\frac{\partial p_z}{\partial r} - V_{z\theta}B_\zeta + V_{z\zeta}B_\theta \tag{3.27}$$

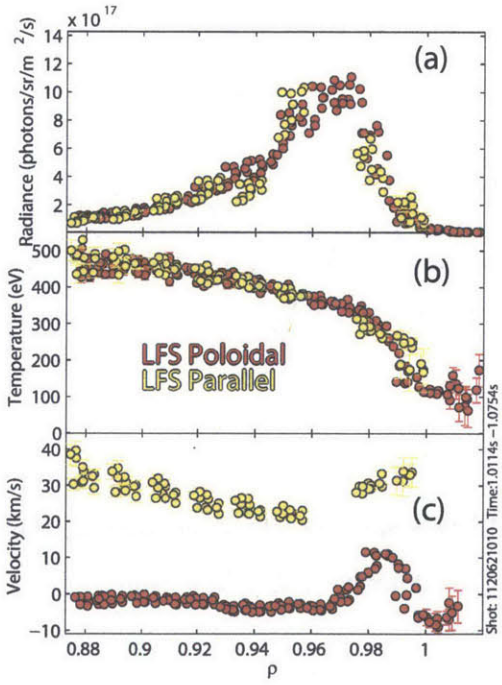

Figure 3-21: Profiles from the GP-CXRS system. (a) radiance, (b) temperature, and (c) poloidal and parallel velocity. ρ here is a normalized major radius coordinate, roughly equal to r/a.

3.6.5 Impurity Density with GP-CXRS

The impurity density can be calculated using Eq. (3.14) with simulated n_D values, or measured neutral emission. The simulations are sensitive to input electron density and temperature profiles, including in the SOL. The SOL n_e and T_e profiles are not routinely measured on Alcator C-Mod in RF heated plasmas. Additionally, simulations don't resolve the time dependence of the gas puff. For these reasons, the measured neutral emission is generally preferred to the neutral simulations. In order to use the measurement, we must relate the excited neutral density, $n_D(n^D = 2)$ to the measured D_α radiance, I_{D_α}. The density $n_D(n^D = 2)$ can be related to the D_α emissivity, ε_{32}, with simple algebra and using the general equations relating emissivity to PEC coefficients[52]: $\varepsilon_{jk} = PEC^{EXC}_{jk} n_e n_D(n^D = 1)$ and spontaneous emission: $\varepsilon_{jk} = n_D(n^D = j)A_{jk}$. The expression for $n_D(n^D = 2)$ (Eq. 3.8) was found using these two general equations for the Lyman-α transition ($n^D = 2 \rightarrow 1$). If we solve for $n_D(n^D = 1)$ in Eq. (3.8), and plug it into the equation for ε_{32}, we arrive at the desired equation relating excited state neutral density $n_D(n^D = 2)$ to the D_α emissivity, ε_{32}:

$$n_D(n^D = 2) = \frac{1}{A_{21}} \frac{PEC^{EXC}_{21}}{PEC^{EXC}_{32}} \varepsilon_{32} \tag{3.28}$$

where ε_{32} is the D_α emissivity in $[photons/s/m^3]$, A_{21} is the Einstein A coefficient $[s^{-1}]$ for the $n^D = 2 \rightarrow 1$ transition, and the PEC^{EXC} coefficients are photon emissivity coefficients from ADAS $[photons/s \cdot m^3]$. Turning again to Eq.(3.14), as long as q_{eff} and n_{Az+} are constant over the optical line-of-sight through the gas puff neutral cloud, they can be removed from the integral, leaving $\int_{LOS} dl\, n_{D,i}$. These assumptions were verified using 3D OSM-EIRENE simulations. Plugging in Eq. (3.28), and noting that the PEC coefficients depend on n_e and T_e, which likewise will be assumed constant

over the intersection of the optical line-of-sight and the emission region, gives:

$$\begin{aligned} n_{A^{z+}} &= \frac{4\pi I_{cx}}{q_{eff,2}(n',n'')\frac{1}{A_{21}}\frac{PEC_{21}^{EXC}}{PEC_{32}^{EXC}}\int_{LOS} dl\,\varepsilon_{32}} \\ &= \frac{A_{21}}{q_{eff,2}(n',n'')}\frac{PEC_{32}^{EXC}}{PEC_{21}^{EXC}}\frac{I_{cx}}{I_{D_\alpha}} \\ &= F\left(n_e,T_e,T_i,T_D,Z_{eff},n',n''\right)\frac{I_{cx}}{I_{D_\alpha}} \end{aligned} \tag{3.29}$$

where I_{D_α} is the D_α line-integrated emissivity (radiance) in $[photons/s/m^2/ster]$, and F is an atomic physics factor, with the dependencies on background plasma parameters shown explicitly. For typical plasma profiles in the pedestal region, this atomic physics factor varies by less than a factor of 2, a significant benefit since then the impurity density is determined mainly by the measured impurity and neutral emission. It should be noted that the PEC coefficients used throughout this thesis were from an older ADAS version, which give too low neutral excited state fractions[85, 86]. Comparing the B^{5+} impurity density using the newer ADAS2010 code version shows that the impurity densities presented in this thesis are overestimated by 20-25%. While this affects the absolute level, it will not affect the comparison of LFS to HFS impurity density, since both will use these same PEC coefficients.

An example of the measured I_{D_α} signal is shown in 3-22, with the simulated I_{D_α} from OSM-EIRENE. The large discrepancy between measurement and simulation in the SOL ($\rho > 1$) could be due to overestimation of the molecular D_2 contribution to the D_α light, or incorrect inputs into the simulation (i.e. electron density and temperature in the SOL).

3.7 D_α Analysis

As the D_α light isn't spectrally resolved (see Section 3.5), in principle all that is needed to derive the D_α radiance, I_{D_α}, is to apply a calibration factor to the measured

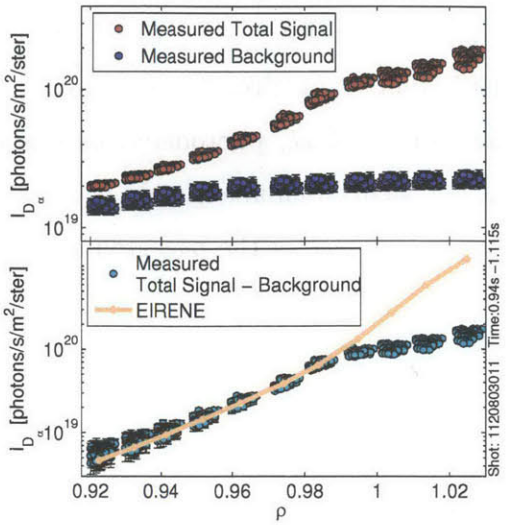

Figure 3-22: (a) Measured D_α radiance, with the total (active + background) in red, and the background in blue. (b) Measured D_α radiance (I_{D_α}) in cyan, resulting from subtracting the background from the signal in (a). I_{D_α} simulated from OSM-EIRENE is shown in orange, showing good agreement with measured signal on confined flux surfaces.

voltages (see Appendix E). The equation for the measured I_{D_α} is:

$$I_{D_\alpha} = \frac{C_{cal}}{T_{peri}\, T_{relay}\, R_{f,plasma}} V_{plasma} \tag{3.30}$$

where C_{cal} is a measured calibration factor (see Appendix E), T_{peri} and T_{relay} are periscope and fiber transmissions, $R_{f,plasma}$ is the photodetector transimpedance amplifier feedback resistance (or gain), and V_{plasma} is the voltage measured by the D_α photodetectors.

In practice, however, care must be applied in removing background D_α contributions that can change over the course of the gas puff. These background contributions can come from neutrals spreading in unconfined plasma region, and drifting into the optics field of view, or changing plasma conditions, i.e. enhanced recycling. As the views close to the separatrix have a large enhancement, they are not as sensitive to the background variations. The core-most views, on the other hand, have much lower signal, comparable to the pre-puff D_α light levels, and so are very sensitive to any

changes in background emission.

To properly account for these changes, one would want an entirely separate periscope, removed from the puff to monitor background D_α emission in a similar geometry. Given that the number of D_α photodetectors was limited, most needed to measure the active gas puff neutral emission, only one background D_α view was employed, to give the time dependence of the background emission. This view was on the LFS poloidal periscope, and was slightly further into the core than the last view on the LFS poloidal periscope viewing the gas puff.

An example of how this background view is applied to the data is shown in Figure 3-23. Here, we've normalized all of the measured, active D_α light at a time $t = 1.24$ s, for the 14 views. The red profiles are the active I_{D_α} without the background removed, which shows a substantial variation in fall-off over time, which is unexpected. By removing the background levels, scaled to vary in time with the measured signal from the single background D_α view, we compute the black profiles, which all show a much similar time trace, consistent with the expectation from the NINJA system. Also shown are the time traces for the BV radiance, which also agrees with the falloff off corrected I_{D_α} profiles, given further confirmation of the technique.

3.8 Comparison to Beam-based CXRS

In addition to the GP-CXRS system, Alcator C-Mod also has a traditional LFS CXRS system viewing a high-energy diagnostic neutral beam (DNB), that produces 50 keV hydrogen neutrals, with a total current of 7 A [74, 71]. This provides a benchmark for comparing the resulting profiles derived from both systems. From Fig. 3-24 we can see the benefit of the GP-CXRS, especially in the pedestal region (for this shot, $0.97 < \rho < 1$) over that of the C-Mod beam based system. The active signal radiance in the pedestal is much higher for the GP-CXRS system in the pedestal region, where the beam based system has little signal enhancement. This also shows that $\rho \sim 0.87$ is the furthest in point for which the GP-CXRS has comparable signal enhancement to the beam based system. Further in the signal will continue falling exponentially,

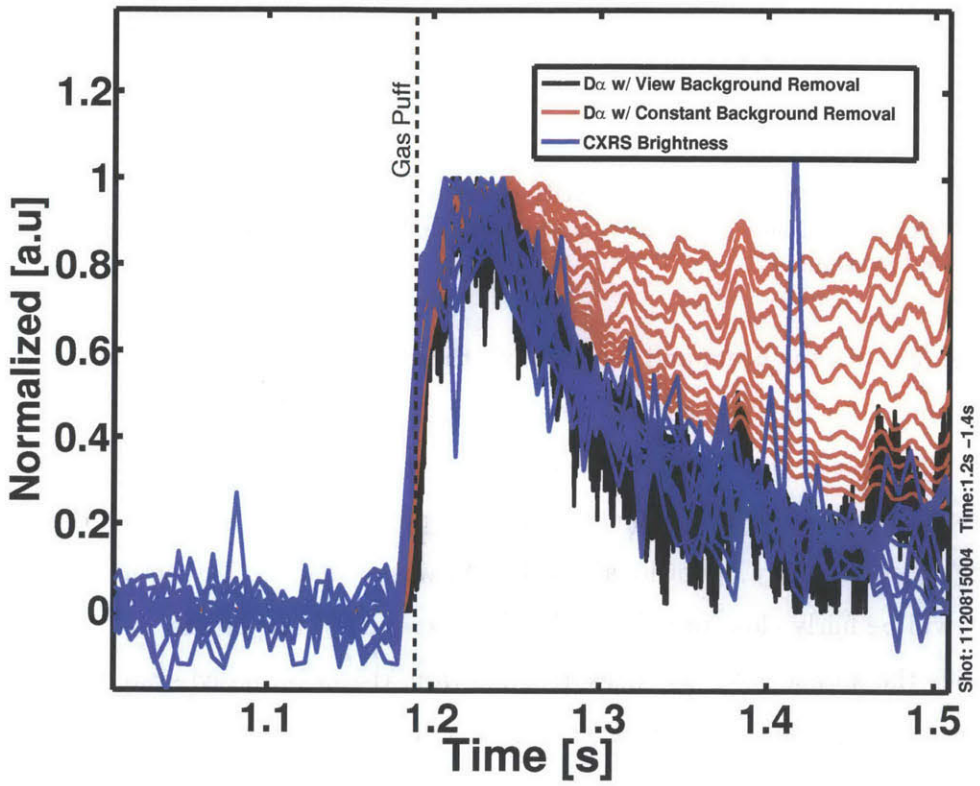

Figure 3-23: D_α background removal result. In red is shown the measured I_{D_α} for each view, which shows a large variation in fall-off time. By removing background D_α light, the profiles in black are obtained. These match the fall-off of the BV radiance measured by the GP-CXRS system, shown in blue. All profiles are normalized to $t \approx 1.25$ s

limiting the GP-CXRS to measurements for $\rho > 0.85$.

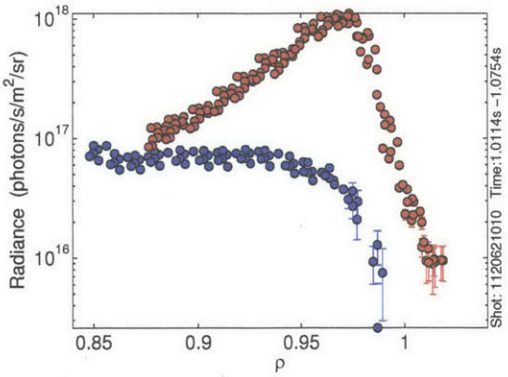

Figure 3-24: Radiance from GP-CXRS (red) and DNB-CXRS (blue). The large signal, especially in the pedestal region, gives GP-CXRS great advantage over the beam based system.

For shots with the beam and the gas puff, the two CXRS systems produce similar n_Z, T_Z, and v_θ for the B^{5+} species, show in Fig. 3-25.

The striations in the GP-CXRS measured n_z are due to not having a background D_α view for this shot. Unfortunately, there were no plasma discharges with the DNB working when the fully operational GP-CXRS was available. The actual impurity density will be fairly close to the middle- to upper-part of this profile.

Notice the absence of $T_{B^{5+}}$ measurements from the beam based system outward from the top of the pedestal. The CXRS signal enhancement with the C-Mod DNB is often too low to resolve the pedestal temperature and velocities completely, a major detraction for the Alcator beam based CXRS system. The high signal to background ratio of GP-CXRS light may not be an advantage for LFS CXRS measurements on machines with heating beams, which can have comparable signal to background ratios. Additionally, beam based CXRS systems have the advantage that the beam attenuation is small over the pedestal region, allowing for smaller systematic uncertainties in determining the impurity density profile. For these situations, the smaller width of the gas puff may still be beneficial, depending on machine size. Ultimately, the comparison of a LFS beam-based versus GP-CXRS system will depend on the properties of the beam and the gas puff achievable. Even when a LFS GP-CXRS isn't

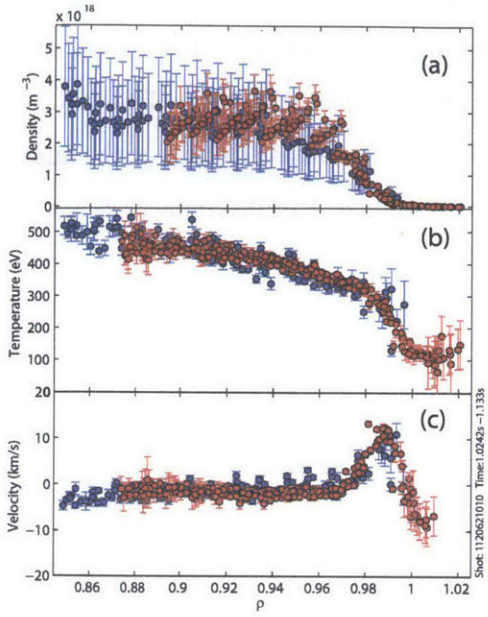

Figure 3-25: Profiles of boron (B^{5+}) (a) density, (b) temperature, and (c) poloidal velocity from the GP-CXRS system (red) and the beam-based CXRS system (blue).

needed, GP-CXRS is still attractive for making CXRS measurements at locations not accessible by heating beams, such as the HFS measurements on ASDEX Upgrade.

3.9 Summary

The GP-CXRS technique developed in this chapter allows measurements of ion parameters in the edge/pedestal region, with the benefits of large signal to background ratio, simple hardware, flexibility in measurement locations, and narrow emission region. The physics basis for the technique was reviewed, focusing on the characteristics of neutral transport and charge-exchange reactions at low energy. Using OSM-EIRENE simulations the gas puff neutral cloud was shown to have a canonical shape, but a large range in neutral density, varying with background density and temperature profiles. These neutral density profiles require a numerical kinetic neutral transport code to properly describe. For calculations of ion density, or expected CXRS signal, the thermal-thermal effective CX rate coefficient (q_{eff}) must be

calculated, since the gas-puff neutrals have a thermal distribution. Cross-sectional effects were shown to be a small correction to the measured temperature and velocity ($< 15\%$). The hardware for the Alcator C-Mod GP-CXRS diagnostic was presented, along with measured spectra and profiles. Details of the analysis were presented, both for CXRS spectra and D_α radiance. Profiles measured with a LFS GP-CXRS system favor very well in comparison with the beam-based CXRS system.

Chapter 4

Pedestal Impurity Profiles at Two Poloidal Locations

In this chapter we present measured pedestal impurity profiles at two separate poloidal locations, the LFS and HFS midplane. These profiles include boron density, poloidal and parallel velocity, and temperature. We discuss the details of aligning the profiles in order to satisfy parallel force balance. This will be crucial in determining the level of in-out impurity asymmetry on a flux surface and the poloidal variation in background plasma parameters, in addition to interpreting the measured impurity flows.

All profiles are plotted versus the ρ coordinate, which is the normalized LFS midplane major radius, $\rho = \frac{R_{mid}(\psi)-R_0}{R_{bdry}-R_0}$, where $R_{mid}(\psi)$ is the major radius at the LFS midplane of a particular flux surface, ψ, R_{bdry} is the major radius at the LFS midplane of the the last closed flux surface (LCFS), and R_0 is the major radius of the magnetic axis. The convention used in describing velocities is the same as used in other Alcator CXRS studies[74, 35]. This convention is that poloidal velocities are positive if upward at the LFS midplane, and parallel velocities are positive if in the clockwise direction if viewed from above. We use this same definition even if the magnetic field and/or current are reversed.

4.1 Profile Alignment

The question of which flux surface a given physical location corresponds to is an important one, that can significantly affect the results and interpretation when comparing profiles measured at two separate poloidal location.

In order to compare the LFS and HFS impurity profiles, accurate diagnostic sight line registration must be done to determine which flux surface the sight line measurement corresponds to. These diagnostic spatial calibrations have been shown to be reproducible to within $\sim$1 mm in real space.

Impurity profiles are then mapped to each other using reconstructed flux surfaces. On Alcator C-Mod, magnetic flux surface reconstructions are done using the code EFIT[87], which solves the Grad-Shafranov equation, a partial differential equation governing the spatial variation of the poloidal magnetic flux in an axisymmetric plasma. Inputs into the code are magnetic measurements at the vessel walls, and spatially resolved plasma pressure and current profiles. The magnetic equilibrium solution is optimized to match these inputs. In general C-Mod operation, canonical pressure and current profiles are input, without resorting to measurements. This can lead to significant misclassification of the flux surface labels in the pedestal, as the typical pressure and current profiles lack the strong gradients found in the pedestal. Additionally, the statistical error of the EFIT determined location of the last closed flux surface (LCFS) is $\sim$5 mm[88].

This spatial misclassification of flux surfaces can be larger at different poloidal locations. In general, points closer to magnetic diagnostics are more accurate, so we expect the HFS midplane flux surface registration to be the most accurate compared to the top of the plasma or the LFS midplane. The LFS midplane region is especially prone to EFIT reconstruction errors due to the use of partial flux loops[89], which are necessitated by the presence of horizontal port openings. An example of the effect of neglecting the strong H-mode pressure profile on the EFIT-calculated magnetic equilibrium is shown in Figure 4-1. Plotted is the difference in ρ using kinetic EFIT (which uses measured, rather than canonical, plasma profiles) and the normal EFIT

($\rho_{KEFIT} - \rho_{EFIT}$) for the LFS midplane, top of the plasma, and HFS midplane. As seen, these differences can vary shot to shot, but the LFS consistently has a larger difference, while the HFS and top show smaller differences, with differing signs. It should be noted here that these differences are constant across the profile, such that a singular shift is needed across the pedestal region for profiles at a particular poloidal angle.

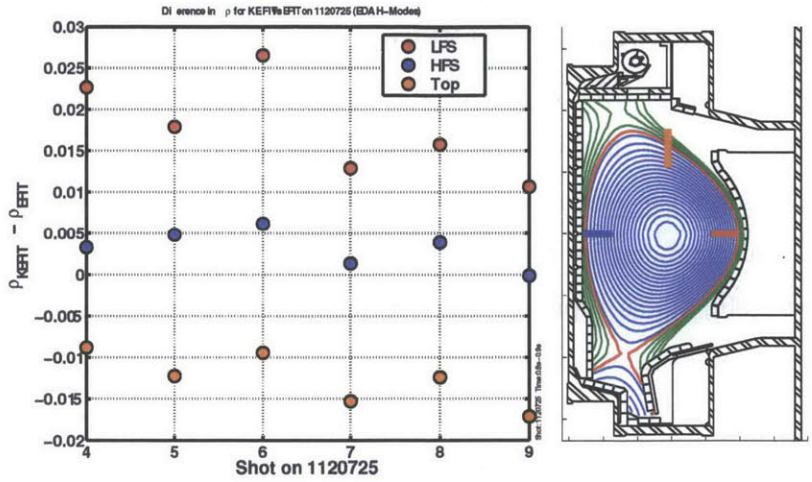

Figure 4-1: Difference between normal and kinetic EFIT calculated ρ values for spatial points at the LFS midplane (red), top (orange), and HFS midplane (blue) of the plasma. The LFS and HFS are where the CXRS measurements are made, and the top is where the electron profile measurements are made by the Thomson scattering system. Also shown is a poloidal flux surface reconstruction, with the measurement locations marked in their respective colors (extent of measurement region is increased here for visual effect).

Normally, kinetic EFIT reconstructions are not available, and besides, may have statistical uncertainties large enough to introduce substantial errors in the alignment of profiles. A general method of aligning the profiles based on the profiles themselves is desirable. In general, we wish to align four sets of quantities:

1. Impurity profiles measured at the LFS midplane (n_{zL}, T_{zL}, V_{zL})
2. Impurity profiles measured at the HFS midplane (n_{zH}, T_{zH}, V_{zH})
3. Electron profiles measured at the top of the plasma (n_e, T_e)
4. Separatrix

Aligning any of the first three sets of profiles to the separatrix gives an *absolute* alignment of that profile to the flux surfaces of the plasma.

4.1.1 Previous Alignment Based on Temperature Equilibration

In past studies[71, 35] using the CXRS system on Alcator C-Mod, impurity profiles were aligned so that both the LFS and HFS impurity temperature profiles matched the electron temperature profile. This will be referred to as the T_z-alignment. The basic argument was based on the high collisionality of most C-Mod plasmas, which tends to thermally couple the electrons and ions. Additionally, arguments can be made that the electron temperature at the separatrix must satisfy parallel heat conduction to the divertor[90], which typically leads to electron temperatures at the separatrix of $\approx$100eV in H-mode plasmas, with very small variation. Since this sets a stringent condition on the poloidal variation of the electron temperature, it was thought then that in turn it sets a stringent condition on the poloidal variation of the impurity ion temperature, since they were assumed to be thermally coupled to the electrons.

LFS and HFS E_r don't match when profiles aligned by T_z

However, with the expanded set of CXRS measurements made as part of this thesis, which completed the measurements at the LFS and HFS needed to measure the radial electric field (E_r), a significant discrepancy between the LFS and HFS E_r was observed when aligning LFS and HFS T_z profiles[82] (see the middle column of Figure 4-2 for an example). This in turn would lead to a large poloidal variation in the electrostatic potential ($\Phi = \Phi_0 - \int_{r_0}^{r} dr E_r$, where Φ_0 is the electrostatic potential at position r_0, and r is a real space coordinate which varies poloidally). Normally, temperature and electrostatic potential (Φ) are both considered flux functions to lowest order[32, 31].

4.1.2 Profile Alignment Satisfying Parallel Momentum

In order to determine a more stringent requirement for the alignment of the LFS and HFS profiles, a solution was sought which satisfied parallel momentum balance. We

will use the general momentum conservation equation for any species j, Equation 2.3, ignoring external momentum sources:

$$m_j n_j \left(\frac{\partial \mathbf{V}_j}{\partial t} + \mathbf{V}_j \cdot \nabla \mathbf{V}_j \right) = -\nabla p_j - \nabla \cdot \overleftrightarrow{\pi}_j + Z_j e n_j \left(\mathbf{E} + \mathbf{V}_j \times \mathbf{B} \right) + \mathbf{R}_j \qquad (4.1)$$

where all terms have been defined after Equation 2.3 (see also the Glossary).

Electron Profile Alignment

For the electrons we can neglect the electron inertia, viscosity, and friction (see Appendix C for detailed derivation and term ordering). If we assume the electron temperature is constant on a flux surface, we can solve the electron parallel momentum equation directly, which results in a Boltzmann relation for the electrons:

$$n_e(\psi, \theta) = n_{eL} \exp\left(\frac{e}{T_{eL}} \left[\Phi(\psi, \theta) - \Phi_L \right] \right) \qquad (4.2)$$

This shows that the poloidal variation of the electron density is directly related to the poloidal variation of the electric potential.

The assumption that T_e is constant on a flux surface is loosely based on the requirement that the electron temperature at the separatrix has to satisfy parallel heat conduction in the SOL. Also, if parallel heat conduction dominates the heat transport, the poloidal variation of electron temperature will be a factor of $\sqrt{m_D/m_e} \sim 60$ smaller than the poloidal variation of ion temperature, due to the electron parallel heat conduction being much faster than the ion parallel heat conduction[82, 91, 92, 93].

The equation for the electron temperature at the separatrix, $T_{e,sep}$, which satisfies parallel heat conduction to the divertor is given by[94]:

$$T_{e,sep} = 7.9 \left(\frac{P_{SOL}\, q^2}{\lambda_{T_e}} \right)^{2/7} \qquad (4.3)$$

where P_{SOL} is the power crossing the separatrix (including radiation losses), and

λ_{T_e} is the electron temperature decay length in the scrape-off layer. Equation 4.3 gives a method to align the electron profiles to the separatrix (in reality, determine where in real space the separatrix is based on the spatial calibration of the electron measuring diagnostic). This then determines *absolutely* where the measured electron profiles are located in the plasma.

Electron profiles absolutely aligned to separatrix through SOL power balance

Impurity Profiles - Relative Alignment

Building off the results from the electron profile alignment, we now determine a method of aligning the LFS/HFS impurity profiles *relative* to each other. Consider the total momentum equation, or the sum of the individual momentum equations for electrons, main ions, and a single impurity ion species. The friction forces will disappear, since by definition $\mathbf{R}_{jk} = -\mathbf{R}_{kj}$, and so $\sum_{j=e,i,Z} \mathbf{R}_j = 0$. The electric potential term will also disappear, as the prefix is $n_i + Zn_z - n_e$, which due to quasi-neutrality is identically 0. Assuming the orderings shown in Appendix C, this reduces to:

$$\mathbf{b} \cdot \nabla(p_e + p_i) = -m_i n_i \mathbf{b} \cdot \mathbf{V_i} \cdot \nabla \mathbf{V_i} - \mathbf{b} \cdot \nabla \cdot \overleftrightarrow{\pi}_i \tag{4.4}$$

The main ion inertia and viscosity terms shown in equation 4.4 may become important in the pedestal region, but without further measurements of the main ion velocity, or more complete theoretical understanding of the form of these equations, we will neglect them for the sake of making progress. This then reduces to simply $\mathbf{b} \cdot \nabla(p_e + p_i) \approx 0$, or in other words that the total plasma pressure is constant on a flux surface. As shown in Appendix C, we can then reduce the equations to:

$$
\begin{aligned}
n_e(\psi,\theta) &= \frac{T_{eL}+T_{zL}}{T_{eL}+T_z} n_{eL} + Z\frac{n_z T_z - n_{zL}T_{zL}}{T_{eL}+T_z} \\
n_i(\psi,\theta) &= \frac{T_{eL}+T_{zL}}{T_{eL}+T_z} n_{eL} - \frac{Z n_{zL}T_{zL} + (ZT_{eL}+T_z)n_z}{T_{eL}+T_z} \\
\Phi(\psi,\theta) &= \Phi_L + \frac{T_{eL}}{e}\ln\left(\frac{T_{eL}+T_{zL}}{T_{eL}+T_z} + Z\frac{\frac{n_z}{n_{eL}}T_z - \frac{n_{zL}}{n_{eL}}T_{zL}}{T_{eL}+T_z}\right)
\end{aligned}
\tag{4.5}
$$

Note that we have assumed $T_i = T_z$, as the ion-impurity energy equilibration is much faster than the processes that drive poloidal temperature asymmetries, or the ion-electron energy equilibration time[82].

The expected E_r at the HFS can then be calculated with the relation $E_r = -\frac{\partial \Phi}{\partial r}$:

$$
\begin{aligned}
E_{rH} &= -\left.\frac{\partial \Phi}{\partial r}\right|_H \\
&= \frac{dr_L}{dr_H}E_{rL} - \frac{\partial}{\partial r_H}\left[\frac{T_{eL}}{e}\ln\left(\frac{T_{eL}+T_{zL}}{T_{eL}+T_{zH}} + Z\frac{\frac{n_{zH}}{n_{eL}}T_{zH} - \frac{n_{zL}}{n_{eL}}T_{zL}}{T_{eL}+T_{z,H}}\right)\right]
\end{aligned}
\tag{4.6}
$$

where subscript 'L' refers to quantities at the LFS, and subscript 'H' at the HFS.

LFS and HFS impurity profiles aligned relative to each other through parallel force balance, essentially matching E_r

As seen, the resulting equation for the HFS E_r only depends on quantities which we measure (except for dr_L/dr_H, e.g. the flux expansion at the LFS and HFS, which is taken from EFIT). With the measured profiles of T_e, $n_{e,L}$, T_{zL}, T_{zH}, n_{zL}, n_{zH}, and E_{rL} we can optimize the shift between the LFS and HFS impurity profiles until the measured HFS E_r best matches the expected HFS E_r from equation 4.6.

In most cases studied, the second term on the RHS of Equation 4.6 makes a smaller contribution than the first term, the LFS E_r. This means that the measured E_{rL} and E_{rH} can be used to give an approximate *relative* alignment of the LFS and HFS impurity profiles. This arises due to the logarithmic sensitivity of the pressure balance to in-out temperature asymmetries.

Impurity Profiles - Absolute Alignment

Up until this point, we haven't specified a way to align LFS and HFS impurity profiles to the electron profiles (which would also allow *absolute* alignment of the impurity profiles, since the electron profiles are absolutely aligned, see the above discussion on electron profile alignment). This could potentially be important in the LFS and HFS alignment, due to the dependence of the expected HFS E_r on n_e and T_e. The location of the electron profiles with respect to the impurity profiles is also important since n_e and T_e are used in the calculation of the impurity density (Equation 3.29).

There is some precedent for the idea that the main ion diamagnetic term balances the radial electric field, i.e. $E_r \approx \frac{1}{en_i}\frac{dp_i}{dr}$. If this were true, we could calculate a third measured E_r profile, using $n_i = n_e - Zn_z$ and the measured impurity temperature, $T_i \approx T_z$ to calculate p_i. This would then allow us to align the impurity profiles to the electron profiles by matching the measured E_r. However, it isn't clear whether the main ion perpendicular velocity is negligible on Alcator C-Mod. In DIII-D, measurements in helium plasmas showed large main ion velocities[95], and both poloidal and toroidal velocities made significant contributions to the E_r calculation. Recent measurements in ASDEX-Upgrade showed the opposite, that the E_r calculated from main ion parameters was dominated by the diamagnetic term alone[96]. The resolution of these conflicting results may lie in the collisionality regime which they were made (banana for DIII-D, Pfirsch-Schluter for ASDEX), as at lower collisionality orbit squeezing can become more important in regions of strong E_r[12], which will reduce the pressure gradient. C-Mod pedestals are generally in the plateau collisionality regime. On C-Mod L_{T_z} is much smaller than the ASDEX L_{T_i}, possibly indicating the main ion velocity could be more important for C-Mod ($V_{\theta,i} \propto dT_i/dr$). Without main ion measurements, it's unclear whether this could be a useful method of aligning the impurity profiles to the electrons profiles.

In order to *absolutely* align the impurities, we will make the ansatz that the top of the impurity ion temperature pedestals are *at or outside* of the top of the electron temperature pedestal. This tends to locate the E_r well minimum measured from the

impurity profiles at the LFS and HFS close to the minimum in the E_r diamagnetic term calculated from the electron n_e and T_e profiles. Although this leaves the impurity profiles under constrained in their alignment to the electron profiles (and in turn to their *absolute* alignment), it will have a negligible effect on the *relative* LFS to HFS impurity profile alignment, as the impurity temperature poloidal variation will have a small effect on the expected HFS E_r (Equation 4.6) and the impurity density calculation is negligibly affected by variations of n_e and T_e about these small shifts around this nominal alignment. This alignment procedure, based on satisfying total pressure (electron and main ion) constancy on a flux surface, will be referred to as E_r-alignment, even though it includes the poloidal temperature asymmetry modification to expected HFS E_r, as shown in Equation 4.6.

E_r-alignment undercontrains absolute alignment of impurities to electrons and the separatrix. Relative alignment (LFS/HFS) is robust.

An example of the T_z- and E_r-alignment procedure is shown in Figure 4-2. Shown are the original, unshifted density and temperature profiles, mapped using normal EFIT. Following are the profiles aligned to match all temperatures, which shows the mismatch of the measured LFS and HFS E_r. The final alignment is obtained by shifting the LFS impurity profiles outwards until the expected and measured HFS E_r match. This makes it so that both the LFS and HFS T_z profiles are at or outside of the T_e pedestal. In total, these shifts for the LFS system are $\Delta\rho \sim 0.032$, or ~ 7 mm, while for the HFS system they are $\Delta \sim 0.0061$, or ~ 1.4 mm. It should be noted that within the error bars, there is an additional allowable shift of $\rho \sim 0.002$ which still satisfies matching the HFS E_r to the calculated HFS E_r. While 7mm is seemingly small and insignificant, not applying these correct shifts leads to gross differences in electric potential[82].

4.1.3 Plasma Sweeps

To aid in the alignment, a technique of sweeping the plasma position slowly to fill in spatial gaps in profiles was used. This has been used successfully in other machines as well[97, 64] to give more detailed pedestal profiles than would be available with fixed spatial views. These plasma sweeps generally moved the entire plasma by 4mm over 100-200ms, so the minor radius remained stationary during the sweep.

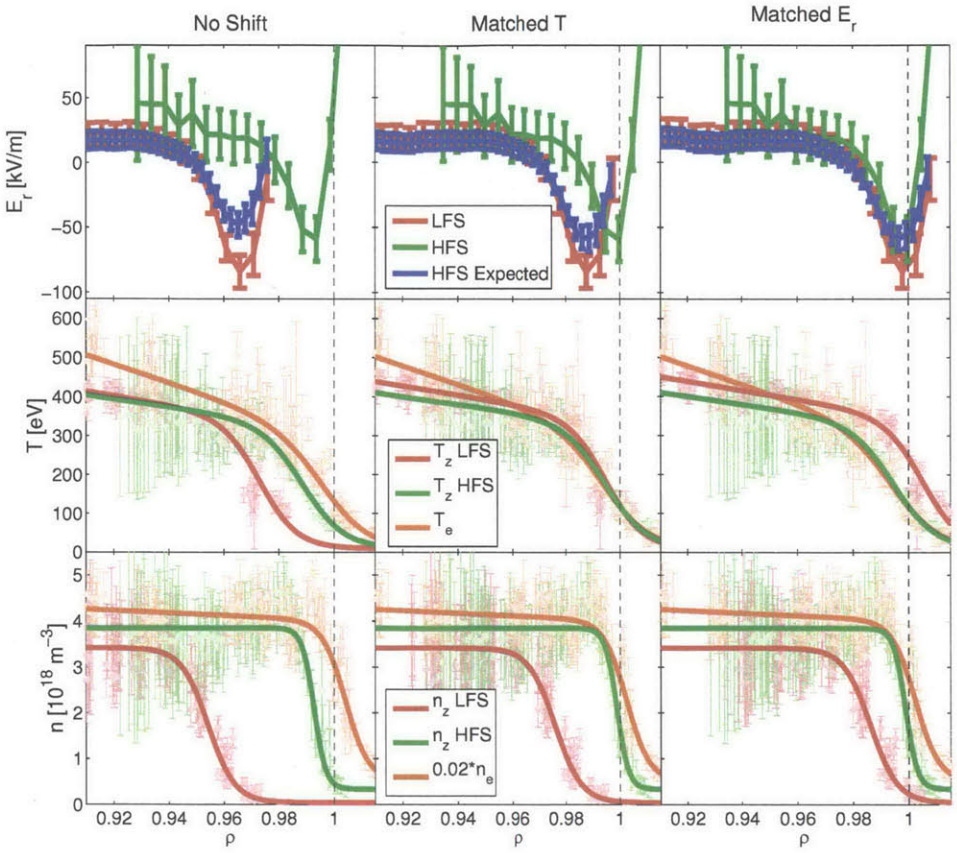

Figure 4-2: Example of the alignment technique for profiles in an EDA H-mode. In the first column are shown profiles with their calibrated position. The second column shows the profiles when the LFS and HFS T_z profiles are matched. The third column shows the alignment procedure used throughout this thesis, the E_r-alignment, where profiles are shifted until the HFS measured E_r matches the expected (Equation 4.6).

4.1.4 Alignment Summary

To summarize the alignment procedure, the electron T_e profile is used to *absolutely* constrain the position of the measured electron profiles to its corresponding flux surfaces in the plasma (i.e. to the separatrix). T_e is assumed to be a flux function, while n_e is allowed to vary poloidally, determined by the poloidal variation in electric potential, Φ. The LFS and HFS impurity profiles are shifted such that the measured T_z pedestal top location is *at or outward* of the T_e pedestal top. The LFS and HFS

impurity profiles are aligned *relative* to each other by matching the expected HFS E_r to the measured HFS E_r, using Equation 4.6.

As this alignment procedure does include a number of assumptions that remain to be validated, at various points throughout this thesis, we will compare profiles using the T_z-alignment versus the E_r-alignment. At various parts we will also point out the relative position of quantities, such as the pedestal location of the impurity density with respect to the pedestal location of the impurity temperature, and how these change in various plasma operational regimes. However, for the remainder of this chapter, and in general throughout this thesis, the presented profiles will be aligned exclusively using the E_r-alignment (i.e. based on total pressure conservation on a flux surface).

4.2 L-Mode Profiles

In general, accurate boron measurements are difficult in Ohmic L-mode plasmas due to a reduced level of boron in the plasma (leading to lower signal). The HFS system has especially low signal during Ohmic L-modes. However, low levels of RF power, with accompanying increased boron levels, can be input without the plasma transitioning to higher performance plasmas such as H-mode and I-mode. Especially beneficial are RF heated plasmas with the active X-point in the unfavorable ion ∇B drift direction, since they require approximately 2x more input power to transition into H-mode[26].

Shown in Figure 4-3 are profiles from such an L-mode with the active-X point in the unfavourable ion ∇B drift direction. This RF-heated L-mode plasma had $I_p = -1.1$ [MA], $T_e^{ped} = 400$ [eV], $n_e^{ped} = 0.95 \times 10^{20}$ [m^{-3}], $P_{RF} = 1.5$ [MW], and $B_0 = -5.8$ [T]. The position of the slight break in slope of $T_{B^{5+}}$, at $\rho \approx 0.96$, is used as the pedestal top location ("ped"). In this plasma, $T_{B^{5+}}$ is at the same level as several H-mode plasmas (see Figure 4-4), but the gradient in T_e and n_e (not shown) are much reduced (i.e. at L-mode levels). Additionally, the density fluctuations measured from reflectometry are characteristic of L-mode plasmas.

LFS/HFS impurity density and temperature match in L-mode plasmas.

The impurity density profiles are such that, within error bars, they are matched between the LFS and HFS midplane. The structure follows closely the impurity temperature profile, which lacks a clear pedestal structure, even in this elevated temperature L-mode.

The poloidal velocities, shown in Figure 4-3 are increased to a peak of -8 km/s for the LFS system, much higher than the near zero poloidal velocities in Ohmic L-mode plasmas[74]. Additionally, there is structure not seen in Ohmic L-mode plasmas, with a peak in the ion-diamagnetic drift direction, followed by a peak in the electron-diamagnetic drift direction. As will be shown, a similar structure is observed in the I-mode plasmas. This increased poloidal velocity is most likely connected to the stronger temperature gradient in these RF heated L-mode plasmas, as compared to that in Ohmic L-mode plasmas. The HFS poloidal velocity is overall reduced from the LFS values by an approximate factor of 1.5.

The parallel velocities are both co-current. The HFS velocity is much stronger than the LFS.

4.3 H-Mode Profiles

4.3.1 EDA H-Mode

EDA H-modes feature H-mode pedestal structures in electron density and temperature. The quasi-coherent mode (QCM), characteristic of EDA H-modes, is centered near the separatrix and spans a width of 3mm[98, 99].

Profiles from a typical EDA H-mode are shown in Figure 4-4. The plasma parameters were $I_p = 1.0$ [MA], $T_e^{ped} = 400$ [eV], $n_e^{ped} = 1.5 \times 10^{20}$ [m^{-3}], $P_{RF} = 2.5$ [MW], and $B_0 = 5.4$ [T]. The quantities with "ped" refer to the value of that quantity at the location of the quantities' pedestal top.

n-out asymmetry of n_z present in EDA H-mode

Unlike the L-mode plasma, the LFS and HFS impurity density profiles do not align[100]; there is a clear in-out boron density asymmetry, with the LFS boron density profile shifted inwards towards the core. Note that this asymmetry is opposite

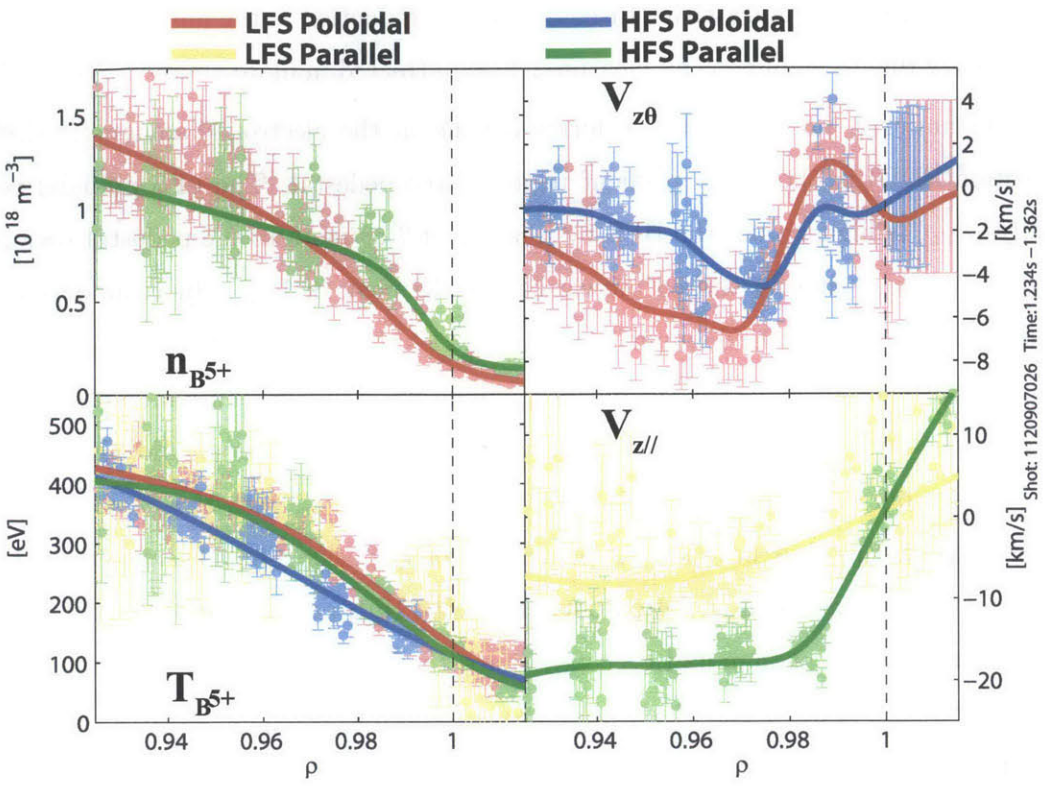

Figure 4-3: LFS and HFS B^{5+} profiles in an RF L-mode plasma

from that expected due to centrifugal effects[101], where strong rotation can push impurities towards the LFS. The HFS boron density is $\gtrsim$2.5x larger at maximum than the LFS boron density in the pedestal region. Note also the difference in the structure of impurity density profiles between the LFS and HFS, with the LFS $n_{B^{5+}}$ pedestal being wider than the HFS. This structural difference will be further discussed in section 5.

Out-in asymmetry of T_z present in EDA H-mode

As mentioned in the section on profile alignment, Section 4.1.2, for H-modes the impurity temperature is also asymmetric between the LFS and HFS. Unlike the impurity density, however, T_z is higher at the LFS, for this shot reaching factors of $>$ 2x that of the HFS impurity temperature. Since the temperature asymmetry is opposite the density asymmetry, the two work to reduce the impurity pressure asymmetry, which, from the individual factors, can be calculated to be $>$ 3x higher on the HFS.

Asymmetry profiles, along with a discussion of the reduction in the impurity pressure asymmetry due to alignment by measured E_r will treated in more detail in Section 5.

The impurity poloidal velocity forms a peak in the electron diamagnetic drift direction(EDD) in the sharp gradient region of the pedestal. The LFS poloidal velocity, $V_{z\theta L}$, is higher than the HFS by a factor of 2 or more in the pedestal region, and the peak is slightly shifted outward from the peak of $V_{z\theta H}$. In H-mode plasmas, studies[74] using LFS impurity profiles on C-Mod showed the E_r well depth, and hence location, is mainly set by the poloidal velocity contribution. This would suggest that when aligning E_r wells the poloidal velocity peaks should also align, opposite to our observation. There are two reasons dealing with the E_r alignment which explain this shift between the poloidal velocity peaks. First, because the HFS impurity density pedestal is shifted outward of the HFS poloidal velocity peak, and has a sharper gradient than its LFS counterpart, the HFS diamagnetic contribution is larger, and shifted outward, which can cause a small outward shift in the location of the E_r minimum. Second, Equation 4.6 predicts a small difference between the LFS and HFS measured E_r, mainly due to any temperature asymmetry. For the H-mode data studied, this always causes the HFS E_r location to be slightly inward of the LFS.

The parallel velocities also show marked differences between the LFS and HFS. The LFS shows the common "notch" near the pedestal top found in several tokamaks[37], subsequently increasing as the separatrix is approached. The HFS $V_{z//}$ is at the same level as the LFS inward of the pedestal top, but then decreases sharply beginning near the LFS "notch", eventually reaching near zero past the separatrix.

The low q_{95} EDA H-mode in Figure 4-4 can be compared and contrasted to an EDA H-mode at higher q_{95}, shown in Figure 4-5. Here the impurity density is in-out asymmetric, as with the lower q_{95} shot, but with a larger maximum asymmetry: $>$ 8x. The impurity temperature asymmetry is similar to before, at maximum around 2x higher at the LFS. Within the error bars of the E_r-alignment, a further shift is possible which would reduce the n_z asymmetry, but increase the T_z asymmetry even further. Irrespective of what the alignment between LFS and HFS is, what is certain is that at higher q_{95}, the LFS impurity density pedestal is further separated from the

LFS n_z pedestal further inward from LFS T_z pedestal at higher q_{95}

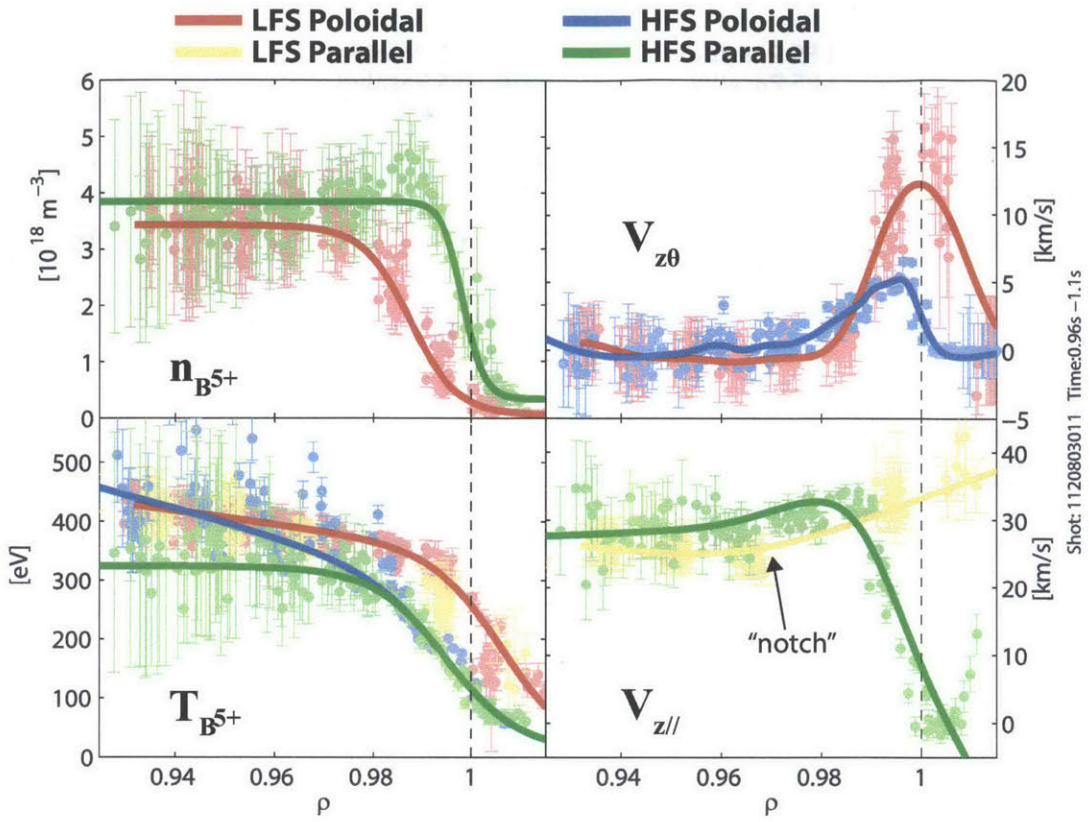

Figure 4-4: LFS and HFS B^{5+} profiles in an EDA H-mode at lower q_{95}

LFS impurity temperature pedestal, whereas the HFS separation between n_{zH} and T_{zH} pedestal locations remains approximately the same.

The LFS poloidal velocity is reduced, and slightly wider for the higher q_{95} shot. This can qualitatively be understood through the conventional neoclassical impurity poloidal velocity equation[102]:

$$V_{z\theta} = \frac{B_\zeta R B_\theta}{\langle B^2 \rangle} \left(\frac{1}{Z} \frac{1}{n_z} \frac{\partial p_z}{\partial \psi} - \frac{1}{n_i} \frac{\partial p_i}{\partial \psi} - \gamma_\theta \frac{\partial T_i}{\partial \psi} \right) \tag{4.7}$$

Here γ_θ is dependent on the collisionality regime, being constant for Pfirsch-Schluter ($\gamma_\theta^{PS} = 1.8$), and depending in a complicated way on the relative size of $v_{E\times B}$ to $v_{th,i}$ in the plateau collisionality regime[103], and the banana regime[23, 102]. Note that we do not expect this expression to necessarily hold in the pedestal region where $\rho_{i\theta} \sim L_\perp$, but use it here as guide, as it has been succesfully compared to

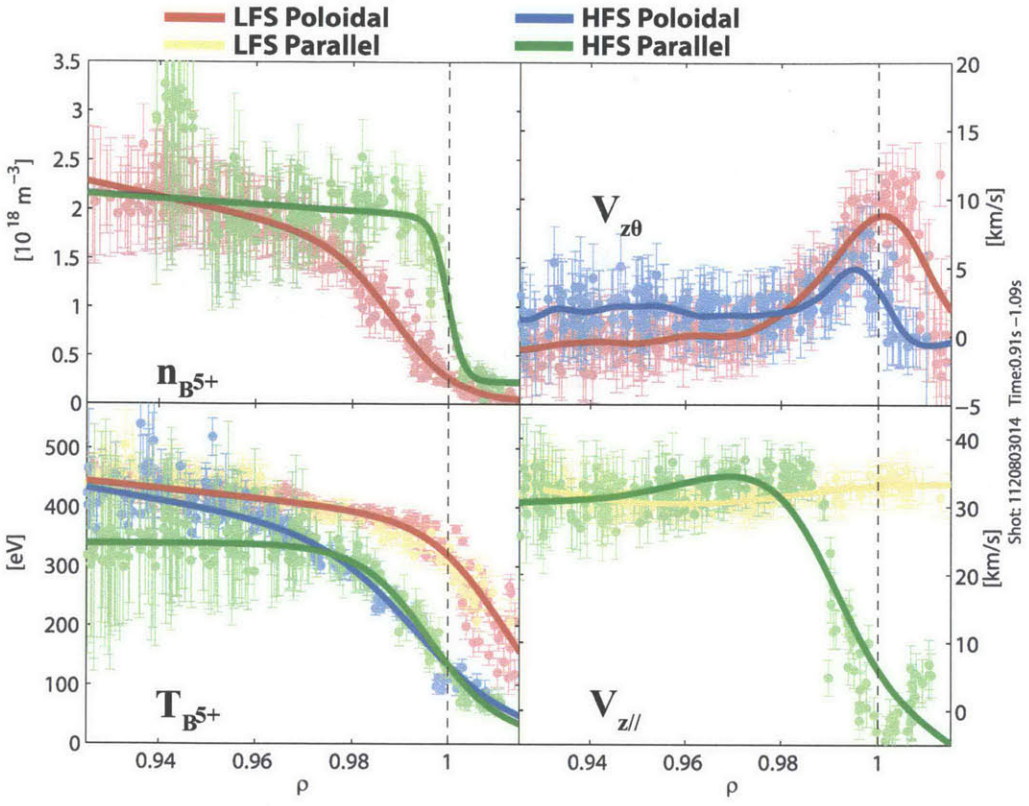

Figure 4-5: LFS and HFS B^{5+} profiles in an EDA H-mode at higher q_{95}

measurement previously[35]. Rewriting using the circular approximation for safety factor $q = \varepsilon \frac{B_\zeta}{B_\theta}$, and the derivative $\frac{\partial}{\partial \psi} = RB_\theta \frac{\partial}{\partial r}$:

$$V_{z\theta} = B_\zeta^3 \left(\frac{\varepsilon R}{q}\right)^2 \left(\frac{1}{Z}\frac{1}{n_z}\frac{\partial p_z}{\partial r} - \frac{1}{n_i}\frac{\partial p_i}{\partial r} - \gamma_\theta \frac{\partial T_i}{\partial r}\right) \tag{4.8}$$

Equation 4.8 suggests that the impurity poloidal velocity will decrease when q_{95} increases, since $V_{z\theta} \propto q_{95}^{-2}$, which agrees with our observation. However, the details of the main ion and impurity gradients need to also be taken into account, as at higher q_{95} both density and temperature pedestal width will increase. The collisionality is also generally lower for higher q_{95}, most likely changing the form and possibly the sign of γ_θ. We also note that the form of γ_θ, and of the general poloidal velocity equation, can be modified by the presence of an impurity density asymmetry[104], in addition to any changes due to global transport effects in the pedestal region, since

$\rho_{\theta,i} \sim L_{\perp}$[22].

A final comment about the poloidal velocity is that $V_{z\theta H}$ does not change as drastically, if at all, compared to the change in the LFS poloidal velocity between the low and high q_{95} EDA H-mode discharges. If Equation 4.8 were to hold, this would have to be born out by a balancing increase in the gradient terms, though if the main ion n_i and T_i are close to flux functions, this would be difficult to meet.

4.3.2 ELM-free H-Mode

ELM-free H-modes exhibit stronger gradients in background plasma parameters than EDA H-modes, but with increased impurity confinement time, leading to periodic radiative collapses of the plasma back into L-mode states before building back up.The plasma density rises during the H-mode phase, while the temperature falls due to the cooling effect of the radiation. The impurity density and temperature also follow this trend.

An example of the LFS/HFS impurity profiles are shown in Figure 4-6. The plasma parameters were $I_p = 1.2$ [MA], $T_e^{ped} = 400$ [eV], $n_e^{ped} = 3 \times 10^{20}$ [m^{-3}], $P_{RF} = 2.75$ [MW], and $B_0 = 5.4$ [T]. These profiles were taken over two ELM-free H-mode phases, each lasting about 80ms, and so are not stationary, with a temperature varying from about 450 eV down to 350 eV. The dynamic nature of ELM-free H-mode plasmas make LFS/HFS alignments difficult, as the necessary shifts will change with the density and temperature changes. Here we have applied a singular shift for the E_r-alignment, and obtained average fitted profiles, but it should be noted that in reality a time varying shift would need to be applied. Unfortunately the plasma sweeps were longer than the ELM-free H-mode phases, so without averaging over time we would not have the spatial coverage needed to resolve the profiles. The time changing nature of the ELM-free may be the cause of the HFS poloidal and parallel core-most temperature values being different, though further investigations are necessary.

The impurity density is again in-out asymmetric, just as in the EDA H-mode cases, though the LFS/HFS profiles are much more similar in shape. The asymmetry factor is still large, approaching ~ 10 in this case, though aligning with time varying

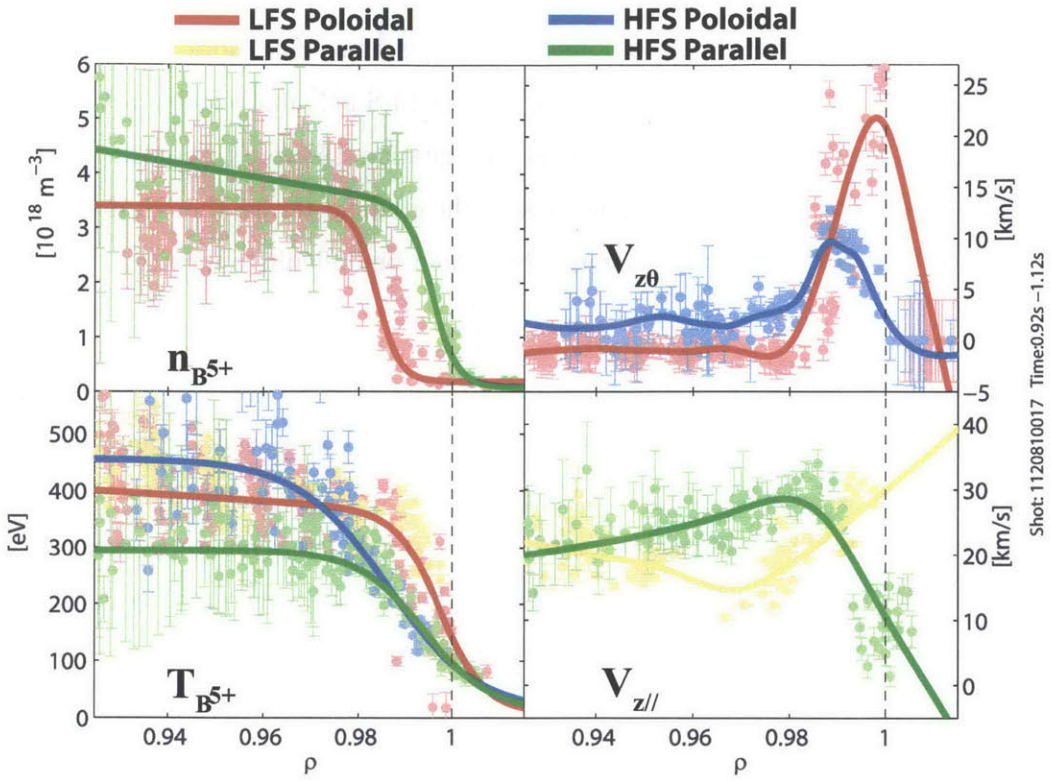

Figure 4-6: LFS and HFS B^{5+} profiles in an ELM-free H-mode

shifts could cause this factor to be lower. The fact that impurity asymmetries exist in ELM-free H-modes gives important evidence of the transport mechanism responsible for the asymmetry, since ELM-free H-modes lack a strong fluctuating mode, which will be further discussed Section 5.

There is an in-out asymmetry in temperature as in the EDA H-mode case, but it is much smaller. As can be asserted from this, for ELM-free H-modes, when the temperatures are aligned, the E_r-alignment is also approximately satisfied. Temperatures at both the LFS and HFS decay at the same rate over time, closely following the electron temperature decay, as would be expected.

The poloidal velocities have much higher peaks, this time for both the LFS and HFS. This again can partly be explained by the conventional neoclassical poloidal velocity expression, which predicts higher $V_{z\theta}$ for lower q_{95}, with which ELM-free H-modes tend to be observed (this ELM-free discharge had $q_95 \approx 3,2$).

The parallel velocities are similar in structure to that found in EDA H-modes, except that the LFS parallel flow has a much more pronounced "notch" near $\rho \approx 0.97$. This leads to a greater separation between LFS and HFS parallel velocities, with higher velocities at the HFS.

4.3.3 ELMy H-Mode

ELMy H-modes on C-Mod are achieved at lower density, with a non-standard magnetic equilibrium used to limit fueling from wall recycling, as discussed in the Introduction. Yet, the electron pedestal pressure is similar to EDA H-modes, since ELMy H-modes also typically achieve higher temperatures than EDA or ELM-free H-modes. The combination of lower density and higher temperature give ELMy H-modes a lower collisionality ($\nu^* \propto n_i/T_i^2$), providing testing grounds for effects of collisionality on impurity transport.

Because of the non-standard magnetic equilibrium, and difficulty in obtaining the right minimized recycling conditions, ELMy H-modes are not run as frequently as other H-mode plasmas on C-Mod. Example profiles from a high performing ELMy H-mode are shown in Figure 4-7. The plasma parameters were $I_p = 0.9$ [MA], $T_e^{ped} = 1000$ [eV], $n_e^{ped} = 1 \times 10^{20}$ [m^{-3}], $P_{RF} = 2.75$ [MW], and $B_0 = 5.6$ [T]. Gap sweeps weren't used on these plasmas, explaining the spatial gaps in the HFS data. This limits the resolution, making alignment between the LFS/HFS profiles difficult, and ultimately limiting the usefulness of these profiles. Nevertheless, general comparisons with the other H-modes can be made.

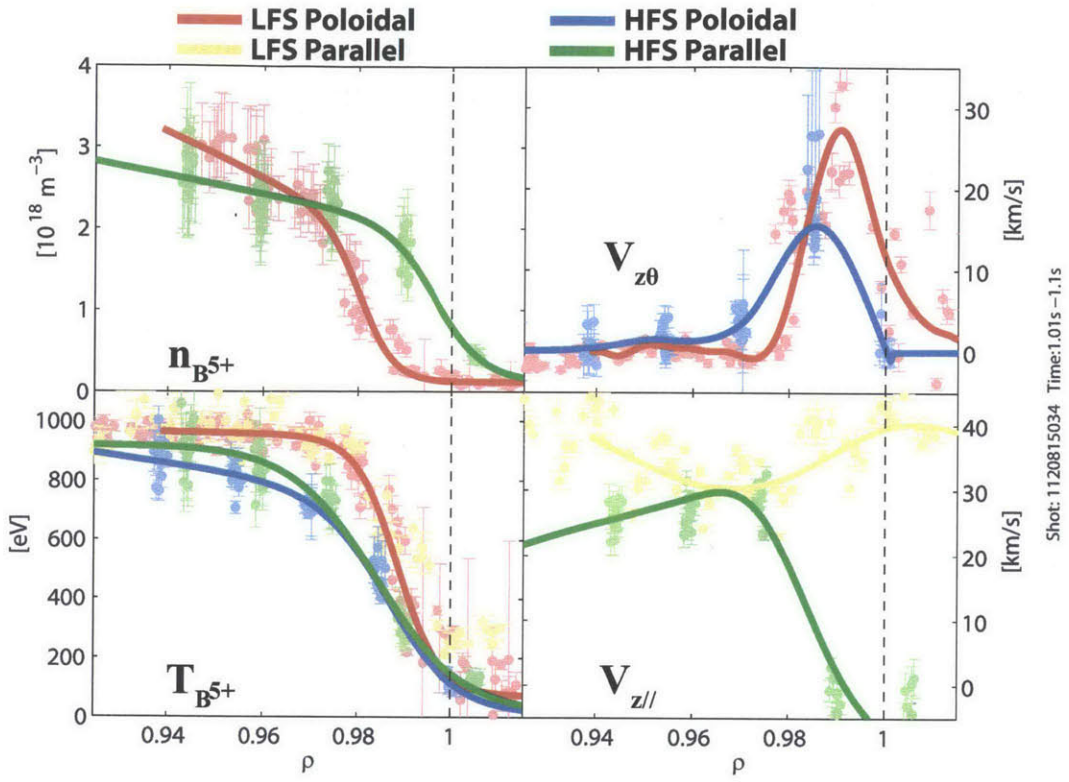

Figure 4-7: LFS and HFS B^{5+} profiles in an ELMy H-mode

The impurity density, like the other H-modes, is again in-out asymmetric, though an accurate asymmetry factor is difficult to quantify due to the gaps in the HFS data. The impurity density fraction is slightly higher, between 2-3% of n_e, compared to the typical 1-2% in other H-modes.

The impurity temperature is large, reaching 1000 eV, more than 2x larger than the other H-modes we've seen. However, the gradient scale length itself, L_{T_z}, is of the same order as, for example, that of the ELM-free H-mode in Figure 4-6. Similar also to the ELM-free H-mode is the relatively small impurity temperature asymmetry, here staying below 1.5x at maximum, with the peak asymmetry occurring near the LFS T_z pedestal top.

The poloidal velocity is much than any of the H-modes shown, with peaks of 25 km/s and 15 km/s for the LFS and HFS, respectively. The relative peak locations are similar to the other H-modes, with the LFS being shifted slightly outward of the

HFS. The larger $V_{z\theta}$ values for this ELMy discharge can again be understood with the conventional neoclassical expression for poloidal velocity, this time expanding the pressure gradient terms to write:

$$V_{z\theta} = B_\zeta^3 \left(\frac{\varepsilon R}{q}\right)^2 T_i \left[\frac{1}{Z}\frac{1}{n_z}\frac{\partial n_z}{\partial r} - \frac{1}{n_i}\frac{\partial n_i}{\partial r} - \left(\gamma_\theta + 1 - \frac{1}{Z}\right)\frac{1}{T_i}\frac{\partial T_i}{\partial r}\right] \qquad (4.9)$$

here we approximated $T_i \approx T_z$. If then the gradient scale lengths are similar between H-modes, we would expect a simple linear relation of $V_{z\theta}$ with T_i, which was observed on C-Mod previously[74]. The elevated temperatures in this ELMy H-mode appear to be the cause of the higher poloidal impurity velocity, as would be predicted by Equation 4.9.

There are no features distinguishing the parallel velocities from the other H-modes presented here. Perhaps a slightly inward shifted HFS $V_{z//H}$, but otherwise similar magnitudes and structure to other H-modes.

4.4 I-Mode

The I-mode has recently been a subject of intense study on C-Mod because of its enticing potential as a reactor regime with high energy confinement, and low particle confinement. As discussed in the Introduction, Section 1, I-modes are almost always obtained when the ion ∇B drift direction is away from the active X-point. On C-Mod, this is achieved by either running in the upper single null (USN) configuration, with the X-point at the top of the plasma, or by reversing the toroidal magnetic field and plasma current direction. USN configurations have the disadvantage of using the top of the machine for the divertor, which isn't closed, losing some of the particle control and power handling capabilities of the lower divertor. The only disadvantage of reversed field is the week of setup time needed, but the major advantage is the ability to run lower single null (LSN) plasmas, making use of the closed divertor structure at the bottom of the machine. These two ways of running I-mode plasmas exhibit some marked differences which will be presented here.

As the I-mode lacks an electron density pedestal, but does have an H-mode like

temperature pedestal, we can expect some significant variation as well in the impurity profiles. Figure 4-8 shows profiles from a reversed-field I-mode. The plasma parameters were $I_p = -1.3$ [MA], $T_e^{ped} = 900$ [eV], $n_e^{ped} = 9 \times 10^{19}$ [m^{-3}], $P_{RF} = 4$ [MW], and $B_0 = -5.6$ [T]. n_e^{ped} was taken from the same location as the T_e pedestal top, as there isn't a pedestal in n_e.

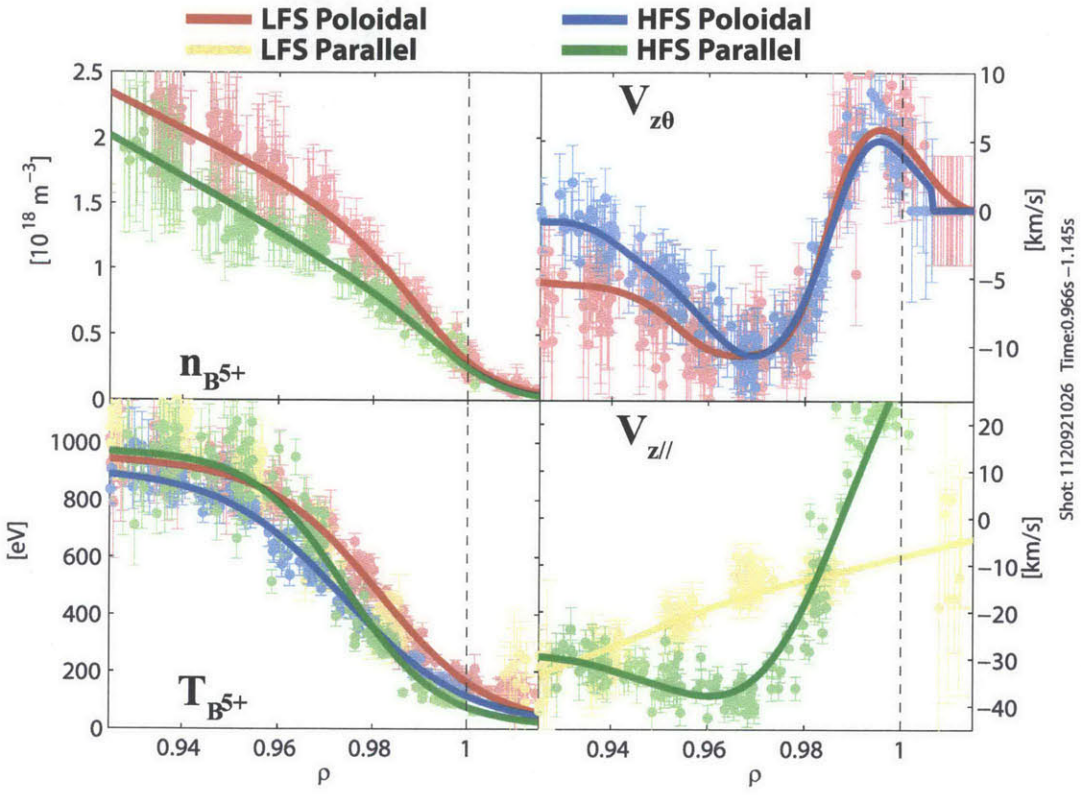

Figure 4-8: LFS and HFS B^{5+} profiles in a reversed field I-mode

LFS/HFS n_z and T_z is symmetric in I-mode, similar to L-mode

Just like the L-mode in Figure 4-3, in the I-mode the impurity density is well matched between the LFS and HFS[40]. While n_z does not form a strong pedestal, like in the H-modes, it has a stronger gradient than the electron density (n_e is basically flat), following closely the impurity temperature profile. Because it follows closely the temperature, the n_z pedestal in I-mode may be due more to ionization physics rather than transport. Relative to the electron density, the boron density is at the same level as H-modes, about 2%.

The LFS $T_{B^{5+}}$ is slightly shifted outwards from the HFS impurity temperatures. While the temperature level is very high in I-mode, here about 900 eV, the $T_{B^{5+}}$ width is much wider than in H-mode, meaning the peak gradient scale length is smaller. However, it also means there is more temperature gradient drive further into the plasma which can drive rotation.

Indeed, in this I-mode we observe larger poloidal rotation further into the plasma than in H-mode, both in the LFS and HFS $V_{z\theta}$. The rotation minimum of -10 km/s near $\rho = 0.96$ is in the electron diamagnetic drift direction (EDD), just as the $V_{z\theta}$ peak in H-mode plasmas. However, in this I-mode there is also a rotation reversal near the separatrix, such that the poloidal rotation is in the ion diamagnetic drift direction (IDD) near the separatrix. This asymmetric poloidal velocity structure translates directly into an asymmetric E_r, leading to a higher shearing rate near the separatrix[82], on the outer-edge of the E_r well. This is in contrast to most H-mode plasmas[74, 105] where the inner edge has the highest shear layer, indicating the turbulence suppression mechanisms may be different for I-mode than H-mode. The point of rotation reversal is at $\rho = 0.986$, which is very close to the point where the collisionality changes regimes from banana to plateau, at $\rho = 0.989$. Since the impurity pressure term and main ion density gradient terms will be small in I-mode, the dominant term in the poloidal velocity equation (Equation 4.8) will be the main ion temperature gradient term. The direction of the poloidal flow will then depend almost solely on the sign of $\gamma_\theta + 1$. In conventional, local neoclassical physics, in the edge region $\gamma_\theta + 1 > 0$ for all collisionalities (see blue trace in Figure 2 of Reference [104], where $k_\parallel = -\gamma_\theta$), implying no poloidal rotation reversal is possible. However, two separate modifications to neoclassical transport in the pedestal region have shown to change the sign from the conventional result, namely including the effects of a strong radial electric field[102, 103] or global transport effects which occur when the main ion orbit width becomes comparable to the density or temperature gradient scale length[22]. A more detailed modelling of I-mode impurity poloidal rotation would be beneficial in understanding the cause of these rotation reversals.

I-mode exhibits poloidal rotation reversal, unexplainable by conventional neoclassical physics

Parallel velocities are similar to the L-mode also, but larger in magnitude. $V_{z//H}$

flips direction at almost the exact location of the poloidal rotation reversal.

Figure 4-9 shows an example I-mode in USN, forward field to contrast to the LFS, reversed field I-mode in Figure 4-8. The plasma parameters were $I_p = 1.2$ [MA], $T_e^{ped} = 500$ [eV], $n_e^{ped} = 1 \times 10^{20}$ [m^{-3}], $P_{RF} = 5$ [MW], and $B_0 = 5.5$ [T].

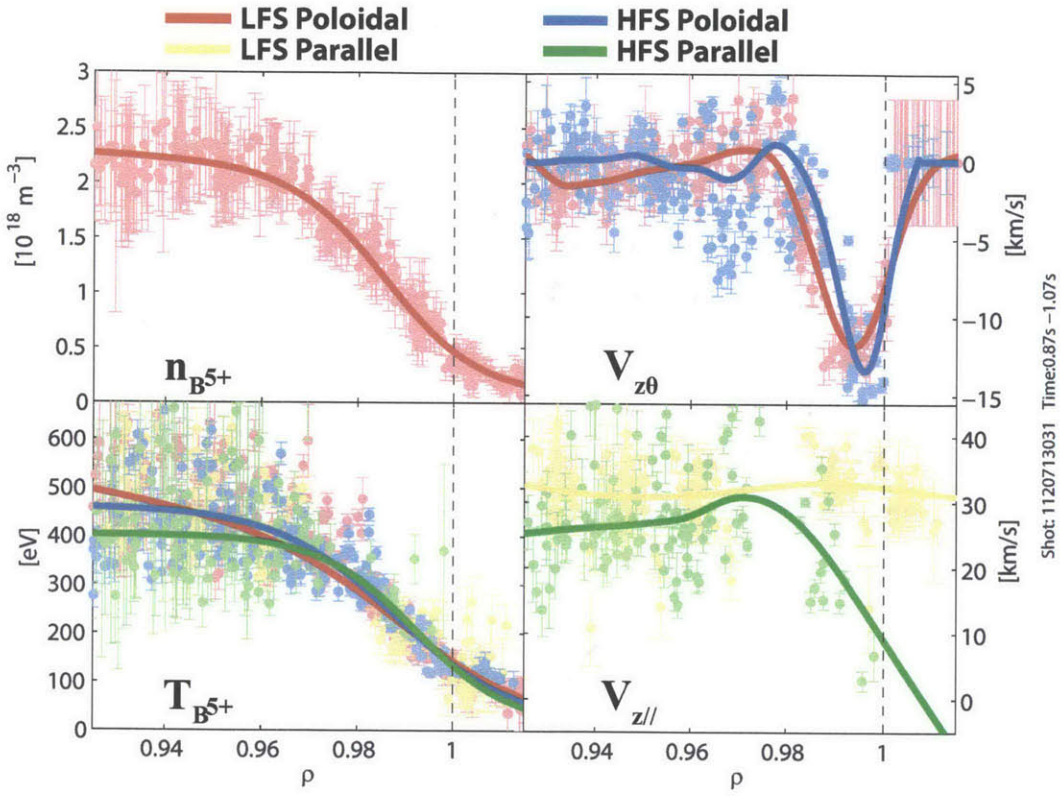

Figure 4-9: LFS and HFS B^{5+} profiles in a forward field I-mode

Unfortunately, the HFS D_α diagnostic wasn't operational for this shot, so the measurement of HFS n_z wasn't available. The position of the peak in the BV radiance between the LFS and HFS was well aligned, suggesting that the boron density is in-out symmetric (in H-mode when there is an in-out boron density asymmetry, the BV radiance peaks between LFS and HFS do not align). The LFS boron density structure follows closely that of the impurity temperature.

The temperature is lower than that of the reversed field I-mode, however, in general, this is not necessarily the case[15]. In this I-mode discharge, the large spread

in temperatures of $\Delta T_z \sim 150$ eV in regions inward of the pedestal top is really a time dependent change in temperature, due to sawteeth heat pulses[106] which propagate from the center of the plasma all the way to the edge. A time trace of the impurity and electron temperature at $\rho \sim 0.947$ is shown in Figure 4-10, which shows that T_e, T_{zL}, and T_{zH} are affected equally by the heat transporting through the plasma. This spread of temperatures is common in I-modes, and is here pronounced because the pedestal temperature is lower. Note that in the temperature pedestal, the spread of temperature is much reduced.

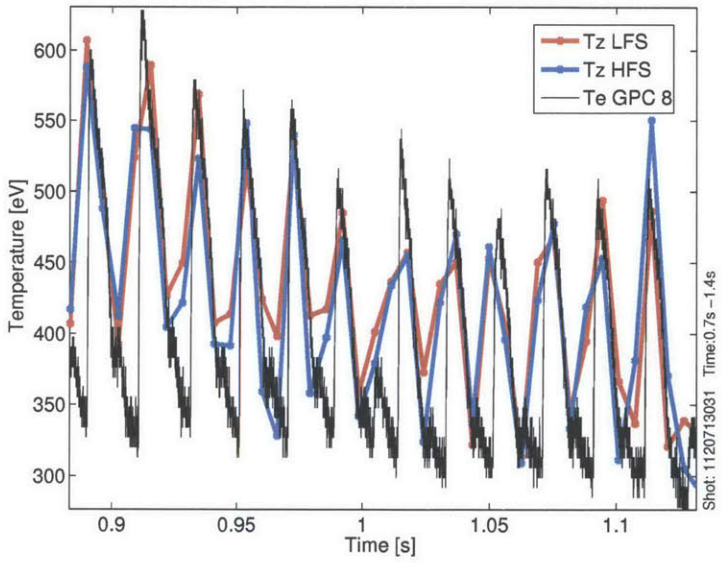

Figure 4-10: Electron temperature and LFS/HFS impurity temperature over time, showing strong sawteeth effects near the pedestal top.

Poloidal velocities are matched well between the LFS and HFS, as in the reversed-B field case. The structure, however, has some important differences. In forward field I-modes, there is very little poloidal velocity in the electron diamagnetic drift direction (EDD). Additionally, the IDD peak near the separatrix is much deeper than in the reversed field I-mode (forward-B: -15 km/s, reversed-B: 5 km/s), though the delta change in poloidal velocity from the region inward of the IDD peak to the IDD peak is similar in magnitude (~15 km/s). The temperature pedestal in this forward field case doesn't extend as far in as that of the reversed-B field case, which may explain

the absence of poloidal rotation in the EDD direction for $\rho < 0.98$.

The parallel velocities are rather unremarkable, being very similar to the H-mode plasmas presented here, which were all forward field.

Chapter 5

In-Out Asymmetries in the Pedestal Region

In this chapter, we will further explore the impurity density and temperature in-out asymmetries that arise in the pedestal region. Additionally, we will explore the level of electron and main ion density in-out asymmetries that can be expected based on the E_r-alignment method of aligning LFS/HFS profiles. Finally, we explore mechanisms which can drive the impurity asymmetries observed.

5.1 Impurity Density Asymmetries

We first further explore the impurity density asymmetries, which are observed in all flavors of H-mode in Alcator C-Mod (see profiles in Section 4 as well as Ref. [100]).

An example of the impurity density asymmetry is shown in Figure 5-1, with profiles taken from Figure 4-4. Here we've plotted the asymmetry in two ways, first by the ratio of the impurity density asymmetries, $A_{n_z} = n_{zH}/n_{zL}$, and second by the asymmetry factor $n_z^{cos} = (A_{n_z} - 1)/(A_{n_z} + 1)$. The impurity density ratio will be useful in the Section 6 in calculating example velocities. The asymmetry factor is more commonly quoted in impurity asymmetry studies, and represents the cosine varying portion of the impurity density asymmetry in the limit that the impurity density is only in-out asymmetric ($n_z/\langle n_z \rangle = 1 - n_z^{cos} \cos\theta$). The sign is chosen so

that n_z^{cos} is positive when the impurity density is higher on the HFS. As seen the peak impurity asymmetry is about a factor of 2.5, peaking very near the separatrix.

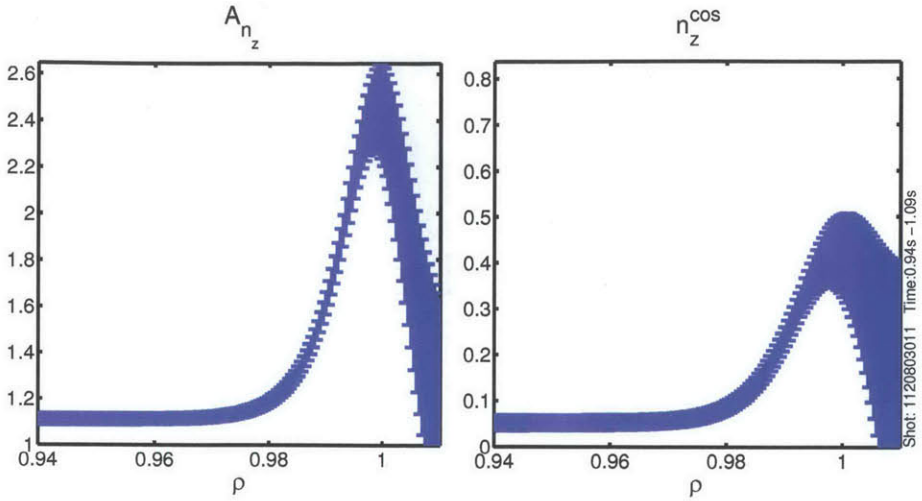

Figure 5-1: Example density asymmetry for an EDA H-mode: (a) asymmetry ratio $A_{n_z} = n_{zH}/n_{zL}$ and (b) asymmetry factor $n_z^{cos} = (A_{n_z} - 1)/(A_{n_z} + 1)$

This asymmetry ratio is much reduced from that which would result from aligning by T_z. Figure 5-2 shows the impurity density asymmetry ratio that results when using the two different alignments, T_z-alignment and E_r-alignment (see Section 4.1), for a number of EDA H-modes. For the T_z-alignment, the asymmetry factors have a wide range, with a mean of about 20. When using the E_r-alignment, which usually requires the LFS impurity density profile moving much closer to the HFS impurity density profile, the asymmetry factor is much reduced, with a mean of about 6.

A very interesting result going from the T_z-alignment to the E_r-alignment (see Section 4.1) is that the impurity pressure asymmetry is also reduced, even more than the density asymmetry since an out-in temperature asymmetry also results. This can be seen in how the profiles change in Figure 4-2 for the different alignments. We show in Figure 5-3 asymmetry factors for impurity density, temperature, and pressure (n_z^{cos}, T_z^{cos}, and p_z^{cos}) in the two different alignments.

Plotted in Figure 5-4 is the difference in the B^{5+} density pedestal location at the HFS minus the LFS, $\Delta\rho_{ped} = \rho_{ped,HFS} - \rho_{ped,LFS}$ versus the edge safety factor, q_{95}, for several H-mode discharges. $\Delta\rho_{ped}$ is shown for when profiles are T_z-aligned (in

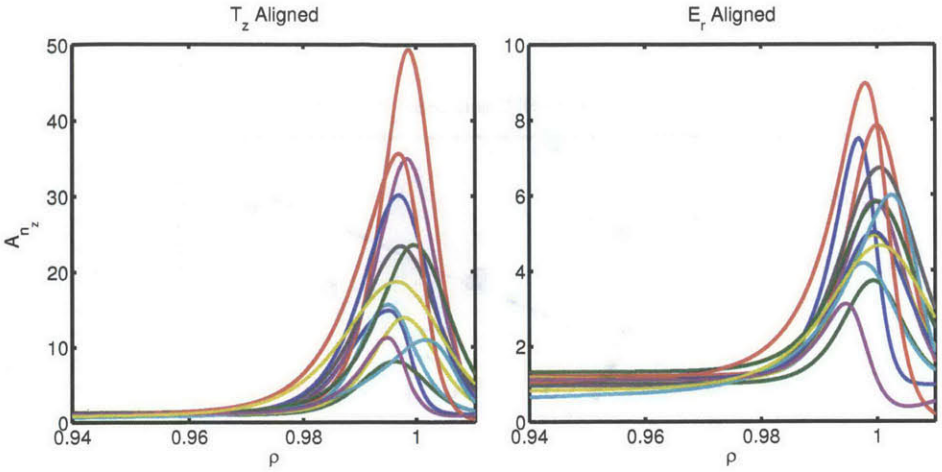

Figure 5-2: Example density asymmetry ratios A_{n_z} for several EDA H-modes: (a) T_z-aligned profiles and (b) E_r-aligned profiles. Note the different y-scales, showing that their is a large reduction in asymmetry ratios when using the E_r-alignment.

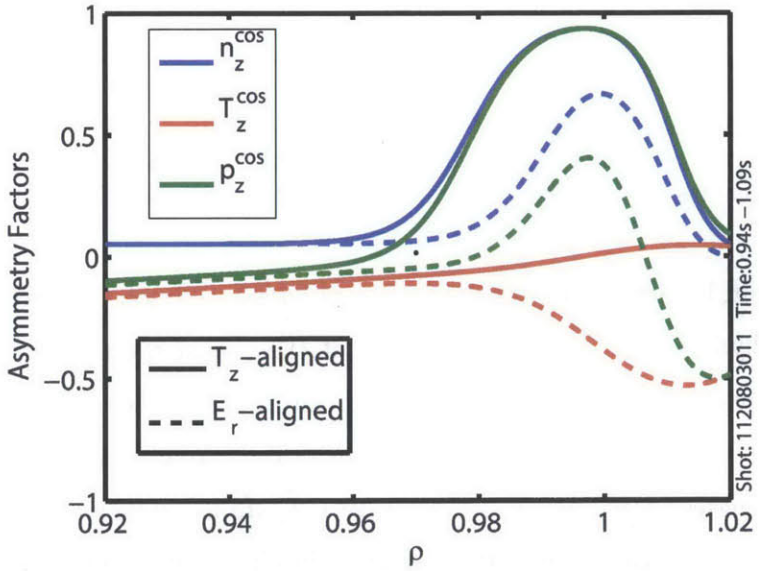

Figure 5-3: Asymmetry factors for impurity density (n_z^{cos}), temperature (T_z^{cos}), and pressure (p_z^{cos}), using both the T_z-alignment and E_r-alignment. The E_r-alignment has a reduced pressure asymmetry, due to the reduction of the density asymmetry, and formation of an opposing temperature asymmetry.

blue) and E_r-aligned (red). An upward trend in $\Delta\rho_{ped}$ with q_{95} is seen. The trend remains relatively unchanged for the different alignments, though the E_r-alignment does slightly decrease $\Delta\rho_{ped}$ at higher q_{95} (here B_ζ was basically fixed, so this corre-

sponds to lower I_p).

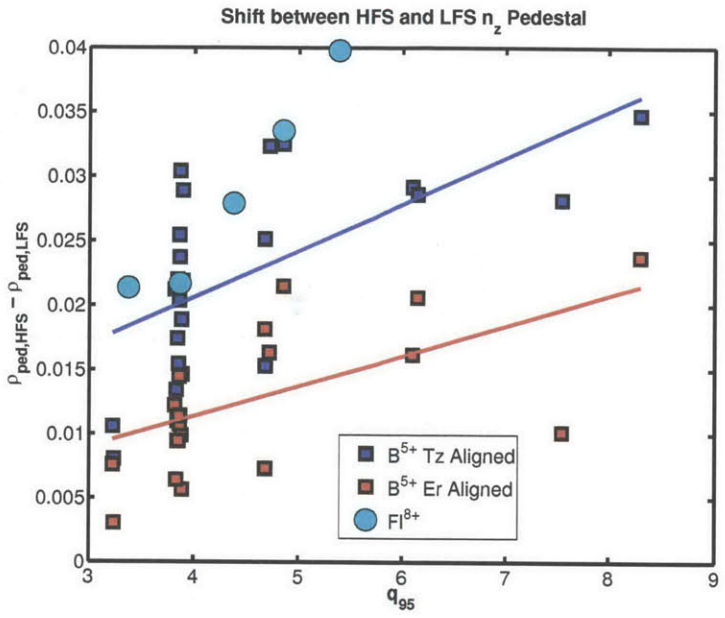

Figure 5-4: Difference between the HFS and LFS n_z pedestal locations ($\rho_{ped,HFS} - \rho_{ped,LFS}$) versus the edge safety factor (q_{95}). Blue results are when using the T_z-alignment, red results are when using the E_r-alignment. Data in light blue is taken from previous results for fluorine[107], measured at the top and LFS midplane.

Also shown in Figure 5-4 are results from a previous study on C-Mod[107], which measured the hydrogen-like fluorine emission at the top of the plasma and at the LFS midplane using a line-integrated measurement of the soft x-ray emission[1]. The spacing between the pedestal locations is similar for the two impurity species, though for fluorine increases more with q_{95}. This may indicate a significant up-down component in the poloidal variation of the impurity density, however without additional information on the B^{5+} at the top of the plasma, or Fl^{8+} at the HFS midplane, this is speculative. Heavier and higher charged impurities are expected to have larger levels of asymmetry[36], since impurity charge and mass weight terms differently in the momentum balance equations. Additionally, the alignment of the soft x-ray emission

[1]The results plotted here are taken directly from Ref [107], and represent the mean values across several hundreds of shots. The Pedersen paper quotes the pedestal location difference in real space, ΔR_{mid}. These were adjusted for the 3mm calibration offset mentioned in the paper, then converted to $\Delta\rho$.

profiles can only rely on EFIT, as the diagnostic doesn't measure T_z or E_r, and so is sensitive to the considerable EFIT errors, as discussed in Section 4.1.

Increasing parallel transport timescale by increasing q alone not responsible for impurity density asymmetry

In reference[107], the cause for the asymmetry increasing with q_{95} was postulated to be a slower parallel transport time scale ($\tau_{\|} \propto q$) relative to perpendicular transport time scales, allowing density asymmetries to form. I-mode cases covering $q_{95} = 3 - 5$ show no signs of an impurity density asymmetry, despite the range of parallel transport time, indicating that increasing $\tau_{\|}$ alone does not produce the impurity asymmetry. To be consistent, however, radial transport time scales need to be calculated. The question of time scales is addressed in more detail in section 5.4.7.

HFS n_z pedestal ~constant in location and width. LFS n_z pedestal widens and shifts inward as I_p decreases

It's important to realize that for H-mode plasmas the growing difference in $n_{B^{5+}}$ pedestal location between the LFS and HFS isn't just a simple shift, but rather the pedestal width on the LFS is also increasing with q_{95}, whereas the HFS boron density pedestal width remains fairly constant. It's noteworthy that through all the changes between the different regimes, the HFS boron density pedestal remains relatively fixed in width and position, while the LFS boron density pedestal width widens and the pedestal position shifts slightly inward depending on plasma parameters, as shown for the H-mode cases in Figure 5-5. This is suggestive that locally transport is changing at the LFS, possibly due to ballooning (i.e. stronger at the LFS) processes, such as collisional transport or certain turbulent modes.

HFS n_z and T_z pedestal locations comparable. LFS n_z pedestal location further in than T_z pedestal.

Independent of what the true LFS/HFS profile alignment is, the relative pedestal location of the impurity density to the impurity temperature at a single location, LFS or HFS, are distinctly different for the LFS vs the HFS in H-mode. On the LFS, the temperature pedestal is much further out than the impurity density pedestal. The HFS on the other hand has almost matching n_z and T_z pedestal locations, with the density pedestal shifting slightly inward for lower plasma current discharges. These statements are shown graphically in Figure 5-6. Note that the electron density and temperature pedestals tend to align[19], similar to the HFS impurity density and temperature profiles.

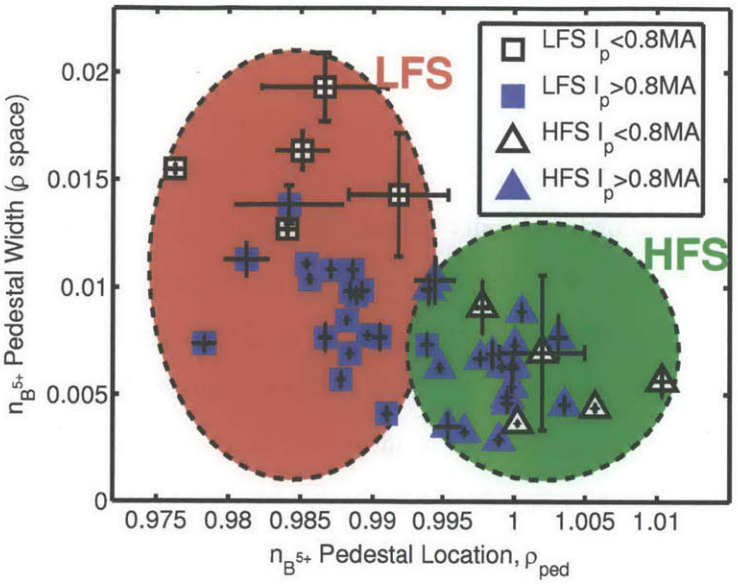

Figure 5-5: Impurity density pedestal location (ρ_{ped}) vs width for the LFS and HFS. For lower I_p plasmas, the LFS pedestal width increases significantly.

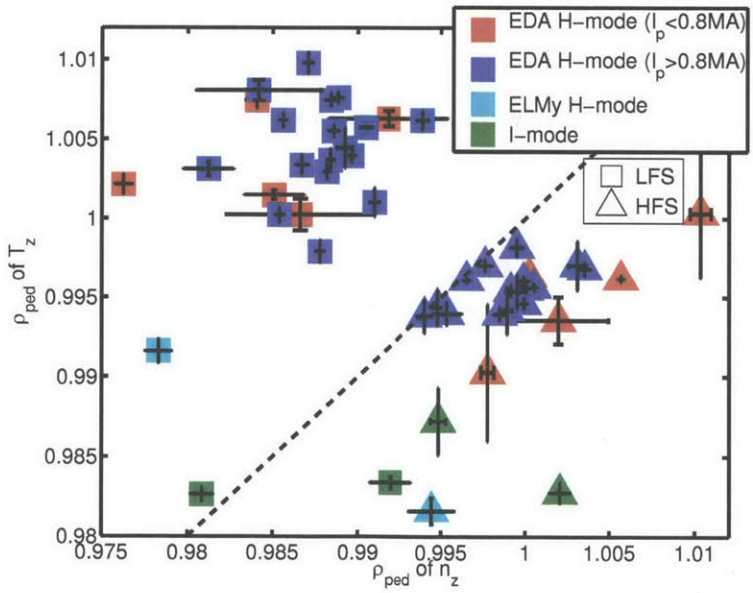

Figure 5-6: Pedestal locations (ρ_{ped}) of the impurity temperature and density. The LFS has a density pedestal shifted inward significantly from the measured temperature pedestal

5.2 Verification of Alignment Technique

Having observed these large impurity density asymmetries, here we consider two topics to explore the validity of the alignment technique. First, we test whether power balance is satisfied with the large impurity temperature asymmetries that result from the alignment. Second, we explore evidence of an electron density asymmetry, which is inferred from the momentum balance equations used in the E_r-alignment.

5.2.1 Power Balance

As a verification check on the assumptions made in aligning the LFS/HFS profiles, we here calculate the power carried in the region of temperature asymmetry, and compare it with the net power in the plasma.

Because of the in-out temperature asymmetry, heat will flow from the LFS to the HFS. The total power carried in the pedestal region due to this heat flow can be calculated using the following as:

$$\begin{aligned} P &= \int d\mathbf{A} \cdot \bar{\mathbf{q}} \\ &= \int dR 2\pi R \frac{B_\theta}{B} \bar{q}_{||} \\ &= \int d\psi \frac{2\pi}{B} \bar{q}_{||} \end{aligned} \tag{5.1}$$

where P is the power in Watts, and $\mathbf{q}$ is the average heat flux. We calculate an average $q_{||}$ on a flux-surface between the LFS and HFS:

$$\begin{aligned} \bar{q}_{||} &= \frac{\int_{LFS}^{HFS} d\ell_\theta \, q_{||}}{\int_{LFS}^{HFS} d\ell_\theta} \\ &\approx \frac{\int_{LFS}^{HFS} d\ell_\theta \, q_{||}}{L_{||}} \end{aligned} \tag{5.2}$$

where $L_{||} = \pi q R_0$ is the connection length and here q is the safety factor.

For a simple estimate we use Spitzer conductivity, which is the short mean free path form, $q_{||} = -\kappa_{0i} T_i^{5/2} \mathbf{b} \cdot \nabla\theta \frac{\partial T_i}{\partial \theta}$. The validity of this estimate will be discussed at the end of this section. Using the form for $q_{||}$ in Equation 5.2:

$$\begin{aligned} \bar{q}_{\|} &\approx \frac{-\int_{LFS}^{HFS} d\theta\, r\kappa_{0i} T_i^{5/2} \mathbf{b}\cdot\nabla\theta \frac{\partial T_i}{\partial\theta}}{L_{\|}} \\ &\approx \kappa_{0i} \frac{r\langle \mathbf{b}\cdot\nabla\theta\rangle}{L_{\|}} \frac{2}{7}\left[T_{iL}^{7/2} - T_{iH}^{7/2}\right] \end{aligned} \tag{5.3}$$

Using Equation 5.3 in Equation 5.1 we arrive at the estimated Spitzer power carried in the pedestal region, inferred from the temperature asymmetry:

$$P = \kappa_{0i} \frac{a\langle \mathbf{b}\cdot\nabla\theta\rangle}{L_{\|}} \frac{2}{7} \int d\psi \frac{2\pi}{B}\left[T_{iL}^{7/2} - T_{iH}^{7/2}\right] \tag{5.4}$$

Using measured impurity temperature profiles (assuming that $T_i = T_z$) from an EDA H-mode (Figure 4-5), we plot in Figure 5-7 the estimated Spitzer power using Equation 5.4 for various shifts between the LFS and HFS profiles ($\Delta\rho = 0$ corresponds to the LFS/HFS temperature aligned case). As $\Delta\rho$ increases, the LFS profiles are shifted outward, increasing the in-out T_z asymmetry. The horizontal dashed red line indicates the P_{net} measured in this plasma, calculated as $P_{net} = P_{icrf} + P_{ohm} - P_{rad} - \frac{dW}{dt}$, where the four terms are the power from the ICRF, Ohmic, radiation, and time derivative of the plasma stored energy. The vertical black line shows the location of the E_r-alignment shift. When the outward shift to the LFS profiles from the temperature aligned position is $\Delta\rho > 0.008$, the Spitzer estimated power exceeds the net power in the plasma. On this basis, there is concern as to whether the suggested main ion temperature asymmetry is physically supportable.

There are, however, a number of reasons not to abandon the E_r-alignment. Since most of the C-Mod pedestal region is in the plateau regime, where the effective collision mean free path exceeds the connection length, the Spitzer form for the parallel heat flux is not justified. A fully kinetic calculation of heat flux is really required, which will almost certainly indicate that the Spitzer power estimate is too high. Indeed, even in regions of high collisionality where Equation 5.2 would seem to be valid, kinetic effects need to be accounted for, since the majority of the heat flux is carried by superthermal ions[108]. Additionally, the strong gradients in the pedestal region have a large effect on the poloidal variation of the radial heat flux[22], which would need to be accounted for in the power balance calculation. Second, there may be

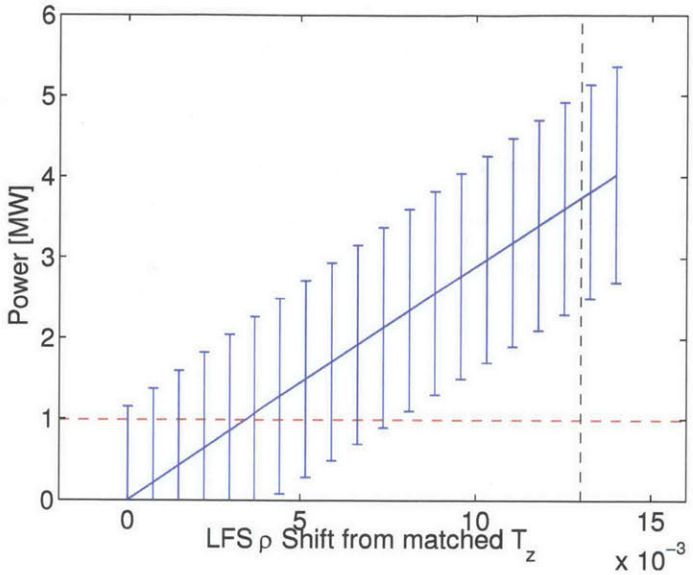

Figure 5-7: Spitzer-conductivity power flowing in the pedestal region from the LFS to the HFS versus shifts in the LFS profiles outwards (causing more asymmetric LFS/HFS temperature profiles). Red dashed line shows the total net power in the plasma, P_{net}. Black dashed line the shift from the E_r-alignment.

mechanisms which allow T_i to vary from T_z, which would allow a smaller poloidal variation in T_i, reducing the power being carried in the pedestal region.

Nevertheless, it is possible that terms we discarded in the parallel momentum balance,such as main ion viscosity and main ion inertia, are important enough that they would cause the alignment to be closer to the T_z matched alignment. While we continue with the E_r-alignment in this chapter, we will note that in the context of impurity density asymmetries, this alignment is the least severe, as using the T_z-alignment will only increase the measured in-out impurity density asymmetry[100].

5.2.2 Electron and Ion Density Asymmetries

We can additionally now explore the implied variation in the background electron and main ion density based on the measurements of impurity density and temperature. Given the trace levels of the boron density, the temperature asymmetry will be the dominant term in the variation of n_e and n_i (see equation 4.5). Since in general on

a given flux surface the impurity ion temperature is higher at the LFS, this will lead to an electron density higher on the HFS in order to conserve total pressure (electron and main ion) on a flux surface (again, we assume $T_i = T_z$).

2x higher n_e on HFS expected from T_z asymmetry

An example of the expected HFS n_e is shown in Figure 5-8, derived using EDA H-mode profiles from Figure 4-4. Also shown in the lower plot is the asymmetry factor, $A = n_{eH}/n_{eL}$, reaching a maximum value of ~2. Note however that this maximum is in the SOL, whereas using the temperature asymmetry to infer the poloidal variation in n_e is only valid strictly within the closed-field line regions.

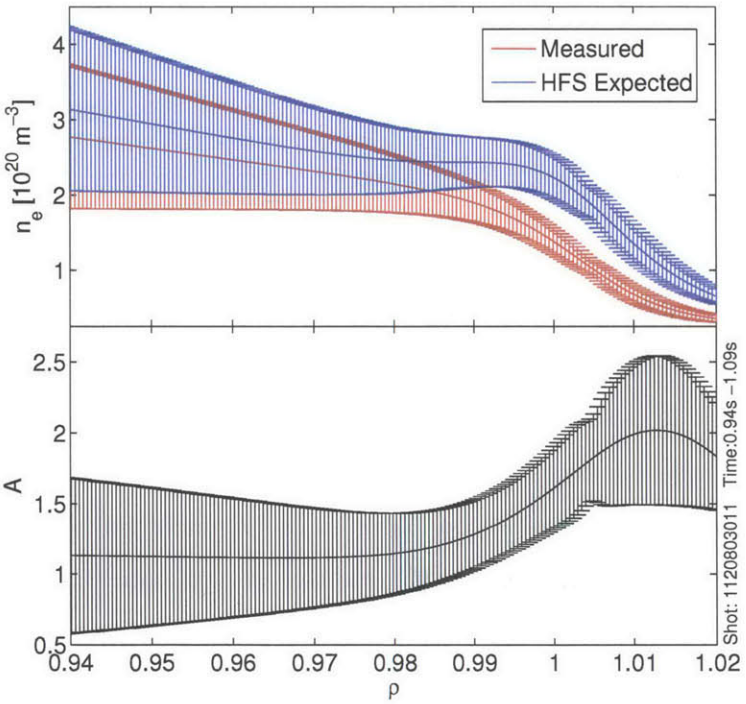

Figure 5-8: Measured electron density, and the resulting expected HFS electron density based on the impurity temperature asymmetry, and Equation 4.5.

We again note that the alignment of the impurity profiles to the electron profiles isn't well constrained (the *relative* alignment of LFS to HFS impurity profiles is well constrained, but the *absolute* location is not). This gives some variability in what the inferred HFS n_e and n_i would be. Additionally, the measured n_e in Figure 5-8

is actually measured at the top of the plasma (see Figure 4-1), but is used here as a proxy for the LFS n_e. If there is a simple cosine poloidal dependence, the HFS n_e would be reduced even further. The results shown here can be seen as an upper limit on the HFS to LFS n_e asymmetry factor. If the LFS and HFS impurity profiles were aligned such that the steep gradient region of T_z from the HFS and LFS were equal but opposite radial distances from the steep gradient region of T_e (this alignment minimizes the electron to impurity temperature), the asymmetry factor in Figure 5-8 would reduce down to $\sim$1.5 at maximum. An additional caveat is if the main ion temperature T_i doesn't vary poloidally as much as the impurities, this asymmetry in electron density will also be reduced (since it's really the asymmetry in T_i and T_e that sets the n_e asymmetry; in this thesis we've assumed $T_i = T_z$ everywhere).

As this is a sizeable difference in electron density, the penetration of neutrals will be different on the LFS than the HFS. We can roughly approximate the neutral density at a particular location as $n_D \propto \exp(-\int d\ell n_e)$ [50], where the integral is along the neutral propagation direction. This implies that at the HFS the neutral density will be attenuated earlier than at the LFS, since we expect the HFS n_e to be higher.

These neutral density differences may be observable on the measured D_α radiance. Unfortunately, the instantaneous flow rate for each gas delivery capillary is not well characterized, making comparisons of the absolute values of I_{D_α} between the LFS and HFS unusable. However, the gradient scale lengths of D_α radiance, $L_{I_{D_\alpha}}$, may be of use, as it will reach a minimum further out if the electrons density pedestal is further out. The measured inverse gradient scale lengths of D_α radiance are shown in Figure 5-9. The vertical lines shown are the expected location of the maximum in $L_{D_\alpha}^{-1}$, obtained from OSM-EIRENE simulations shown in Figure 5-10. Two OSM-EIRENE simulations were run: the case when n_e, T_e, and T_i are flux functions, and the case where T_i and hence n_e vary as depicted in Figure 5-8. The solid lines show the case when background parameters are flux functions, and the dashed lines shows the case when the impurity profiles are shifted for E_r-alignment, resulting in a varying T_z and n_e. As seen in Figure 5-9, the location of maximum measured LFS $L_{D_\alpha}^{-1}$ matches well

with the simulation. The HFS is closer to the E_r-aligned case, but sits in between the two cases, suggesting the electron density pedestal could be further outward at the HFS. Additionally, the magnitude of the inverse gradient scale length is much larger at the HFS, which can not be explained by flux-surface spacing alone, indicating that the HFS n_e profile may also be narrower in width.

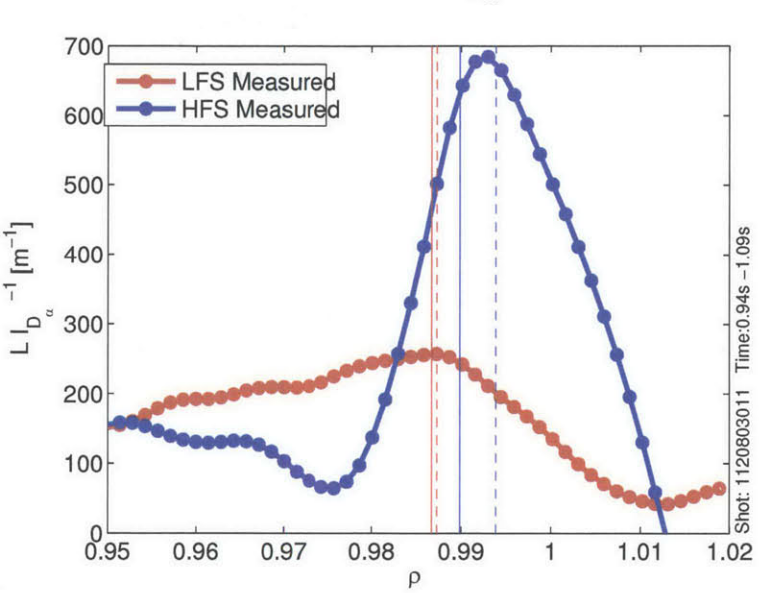

Figure 5-9: Simulated I_{D_α} for the LFS and HFS, for two separate cases: (1) Normal, where n_e, T_e, and T_i are flux functions and (2) E_r-aligned, where n_e and T_i vary poloidally. The vertical lines show the radial location of the minimum gradient scale length for the respective case.

The OSM-EIRENE simulated I_{D_α} for both the LFS and HFS are shown in Figure 5-10. The simulated LFS I_{D_α} isn't affected much between the two cases, since the only thing that changes for the LFS is an increased T_i. The simulated HFS I_{D_α} for the E_r-alignment begins decaying further out, as expected due to the increased n_e on the HFS. The vertical lines show the location of the minimum gradient scale length of the D_α radiance for the respective cases, the same vertical lines shown in Figure 5-9. The difference in the locations for the two HFS cases is $\Delta\rho \sim 0.004$, a fairly small shift. This is approximately half of the difference in the electron density pedestal locations between the two HFS cases (see Figure 5-8).

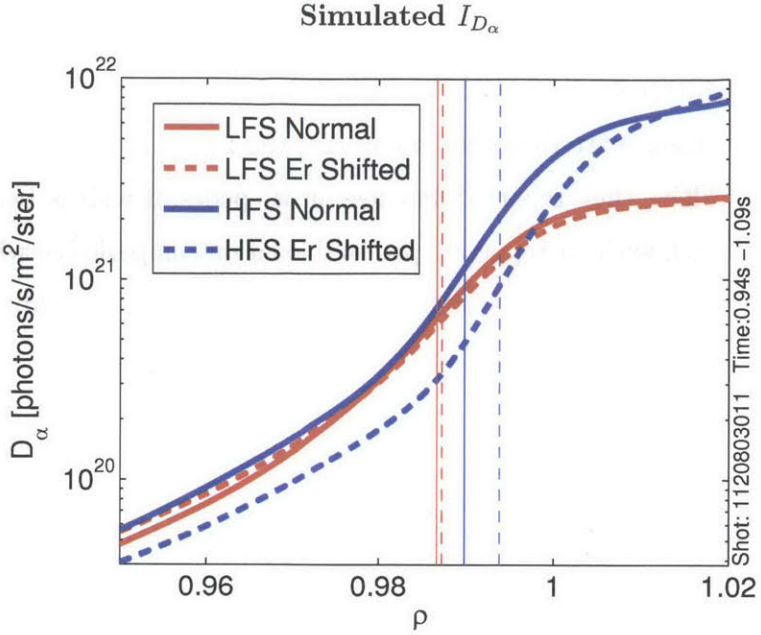

Figure 5-10: Simulated I_{D_α} for the LFS and HFS, for two separate cases: (1) Normal, where n_e, T_e, and T_i are flux functions and (2) E_r-aligned, where n_e and T_i vary poloidally. The vertical lines show the radial location of the minimum gradient scale length for the respective case.

We should note that not accounting for a poloidally varying n_e will *not* have a large effect on the derived impurity density, which depends on n_e through the CX rate coefficient and the ADAS PEC coefficients. The atomic physics prefactor F in Equation 3.29 for the density and temperature ranges of the C-Mod pedestal varies by less than <20%, except at the low density ($<2\times10^{19}\mathrm{m}^{-3}$) and temperatures (<100 eV) range, which anyway won't affect the impurity density except slightly at the very bottom of the pedestal. The electron density variation then is essentially encoded in the measured D_α radiance.

In conclusion, the measured D_α gradient scale lengths at the LFS and HFS give support to the possibility of a poloidally varying electron density. More insight on C-Mod could be gained using the measured D_α, though a better test would be the absolute values of I_{D_α}, which would require work on measuring and understanding the instantaneous flow rate of the separate LFS and HFS gas systems. Given the uncertainties in gradients of measurements (especially exponentially decreasing quan-

Gradient scale lengths of D_α radiance suggest a poloidal variation of n_e

tities), simulations, and the small shift in the expected I_{D_α}, the preferred method of determining the true level of poloidal variation in n_e would be direct measurements with a Thomson scattering system covering the LFS and HFS, such as found on MAST[109]. There they report differences in n_e pedestal widths between LFS and HFS[109], though without reporting pedestal location comparisons, which is how this effect would be most manifest from inspection of Figure 5-8. Additionally, we note there have been n_e asymmetries observed in closed-field line regions close to the limiter on Alcator-C[110].

5.3 Impurity Density Profile Modelling

A natural question to ask is: what is the expected impurity density profile? There is evidence from Alcator C-Mod[69] and ASDEX Upgrade[37] that the impurity density profiles in the pedestal region are well described by neoclassical transport processes. In these studies, 1D radial impurity transport codes were used to numerically solve the impurity transport problem. It's important to note that the neoclassical transport coefficients used were derived with theory which is violated in the pedestal region (since actually $\rho_{i\theta} \sim L_\perp$), and that radial transport can become comparable to parallel transport in the pedestal region, violating the 1D treatment. Nevertheless, similar 1D radial impurity transport simulations were done as part of this thesis to gain further insight into the expected impurity density profiles.

STRAHL[34], a 1D impurity transport code, was used to model the impurity density profile. STRAHL self-consistently solves the charge-state coupled impurity continuity equations:

$$\begin{aligned} \frac{\partial \langle n_z \rangle}{\partial t} &= -\nabla \cdot \Gamma_{zr} + S_z^n \\ &= \frac{1}{r}\frac{\partial}{\partial r}\left(D_z \frac{\partial \langle n_z \rangle}{\partial r} - V_z^{conv} \langle n_z \rangle \right) + S_z^n \end{aligned} \tag{5.5}$$

where the radial impurity particle flux Γ_{zr} is assumed to follow a diffusion/convection form, $\Gamma_{zr} = -D_z \frac{\partial \langle n_z \rangle}{\partial r} + V_z^{conv} \langle n_z \rangle$. Here $\langle\rangle$ denotes a flux-surface average. In STRAHL, care is taken to correctly do a flux surface average of diffusion/convection

coefficients, and the radial coordinate actually refers to a normalized flux-volume representation, $r = \sqrt{V/2\pi^2 R_0}$, so that the full shaped magnetic geometry is accounted for (i.e. not a cylindrical approximation). The charge-state coupling comes through the source term, S_z^n:

$$\begin{aligned} S_z^n &= - (n_e S_z^{ion} + n_e S_z^{rec} + n_D S_z^{cx}) \langle n_z \rangle \\ &+ n_e S_{z-1}^{ion} \langle n_{z-1} \rangle \\ &+ (n_e S_{z+1}^{rec} + n_D S_{z+1}^{cx}) \langle n_{z+1} \rangle \end{aligned} \tag{5.6}$$

where S^{ion}, S^{rec}, and S^{cx} are the ionization, recombination, and charge-exchange rate coefficients, respectively.

Neoclassical diffusion and convection coefficients can be calculated by the STRAHL code using the NEOART package[34]. While both Pfirsch-Schluter and banana-plateau coefficients are calculated, the Pfirsch-Schluter terms will almost always dominate in the pedestal region of C-Mod plasmas (since the impurities are almost always highly collisional). The form for these coefficients is:

$$\begin{aligned} D_z^{PS} &= \frac{\langle RB_\zeta \rangle^2}{(\partial\psi/\partial r)^2} B^2 \left(\langle B^{-2} \rangle - \langle B^2 \rangle^{-1} \right) \rho_i^2 \nu_{ii} \\ V_z^{PS} &= D_z^{PS} Z \left[\frac{1}{L_{n_i}} + \gamma_T \frac{1}{L_{T_i}} \right] \end{aligned} \tag{5.7}$$

where the $\rangle\langle$ brackets denotes averaging over the flux-surface, and all quantities have their normal meaning, except the gradient scale lengths here can be positive or negative, $L_y = y/(\partial y/\partial r)$. These neoclassical coefficients are valid for arbitrary shaping of the plasma cross-section. Note that the diffusion coefficient is independent of impurity species, but the convective coefficient scales linearly with Z.

As L_{n_i} will always be negative for a monotonically decreasing ion density, main ion density gradients will cause an *inward* flux of impurities through convection. Temperature gradients, found in the convective term, can either cause an *outward* impurity flux Γ_z if γ_T is positive, or an *inward* impurity flux if γ_T is negative. In STRAHL, the γ_T parameter is given by:

$$\gamma_T = H_z^{PS}/K_z^{PS}$$
$$\begin{aligned} K_z^{PS} &= 1 - \frac{0.52\alpha}{0.59 + \alpha + 1.34(\epsilon^{3/2}\nu_i^*)^{-2}} \\ H_z^{PS} &= -\frac{1}{2} + \frac{0.29 + 0.68\alpha}{0.59 + \alpha + 1.34(\epsilon^{3/2}\nu_i^*)^{-2}} \end{aligned} \tag{5.8}$$

where $\alpha = Z^2 n_z/n_e$. It should be noted that the form for V_z^{PS} here varies slightly from the form by Rutherford[111], in that the numerical coefficient which multiplies the temperature gradient in Rutherford is effectively $\gamma_T = H^{PS}/K^{PS} - 1/Z$ (ignoring the collisionality term in K_z^{PS} and H_z^{PS}). It's unclear why the $1/Z$ term doesn't appear in the V_z^{PS} found in NEOART and several publications[93, 33], though it seems to be due to the Rutherford expressions being only valid for the extreme Pfirsch-Schluter regime, i.e. the main ions and the impurities in the Pfirsch-Schluter regime[112, 113]. In the C-Mod pedestal region, plasmas tend to be in the mixed regime, where main ions are in the plateau regime, and impurities are in the Pfirsch-Schlutter regime. There are some indications that the $1/Z$ term is simply neglected[112], since for high Z the term is negligible. However, for low-Z impurities such as boron it makes the difference in the direction of the flux due to the temperature gradient. It should be noted that the experimental study by Pedersen[69] made use of the Rutherford equations, while those by Putterich[37] used the more generally used form used in STRAHL.

Inputs into STRAHL include the D_z and V_z^{conv} coefficients, electron profiles (n_e and T_e), and neutral density profiles (n_D). Optionally, neoclassical D_z and V_z^{conv} coefficients can be used, which are calculated internally by the package NEOART. These neoclassical coefficients require additional inputs of various magnetic geometry quantities.

Shown in figure 5-11 are the n_e and T_e profiles from an EDA H-mode which were used as inputs into STRAHL. These are from the measured electron profiles at the top of the machine, which if n_e had a dominant $\cos(\theta)$ dependence, would represent the flux surface average n_e (which is what is required as input into STRAHL). Not shown are the input n_D profiles, which was assumed to follow typical C-Mod profiles[50],

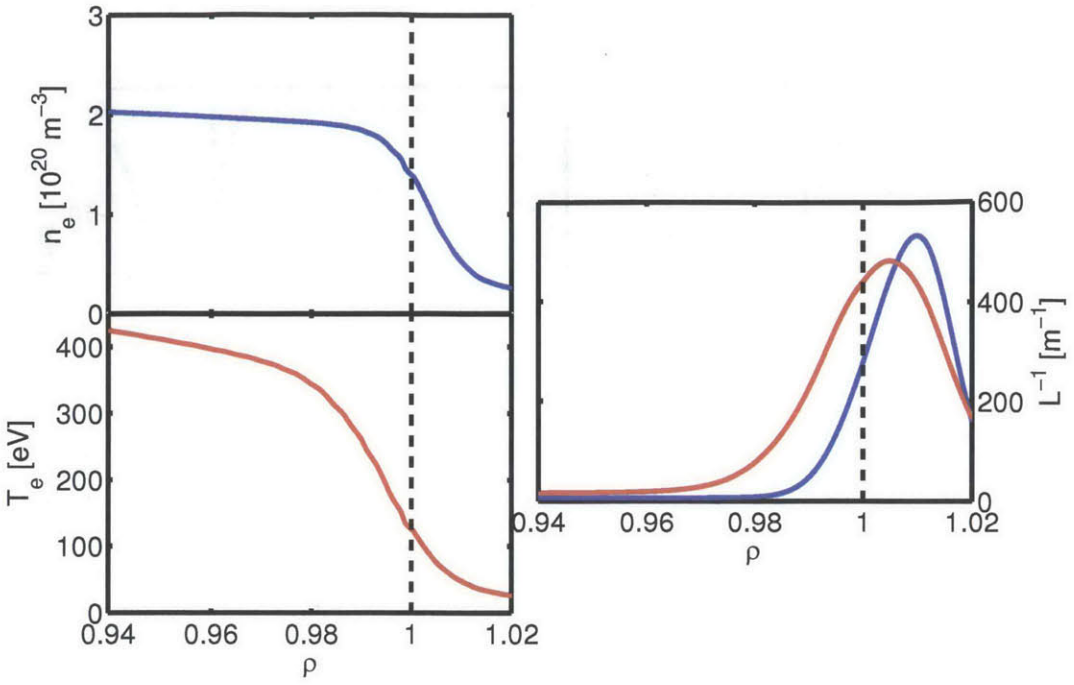

Figure 5-11: n_e and T_e inputs into STRAHL, along with a plot of the gradient scale lengths.

though the results of the STRAHL simulation were not affected by the n_D profiles. As seen in Figure 5-11, in the scale lengths there is a significant temperature gradient in a region with little density gradient. This initially led to a positive V/D in that region, which in turn causes a peaked impurity density profile (one can show that in steady-state, in the absence of sources, $V/D = 1/L_{n_z}$). As peaked impurity density profiles are not observed in the impurity density measurements, the V coefficient was modified to be less than 0 everywhere, which in effect decreases the γ_T coefficient of temperature profile gradient scale length in the region $0.98 \lesssim \rho \lesssim 0.995$. This may be due to an actual difference in the theoretical coefficient, an indication of increased anomalous transport, or simply a measurement error in the electron profiles. The resulting modified neoclassical D_z and V_z^{conv} coefficients, as calculated by STRAHL and used in the impurity transport simulation, are shown in Figure 5-12. The diffusion has been increased to a typical core level of anomalous diffusion, $D_z = 0.5$ m^2/s,

inward of the pedestal region, $\rho < 0.972$, and further out into the SOL $\rho > 1.03$.

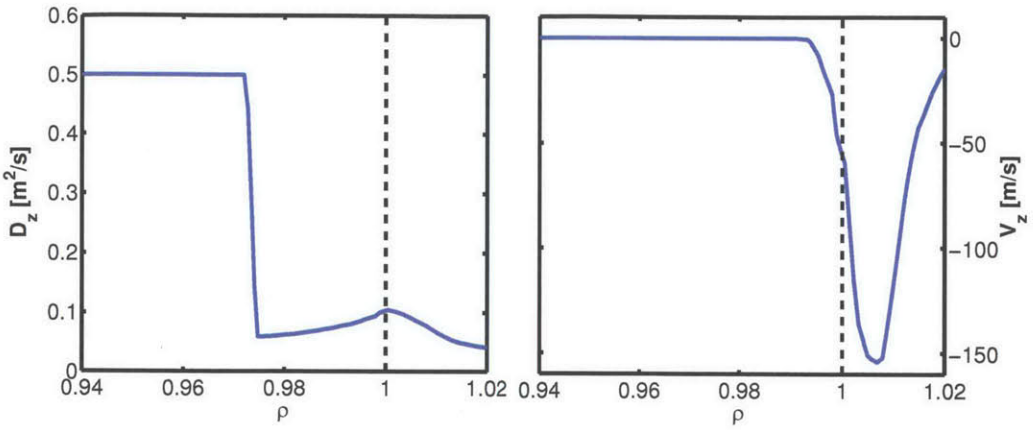

Figure 5-12: D_z and V_z^{conv} inputs into STRAHL. Values for $\rho > 0.98$ are neoclassical values, except that V_z^{conv} was flattened where V_z^{conv}/D_z was positive, otherwise large impurity peaking was predicted. Outside of the pedestal region, anomalous diffusion values are used.

STRAHL simulated n_z close to HFS measured n_z. 1D radial impurity transport may not be sufficient in the pedestal region

The resulting STRAHL-simulated B^{5+} density profile is shown in Figure 5-13, along with impurity densities measured at the LFS and HFS in red and green respectively, and the scaled electron density in orange. As seen, the STRAHL simulated $\langle n_{B^{5+}} \rangle$ is much closer to the measured HFS $n_{B^{5+}}$, with the LFS being much further shifted in. This could be an indication of an anomalous transport mechanism located in a narrow poloidal region around the LFS midplane, or that the 1D radial transport formulation isn't sufficient to describe pedestal impurity transport.

5.4 Drives for In-Out Impurity Asymmetries

Having shown that large differences can exist between the LFS and HFS pedestal B^{5+} impurity density, we now move on to explore potential candidates causing this in-out asymmetry. Specifically, we explore whether boron particle sources from the inner-wall, fluctuation-driven transport, or increased radial transport can drive impurity density asymmetries.

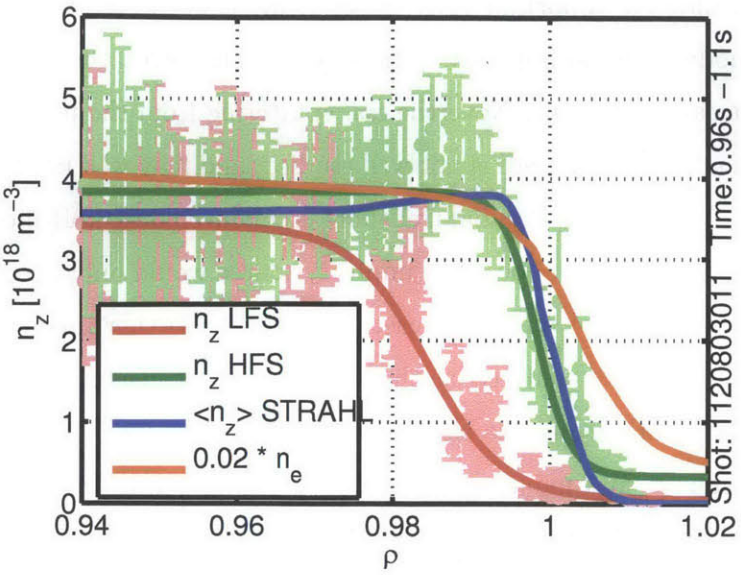

Figure 5-13: STRAHL simulated B^{5+} impurity density, along with measured LFS and HFS impurity density, and scaled electron density n_e.

5.4.1 Impurity Sources

One hypothesis is that a localized source of impurities at the HFS is causing a build-up of impurity density there. Such a poloidally asymmetric source could be caused by, for example, sputtering from the inner-wall of the tokamak. The outer-wall has much less material surfaces in close contact with the plasma since non-axisymmetric limiters are used, and the LFS impurity density is measured far from material surfaces, in comparison with the HFS impurity measurements which are typically less than 2 cm away from the inner wall. However, these impurity neutrals would have to ionize up to B^{5+}, and be radially transported faster than the parallel equilibration time.

Already we have some empirical evidence that such a localized source is NOT the cause. First, boron is a non-recycling impurity (i.e. chemically adheres to metal material surfaces, and so won't re-enter the plasma once coming into contact with the walls unless re-sputtered). It is well screened from the core plasma when injected from the inner-wall or divertor[114, 24] (i.e. it's mean-free path from these locations is shorter than the gap between the wall and the separatrix). Qualitatively this is thought to be due to the inner-wall acting as a continuous particle sink, though SOL

flows may also play an important role. Second, the pedestal impurity density in I-mode and L-mode show no impurity density asymmetry, even though similar levels of ICRF power can be present. Nevertheless, sputtering from the inner-wall in these different plasma operation modes is not well studied, and may well be enhanced in H-mode plasmas. Additionally, if radial transport is enhanced only in H-mode (e.g. by a particle pinch), the effect of a localized impurity source would only become apparent in H-mode, in the pedestal region at least. In order to further investigate whether localized impurity sources could cause the in-out impurity density asymmetry, dedicated experiments were devised to change conditions at the inner-wall, decreasing or increasing the source, and monitoring any changes in the measured in-out impurity density asymmetry in the pedestal. Specifically, two types of experiments were run:

1. Decrease Inner Gap: The gap between the plasma and the inner-wall was decreased during a shot, which acts to increase the sputtering from the inner-wall due to the higher incident heat and particle flux at that location.

2. Flip Magnetic Topology: The magnetic topology was changed by sweeping the secondary separatrix (SSEP) to go from LSN to DN, and finally to USN. This has been shown to change the direction of the SOL convective flows [115], which could affect how a localized impurity source is transported into the plasma. Additionally, the recycling changes in DN, due to the large reduction in radial width of the SOL plasma at the inner wall.

For these experiments, the boron source from the inner-wall was monitored by imaging the BII line (412.2 nm), with optical views from the A-side periscope, which are purely radial views focused on the inner wall, at varying heights. View 1 focuses near the top divertor, while view 12 is focused just below the midplane, as shown in Figure 5-14. The D_γ line (433.2 nm) was measured in the same spectra, allowing comparison of the relative increase of boron particle flux compared to deuterium particle flux. These spectral lines were measured using an $f/4$ Czerny-Turner spectrometer, with a 600 lines/mm grating.

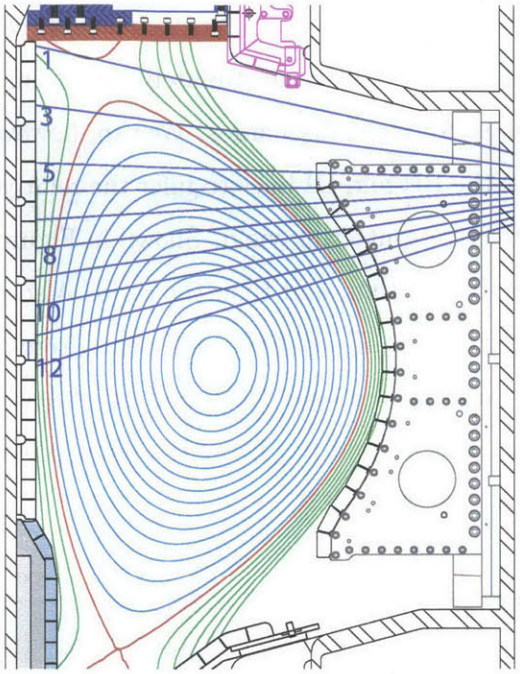

Figure 5-14: Optical views used to monitor the inner-wall. For reference, view 12 intersects the inner-wall at the height where the inner-wall parallel CXRS views are.

5.4.2 Measuring Particle Flux

The measured line-integrated emissivity, $I_z^{j\to k}$ (i.e. radiance), for impurity z and transition $j \to k$, can be used to derive the particle flux Γ_z using atomic physics calculations encapsulated in the so called S/XB coefficients [116], which gives a measure of 'ionizations per photon'. This allows a simple relation:

$$\Gamma_z = 4\pi \, (S/XB)_z^{j\to k} \, I_z^{j\to k} \tag{5.9}$$

The assumptions built into this relationship are: (1) the ion fully ionizes within the optics line-of-sight (2) recombination and charge-exchange are negligible and (3) the (S/XB) coefficient is approximately constant over the emission region. The (S/XB) coefficients used here for BII and D_γ were derived from ADAS. The (S/XB) coefficients are dependent on the background electron density and temperature, $(S/XB) = (S/XB)(n_e, T_e)$. This means that caution must be applied in interpreting changes in

radiance, $I_z^{j\to k}$, as they can be due to either (a) a change in particle flux, Γ_z or (b) a change in the background n_e and T_e. Unfortunately, the n_e and T_e weren't measured at the inner-wall midplane for these discharges. We can, however, use the ratio of the (S/XB) coefficients for the BII and DI lines to infer the relative change of the flux of B^{1+} to D^{0+}, i.e. the effective sputtering yield. Shown in Figure 5-15 are the separate (S/XB) coefficients for BII and DI, and then the ratio. Also plotted are white lines representing a 0.5x decrease of the (S/XB) coefficients from the value at the white doe, $n_e = 1 \times 10^{19}\,\mathrm{m}^{-3}$ and $T_e = 25$ eV. Note that in reality, the n_e and T_e used to evaluate the SXB coefficients should be the at the point of emission, and so can be slightly different for BII and DI.

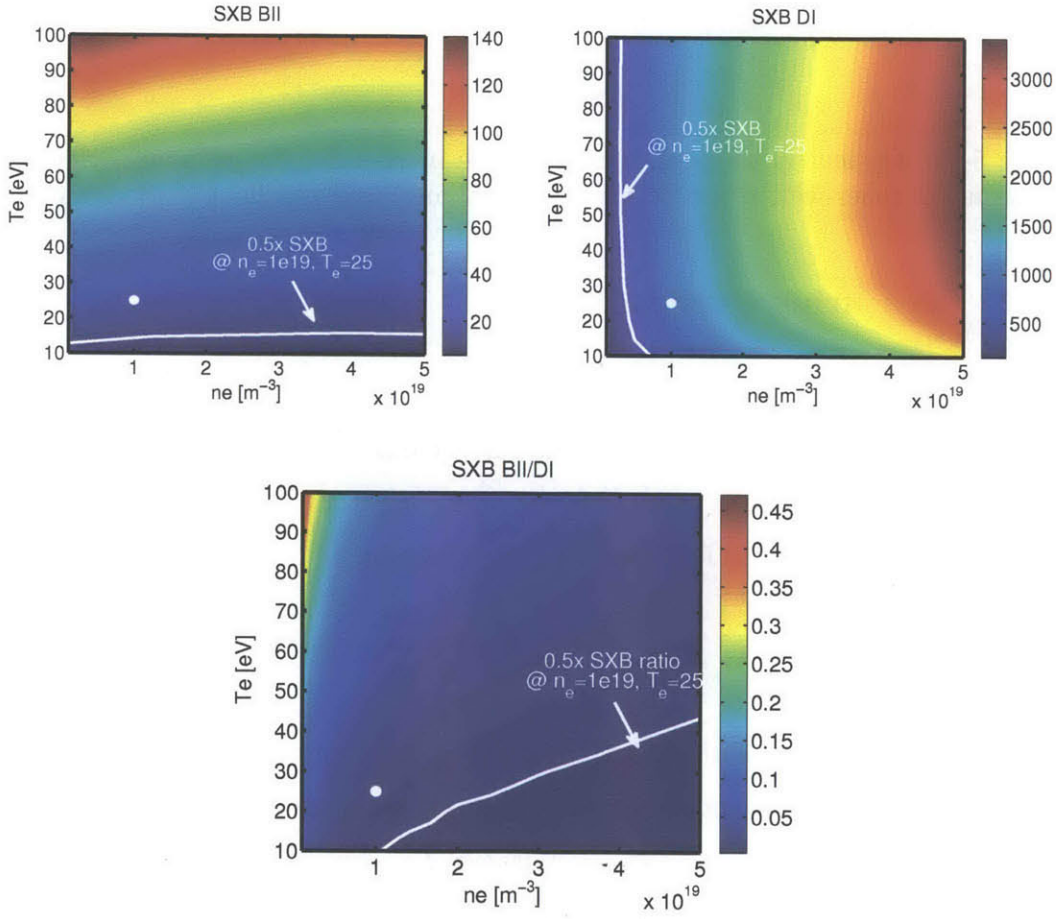

Figure 5-15: (S/XB) coefficients for the BII and DI line in (a) and (b) respectively, and then the ratio of BII to DI (S/XB) coefficients. White lines are where the SXB coefficient is 0.5x the value at the white dot

As seen, the separate (S/XB) coefficients are almost orthogonal in their n_e and T_e dependence: the BII coefficients vary weakly with density and strongly with temperature, while the DI coefficients vary weakly with temperature and strongly with density, though for $T_e < 20\,eV$ a stronger temperature dependence appears.

The BII to DI S/XB ratio, combined with measurements of the BII and DI radiance, give a qualitative measure of the effective sputtering yield. The theoretical sputtering yield of B^{0+} particles per incident D^{1+} particle is shown in Figure 5-16. As shown, the theoretical yield increases approximately linearly with T_e until $T_e > 40eV$, after which the theoretical yield is basically constant.

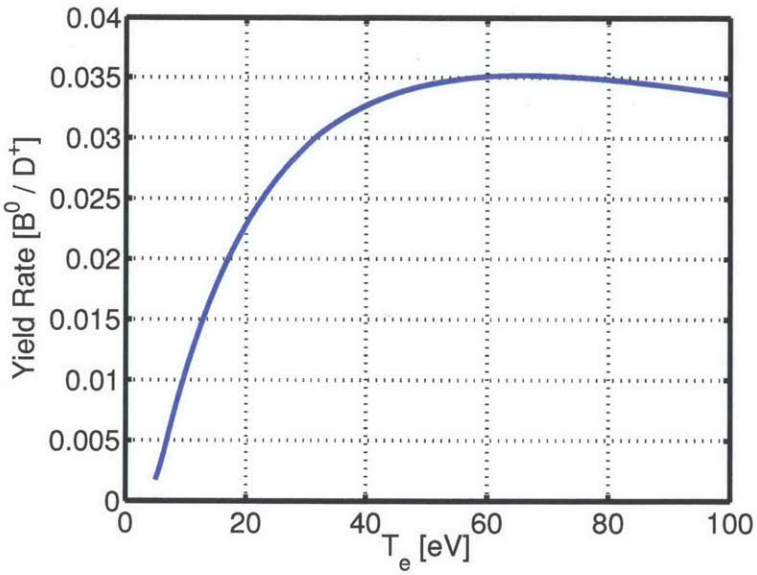

Figure 5-16: Theoretical yield of B^{0+} per incident D^{1+} ion

5.4.3 Decrease Inner Gap

The gap between the separatrix and the inner-wall is normally ≈10 mm in diverted plasmas. For these experiments, the gap was nominally set to 14 mm, then reduced to 2 mm over a time period of 40 ms, in an effort to increase the particle and heat flux to the inner-wall, enhancing the boron erosion from the inner-wall. An example of such a shot is show in Figure 5-17, with the radiance of the BII line, DI line, and

the inner gap. As seen, as the inner-gap decreases, a concurrent increase in the BII line is seen for the views near the inner-wall midplane (A-side 10-12), while views higher on the inner-wall are unchanged. For the DI line, there is also a concurrent increase with decreasing inner-gap, though all channels observe an increase. We can

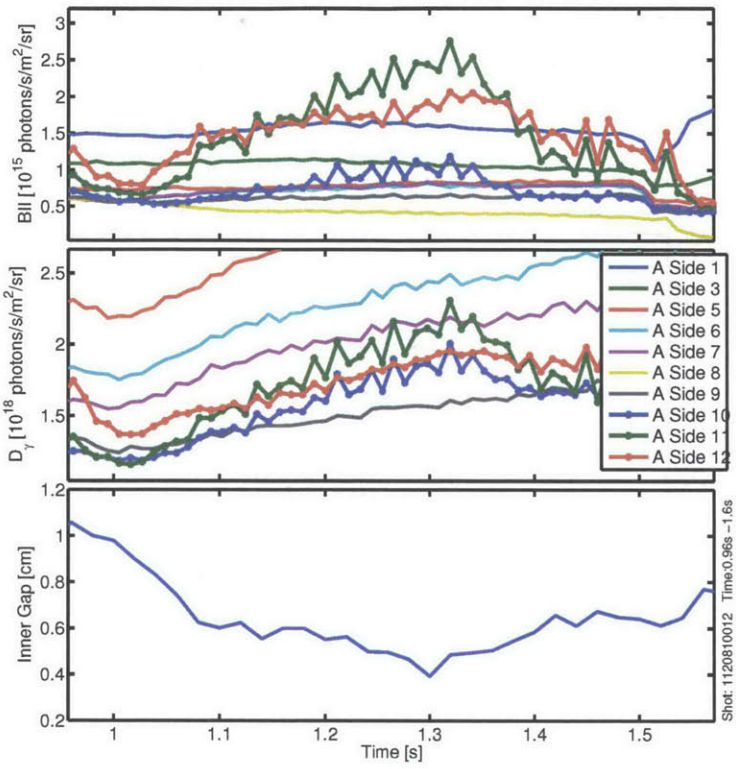

Figure 5-17: BII and DI radiance during inner gap scan, measured with the optical views in Figure 5-14.

immediately see from the flux surface geometry why only views A-side 10-12 see a large increase. Figure 5-18a shows the geometry at t=0.96s, when the gap is large, which shows that all open field lines which map from the LFS midplane continue to the HFS divertor. In contrast, Figure 5-18b shows the geometry at t=1.29s, when the inner gap reaches its minimum, which shows that the open field lines which map from the LFS midplane intersect the inner-wall. In other words, at this time the plasma LFS SOL is in a sense 'limited' on the inner-wall, which will lead to an increased heat

flux onto the inner-wall at points below $Z \sim 9$cm. This is exactly the region of views A-side 10-12, which see the increased BII and DI radiance.

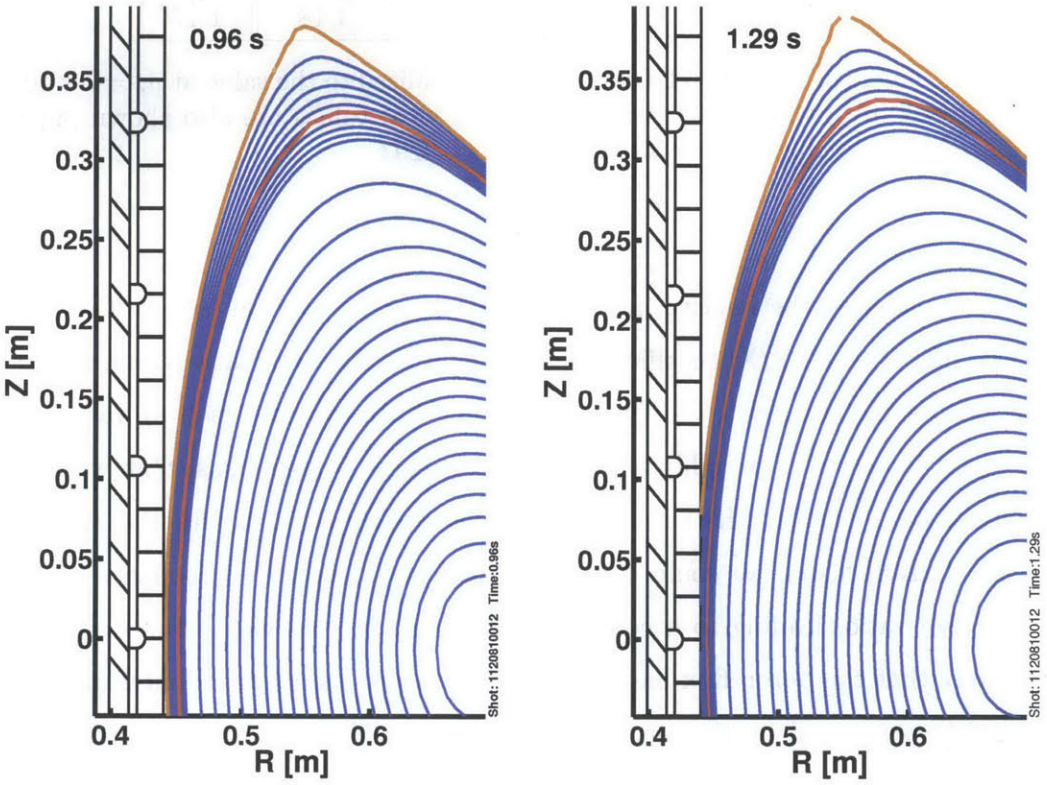

(a) (b)

Figure 5-18: Flux surface geometry (a) with a large inner-gap, ~10 mm and (b) with a small inner-gap, ~4 mm. The separatrix is in red, and the last flux surface to map from the outer midplane is shown in orange.

Since the BII radiance is increasing for views near the inner-wall midplane, this indicates that either the S/XB coefficients are changing (by changes in n_e and T_e) or the boron particle flux is increasing, as per equation 5.9. Since the BII S/XB coefficient is relatively insensitive to changes in n_e, as shown in Figure 5-15, T_e would have to *decrease* if the boron particle flux was constant as the radiance increases. This is unlikely, since the B^{1+} ionization stage will exist at a relatively fixed T_e. We conclude that as the inner gap is shortened, the boron source is increasing.

T_e[eV] ↓ n_e[m^{-3}] →	Ratio of BII / DI SXB			Yield
	1×10^{19}	3×10^{19}	5×10^{19}	
10	1.00	0.43	0.26	0.37
30	2.27	1.00	0.62	1.00
50	4.20	1.88	1.18	1.17

Table 5.1: Change in the BII to DI SXB ratio, normalized to the value at $n_e = 3\times10^{19}$ m^{-3} , $T_e = 30$ eV, which is 0.0103. Theoretical yield values are also shown, again normalized to the value at $T_e = 30$ eV, which is 0.0293

Now considering the relative increase of $\Gamma_{B^{1+}}$ to $\Gamma_{D^{0+}}$, we can see in Table 5.1 the ratio of BII to DI S/XB coefficients for several n_e, T_e combinations, normalized to the ratio value at $n_e = 3 \times 10^{19}$m^{-3}, $T_e = 30$ eV. As seen, for each n_e value, the S/XB ratio increases by roughly a factor of 2 for each T_e step, consistent with the theoretical yield changes. If the n_e value increased substantially, with the T_e value staying relatively fixed, we could expect a balancing of the S/XB coefficients with the I_{BII}/I_{DI} ratio, leading to a constant effective sputtering yield. However, it is more likely that the boron flux has increased relative to the neutral deuterium flux, as would be suggested by the fact that an increasing T_e near the wall, and hence incident ion energy to the wall, would increase the sputtered yield as shown in Figure 5-16 and Table 5.1.

Strong boron source from inner-wall does not increase B^{5+} in the pedestal region

Having shown that the boron source is increasing as the inner gap decreases, we now look at the B^{5+} measurements in the pedestal region to determine if there is an observable increase at the HFS, as would be expected if the boron source was rapidly transported radially before symmetrizing on a flux surface. We show in Figure 5-19 the B^{5+} density profiles over the entire inner gap scan. Figure 5-20, we show the B^{5+} density value near the top of the HFS pedestal, $\rho \sim 0.972$. As can be seen, $n_{B^{5+}}$ in the pedestal region doesn't increase as the inner gap decreases, opposite to the boron source. We conclude from these measurements that although there is a strong, local boron source coming from the inner-wall, this does not cause a local increase of fully ionized boron (B^{5+}) in the pedestal region.

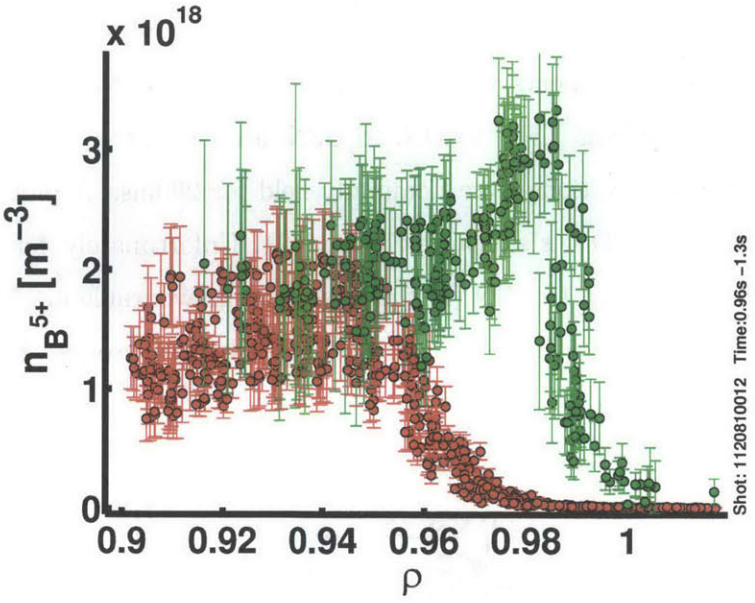

Figure 5-19: B^{5+} density during inner gap scan. LFS in red, HFS in green.

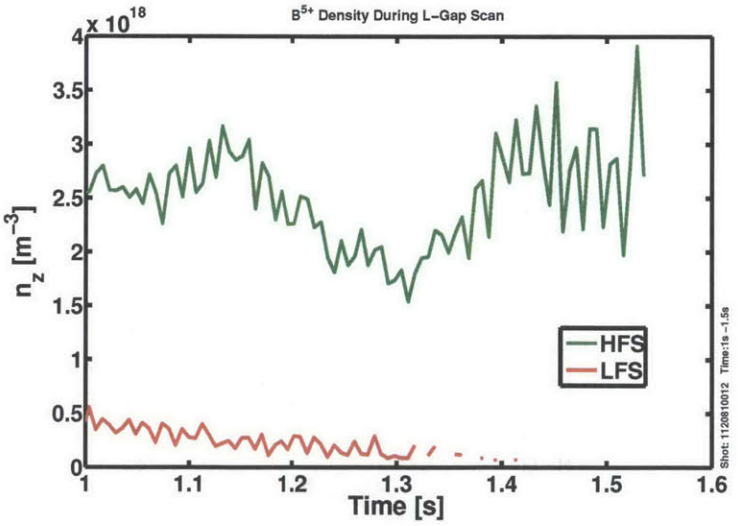

Figure 5-20: B^{5+} density near the pedestal top during the inner gap scan.

5.4.4 Flip Magnetic Topology

Having shown that boron sources from the inner-wall are not a likely cause for the pedestal in-out impurity density asymmetry, we now consider boron sources originating away from the HFS midplane and propagating through the SOL to the HFS midplane. This could occur due to the strong SOL flow structures observed in single-

null plasmas[26]. In double null plasmas, the SOL flows are essentially cutoff to the HFS. To study this, experiments were performed in EDA H-modes which switched the magnetic geometry from LSN, to DN, to USN, all within the same plasma discharge. Each of these positions were nominally held for 200ms. A plot of the flux surface reconstruction in DN is shown in Figure 5-21. Unfortunately, for all of these experiments when switching to USN (in this case, the unfavourable ion ∇B-drift direction), the H-mode would drop out, making the USN times useless. However, the change from LSN to DN is still instructive.

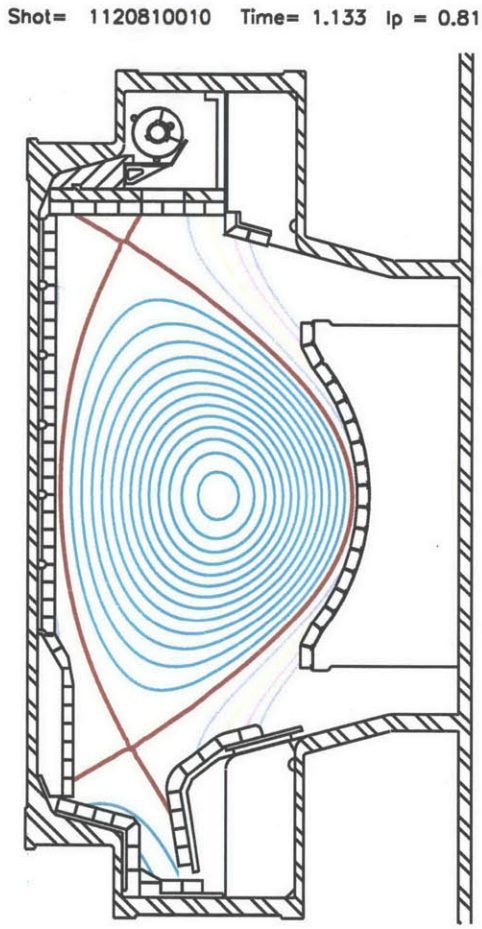

Figure 5-21: Flux surfaces for the double null configuration. With balanced X-points, SOL flows are cut off from the LFS, leaving the HFS SOL at a lower density, and with lower flows.

A plot of the B^{5+} impurity densities measured at the LFS and HFS during the

DN phase is shown in Figure 5-22. Although not shown, this profile is nearly identical to the profiles measured immediately before this time, when the plasma was in a LSN configuration. Changing from LSN to DN made major radius scans too difficult to perform, which leads to the gaps in the HFS impurity density profile. Nevertheless, it remains clear that an in-out impurity density persists in the DN configuration, though by how much isn't clear due to the unfilled HFS profile. We can conclude then, that the in-out impurity density asymmetry in the pedestal region is not caused by sources being transported by convective flows in the SOL from the LFS, as these sources would be effectively cut off from the HFS in this DN plasma.

In-out n_z asymmetry not caused by boron source transported from the LFS through the SOL

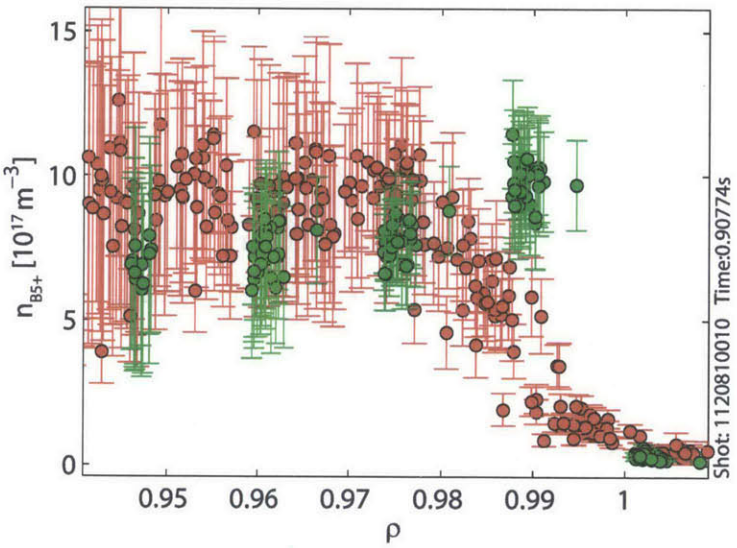

Figure 5-22: Boron impurity density at the LFS and HFS, showing the in-out impurity asymmetry persists during a double-null plasma. This indicates an impurity source in the LFS SOL propagating to the HFS is not the cause of the impurity asymmetry.

5.4.5 Fluctuation Driven Transport

Recalling the discussion of H-modes in Alcator C-Mod in Section 1, of the three main types, two (EDA and ELMy) included a coherent fluctuating mode radially located in the pedestal region, but poloidally localized to the LFS only. As these ballooning-like modes are also correlated with enhanced particle transport in the pedestal, it could

be reasoned that these modes radially expel (or alternatively, pull inwards) impurities at the LFS pedestal faster than the time needed for parallel transport to fill in the vacancy.

The dominant fluctuation driven transport is believed to be due to fluctuating electric potential, which creates a fluctuating $E \times B$ drift of particles, $\tilde{v}_r = \tilde{E}_\theta / B$. If these electrostatic fluctuations have a component in-phase with the fluctuating density, they will cause a radial particle flux:

$$\Gamma_r = \left\langle \tilde{n} \frac{\tilde{E}_\theta}{B} \right\rangle_t \tag{5.10}$$

Here the $\langle\rangle_t$ brackets refer to time average. Radial magnetic field fluctuations along with parallel velocity fluctuations can also drive radial particle transport, but the level of magnetic fluctuations compared with density or potential fluctuations is orders of magnitude smaller in the edge, and therefore won't play a role.

While new measurements with a mirror Langmuir probe[117] are providing precise $\tilde{n}$ and $\tilde{E}_\theta$ in Ohmic EDA H-modes, in general the fluctuating poloidal electric field isn't measured in the pedestal region of ICRF heated plasmas, due to the higher heat flux. We shall here, however, compare qualitatively the line-averaged fluctuating electron density measured with the Phase Contrast Imaging (PCI) diagnostic. PCI is a laser interferometry technique, which passes a 10.6μm CO_2 laser vertically through the plasma and measures phase variations induced by electron density fluctuations, resulting in a measure of $\int \tilde{n}_e d\ell$, where the integral is over the path length of the laser. The C-Mod PCI system has 32 spatially separated channels, allowing resolution of wave-number k_R from 0.5-55 cm^{-1}, and digitization frequencies such that it can resolve frequencies from 2 kHz to 5 MHz[118].

Figure 5-23 shows example fluctuating amplitude frequency spectra measured with PCI for L-mode, I-mode, EDA H-mode, and ELM-free H-mode. It should be noted that for the L- and I-mode, the PCI system doesn't resolve well low frequency, low-k turbulence which may play a significant role in transport. In the plot, the L-mode and I-mode have similar base fluctuating amplitudes (the WCM isn't typically resolved by

the PCI diagnostic). The EDA H-mode also has a base similar to L-mode and I-mode for $f < 100$ kHz, and the QC-mode is apparent in its spectra at $f \approx 80$ kHz. The ELM-free H-mode, however, has significantly reduced baseline fluctuations at lower frequencies, although near $f = 120$ kHz rises above L-mode and I-mode to match the EDA H-mode levels. Although the PCI diagnostic is a line-integrated diagnostic, it has some vertical localization due to sensitivity to the magnetic field pitch angle[119]. We note though that investigations of fluctuations using Gas Puff Imaging (GPI), which is a measurement local to the LFS midplane, also showed[120] that ELM-free H-mode has an overall reduction in fluctuating power in the pedestal region, while the EDA is near L-mode, with a strong peak due to the QCM.

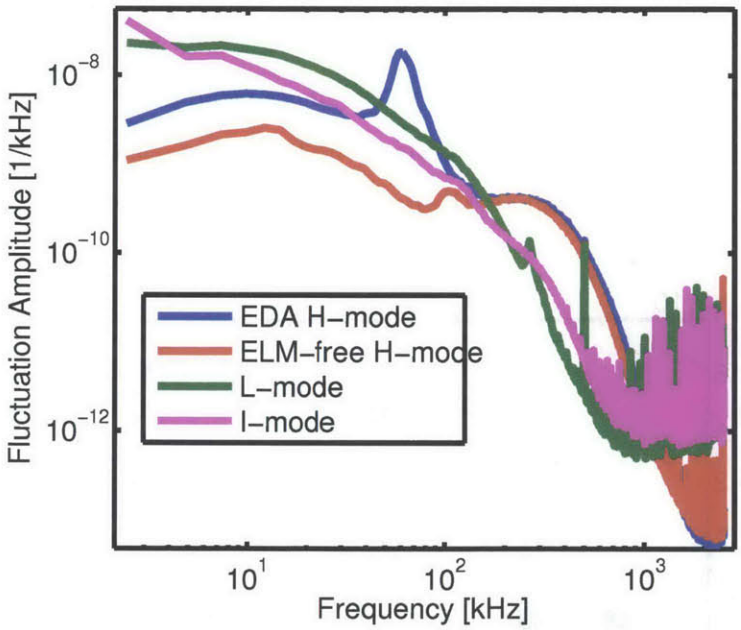

Figure 5-23: Electron density fluctuation frequency spectra, measured with PCI. Note the large reduction in fluctuation amplitude in the ELM-free H-mode.

This overall reduction in the fluctuations in ELM-free H-mode are an indication of reduced fluctuation-driven particle transport, though detailed analysis of the phase relationship of the density fluctuations with the poloidal electric field fluctuations would be needed to make precise comparisons. Since the in-out impurity density asymmetry persists in the ELM-free H-mode (see Figure 4-6), we can infer that fluctuation-driven

Fluctuation-induced transport not root cause of n_z asymmetry, since asymmetry persists in ELM-free H-mode with reduced $\tilde{n}_e$.

transport localized to the LFS is not the primary cause for the in-out impurity density asymmetry we observe in the pedestal region.

Fluctuation induced transport may enhance n_z asymmetry, such as in EDA H-mode

Despite this statement, we can not rule out fluctuation-driven radial transport from being a contributor to enhanced radial particle flux in, for example, EDA H-modes. In Figure 5-24, we plot the total fluctuation amplitude (integrated over k and f) from the PCI diagnostic vs edge safety factor, q_{95}. A linear trend is observed in q_{95}, which was also previously observed for QC-mode fluctuations using reflectometry[99], where it was found $\int n_e \propto (\nu^* q_{95}^2)^{0.56}$, where here ν^* is the mid-pedestal collisionality factor. While this linear trend in fluctuation amplitude versus q_{95} correlates with the LFS/HFS n_z pedestal separation versus q_{95} (see Figure 5-4), further work would be needed to determine if fluctuation-induced transport contributes to the impurity density asymmetry.

This linear trend in q_{95} is very similar to the linear trend in LFS/HFS n_z pedestal separation vs q_{95} (see Figure 5-4), suggesting the QC-mode could play a role in the increased impurity density asymmetry by flushing out impurities at the LFS midplane.

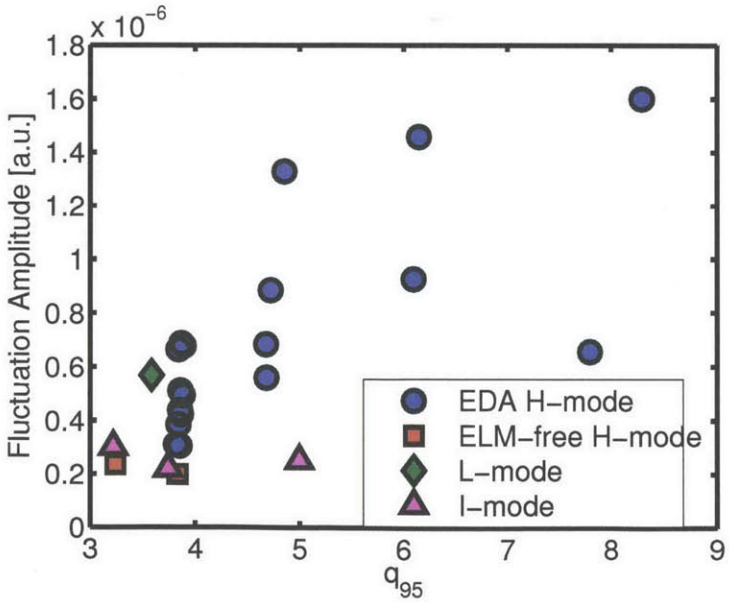

Figure 5-24: Total fluctuation amplitude measured with PCI vs edge safety factor, q_{95}.

5.4.6 Transitions

An empirical observation of transitions from L-mode and H-mode gives a further confirmation of the conditions in H-mode providing the drive for the impurity density asymmetry. In Figure 5-25 are shown profiles from the ELM-free H-mode in Figure 4-6, but here with two different time windows: those during the L-mode phase, after the radiative collapse of the H-mode, and those during the H-mode phase presented previously. As seen, in the L-mode phase, when the electron density and temperature pedestals disappear, the impurity density becomes again symmetric. Then when the H-mode builds up, the impurity density asymmetry develops again. This discharge of time-varying pedestal conditions gives further proof of the H-mode background plasma gradients playing a role in the formation of the impurity density asymmetry.

n_z asymmetry present when H-mode pedestal forms, disappears in L-mode

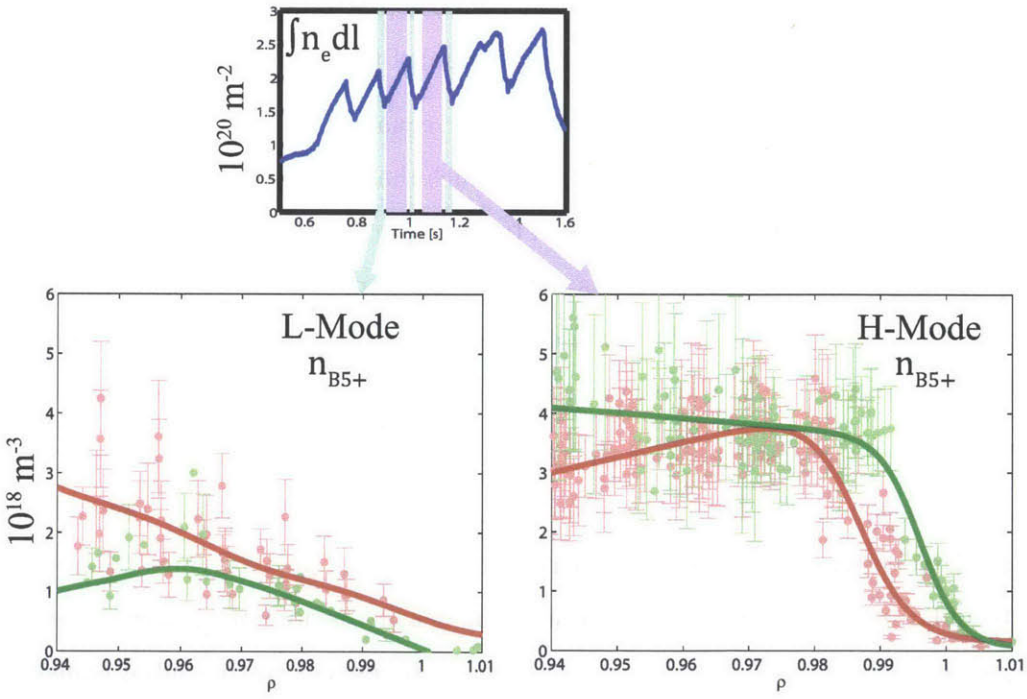

Figure 5-25: Time resolved impurity density profiles during an ELM-free H-mode. The top graph shows the line-averaged electron density, with the H-mode time frames in purple and the L-mode time frames in green. n_z forms an impurity density asymmetry when the plasma is in H-mode, and returns back to the symmetric case when the plasma is in L-mode

5.4.7 Transport Timescales

As discussed in Section 2, in the presence of strong gradients in density and temperature, the radial transport due to simple collisional transport can become comparable to parallel transport time scales. This can affect the impurity density in two ways: (1) if the radial transport was poloidally symmetric, a poloidally asymmetric impurity source could be quickly transported inwards, leading to an impurity density asymmetry and (2) if the radial transport was poloidally asymmetric, impurities can be locally expelled or pulled inwards, similar to the effect of ballooning transport caused by fluctuations. As shown previously, we have experimental evidence that an impurity source at the HFS does not affect the impurity density asymmetry, so the first method through which radial transport can cause an impurity density asymmetry can be neglected. Here we focus on the second method, that of a poloidally asymmetric radial transport becoming comparable to the parallel transport processes.

In impurity transport studies, the continuity equation (Equation 2.2) is usually solved by assuming a separation of timescales, such that parallel and cross-field transport can be solved separately, since parallel transport in the core plasma is much faster than cross-field transport. This allows solving a one-dimensional equation in the direction of interest. However, if the timescales for parallel and perpendicular transport become comparable, the full two-dimensional equation would have to be dealt with.

Here we will make estimates for the transport time scales, and also investigate the poloidal variation of said timescales. We consider two separate processes that work to symmetrize density on a flux surface: parallel diffusion and poloidal convection. Note that toroidal rotation will not play a role if the density asymmetry is axisymmetric, since then $\nabla \cdot n_z V_{z\zeta} = 0$. We then compare these timescales to the radial transport timescale.

Parallel Diffusion ($\tau_{\|}$) If ions could free stream along the magnetic field lines, uninhibited by collisions, the parallel transport time would simply involve the parallel

transit length, divided by the ion sound speed (thermal velocity):

$$\tau_{\|} = \frac{L_{\|}}{v_{th}} = \frac{\pi q R_0}{\sqrt{\frac{2T_z}{m_z}}} = \frac{\pi}{\sqrt{2}} q R_0 \sqrt{\frac{m_z}{T_z}}$$

However, most impurities are highly collisional in the pedestal region (this is certainly true for boron, Z=5, due to the strong Z^2 scaling of collision frequency), meaning they will undergo several collisions before they can complete a full poloidal circuit on the flux surface. In this case, the parallel diffusion and/or convection will transport the impurities. The parallel diffusion coefficient is given as:

$$D_{\|,z} = v_{th,z}^2 / \nu_{zi}$$

Note that only impurity-ion collisions are included, as they are the only collisions that will lead to diffusion (self-collisions will not). This then leads to a parallel transport timescale of

$$\tau_{\|} \sim \frac{L_{\|}^2}{D_{\|,z}} = \frac{(\pi q R_0)^2}{v_{th,z}^2 / \nu_{zi}} = \pi^2 \nu_{zi} \frac{q^2 R_0^2}{v_{th,z}^2}$$

Here half of the parallel transit length $L_{\|}$ was used, since it's for source considerations, which we care about travelling to the other side of the machine.

Poloidal Convection (τ_θ) Asymmetries can also be reduced by poloidal flows:

$$\tau_\theta \sim \frac{L_\theta}{V_\theta} \tag{5.11}$$

Radial Diffusion/Convection (τ_r) Often cross-field transport is modelled by a diffusion/convection form for the flux, $\Gamma_{zr} = n_z V_{zr} = -D_z \frac{\partial n_z}{\partial r} + V_z^{conv} n_z$, as explained in Section 5.3.

The radial transport (or cross-field transport) can be dominated by diffusion or convection. The general form combining both is:

$$\tau_\perp \sim \frac{L_r}{V_{zr}} \sim \frac{L_r}{-D_z \frac{1}{n_z}\frac{\partial n_z}{\partial r} + V_z^{conv}} \tag{5.12}$$

The scale length L_r will be the minimum of the distance travelled of interest and the perpendicular gradient scale length. Almost always, the impurity density gradient scale length is used, $|L_\perp| = n_z \left|\frac{dn_z}{dr}\right|^{-1}$.

We can try to derive D_z and V_z^{conv} from measured profiles and an impurity transport code, such as STRAHL, but without time dependent changes to the impurity density, we can not uniquely determine D_z and V_z^{conv}, only the ratio V_z^{conv}/D_z. In order to have a lower limit on these coefficients, we will use the neoclassical form. This is not without justification; in addition to the heuristic assumption that turbulent transport is suppressed in the pedestal, such that neoclassical transport is dominant, studies in ASDEX-Upgrade have shown neoclassical transport to well describe the LFS impurity pedestal shape and location for several low-Z impurities[37]. Note that the neoclassical form represents the *minimum* level of transport we would expect. If the diffusion is actually larger, the radial transport timescales presented there will only become faster.

The neoclassical diffusion coefficient for impurities should scale as $D_z^{neo} \sim q^2 \rho_z^2 \nu_{zi}$. Here we will use the flux-surface average D_z and V_z^{conv} from Equation 5.7.

Note that normally the diffusion will dominate over convection, but in the pedestal region, the large gradient scale lengths can make convection important.

Here we should make an important note about the poloidal variation of the radial transport timescale. First, the gradient scale lengths will be larger on the HFS, since the physical spacing between flux surfaces on the HFS is larger than at the LFS. Second, while Equation 5.7 presents the flux-suface averaged diffusion and convection coefficients, in reality D_z and V_z^{conv} will vary on a flux-surface (normally, this doesn't matter since the parallel transport is fast enough to cause the impurities to sample the radial transport on the entire flux surface). From the simple random walk problem, the diffusion coefficient strongly varies with magnetic field, $D_r \propto B^{-2}$, so locally, the diffusion on the HFS will be much lower. Taken together, for similar n_z profiles, the

radial transport is slower on the HFS.

Ionization Time (τ_{ion}) Another process that may be important in considering the transport of sources is the ionization time, i.e. how long will it take a neutral impurity to completely ionize. If the radial transport is faster than the ionization time, a poloidally localized source could be transported further into the plasma, causing a poloidal asymmetry. The simple ionization rate for a species with charge Z is:

$$\tau_{ion}^{z} = \frac{1}{n_e S_{ion}^{z}} \tag{5.13}$$

where S_{ion} is the ionization rate coefficients. In reality, determining the ionization time for the fully-stripped boron requires coupling ionization and recombination (loss and source terms) for each charge state leading up to B^{5+}. But for the pedestal temperatures of interest, recombination can safely be neglected. Take the case where a neutral is suddenly introduced at a particular position in the plasma. The ionization time we calculate here is the time it takes to completely ionize that neutral, i.e. the sum of the individual ionization times of the individual ionization stages:

$$\tau_{ion} = \sum_{z} \tau_{ion}^{z} = \sum_{z} \frac{1}{n_e S_{ion}^{z}} \tag{5.14}$$

This will be an upper bound on the ionization time, since really we should consider the ionization time for a source atom charge state which enters into a region of strong radial transport. However, the majority (80%) of this ionization time is spent ionizing the final charge state, B^{4+}.

For boron, the ionization rate coefficients were taken from an ADAS data file used in STRAHL (scd00_b.dat), and checked against analytic expressions[121].

Timescale Example These timescales of interest are plotted in Figure 5-26 for a 1MA EDA H-mode, with the bottom graph showing the LFS and HFS impurity density profiles, from which the gradient scale lengths L_{n_z} were calculated. The radial diffusion timescale in orange was calculated using a flux-surface averaged impurity

density, assuming a dominant in-out asymmetry ($n_z = \langle n_{z,0} \rangle (1 + n_1 \cos\theta)$). As a limit, the LFS and HFS n_z profiles were used separately to calculate τ_r, and are plotted in the thinner orange lines. The poloidal transport time scale τ_θ was calculated using the measured LFS/HFS poloidal velocities, and assuming in between that $V_{z\theta}$ varies as $V_{z\theta} = K_z(\psi) B_\theta / n_z$. Again, as a limit τ_θ was also calculated with LFS and HFS measured $V_{z\theta}$, and are shown in the thinner purple lines.

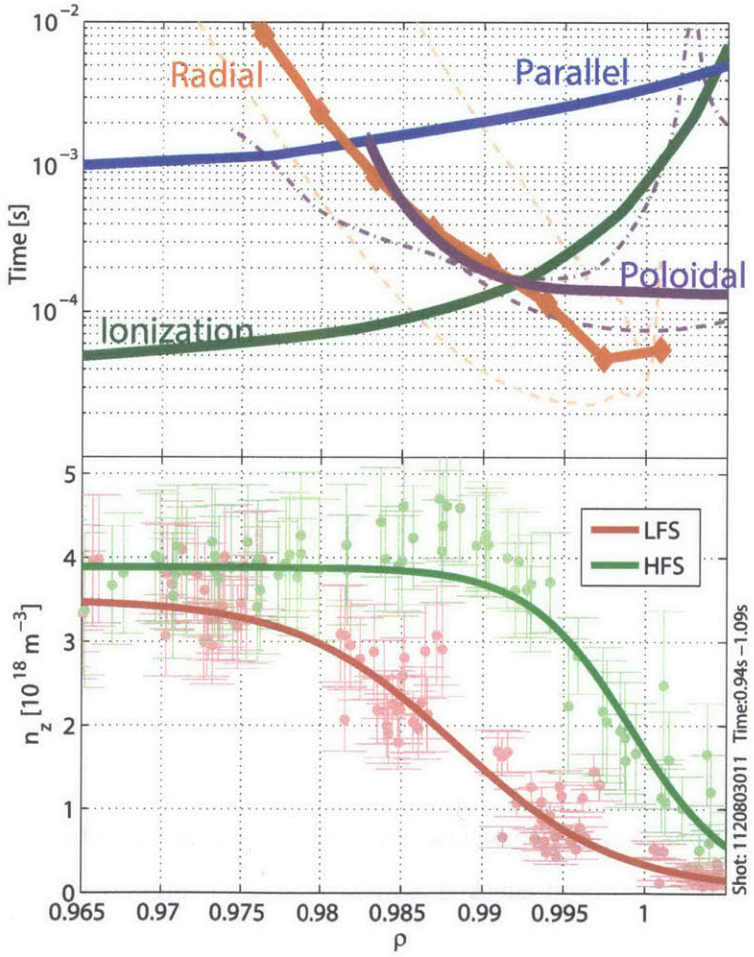

Figure 5-26: Timescales for a 1 MA EDA H-mode. LFS/HFS impurity density profiles are also shown.

Several interesting features are apparent. The radial transport becomes faster

than the diffusive parallel transport near the top of the LFS impurity density profile. However, the poloidal transport can still act to symmetrize the impurity density on the flux surface. The radial transport process is comparable to the poloidal timescale in the region beginning at $\rho \approx 0.98$, which is near the T_e pedestal top. This suggests that the impurity particle transport can not be treated as a 1D problem, but rather we must face up to the 2D, perpendicular and parallel coupled transport equation. The radial transport timescale becomes faster than the poloidal at $\rho \approx 0.992$, near the n_e and n_{zH} pedestal tops. In principle, this separation of timescales may again allow a 1D treatment of the radial transport, using local gradients instead of flux-surface averaged. As could be expected, the ionization time τ_{ion} is faster than all other processes in the core most regions. However, for $\rho > 0.992$ both the radial and poloidal transport timescales become faster than the ionization, potentially meaning sources in this region can be transported inward before completely ionizing.

Radial timescale comparable to poloidal timescale, must treat simultaneously in impurity transport

Based on timescales alone, we could postulate that the increased radial transport compared to the poloidal transport is a primary cause of the in-out impurity density asymmetry. While the radial transport timescale we've shown in Figure 5-26 is based on a flux-surface averaged diffusion and convection coefficient, in reality the radial transport flux varies strongly with poloidal position[91, 122]. In regions of low radial transport compared to parallel or poloidal transport, such as the core, this poloidal variation of radial transport doesn't matter, since the parallel transport is so fast that impurities will sample all of the flux surface, averaging out the poloidal variation in radial transport. However, when the radial transport process happens on a timescale faster than that of parallel or poloidal, impurities will start to only sample the radial transport at the poloidal location where they entered the region of strong radial transport. Since the radial transport can vary strongly poloidally, this can give rise to impurity density asymmetries.

However, comparing to the timescales for an I-mode discharge in Figure 5-27, we can see that the timescale picture is qualitatively similar: the flux-surface average radial transport is close to or faster than the poloidal transport time in the region of the temperature pedestal ($\rho > 0.98$). Yet as also shown in Figure 5-27, and was

I-mode radial and poloidal transport timescales also comparable in pedestal, but n_z is symmetric

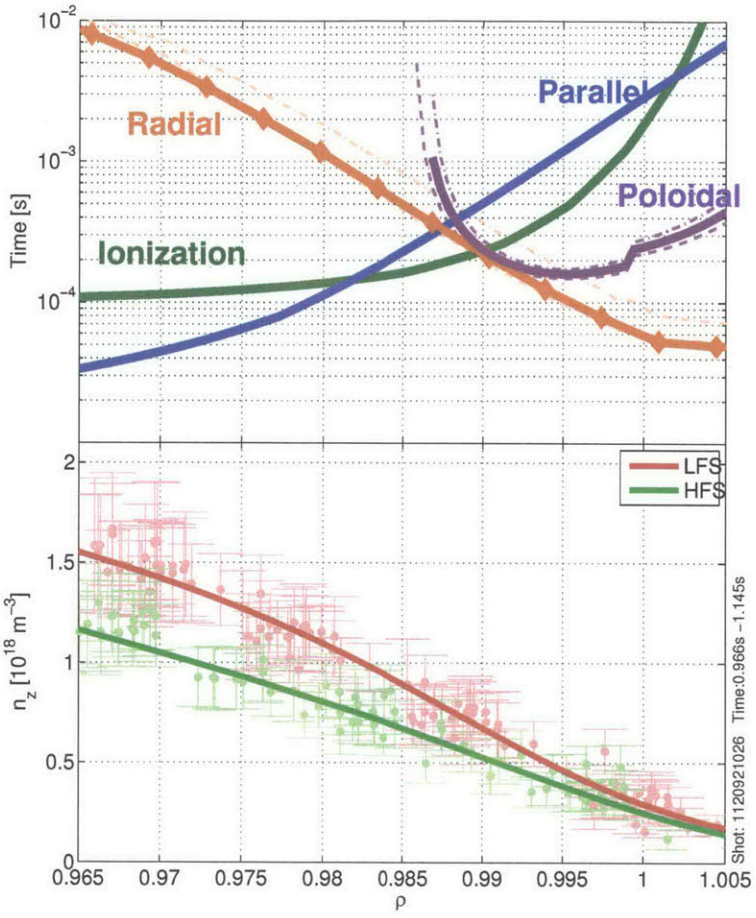

Figure 5-27: Timescales for a 1.3 MA I-mode. LFS/HFS impurity density profiles are also shown.

previously shown in Chapter 4, the impurity density is basically symmetric between the LFS and HFS, seemingly unaffected by the increased radial transport.

We stress that caution must be used in interpreting the timescales in Figure 5-26 and Figure 5-27. The timescales are approximate, especially considering that the true flux-surface average impurity density isn't well defined. Here we have assumed a dominant in-out cosine variation in n_z. However the STRAHL results and previous measurements of fluorine at the top and LFS midplane would suggest that perhaps the impurity density varies only locally in a narrow poloidal extent centered around the

LFS midplane. Also, the transport coefficients used to determine the radial impurity flux, and hence τ_r, are the conventional, 1D neoclassical transport coefficients (but with measured impurity density gradients), which will most likely be incorrect in the presence of strong gradients[22].

H-mode has a predicted strong inward radial impurity flux near separatrix, due to n_i gradient, while I-mode has only outward radial flux

However, there is a robust neoclassical transport effect of n_i gradients driving *inward* convection of impurity particle flux (see Section 5.3). Because H-modes have a strong main ion density pedestal, and I-modes do not, heuristically we can expect a stronger inward impurity particle flux in H-mode plasmas. This is consistent with and a potential mechanism for the empirical observation that the global impurity confinement time is longer in H-mode than in I-mode[123]. This difference in *direction* of radial impurity flux between H-mode and I-mode could also then be the cause of the impurity density asymmetry observed in H-modes. Additionally, because of the poloidal variation in n_i, inferred from the T_z asymmetry (see Figure 5-8), in H-mode the n_i at the LFS will actually be further inward, which would result in a stronger inward radial impurity flux at the LFS. Because the poloidal variation of n_i is less in I-mode than H-mode, this could even further enhance inward impurity particle flux at the LFS in H-mode, and drive stronger in-out impurity density asymmetries.

The above discussion on the role of the main ion (or n_e) gradient driving inward radial impurity flux preferentially at the LFS, with stronger n_e gradients further inward at the LFS due to the poloidal variation of n_e, are suggestive only, and haven't been used yet in a transport code to show that they do reproduce the measured poloidal variation in impurity density. Certainly, the strong outward radial impurity flux due to the outward diffusive flux could be flushing impurities outward preferentially at the LFS, though it would then be unclear why in I-mode impurity density asymmetries don't form, since in I-mode the radial transport is comparable to the poloidal transport timescales. To fully unravel these differences, a more complete impurity modelling retaining 2D effects ($\tau_r \sim \tau_\theta$, and $\rho_{\theta,i} \sim L_{n_i}, L_{T_i}$) is necessary. Additionally, as the n_e pedestal spans the separatrix, it may be important to treat the pedestal and SOL as a single connected system, whereas in most modelling efforts they are usually treated separately.

5.5 Summary

In this chapter we have explored in more detail the asymmetries which arise in impurity density and temperature in the H-mode pedestal region. In-out impurity density asymmetries in H-mode plasmas have a peak asymmetry value of 2.5 to 9, always with higher densities at the HFS. The n_z pedestal on the LFS shows marked changes with changing plasma current, namely that the width widens, and the location shifts in slightly with decreasing plasma current. A comparison of pedestal locations of n_z and T_z at the LFS shows that the n_z pedestal is consistently further shifted in than the T_z pedestal, whereas for the HFS the pedestal location of the two quantities generally align.

As a verification the LFS/HFS alignment, measured impurity temperature asymmetries were used to determine if Spitzer power balance was satisfied. It was found that, using a simple fluid model of parallel heat flux, the power flowing in the pedestal region due to the in-out T_z asymmetry would exceed the net power in the plasma. This motivates further studies into the correct parallel heat flux form in the pedestal, whether $T_i = T_z$ in the pedestal, and whether the main ion viscosity and inertia terms become important in the pedestal. While these subjects could modify the alignment, leading to decreased impurity temperature asymmetries, the impurity density asymmetry would only increase.

An additional exercise was undertaken to determine if measured D_α emission is consistent with a poloidal variation in n_e, leading to a HFS n_e shifted further outward, as would be inferred from the T_z asymmetry. Measurements of the D_α radiance are not inconsistent with such an n_e asymmetry.

1D impurity modelling with STRAHL shows that, using conventional neoclassical physics, the expected flux-surface averaged impurity density aligns closely to the HFS n_z, suggesting that either (a) the impurity density is only asymmetric in a very narrow poloidal extent at the LFS or (b) 2D modelling of impurity transport is required to fully describe C-Mod impurity densities in the pedestal region or (c) other anomalous radial transport mechanisms are present at the LFS.

Explanations for the impurity density asymmetry were explored, including localized sources, fluctuation driven transport, and enhanced collisional radial transport. Localized sources from the inner-wall, and from the LFS SOL were shown to not affect the level of B^{5+} in the pedestal region. Fluctuations were ruled out as the sole cause of the n_z asymmetry, as ELM-free H-modes exhibit reduced electron density fluctuation levels, but still develop an impurity density asymmetry. Finally, radial transport processes using conventional neoclassical transport coefficients were shown to be comparable to measured poloidal transport timescales, and much faster than parallel transport timescales, signifying again that a 2D treatment of impurity particle transport may be necessary. However, I-mode plasmas exhibited similar coupling of timescales, but without in-out n_z asymmetries, indicating that the radial transport magnitude may not be the determining factor in the impurity density asymmetry. It was highlighted that neoclassical theory predicts that main ion density gradients drive an *inward* convection of impurities, which, when considered along with the poloidally varying n_i in H-mode, could drive a stronger inward impurity particle flux locally at the LFS, leading to impurity density asymmetries. The presence of an inward impurity flux driven by an main ion density pedestal is also consistent with the observed global impurity confinement being long in H-mode, while being short in I-mode. While this appears to be the most plausible mechanism for driving the impurity density asymmetry, actual impurity transport modelling with coupled 2D radial and poloidal/parallel impurity transport is needed to determine if such a mechanism can reproduce the measured impurity profiles.

Chapter 6

Variation of Impurity Flows on a Flux Surface

Having observed the impurity density variation, and possible causes, we now turn our attention to the subject of poloidal variation of bulk impurity flows on a flux surface. Specifically, we use the poloidal velocity measurements to determine if the divergence of radial impurity flux becomes significant in the pedestal region. Additionally, we explore whether the perpendicular impurity flow is accurately described to lowest order by the $\mathbf{E} \times \mathbf{B}$ and diamagnetic flows. As will be explained, these two topics can be framed in the question of whether the quantities K_z and ω_z (see Equation 2.8) are flux functions. Combined with the information on poloidal variation of impurity density, this will give us a clearer understanding of impurity transport in the pedestal region.

6.1 Poloidal Velocity Flux Function Comparison

As described in Appendix A, for any plasma species j, the poloidal velocity flux function K_j, which is a measure of the conservation of poloidal flux $\Gamma_{j\theta} = n_j V_{j\theta}$, is expected to be conserved when three conditions are met: (1) the particle density doesn't vary in time (steady-state), (2) particle sources are negligible ($S_j^n \approx 0$), and (3) the divergence of *radial* flux is negligible ($\nabla \cdot (n_j V_{jr} \hat{r}) \approx 0$), i.e. that all

flows perpendicular to the magnetic field are tangential to the flux surface. With the measurements of impurity density n_z and impurity poloidal velocity $V_{z\theta}$ at two separate poloidal locations, the LFS and HFS midplane, we can determine if these three assumptions are valid collectively for the B^{5+} species.

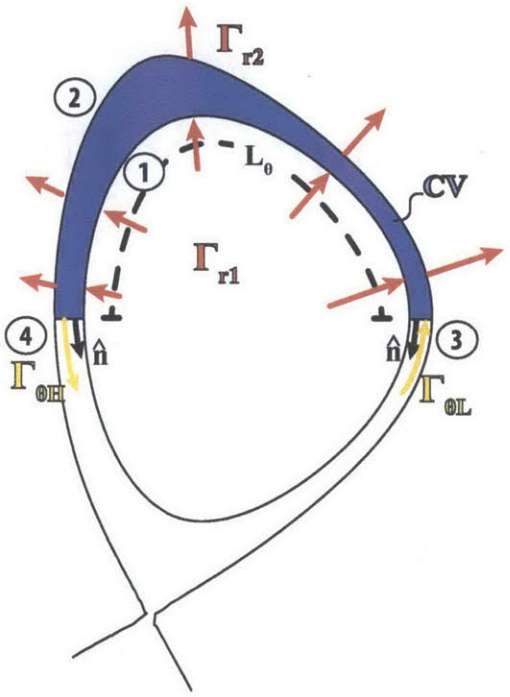

Figure 6-1: Control volume used to infer divergence of the radial flux from the poloidal flux. The shaded blue region is the control volume, covering the top half of the plasma. Poloidal flux $\Gamma_{\theta L}$ enters the control volume at the LFS through surface 3, and a poloidal flux $\Gamma_{\theta H}$ exits the control volume at the HFS through surface 4. If these poloidal fluxes (modified for flux surface spacing) don't match, this indicates the presence of a net radial flux (i.e. $\Gamma_{zr1} \neq \Gamma_{zr2}$) or a particle source or sink in the control volume. Control volume radial width is not drawn to scale.

The situation is depicted in Figure 6-1. A control volume, shown in blue, is chosen to cover the top half of the plasma between two flux surfaces. The ends of the control volume, surface 3 at the LFS and 4 at the HFS, have equal areas in flux space. If the poloidal flux ($\Gamma_{z\theta}$) entering the control volume on the LFS does not equal the poloidal flux leaving the control volume on the HFS, this must be balanced by either a net radial flux ($\Delta\overline{\Gamma}_{zr} = \overline{\Gamma}_{zr2} - \overline{\Gamma}_{zr1}$) out of the control volume or a particle sink or source

(S_z^n) within the control volume. Subscript Z refers to the impurity particle species. This simple picture of particle conservation in this control volume is treated more quantitatively in Appendix B, giving at the end an equation relating the mismatch in LFS/HFS poloidal flux to the net radial flux leaving the control volume, $\Delta\overline{\Gamma}_{zr}$:

$$\Delta\overline{\Gamma}_{zri} \approx \int_{\psi_1}^{\psi_2} d\psi \, S_z^n \frac{\partial r}{\partial \psi} - \frac{1}{R_c L_\theta} \int_{\psi_1}^{\psi_2} d\psi \left[\frac{\Gamma_{z\theta H}}{B_{\theta H}} - \frac{\Gamma_{z\theta L}}{B_{\theta L}} \right] \tag{6.1}$$

The first term on the RHS is due to sources, the second term on the RHS of Equation 6.1 is the poloidal flux mismatch term.

Shown in Figure 6-2 is an example of the calculated $K_z = n_z V_{z\theta}/B_\theta$ both at the LFS and HFS for a 1MA EDA H-mode (see profiles in Figure 4-4). The width of the profiles represent the vertical error bars associated with the measurement. Error bar calculations here include a 2 km/s systematic error bar in the poloidal velocity, a level deemed possible from the current method of wavelength calibration for the measuring instrument. This velocity error bar dominates the error bar of K_z. The error bar of K_z rises further inward as the density rises. As seen in Figure 6-2, within the measurement error bars, K_z is a conserved quantity between the LFS and HFS. This would suggest that the divergence of radial flux of B^{5+} is small in the pedestal region, and also that particle sources do not have a large effect on the transport of B^{5+} there.

Divergence of poloidal flux conserved between LFS and HFS within error bars, suggesting divergence of radial flux may be small

Using the same data but instead using the T_z-alignment (see Section 4.1) reveals a significant mismatch between the LFS and HFS K_z in the region of $0.989 \leq \rho \leq 1.0$, as shown in Figure 6-3. For reference, this region roughly overlaps with the electron temperature pedestal region. If the LFS and HFS impurity profiles were aligned by matching T_z, one would infer a very large divergence of radial flux.

From poloidal flux, large divergence of radial flux inferred if profiles aligned by T_z

The seemingly slight mismatch in K_z when aligning LFS/HFS profiles with the T_z-alignment, shown in Figure 6-3, has a large effect on the inferred poloidal velocity. The expected LFS poloidal velocity, $V_{z\theta}^{exp}$ can be calculated using the typical tokamak velocity Equation 2.8:

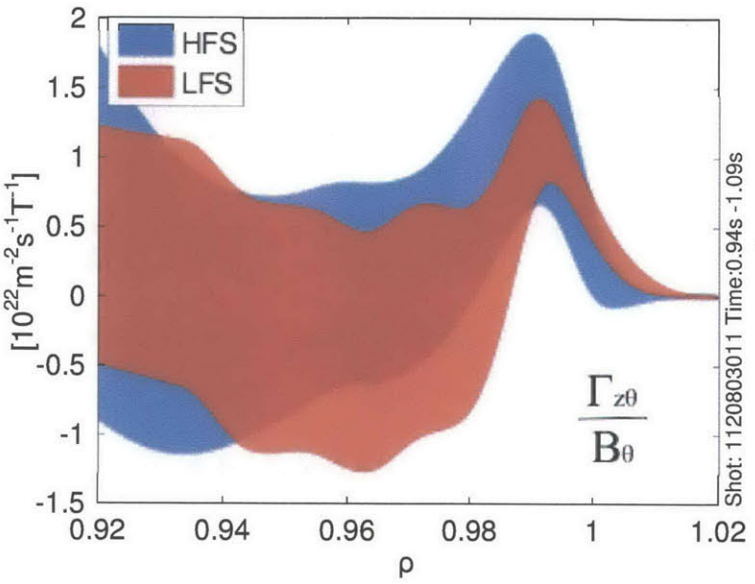

Figure 6-2: $K_z = \Gamma_{z\theta}/B_\theta$, measured at the LFS (red) and HFS (blue), using the E_r-alignment procedure (see Section 4.1). Within error bars, a good match is found, consistent with $K_z = K_z(\psi)$.

$$V_{\theta,L}^{exp} = V_{\theta,H}^{meas} \frac{n_{z,H}}{n_{z,L}} \frac{B_{\theta,L}}{B_{\theta,H}} \tag{6.2}$$

Shown in Figure 6-4 are the measured LFS and HFS poloidal velocity, along with the expected LFS poloidal velocity, for both types of alignments, E_r- and T_z-alignment. As expected from the K_z results, with the E_r-alignment, the expected LFS velocity matches the measured well. However, the mismatch in K_z that occurs for the T_z-aligned case leads to an expected LFS poloidal velocity reaching ~60 km/s, much higher than the measured peak of ~10 km/s.

The result of Figure 6-2, that within error bars the poloidal flux is conserved around a flux surface in the pedestal region since $K_z = K_z(\psi)$, is observed in all H-modes types, regardless of the size of the in-out impurity density asymmetry or poloidal velocity magnitude. As an example, Figure 6-5 shows the K_z profiles for an ELMy H-mode, the same ELMy H-mode discharge of Figure 4-7. This H-mode has a much lower collisionality, with most regions of the pedestal in the banana regime.

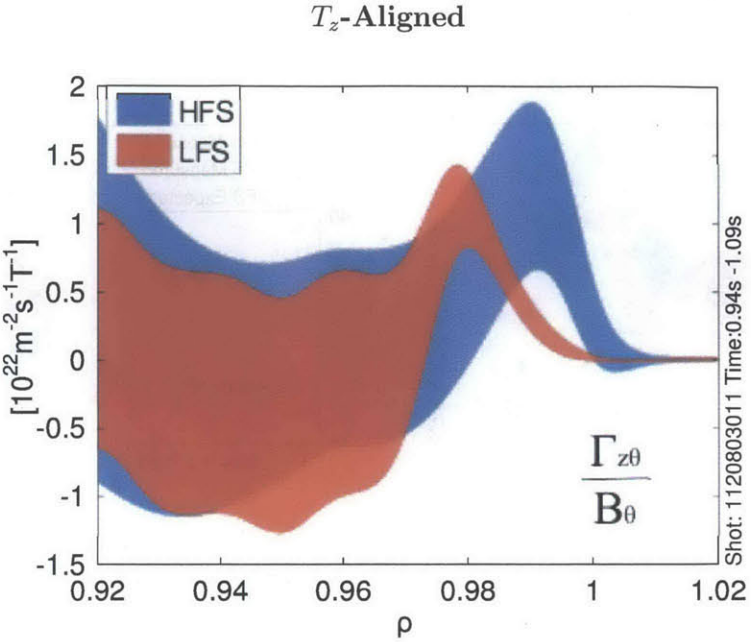

Figure 6-3: $K_z = \Gamma_{z\theta}/B_\theta$, measured at the LFS (red) and HFS (blue), using the T_z-alignment procedure (see Section 4.1). In contrast to the E_r-aligned case, Figure 6-2, a sizeable difference exists between the LFS and HFS.

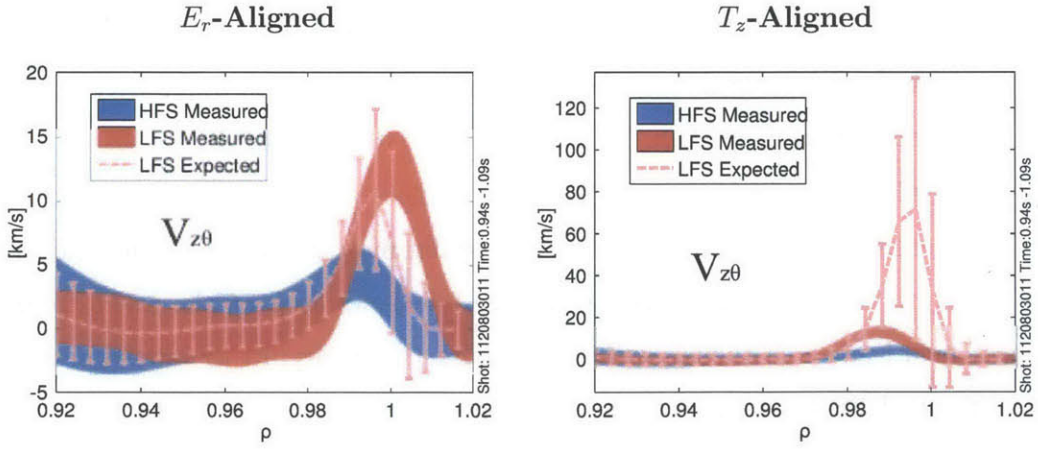

Figure 6-4: LFS expected and measured poloidal velocity when LFS/HFS profiles are aligned using (a) E_r-alignment and (b) T_z-alignment

Additionally, the poloidal velocity was considerably larger. Despite the differences in this ELMy H-mode, the K_z profiles on the LFS and HFS match well within the error bars. The expected LFS poloidal velocity evaluated using equation 6.2 is also shown

in Figure 6-5.

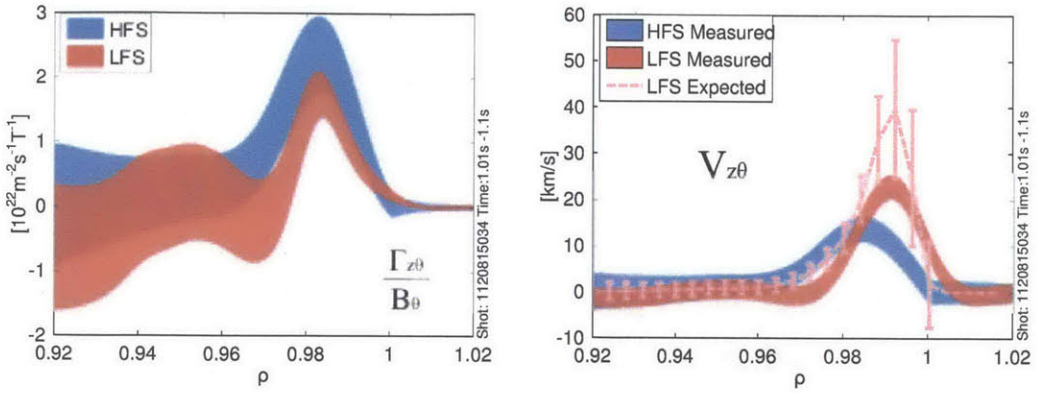

Figure 6-5: (a) $K_z = \Gamma_{z\theta}/B_\theta$, measured at the LFS (red) and HFS (blue), using the E_r-alignment procedure for an ELMy H-mode. Good agreement is found, suggesting the poloidal flux is conserved on a flux surface. (b) Corresponding expected LFS poloidal velocity.

EDA H-mode discharges at low plasma current exhibit, like other H-modes, matching LFS/HFS poloidal flux within error bars. However, noticeable differences in the structure between the LFS and HFS are observed, shown in Figure 6-6. The LFS $\Gamma_{z\theta}/B_\theta$ peaks further inward than the HFS quantity, due to a LFS impurity density that is shifted inward more than the normal current case, Figure 6-2.

I-mode plasmas, which have very different velocity structures, and symmetric impurity density between the LFS and HFS, exhibit matching K_z values for the LFS and HFS, just as in H-mode plasmas. Figure 6-7 shows an example, taken from a reversed field I-mode. Although within error bars, the values further inward between the LFS and HFS are well off shifted from each other, which needs to be further explored.

In summary, in the pedestal region in H-mode and I-mode, the poloidal flux normalized to the poloidal magnetic field (K_z) matches within error bars between the LFS and HFS, when aligning profiles using the E_r-alignment. When aligning LFS/HFS profiles by T_z, there is a significant discrepancy in K_z between the LFS and HFS, indicating that in the T_z-aligned case, the divergence of radial impurity flux is larger.

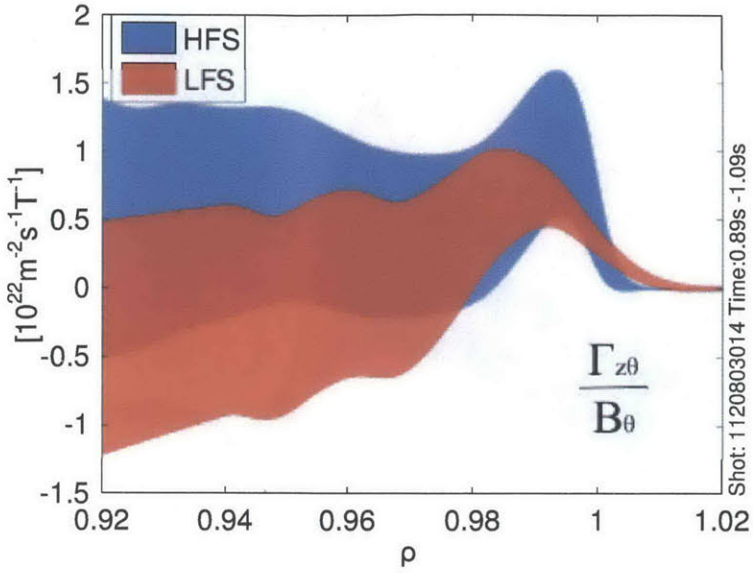

Figure 6-6: $K_z = \Gamma_{z\theta}/B_\theta$, measured at the LFS (red) and HFS (blue), using the E_r-alignment procedure (see Section 4.1) for a high q_{95} EDA H-mode. A good match is again found, however the peak positions are noticeably shifted compared to the low q_{95} EDA H-mode in Figure 6-2.

6.2 Toroidal Flux Function Comparison

We now turn our attention to the toroidal velocity function, ω_z. As shown in Appendix A, this quantity is actually representative of the fluid velocity perpendicular to the magnetic field. From the results of the previous section, within error bars we expect the perpendicular velocity to be tangential to flux surfaces, i.e. with only a small radial component, and so the form of Equation A.2 should hold. In this form, ω_z is still allowed to vary poloidally (see Equation A.3). The question then becomes if the form of Equation A.4 also holds, which assumes the perpendicular velocity is to lowest order composed of the $\mathbf{E} \times \mathbf{B}$ drift and impurity diamagnetic drift, and that potential and impurity pressure are flux functions. Already we have seen that impurity pressure is *not* a flux function (see Section 5), but, due to the E_r-alignment, potential is *close* to a flux function. If then the $\mathbf{E} \times \mathbf{B}$ dominates over the impurity diamagnetic drift, then ω_z would be a flux function to lowest order. Additionally, other terms such as ion-impurity friction may become important in the perpendicular

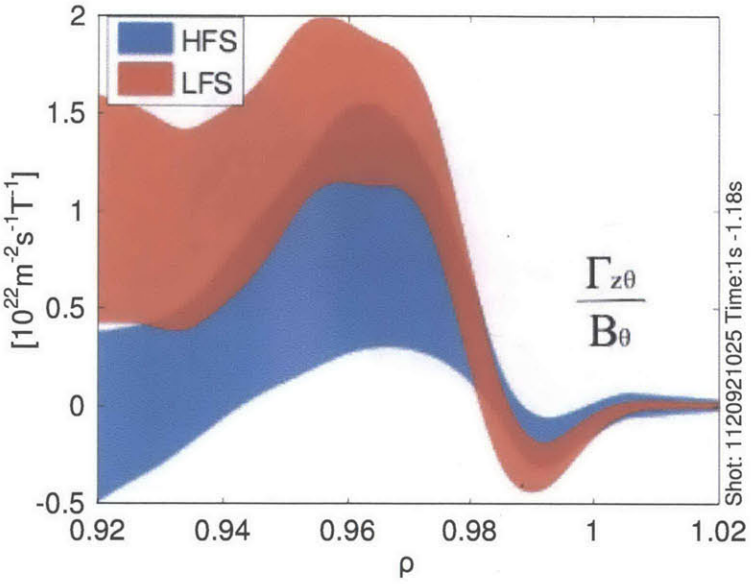

Figure 6-7: $K_z = \Gamma_{z\theta}/B_\theta$, measured at the LFS (red) and HFS (blue), using the E_r-alignment procedure (see Section 4.1) for a reversed field I-mode.

velocity, which would again allow the term ω_z to vary poloidally. By using velocity measurements to calculate ω_z, and comparing the LFS and HFS values, we are then able to determine whether perpendicular velocity is to lowest order due to the $\mathbf{E} \times \mathbf{B}$ drift.

Calculating ω_z from velocity measurements is more complicated than K_z since ω_z is composed of both poloidal and parallel velocities. To compare ω_z values at the LFS and HFS, we must take into consideration the angle of the optical line-of-sight (LOS) with the magnetic field to determine the correct projection of the expected velocity vector. This can be important for the parallel periscopes, since their LOS won't be exactly parallel to the magnetic field for every plasma discharge, as the magnetic field geometry can change. To compare measured velocity to experiment, we must take the dot product of the LOS vector with the velocity vector, Equation A.1. A generic LOS vector with angle γ to the toroidal direction is:

$$\hat{\ell} = \cos\gamma\hat{\zeta} + \sin\gamma\hat{\theta}$$

Here we've ignored any radial component of the LOS vector, as these are small for the CXRS periscope. The expected velocity, V_z^{exp}, along such a LOS is calculated taking the dot product of Equation A.1 and the LOS vector:

$$\mathbf{V}_z^{exp} \cdot \hat{\ell} = \frac{K_z(\psi)}{n_z} [B_\zeta \cos\gamma + B_\theta \sin\gamma] + \omega_z R \cos\gamma \tag{6.3}$$

The LFS parallel periscope has an angle of $\gamma_L \approx 7°$ with the toroidal direction, and the HFS parallel periscope has an angle of $\gamma_H \approx 8.5°$. The measured velocity from these parallel periscopes measure we will refer to as $V_{z\|}^{meas}$ even if the optical LOS isn't perfectly parallel to the magnetic field. Substituting Equation 6.2 for K_z, and rearranging we arrive at:

$$\begin{aligned} \omega_z &= \frac{1}{R}\left[\frac{1}{\cos\gamma} V_{z\|}^{meas} - V_{z\theta}^{meas}\left(\tan\gamma + \frac{B_\zeta}{B_\theta}\right)\right] \\ &\approx \frac{1}{R}\left[V_{z\|}^{meas} - V_{z\theta}^{meas}\frac{B_\zeta}{B_\theta}\right] \end{aligned} \tag{6.4}$$

Note that while the measured parallel velocity is generally larger than the poloidal, the poloidal velocity still contributes significantly to the ω_z calculation since it is multiplied by B_ζ/B_θ.

Shown in Figure 6-8 are the calculated LFS and HFS ω_z for the same EDA H-mode as Figure 6-2. Similar to the K_z calculations, the calculated ω_z match between LFS and HFS within error bars. A deviation is found for $\rho > 1.01$ which, if these profiles are truly absolutely aligned to the separatrix, is not a concern since we expect the flows in the SOL to be controlled additionally by boundary conditions with material surfaces.

Also similar to the K_z calculations is the deviation between the ω_z on the LFS and HFS that arises when LFS/HFS are aligned using temperature (T_z-alignment), shown in Figure 6-9, though for ω_z the region of disagreement is $0.978 \leq \rho \leq 0.99$, whereas for K_z it's a little further out ($0.989 \leq \rho \leq 1.0$).

The expected parallel velocities can be calculated using Equation 6.4 and 6.3.

E_r-Aligned

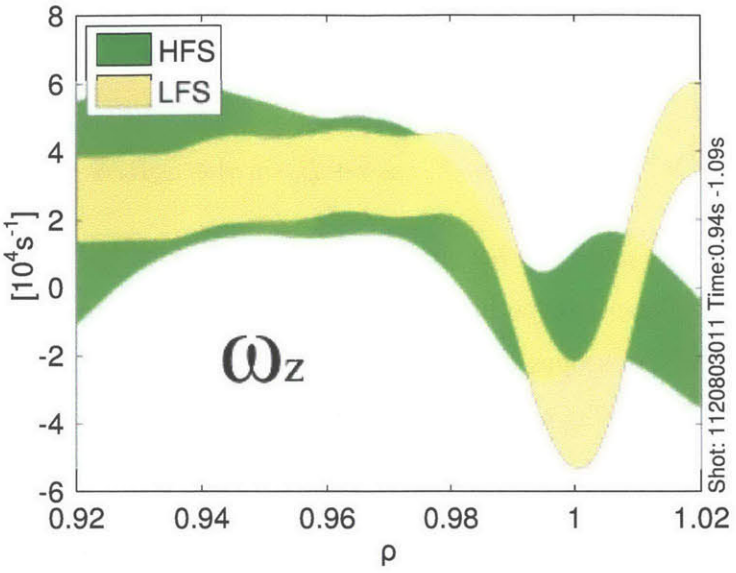

Figure 6-8: ω_z, measured at the LFS (yellow) and HFS (green), using the E_r-alignment procedure (see Section 4.1). Within error bars, a good match is found for $\rho < 1.01$, consistent with ω_z being a flux function.

Substituting velocity measurements from the HFS gives the following equation for the expected LFS parallel velocity:

$$V_{//L}^{exp} = \cos\gamma_L \left\{ V_{\theta H}^{meas} \left[\frac{n_{zH}}{n_{zL}} \frac{B_{\theta L}}{B_{\theta H}} \left(\frac{B_{\zeta L}}{B_{\theta L}} + \tan\gamma_L \right) - \frac{R_L}{R_H} \left(\frac{B_{\zeta H}}{B_{\theta H}} + \tan\gamma_H \right) \right] + V_{//H}^{meas} \frac{R_L}{R_H} \frac{1}{\cos\gamma_H} \right\} \tag{6.5}$$

The LFS measured and expected velocities are plotted in Figure 6-10. As expected from the ω_z calculations, the E_r-aligned case shows good agreement between $V_{z\|}^{meas}$ and $V_{z\|}^{exp}$, except outside of $\rho > 1.01$. The T_z-aligned case would predict extremely large LFS parallel velocities, greater than ~100 km/s, much larger than the measured ~30 km/s.

This result that the calculated ω_z matches between the LFS and HFS within error bars is a general result of H-modes studied, with no significant changes or deviations.

Finally, we show calculated ω_z in Figure 6-11 for the I-mode case of Figure 6-7.

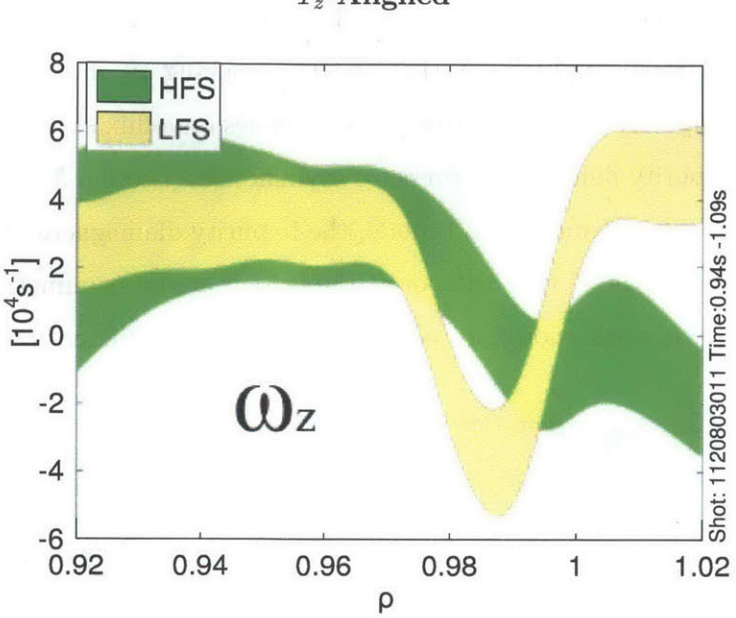

Figure 6-9: ω_z, measured at the LFS (yellow) and HFS (green), using the T_z-alignment procedure (see Section 4.1). In contrast to the E_r-aligned case, Figure 6-8, a sizeable difference exists between the LFS and HFS.

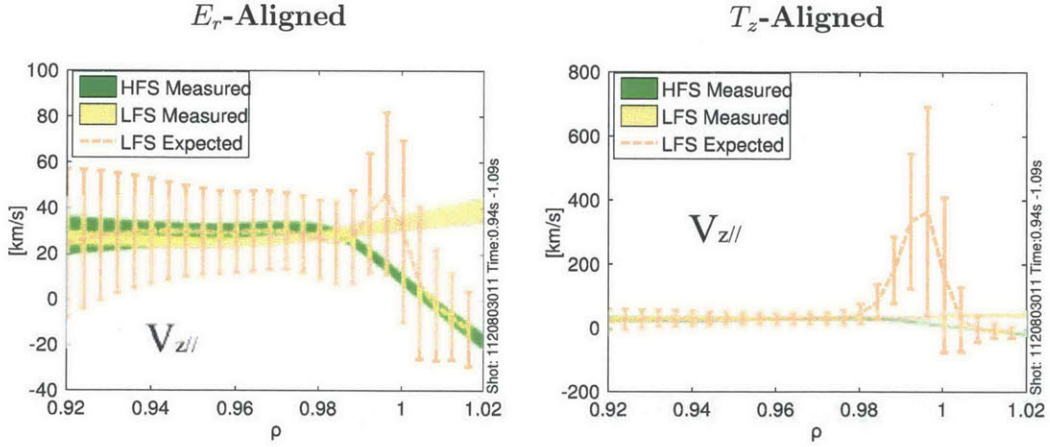

Figure 6-10: LFS expected and measured parallel velocity when LFS/HFS profiles are aligned using (a) E_r-alignment and (b) T_z-alignment

In the I-mode, ω_z matches between the LFS and HFS for most of the profile, then deviates for $\rho > 0.995$.

We can conclude then from the calculated ω_z at the LFS and HFS that, given

the proper alignment and within the error bars of our measurements, ω_z is a flux function. Recall from Appendix A that strictly speaking ω_z should *not* be a flux function if the impurity density and/or pressure varies on a flux surface. Since we do observe large impurity density and pressure asymmetries (Section 5), this points out that in the pedestal of H-mode and I-mode, the impurity diamagnetic drift ($\frac{1}{Ze n_z}\frac{\partial p_z}{\partial \psi}$) is small compared to the $\mathbf{E} \times \mathbf{B}$ drift, or at the least that the asymmetric part of the diamagnetic term is weak enough to not make a significant difference.

$\mathbf{E} \times \mathbf{B}$ dominates perpendicular impurity velocity, since $\omega_z = \omega_z(\psi)$

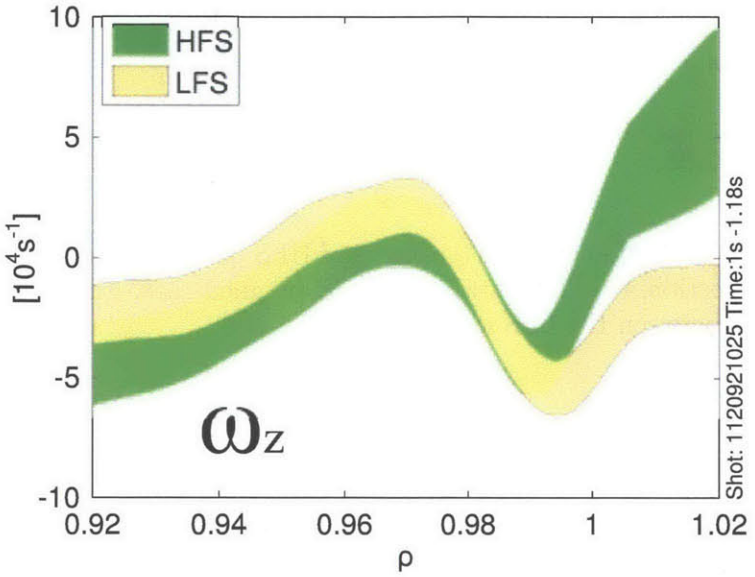

Figure 6-11: ω_z, measured at the LFS (yellow) and HFS (green), using the E_r-alignment procedure (see Section 4.1) in a reversed field I-mode.

6.3 Comparing Inferred to Neoclassical Radial Flux Divergence

A comparison can be made between the radial transport predicted from the balance of measured poloidal flux and the expected neoclassical radial transport. To make this comparison, we will calculate the derivative of Γ_{zr} with respect to ψ, essentially the radial divergence. Using Equation 6.1, we have $\partial/\partial\psi\left(\Delta\overline{\Gamma}_{zr}\right) = \partial/\partial\psi\overline{\Gamma}_{zr} - \cancel{\partial/\partial\psi\overline{\Gamma}_{zr1}}$. This leaves us with:

$$\frac{\partial \overline{\Gamma}_{zr}}{\partial \psi} = S_z^n \frac{\partial r}{\partial \psi} - \frac{1}{R_c L_\theta} \left[\frac{n_{zH} V_{z\theta H}}{B_{\theta H}} - \frac{n_{zL} V_{z\theta L}}{B_{\theta L}} \right] \tag{6.6}$$

We can also calculate this divergence by taking the ψ-derivative of the diffusion/convection form of the radial flux (see Section 5.3), and using the neoclassical D and V coefficients:

$$\frac{\partial \Gamma_{zr}}{\partial \psi} = -\frac{\partial}{\partial \psi} \left(D_z^{neo} \frac{\partial \langle n_z \rangle}{\partial \psi} \langle RB_\theta \rangle + V_z^{neo} \langle n_z \rangle \right) \tag{6.7}$$

In Figure 6-12 we compare these two methods of calculating the radial divergence. Since $\Gamma_{z\theta}/B_\theta$ matches at the LFS and HFS, Equation 6.6 gives $\frac{\partial}{\partial \psi}\Gamma_{zr}$ that is zero within error bars. The radial flux divergence calculated with the neoclassical diffusion and convection coefficients from Figure 5-12 is shown in blue, and shows differences outside of the error bars, especially near the separatrix. A few reasons could explain some of this difference. First, it is far from certain that the conventional neoclassical radial impurity flux is correct, and has been shown to *decrease* as density and temperature gradients increase[124, 56]. Second, these two quantities are not entirely the same, as that based on the poloidal flux is really for half of a flux surface, while the neoclassical result is a full flux-surface average. Third, sources may be important for the radial flux calculation using measured poloidal fluxes (Equation B.4). Sources have not been accounted for in the red trace in Figure 6-12.

We should note that if the velocity systematic error bars can be reduced, more accurate radial flux calculations from poloidal flux measurements could produce inferred radial flux measurements with error bars not crossing zero. Further work is needed to determine if this method of using the poloidal flux to infer the radial impurity flux is viable and useful.

6.4 Summary

In conclusion, we've verified that, within error bars, K_z and ω_z are indeed flux functions for the B^{5+} species. This would signify that the divergence of radial flux is

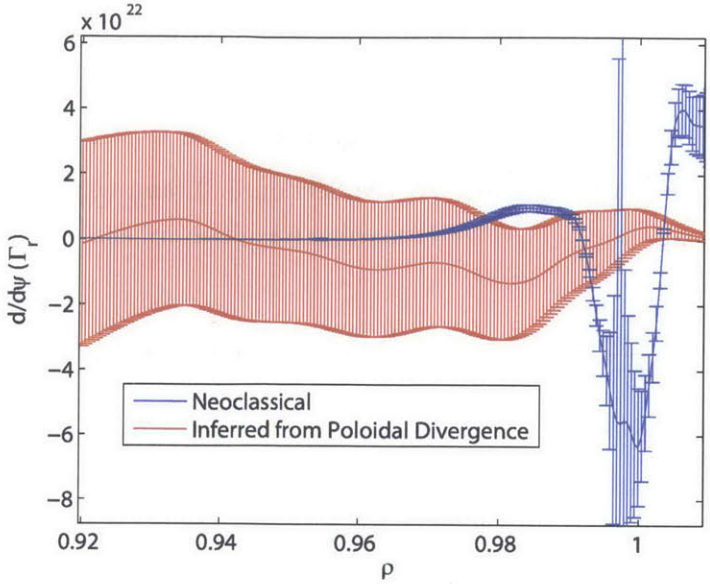

Figure 6-12: Divergence of radial flux, $\frac{d}{d\psi}\Gamma_{zr}$ calculated using the neoclassical coefficients, and inferred from the measured poloidal flux. The neoclassical is larger than the inferred measured near the separatrix, though sources have not been accounted for. Same discharge as Figure 6-2.

small, and that the perpendicular velocity is dominated by the $\mathbf{E} \times \mathbf{B}$ drift. We must stress here, however, that if the systematic error bars of the measured velocity are reduced through improved wavelength calibrations, a more detailed comparison can be made, which may reveal a difference in the calculated K_z and ω_z on the LFS and HFS. The error bars due to photon statistics alone are smaller than 0.5 km/s in the pedestal region, which would allow resolving radial fluxes on the order of that predicted by one-dimensional neoclassical transport.

A comparison of the divergence of radial flux calculated by balancing the poloidal flux out of a region, and also by taking the divergence of the neoclassical radial flux, show that the neoclassical radial transport is within the large error bars of the radial transport inferred by the poloidal flux, except close to the separatrix, where sources may play a dominant role.

As a note on future work, if more accurate measurements of the poloidal flux unequivocally showed K_z *is* conserved on a flux surface, then the radial transport could be described as a one dimensional process. In this case, comparisons with advanced

neoclassical theories such as Helander, Fulop, Landremann [124, 56, 104], based on enhanced impurity-ion friction causing impurity asymmetries, could be used or possibly extended to compare with measurements. These theories predict maximum impurity density asymmetries of $(B_{\zeta H}/B_{\zeta H})^2 \sim 4$, lower than observed on C-Mod (see Section 5), and are not ordered to allow large ion temperature variations, but could be used as a starting point for future work.

Chapter 7

Summary, Discussion, and Future Work

7.1 Summary

We begin by listing the accomplishments of this thesis which answer the questions and work set out in the Background Section 2:

1. **Compare gas puff CXRS to high energy beam CXRS**

   A gas puff system was installed on the LFS, complete with new capillary and gas plenum systems. Impurity density, temperature, and poloidal velocity from the GP-CXRS were shown experimentally to compare favorably to neutral beam CXRS for the LFS system, see Section 3.8. Other issues concerning diagnostic effects were accounted for, see Section 3 and Ref. [100].

2. **Determine if K_z is a flux function**

   Analysis and operation of a newly installed HFS poloidal periscope, along with the added capability of measuring impurity density at the LFS and HFS (see next item) allowed comparing poloidal flows to the expected variation. From the measured LFS and HFS poloidal fluxes, it was determined that within error bars K_z is a flux function. Additionally, a newly installed periscope at the LFS made measurements of the parallel velocity with the GP-CXRS system, allow-

ing complete characterization of the poloidal and parallel flows with GP-CXRS only. This further allowed comparisons of ω_z, which was also determined to be a flux function within error bars, deviating only in regions of the SOL. The complete set of poloidal and parallel views, along with the developed impurity density measurement technique using GP-CXRS (see next item), allowed a determination of the radial electric field, E_r, at both the LFS and HFS. An alignment technique was developed based on parallel momentum conservation, and proved crucial to correctly comparing LFS and HFS profiles.

3. **Measure impurity density at the HFS and LFS-HFS Impurity Density Asymmetry**

   A diagnostic technique was developed to measure the impurity density making use of measured neutral emission in tandem with the measured impurity emission. A new D_α photodetection system was developed and installed to measure this neutral emission. These measurements confirmed the existence of a strong in-out impurity density asymmetry in H-mode plasmas, with a buildup on the HFS. Asymmetry ratios of A_{n_z} from 2.5 to 9 were measured, with increasing asymmetries at higher q_{95}[100].

4. **Role of background plasma gradients on pedestal impurity transport**

   Further investigations showed symmetric LFS/HFS impurity density profiles in low n_e gradient plasmas, such as L-mode and I-mode, suggesting that ∇n_e plays a dominant role in the impurity density asymmetry. Neoclassical impurity radial flux was shown to be directed inward in H-mode, opposite that of I-mode, further corroborating the effect of the n_e gradients in H-mode playing a role in the impurity density asymmetry. Poloidal and radial transport timescales were shown to be comparable, suggesting the need to treat these two transport processes simultaneously in a 2D impurity transport code.

5. **Role of impurity sources on pedestal impurity transport**

   Experiments which enhanced the boron particle source at the HFS showed no significant change in the observed pedestal impurity density asymmetry. Other

experiments choking the SOL flow to the HFS, preventing possible LFS boron sources from propagating to the HFS, gave similar results. We can conclude that these two source mechanisms do not significantly affect impurity transport in the pedestal region.

7.2 Discussion

The results and experimental observations in this thesis provide another step in understanding how impurities transport into the plasma, and what role the pedestal plays in impurity transport and plasma performance. Much work is left in matching these experimental observations with a theoretical picture, and reconciling with other experiments. There is a common held belief in the tokamak community that conventional, local neoclassical transport can explain the impurity transport in the pedestal region. The findings of this thesis call this belief into question, and warrant further investigations into the subject with experiment, theory, and simulation. Radial transport appears to be more important in the pedestal region than conventional neoclassical physics would retain, though it is not clear if the radial transport effects were retained, how different the impurity transport would be in an average sense from the conventional picture. Certainly if radial impurity transport is large enough, and enhanced at specific poloidal locations, this could provide an effective "hole" in the transport barrier through which impurities will preferentially enter or exit.

Already important simulation and theoretical work is forthcoming, focused on including the global effects caused by large gradients in the density and temperature[22, 7, 91, 23, 125]. Analytical formulas for pedestal transport are beneficial, but ultimately the complexity of the problem will likely necessitate a computational solution.

7.3 Future Work

Future work here will be divided into C-Mod specific diagnostic and physics topics, and general diagnostic and physics topics.

7.3.1 C-Mod

At time of writing, Alcator C-Mod has recently been saved from shutdown, and is currently operational, giving the possibility to improve on the GP-CXRS diagnostic and further explore the pedestal physics discussed in this thesis.

Several improvements should be made to the Alcator edge CXRS diagnostic, some which may require some effort. First, the lab space location of the spectrometers is such that wavelength recalibrations are needed quite frequently. Moving the spectrometer/CCD cameras to a more stable location, or replacing with a sturdier table, will ensure velocity measurements are stable for long periods of time, without excessive recalibrations. Additionally, improved inter- or intra-shot wavelength calibrations should be investigated. For example, using a small integrating sphere with a neon lamp for the intra-shot neon source, to ensure uniform light on each of the six CCD columns. Current work by C. Theiler on inter-shot calibrations using neon ECDC in the machine may provide a way to calibrate all used channels simultaneously.

The LFS parallel viewing periscope ("TOR_GPI") could be upgraded. In its design, compromises had to be made in the viewing angle, so that currently all views aren't exactly tangent to the flux surface where the periscope focuses. This was done since a port is where the periscope would ideally be placed. Fixing this situation would require moving the entire LFS GP-CXRS in-vessel assembly, not a small task. This would also allow creating an improved viewing dump to minimize stray light reflections. Another upgrade to TOR_GPI would be a new fiber bundle, with a second row of fibers similar to the LFS poloidal periscope. This would allow densities to be measured with the parallel periscope; the parallel periscope will be less susceptible to instrumental issues for the density measurement, and would be closer to how the HFS impurity density is measured.

A current detraction from the GP-CXRS system is its potential to perturb the plasma (especially low density plasmas) through gas fueling and/or RFpower trips, due to increased neutral density at the ICRF antennas. The current gas delivery system is simple, but slow and ineffective in its gas delivery for the purposes of GP-

CXRS (most of input gas does not reach the regions of interest). An improved valve, perhaps with a piezo-electric drive and/or a super-sonic nozzle, could be controlled on fast timescales and allow more control over the gas flow into the chamber, allowing GP-CXRS to be used more frequently. It could also allow multiple pulses during a shot, to give time for background frames after a pulse also.

The impurity density measurement using D_α for measurement of neutral emission could be further refined, improving the understanding and ability to remove any time-changing background neutral density.

As to the pedestal physics studied here, more statistics would be very useful. The full GP-CXRS system, complete with LFS and HFS impurity density measurements, was only operational for a short time of the duration of this thesis. With the system now well in place, further studies to improve and expand the dataset with complete LFS/HFS impurity profiles, *with gap scans to enhance resolution* would be beneficial. The importance of the gap scans is paramount, as the LFS/HFS alignment without such scans is extremely difficult. Specific regimes which are lacking full data coverage are the ELMy H-mode and reversed field H-modes.

Developing the knowledge and tools necessary to run kinetic EFIT's on C-Mod in a more automated and regular way would be useful in giving a better idea of where the alignment of LFS/HFS profiles should be initially. Many of these tools exist in the Osborne toolbox, but need to be explored further in terms of varying alignments of T_e and T_z.

7.3.2 General

Already, ASDEX-Upgrade has a well-working GP-CXRS on the HFS. Further investigations on other tokamaks of poloidal variation of impurity density, along with other pedestal parameters, would be useful.

Throughout this thesis, a glaring hole in several areas has been the absence of main ion measurements. The E_r-alignment procedure really depends on T_i, not T_z (in this thesis the two were assumed equal), and the validity of the procedure depends on the main ion rotation being below certain levels for the inertia and viscosity terms

to not matter (see Appendix A). Beyond the topics of this thesis, several important physics questions regarding the formation, sustainment, and future performance of the pedestal region rely on understanding the main ion behavior there. Main ion CXRS is a very difficult diagnostic, due to spatial delocalization, but the measurement of the main ions would be very beneficial to furthering the studies of pedestal physics.

Although several mechanisms were explored to explain the density asymmetries and velocity structure, everything in this thesis focused on analytical expressions. Efforts to model or simulate the Alcator C-Mod pedestal regions, including the sharp gradients in density and temperature, would greatly contribute to understanding the drives and implications. Certainly work with full-f codes (e.g. XGC0), which in principle can simulate the complicated scale lengths of the pedestal region, would be the most favorable approach, but also the most costly in terms of initial investment and actual run time. An extension of the typical 1D impurity transport codes, allowing for poloidally varying diffusion and convection coefficients and solving the 2D continuity equation, could allow interpretive modelling of experimental results. Modelling with fluid codes, including important pedestal impurity transport drives such as inertia and friction, as done at ASDEX[105], may also give insights.

Additionally, work on including the effects of multiple impurity species may be beneficial, if not necessary to fully understand these results. The impurity transport coefficient expressions (Equations 5.7) were for a single impurity in a plasma, whereas more complicated expressions are needed for multiple species[93, 126, 33]. While boron is usually the dominant impurity species on Alcator C-Mod, the recent increase in use of low-Z seeding to improve plasma performance has resulted in higher levels of other impurities, such as neon or nitrogen. Measurements of these species, and consideration of their effects if any on the boron impurity transport would be useful.

Appendix A

Velocity Flux Functions

The basic form of the bulk velocity for any species in a tokamak plasma, under certain assumptions which will be detailed, is described by the following equation:

$$\mathbf{V}_j = \frac{K_j(\psi)}{n_j}\mathbf{B} + \omega_j(\psi)R\hat{\zeta} \tag{A.1}$$

where j is the species, ψ is the poloidal flux, $K_j(\psi)$ and $\omega_j(\psi)$ are (as of yet) undetermined flux functions, n_j is the density of the species j, $\mathbf{B}$ is the vector magnetic field, R is the major radius, and $\hat{\zeta}$ is a unit vector in the positive toroidal direction vector (clockwise if viewing the machine from the top).

Here we describe the derivation of this expected form of the bulk velocity in a plasma. Assumptions will be outlined and discussed in the context of impurity velocities.

A.1 General Derivation

We begin by assuming steady-state, and that we are in a source-free region, so that the continuity equation gives us:

$$\nabla \cdot (n_j \mathbf{V}_j) = 0$$

Now we will assume that the radial velocity is small, i.e. that *the perpendicular flows all stay within a flux surface.* We can write this generically as:

$$\mathbf{V}_\perp = -\omega_j(\psi,\theta)\frac{\mathbf{B}\times\nabla\psi}{B^2} \tag{A.2}$$

The B^2 was chosen as a normalization constant, so that the arbitrary function $\omega_j(\psi,\theta)$ has units of [1/s]. Note that here we allow ω_j to vary poloidally, but for the derivation to hold, must be axisymmetric, i.e. $\omega_j \neq \omega_j(\zeta)$.

The magnetic field in a tokamak[31] can be represented as $\mathbf{B} = I(\psi)\nabla\zeta + \nabla\zeta\times\nabla\psi$, so that $\mathbf{B}\times\nabla\psi = I(\psi)\mathbf{B} - RB^2\hat{\zeta}$. This gives the diamagnetic velocity term as:

$$n_j\mathbf{V}_{j\perp} = -n_j\,\omega_j(\psi,\theta)\frac{I(\psi)\mathbf{B} - RB^2\hat{\zeta}}{B^2} \tag{A.3}$$

Applying this equation to the steady-state continuity equation we get:

$$\begin{aligned}
\nabla\cdot(n_j\mathbf{V}_j) &= \nabla\cdot\left(n_jV_{j\parallel}\hat{b}\right) + \nabla\cdot(n_j\mathbf{V}_{j\perp}) \\
&= \mathbf{B}\cdot\nabla\left(\tfrac{n_jV_{j\parallel}}{B}\right) + \tfrac{n_jV_{j\parallel}}{B}\cancelto{0}{\nabla\cdot\mathbf{B}} - \nabla\cdot\left(\tfrac{I(\psi)\mathbf{B}-RB^2\hat{\zeta}}{B^2}n_j\,\omega_j(\psi,\theta)\right) \\
&= \mathbf{B}\cdot\nabla\left(\tfrac{n_jV_{j\parallel}}{B}\right) - \nabla\cdot\left(\tfrac{I(\psi)\mathbf{B}}{B^2}n_j\omega_j(\psi,\theta)\right) + \cancelto{0}{\nabla\cdot\left(R\hat{\zeta}n_j\,\omega_j(\psi,\theta)\right)} \\
&= \mathbf{B}\cdot\nabla\left(\tfrac{n_jV_{j\parallel}}{B}\right) - \nabla\cdot\left(\tfrac{I(\psi)\mathbf{B}}{B^2}n_j\,\omega_j(\psi,\theta)\right) \\
&= \mathbf{B}\cdot\nabla\left(\tfrac{n_jV_{j\parallel}}{B} - \tfrac{I(\psi)}{B^2}n_j\,\omega_j(\psi,\theta)\right)
\end{aligned}$$

This expression, from continuity, equals 0. Any function where there isn't a gradient along magnetic field lines (i.e. $\mathbf{B}\cdot\nabla() = 0$) is a flux function, so:

$$\frac{n_jV_{j\parallel}}{B} - \frac{I(\psi)}{B^2}n_j\,\omega_j(\psi,\theta) = K_j(\psi)$$

Combining with the perpendicular velocity, we get:

$$\begin{aligned}
n_j\mathbf{V_j} &= K_j(\psi)\,\mathbf{B} - \tfrac{I(\psi)\mathbf{B}}{B^2}n_j\,\omega_j(\psi,\theta) - \tfrac{I(\psi)\mathbf{B}-RB^2\hat{\zeta}}{B^2}n_j\,\omega_j(\psi,\theta) \\
&= K_j(\psi)\,\mathbf{B} + n_j\,\omega_j(\psi,\theta)R\hat{\zeta}
\end{aligned}$$

In this general derivation, we have shown that we can derive the typical flow

equation form without forcing ω_j to be a flux function. Additionally, no assumptions were needed about the density n_j, so that it is allowed to vary poloidally. As we will see in the next section, the reason ω_j is typically assumed to be a flux function is because the lowest order perpendicular drift velocities ($E \times B$ and diamagnetic) force us to assume ω_j is a flux function, otherwise the assumption that radial flows are negligible breaks down.

A.2 Lowest Order Drift Derivation

The general momentum equation is:

$$m_j n_j \left(\frac{\partial \mathbf{V}_j}{\partial t} + \mathbf{V}_j \cdot \nabla \mathbf{V}_j \right) = -\nabla p_j - \nabla \cdot \overleftrightarrow{\pi}_j + Z_j e n_j \left(\mathbf{E} + \mathbf{V}_j \times \mathbf{B} \right) + \mathbf{R}_j$$

Taking the cross product with the magnetic field direction ($\hat{b}$) we arrive at:

$$\hat{b} \times \left(\mathbf{E} + \mathbf{V}_j \times \mathbf{B} \right) = \frac{\hat{b} \times \left(\nabla p_j + \nabla \cdot \overleftrightarrow{\pi}_j - \mathbf{R}_j + m_j n_j \left(\frac{\partial \mathbf{V}_j}{\partial t} + \mathbf{V}_j \cdot \nabla \mathbf{V}_j \right) \right)}{Z_j e n_j}$$

Using the vector identity $\mathbf{A} \times (\mathbf{B} \times \mathbf{C}) = \mathbf{B}(\mathbf{A} \cdot \mathbf{C}) - \mathbf{C}(\mathbf{A} \cdot \mathbf{B})$, we can write $\hat{b} \times \mathbf{V}_j \times \mathbf{B} = B \left[\mathbf{V}_j \left(\hat{b} \cdot \hat{b} \right) - \hat{b} \left(\hat{b} \cdot \mathbf{V}_j \right) \right] = B \left[\mathbf{V}_{j\perp} + V_{j\parallel} \hat{b} - \hat{b} V_{j\parallel} \right] = B \mathbf{V}_{j\perp}$. So we arrive at an equation for the perpendicular velocity:

$$\mathbf{V}_{j\perp} = \frac{\mathbf{E} \times \mathbf{B}}{B^2} + \frac{\hat{b} \times \left(\nabla p_j + \nabla \cdot \overleftrightarrow{\pi}_j - \mathbf{R}_j + m_j n_j \left(\frac{\partial \mathbf{V}_j}{\partial t} + \mathbf{V}_j \cdot \nabla \mathbf{V}_j \right) \right)}{Z_j e n_j B}$$

For a low flow ordering ($V \sim \frac{\rho_j}{L} v_{tj}$), consistent with the edge plasma[127], many of these terms will be of lower order, leading to:

$$\mathbf{V}_{j\perp} \simeq \frac{\mathbf{E} \times \mathbf{B}}{B^2} + \frac{\hat{b} \times \nabla p_j}{Z_j e n_j B}$$

If we take $\mathbf{E} = -\nabla \Phi(\psi) = -\frac{\partial \Phi}{\partial \psi} \nabla \psi$, assuming $\Phi(\psi)$ is a flux function, and only the electrostatic piece of the electric field matters (ordering), and also take $p_j = p_j(\psi)$,

then:

$$n_j \mathbf{V}_{j\perp} = \frac{\mathbf{B} \times \nabla\psi}{B^2} \left[n_j \frac{\partial}{\partial\psi}\Phi + \frac{1}{Z_j e}\frac{\partial}{\partial\psi} p_j \right]$$

Note that by assuming $\Phi = \Phi(\psi)$ and $p_j = p_j(\psi)$, we are explicitly ordering the radial flow to be smaller than the poloidal flow (the poloidal flow is roughly in the $\mathbf{B} \times \nabla\psi$ direction). This equation is now in the form of the general perpendicular velocity equation (Equation A.3), with:

$$\omega_j = -\left[\frac{\partial}{\partial\psi}\Phi + \frac{1}{Z_j e n_j}\frac{\partial}{\partial\psi} p_j \right] \tag{A.4}$$

We can simply apply the procedure above to arrive at the general flow equation (Eq. A.1).

Note that although we've assumed $\Phi = \Phi(\psi)$ and $p_j = p_j(\psi)$, i.e. that they are flux functions, we have again not needed to make an explicit assumption about the poloidal variation of the density, such that $n_j = n_j(\psi, \theta)$ is allowable, and then $\omega_j = \omega_j(\psi, \theta)$, i.e. ω_j is *not* a flux function. If arguments can be made about the temperature of species j being a flux function, then n_j will also be required to be a flux function, otherwise our assumption that the pressure p_j is a flux function would break down. So the only conditions for which ω_j can be considered constant on a flux surface is if the potential (Φ), pressure (p_j), *and* density n_j are all constant on a flux surface. If we allowed poloidal varying potential and/or pressure, this would result in a perpendicular velocity term directed mainly radially ($\mathbf{B} \times \nabla\theta$ term), which we've assumed to be small. If such terms are important, it would invalidate the velocity form of equation A.1.

Appendix B

Radial Flux Inferred from Poloidal Flux

Here we quantitatively consider the meaning of a discrepancy between the LFS and HFS poloidal flux. To do so, first consider a control volume covering the top half of the poloidal plane, conforming to the flux surfaces, and covering the entire toroidal extent. This is shown in Figure 6-1. Now, we integrate the steady-state continuity equation over this control volume:

$$\int_{CV} dV \nabla \cdot (n_z \mathbf{V}_z) = \int_{CS} d\mathbf{S} \cdot (n_z \mathbf{V}_z) = \int_{CV} dV \, S_z^n \tag{B.1}$$

where we have used Gauss's law to convert the control volume (CV) integral of a divergent quantity to a surface integral of that quantity, with $d\mathbf{S}$ a differential surface area vector, pointing in the direction outward normal to the control surface (CS). If we write the velocity vector in magnetic coordinates (ψ,θ,ζ), the divergence of the toroidal component is identically zero due to axisymmetry ($\nabla \cdot n_z V_{z\zeta} \hat{\zeta} = 0$), leaving:

$$\int_{CS} d\mathbf{S} \cdot \hat{\psi} \, n_z V_{z\psi} = \int_{CV} dV \, S_z^n - \int_{CS} d\mathbf{S} \cdot \hat{\theta} \, n_z V_{z\theta} \tag{B.2}$$

In the absence of sources and sinks, the divergence of poloidal flux exactly balances the divergence of radial flux through any control volume.

Returning to Figure 6-1, the only surfaces that will have normal vectors in the

poloidal direction will be the LFS and HFS midplane ends, surface 3 and 4. A differential surface element of these surfaces can be written as $dS = 2\pi R\,(\partial r/\partial\psi)\,d\psi = 2\pi B_\theta^{-1} d\psi$, with the normal vector directions defined in Figure 6-1, resulting in:

$$\int_{CS} d\mathbf{S}\cdot\hat{\psi}\,\Gamma_{zr} = \int_{CV} dV\,S_z^n - \int_{\psi_1}^{\psi_2} d\psi\,2\pi\left[\frac{n_{zH}V_{z\theta H}}{B_{\theta H}} - \frac{n_{zL}V_{z\theta L}}{B_{\theta L}}\right] \tag{B.3}$$

The surfaces 1 and 2 have differential surface elements of $dS = 2\pi R d\ell_\theta$ in the $-\hat{\psi}$ and $\hat{\psi}$ direction, respectively (for circular flux surfaces, $d\ell_\theta = r d\theta$). This then gives:

$$\begin{aligned}\textstyle\int_{CS} d\mathbf{S}\cdot\hat{\psi}\Gamma_{zr} &\approx \textstyle\int_{\theta=0}^{\theta=\pi} d\ell_\theta\,2\pi\left[R_2\,\Gamma_{zr}\big|_2 - R_1\,\Gamma_{zr}\big|_1\right] \\ &\simeq 2\pi R_c L_\theta\left[\overline{\Gamma}_{zr}\big|_2 - \overline{\Gamma}_{zr}\big|_1\right]\end{aligned} \tag{B.4}$$

where R_c is the major radius centroid of the flux surface, $L_\theta = \int_0^\pi d\ell_\theta$ the half perimeter of the flux surface, and $\overline{\Gamma} = \frac{1}{L_\theta}\int_{\theta=0}^{\theta=\pi} d\ell_\theta\,\Gamma$. This approximation is possible because we are only concerned with the pedestal region, such that $r_2 \simeq r_1 \simeq a$, the minor radius, so that only the derivative terms in the divergence will be important (i.e. Γ_{zr}/r terms are neglected).

The source term will be dominated by ionization of B^{4+}, $S_z^n = n_e n_{B^{4+}} S_{B^{4+}}^{ion}$, for typical C-Mod operations. This is because the recombination rate is low at pedestal temperatures, and the charge-exchange sink term is also low at the typical background neutral densities in C-Mod. Determining the B^{4+} density requires an impurity transport code, such as STRAHL. If we assume the flux surface averaged source term is a function of ψ only, then we can write:

$$\int_{CV} dV\,S_z^n \approx 2\pi R_c L_\theta \int_{\psi_1}^{\psi_2} d\psi\,S_z^n \frac{\partial r}{\partial\psi} \tag{B.5}$$

Equation B.4 allows calculating the total divergence of the radial flux, $\Delta\overline{\Gamma}_{zr} = \overline{\Gamma}_{zr}\big|_2 - \overline{\Gamma}_{zr}\big|_1$, through a particular region. Combining with Equation B.3 and Equation B.5, we can calculate the divergence of the radial flux through our control volume in Figure 6-1 by using measured poloidal flux, $n_z V_{z\theta}$, from the LFS and HFS:

$$\Delta\overline{\Gamma}_{zr} = \int_{\psi_1}^{\psi_2} d\psi \, S_z^n \frac{\partial r}{\partial \psi} - \frac{1}{R_c L_\theta} \int_{\psi_1}^{\psi_2} d\psi \left[\frac{n_{zH} V_{z\theta H}}{B_{\theta H}} - \frac{n_{zL} V_{z\theta L}}{B_{\theta L}} \right] \tag{B.6}$$

If the velocity followed the canonical form (Equation 2.8) we could substitute into Equation B.6 the equation for expected LFS poloidal flow (Equation 6.2) , which would result in the term in the brackets [] being identically zero, so that when the velocity follows the general flow Equation 2.8, and the source term S_z^n is negligible, the divergence of radial flux is zero, as required from the derivation in Appendix A. Therefore, any deviation of the measured poloidal velocity from the expected form translates into an effective radial flux. This effective radial flux could be either an actual radial flux, or due to an impurity particle source/sink.

We can form a cross-field transport timescale, which represents an impurity confinement time in our control volume:

$$\tau_r^{eff} \sim \frac{\int_{CV} dV n_z}{2\pi R_c L_\theta \Delta\overline{\Gamma}_{zr}} \sim \frac{2\pi R_c L_\theta \int_{\rho_1}^{\rho_2} d\rho \, n_z \frac{\partial r}{\partial \rho}}{2\pi R_c L_\theta \Delta\overline{\Gamma}_{zr}} \sim \frac{\int_{\rho_1}^{\rho_2} d\rho \, n_z \frac{\partial r}{\partial \rho}}{\Delta\overline{\Gamma}_{zr}} \tag{B.7}$$

This is representative of the level of radial transport needed to balance both the poloidal flux out of the control volume and the impurity source generated within the control volume.

Appendix C

Parallel Momentum Equations

The momentum equation valid for any species is:

$$m_j n_j \left[\frac{\partial \mathbf{V}_j}{\partial t} + \mathbf{V}_j \cdot \nabla \mathbf{V}_j\right] = -\nabla p_j - \nabla \cdot \overleftrightarrow{\pi}_j + Z_j e n_j \left(\mathbf{E} + \mathbf{V}_j \times \mathbf{B}\right) + \mathbf{R}_j$$

We will assume steady-state, so that $\frac{\partial \mathbf{V}_j}{\partial t} \rightarrow 0$, and $\mathbf{E} = -\nabla\Phi$. The parallel momentum equation is then:

$$m_j n_j \mathbf{b} \cdot \mathbf{V}_j \cdot \nabla \mathbf{V}_j = -\mathbf{b} \cdot \nabla p_j - \mathbf{b} \cdot \nabla \cdot \overleftrightarrow{\pi}_j - Z_j e n_j \mathbf{b} \cdot \nabla\Phi + \mathbf{b} \cdot \mathbf{R}_j \qquad \text{(C.1)}$$

C.1 Electrons

We begin by ordering terms. Here we will assume a low-flow ordering, appropriate for C-Mod: $V_{e\|} \sim V_{i\|} \sim O(\delta_\theta v_{th,i})$, where $\delta_\theta = \rho_{\theta i}/L_\perp$, with $\rho_{\theta i} = m_i v_{th,i}/eB_\theta$ the poloidal ion Larmor radius, and $L_\perp$ the gradient scale length of the main ion temperature or density. For typical C-Mod pedestal parameters, this gives $V_{i\|} < 100$ km/s.

Electron Inertia

$$\frac{m_e n_e \mathbf{b} \cdot \mathbf{V}_e \cdot \nabla \mathbf{V}_e}{\mathbf{b} \cdot \nabla p_e} \sim \frac{m_e n_e V_{e\|}^2 / L_\|}{n_e T_e / L_\|} \sim \left(\frac{V_{e\|}}{v_{th,e}}\right)^2 \sim \frac{m_e}{m_i}\delta_\theta^2 \ll 1$$

Electron Viscosity

$$\frac{\mathbf{b}\cdot\nabla\cdot\pi_e}{\mathbf{b}\cdot\nabla p_e}\sim\frac{p_e\tau_{ee}V_{e\|}/L_\|^2}{p_e/L_\|}\sim\tau_{ee}\frac{V_{e\|}}{L_\|}\sim\sqrt{\frac{m_e}{m_i}}\sqrt{\frac{T_i}{T_e}}\frac{\delta_\theta v_{th,i}}{\nu_{ii}2\pi qR_0}\sim\sqrt{\frac{m_e}{m_i}}\sqrt{\frac{T_i}{T_e}}\frac{\delta_\theta}{\nu^*}\ll 1$$

where we approximated $2\pi\varepsilon^{3/2}\sim 1$, and used the fact that $\nu_{ii}=\nu_{ee}v_{th,i}/v_{th,e}$.Also, we assumed $V_{e\|}\approx V_{i\|}$ If the collisionality became very small, we may have to include the electron viscosity, but generally for the pedestal region with modest collisionalities, it can be ignored.

Electron Friction Force

$$\frac{\mathbf{b}\cdot\mathbf{R}_e}{\mathbf{b}\cdot\nabla p_e}\sim\frac{m_e n_e\nu_{ei}V_{e\|}}{n_eT_e/L_\|}\sim\frac{m_e}{T_e}\sqrt{\frac{m_i}{m_e}}\left(\frac{T_i}{T_e}\right)^{\frac{3}{2}}\nu_{ii}L_\|\delta_\theta v_{th,i}\sim\sqrt{\frac{m_e}{m_i}}\left(\frac{T_i}{T_e}\right)^{\frac{5}{2}}\delta_\theta\nu^*\ll 1$$

Here we used $\nu_{ei}\sim\nu_{ii}\sqrt{\frac{m_i}{m_e}}\left(\frac{T_i}{T_e}\right)^{3/2}$. If the collisionality became very high, we may have to include friction, but generally for the pedestal region it will never reach factors of 40, and so can be ignored.

Putting It All Together

We are left with the equation:

$$\mathbf{b}\cdot[\nabla p_e-en_e\nabla\Phi]=0$$

We now make the ansatz that the electron temperature is a flux function, $T_e=T_e(\psi)=T_{eL}$. For an axisymmetric quantity, $F=F(\psi,\theta)$, $\nabla F=\frac{\partial F}{\partial\psi}\nabla\psi+\frac{\partial F}{\partial\theta}\nabla\theta$, then $\mathbf{b}\cdot\nabla F=\dfrac{\partial F}{\partial\theta}\mathbf{b}\cdot\nabla\theta$ since $\mathbf{b}\cdot\nabla\psi=0$, giving us:

$$\frac{1}{n_e}\frac{\partial n_e}{\partial\theta}-\frac{e}{T_{eL}}\frac{\partial\Phi}{\partial\theta}=0$$

Integrating we obtain our final solution, showing that the electrons follow a Boltzman relation:

$$n_e(\psi,\theta)=n_{eL}e^{\frac{e}{T_{eL}}[\Phi(\psi,\theta)-\Phi_L]} \tag{C.2}$$

where quantites with a subscript 'L' are taken at a fixed poloidal angle, θ_L, but can still vary in ψ.

C.2 Total

We now consider the total momentum equation, or the sum of the individual momentum equations for electrons, main ions, and a single impurity ion species. Now, the friction forces will disapper, since by definition $\mathbf{R}_{jk} = -\mathbf{R}_{kj}$, and so $\sum_{j=e,i,Z} \mathbf{R}_j = 0$. The electric potential term will also disappear, as the prefix is $n_i + Zn_z - n_e$, which due to quasi-neutrality is identically 0. We will also neglect the electron viscosity and inertia, as shown above. This leaves the following equation:

$$\mathbf{b} \cdot [m_i n_i \mathbf{V}_i \cdot \nabla \mathbf{V}_i + m_z n_z \mathbf{V}_z \cdot \nabla \mathbf{V}_z + \nabla(p_e + p_i + p_z) + \nabla \cdot (\pi_i + \pi_z)] = 0$$

Impurity Inertia

$$\frac{m_z n_z \mathbf{b} \cdot \mathbf{V}_z \cdot \nabla \mathbf{V}_z}{\mathbf{b} \cdot \nabla p_i} \sim \frac{m_z n_z V_{z\|}^2 / L_\|}{n_i T_i / L_\|} \sim 2 \frac{m_z n_z}{m_i n_i} \left(\frac{V_{z\|}}{v_{th,i}} \right)^2 \sim Z \frac{n_z}{n_i} \delta_\theta^2 \ll 1$$

Here we have used $\frac{m_z}{m_i} \sim \frac{Z}{2}$ (for deuterium main ions), and that $V_{z\|} \approx V_{i\|}$. Impurity inertia is negligble, as the dominant impurity, boron, typically is at a level of $\frac{n_z}{n_i} \sim 0.01$.

Impurity Viscosity

$$\frac{\mathbf{b} \cdot \nabla \cdot \pi_z}{\mathbf{b} \cdot \nabla p_i} \sim \frac{p_z \tau_{zz} V_{z\|} / L_\|^2}{p_i / L_\|} \sim \frac{n_z T_z}{n_i T_i} \tau_{zz} \frac{V_{z\|}}{L_\|} \sim \frac{1}{Z^2} \sqrt{\frac{m_z}{m_i}} \left(\frac{T_z}{T_i} \right)^{\frac{5}{2}} \frac{\delta_\theta v_{th,i}}{\nu_{ii} 2\pi q R_0} \sim \frac{1}{Z^{\frac{3}{2}}} \left(\frac{T_z}{T_i} \right)^{\frac{5}{2}} \frac{\delta_\theta}{\nu^*} \ll 1$$

where we have used $\tau_{zz} = \frac{1}{\nu_{ii}} \sqrt{\frac{m_z}{m_i}} \frac{n_i}{Z^2 n_z} \left(\frac{T_z}{T_i} \right)^{\frac{3}{2}}$

Impurity Pressure

$$\frac{\mathbf{b} \cdot \nabla p_z}{\mathbf{b} \cdot \nabla p_i} \sim \frac{n_z}{n_i} \ll 1$$

Main Ion Inertia

$$\frac{m_i n_i \mathbf{b}\cdot\mathbf{V}_i\cdot\nabla\mathbf{V}_i}{\mathbf{b}\cdot\nabla p_i} \sim \frac{m_i n_i V_{i\|}^2/L_\|}{n_i T_i/L_\|} \sim \left(\frac{V_{i\|}}{v_{th,i}}\right)^2 \sim \delta_\theta^2$$

This suggests that the main ion inertia may become important in the pedestal region.

Main Ion Viscosity

$$\frac{\mathbf{b}\cdot\nabla\cdot\pi_i}{\mathbf{b}\cdot\nabla p_i} \sim \frac{p_i\tau_{ii}V_{i\|}/L_\|^2}{p_i/L_\|} \sim \tau_{ii}\frac{V_{i\|}}{L_\|} \sim \delta_\theta\frac{v_{th,i}\varepsilon^{\frac{3}{2}}}{\nu_{ii}qR_0} \sim \frac{\delta_\theta}{\nu^*}$$

This also suggests that the main ion viscosity may become important in the pedestal region.

Putting it All Together

Without main ion flow measurements in the pedestal, these orderings can't be confirmed. Various other effects will change transport in the pedestal, which could drastically change the main ion velocity term. As a gross simplification, we will ignore the main ion viscosity and inertia terms, recognizing this may be dangerous. This leads to the lowest order total momentum equation:

$$\mathbf{b}\cdot\nabla\left(p_i+p_e\right) = \frac{\partial}{\partial\theta}\left(p_i+p_e\right) = 0$$

Which gives the result that total pressure is constant on a flux surface:

$$p_e + p_i = C_L(\psi)$$

Using quasi-neutrality, we substitute for n_i and solve for n_e:

$$n_e T_{eL} + \left[\left(n_e - Zn_z\right)\right]T_i = C_L \rightarrow n_e(T_{eL}+T_i) - Zn_zT_i = C_L$$

Solving for C_L using the parameters measured at the LFS:

$$C_L = n_{eL}(T_{eL}+T_{iL}) - Zn_{zL}T_{iL}$$

Then the final equation for n_e:

$$\begin{aligned} n_e &= \frac{C_L}{T_{eL}+T_i} + Z\frac{T_i}{T_{eL}+T_i}n_z \\ &= \frac{T_{eL}+T_{iL}}{T_{eL}+T_i}n_{eL} + Z\frac{n_z T_i - n_{zL}T_{iL}}{T_{eL}+T_i} \end{aligned}$$

A similar method can be used for n_i. Since T_e is a flux function, the Boltzmann relation (Eq. C.2) holds, and we simply need to insert the modified n_e expression to solve for the potential, Φ. We also assume that $T_i = T_z$. Our final set of equations is :

$$\boxed{\begin{aligned} n_e(\psi,\theta) &= \frac{T_{eL}+T_{zL}}{T_{eL}+T_z}n_{eL} + Z\frac{n_z T_z - n_{zL}T_{zL}}{T_{eL}+T_z} \\ n_i(\psi,\theta) &= \frac{T_{eL}+T_{zL}}{T_{eL}+T_z}n_{eL} - \frac{Zn_{zL}T_{zL} + (ZT_{eL}+T_z)n_z}{T_{eL}+T_z} \\ \Phi(\psi,\theta) &= \Phi_L + \frac{T_{eL}}{e}\ln\left(\frac{T_{eL}+T_{zL}}{T_{eL}+T_z} + Z\frac{\frac{n_z}{n_{eL}}T_z - \frac{n_{zL}}{n_{eL}}T_{zL}}{T_{eL}+T_z}\right) \end{aligned}}$$

where quantities without a subscript 'L' vary poloidally, e.g. $n_z = n_z(\psi,\theta)$ and quantities with a subscript are taken at a fixed poloidal angle, θ_L, and depend only on ψ.

Appendix D

Rate Coefficients for Species of Different Temperatures

In laboratory plasmas at typical fusion research densities (n=$10^{16} - 10^{22}\,[m^{-3}]$), it can usually be assumed that on closed field lines the ions and electrons follow local, Maxwellian distributions, and that for the diagnostic time scales of interest that collisions drive the different species to be in thermal equilibrium ($T_i = T_e$). For Gas Puff Imaging (GPI) Charge Exchange Recombination Spectroscopy (CXRS), where donor neutrals are introduced by puffing molecular gas, it is important to account for the fact that the donor neutrals can have a thermal distribution with a temperature different from that of the receiver impurity species. It is then necessary to derive a rate coefficient equation which accounts for these velocity distributions with different temperatures.

D.1 Setup

The general rate coefficient for a two-body process is:

$$\langle \sigma v \rangle = \frac{1}{n_1 n_2} \int \int d\mathbf{v_1} d\mathbf{v_2}\, \sigma(v)\, v\, f_1(\mathbf{v_1})\, f_2(\mathbf{v_2})$$

where $v = |\mathbf{v_1} - \mathbf{v_2}|$is the relative speed, f_1 and f_2 are the velocity distributions

for the two particle species, $\sigma(v)$ the cross-section for the process, and $\int d\mathbf{v}_1 = \int\int\int dv_x dv_y dv_z$. For the case when the two species follow a Maxwellian distribution and are in thermal equilibrium, i.e.:

$$f_1(\mathbf{v}_1) = n_1 \left(\frac{m_1}{2\pi T}\right)^{\frac{3}{2}} e^{-\frac{1}{2}\frac{m_1 v_1^2}{T}} \qquad f_2(\mathbf{v}_2) = n_2 \left(\frac{m_2}{2\pi T}\right)^{\frac{3}{2}} e^{-\frac{1}{2}\frac{m_2 v_2^2}{T}}$$

the rate coefficient reduces to the simple form (see Appendix A of Ref. [62]):

$$\langle \sigma v \rangle = \frac{8\pi}{m_r^2} \left(\frac{m_r}{2\pi T}\right)^{\frac{3}{2}} \int_0^\infty E\,\sigma(E)\, e^{-\frac{E}{T}}\, dE$$

where $m_r = \frac{m_1 m_2}{m_1 + m_2}$ is the reduced mass and $E = \frac{1}{2} m_r v^2$ is the beam reaction energy.

D.2 Different Temperature Derivation

Now derive the rate coefficient equation for different temperatures, i.e. $T_1 \neq T_2$. Using the Maxwellian distributions as above again, we have:

$$\langle \sigma v \rangle = \left(\frac{m_1}{2\pi T_1}\right)^{\frac{3}{2}} \left(\frac{m_2}{2\pi T_2}\right)^{\frac{3}{2}} \int\int d\mathbf{v_1} d\mathbf{v_2}\, \sigma(v)\, v\, e^{-\left(\frac{\frac{1}{2}m_1 v_1^2}{T_1} + \frac{\frac{1}{2}m_2 v_2^2}{T_2}\right)}$$

Instead of the usual Center-of-Mass velocity, define now a "temperature weighted" Center-of-Mass velocity:

$$\mathbf{V} = \frac{\frac{m_1}{T_1}\mathbf{v_1} + \frac{m_2}{T_2}\mathbf{v_2}}{\frac{m_1}{T_1} + \frac{m_2}{T_2}}$$

It can be verified that the velocities can now be written as:

$$\mathbf{v_1} = \mathbf{V} - \frac{\frac{m_2}{T_2}}{\frac{m_1}{T_1} + \frac{m_2}{T_2}}\mathbf{v}$$

$$\mathbf{v_2} = \mathbf{V} + \frac{\frac{m_1}{T_1}}{\frac{m_1}{T_1} + \frac{m_2}{T_2}}\mathbf{v}$$

These two variables, $\mathbf{V}$and $\mathbf{v}$ are an independent basis from $\mathbf{v_1}$ and $\mathbf{v_2}$. Making these

substitutions, with the Jacobian giving $d\mathbf{v_1}d\mathbf{v_2} = d\mathbf{V}d\mathbf{v}$:

$$\langle\sigma v\rangle = \left(\frac{m_1}{2\pi T_1}\right)^{\frac{3}{2}}\left(\frac{m_2}{2\pi T_2}\right)^{\frac{3}{2}}\int\int d\mathbf{V}d\mathbf{v}\,\sigma(v)\,v\,e^{-\frac{1}{2}\left[\left(\frac{m_1}{T_1}+\frac{m_2}{T_2}\right)V^2+\frac{m_1m_2}{m_1T_2+m_2T_1}v^2\right]}$$

Now changing to spherical coordinates with $d\mathbf{V} = V^2 sin(\theta)dVd\theta d\phi = 4\pi V^2 dV$ and $d\mathbf{v} = v^2 sin(\theta')dvd\theta' d\phi' = 4\pi V^2 dv$:

$$\langle\sigma v\rangle = \left(\frac{m_1}{2\pi T_1}\right)^{\frac{3}{2}}\left(\frac{m_2}{2\pi T_2}\right)^{\frac{3}{2}}(4\pi)^2\int_0^\infty dV\,V^2 e^{-\frac{1}{2}\left(\frac{m_1}{T_1}+\frac{m_2}{T_2}\right)V^2}\int_0^\infty dv\,\sigma(v)\,v^3\,e^{-\frac{1}{2}\frac{m_1m_2}{m_1T_2+m_2T_1}v^2}$$

The integral over dV can be carried out immediately, using the change of variables $x = \sqrt{\frac{1}{2}\left(\frac{m_1}{T_1}+\frac{m_2}{T_2}\right)}V$ and using the integral relation:

$$\int_0^\infty x^2 e^{-x^2}dx = \frac{\pi^{\frac{1}{2}}}{4}$$

So that now:

$$\langle\sigma v\rangle = \left(\frac{m_1}{2\pi T_1}\right)^{\frac{3}{2}}\left(\frac{m_2}{2\pi T_2}\right)^{\frac{3}{2}}\frac{1}{\left(\frac{1}{2}\left(\frac{m_1}{T_1}+\frac{m_2}{T_2}\right)\right)^{\frac{3}{2}}}\frac{\pi^{\frac{1}{2}}}{4}\int_0^\infty dv\,\sigma(v)\,v^3\,e^{-\frac{1}{2}\frac{m_1m_2}{m_1T_2+m_2T_1}v^2}$$

At this point we can make a couple of different substitutions in terms of energy. If we substitute a relative beam energy, $E = \frac{1}{2}m_1v^2$:

$$\langle\sigma v\rangle = \left(\frac{m_1}{2\pi T_1}\right)^{\frac{3}{2}}\left(\frac{m_2}{2\pi T_2}\right)^{\frac{3}{2}}\frac{1}{\left(\frac{1}{2}\left(\frac{m_1}{T_1}+\frac{m_2}{T_2}\right)\right)^{\frac{3}{2}}}\frac{\pi^{\frac{1}{2}}}{4}\frac{2}{m_1^2}\int_0^\infty dE\,\sigma(E)\,E\,e^{-\frac{m_2}{m_1+m_2}\frac{E}{T_{eff}}}$$

$$\langle\sigma v\rangle = \sqrt{\frac{8}{\pi}}\left(\frac{m_r}{T_{eff}}\right)^{\frac{3}{2}}\frac{1}{m_1^2}\int_0^\infty dE\,\sigma(E)\,E\,e^{-\frac{m_2}{m_1+m_2}\frac{E}{T_{eff}}}$$

where $T_{eff} = \frac{m_1T_2+m_2T_1}{m_1+m_2}$, and m_r is the reduced mass as defined above.
If we instead substitute the center-of-mass energy $E = \frac{1}{2}m_rv^2$:

$$\langle\sigma v\rangle = \left(\frac{m_1}{2\pi T_1}\right)^{\frac{3}{2}}\left(\frac{m_2}{2\pi T_2}\right)^{\frac{3}{2}}\frac{1}{\left(\frac{1}{2}\left(\frac{m_1}{T_1}+\frac{m_2}{T_2}\right)\right)^{\frac{3}{2}}}\frac{\pi^{\frac{1}{2}}}{4}\frac{2}{m_r^2}\int_0^\infty dE\,\sigma(E)\,E\,e^{-\frac{E}{T_{eff}}}$$

$$\langle \sigma v \rangle = \sqrt{\frac{8}{\pi m_r}} \frac{1}{T_{eff}^{\frac{3}{2}}} \int_0^\infty dE\, \sigma(E)\, E\, e^{-\frac{E}{T_{eff}}}$$

D.3 Numerical Calculation

The $\langle \sigma v \rangle$ can be calculated efficiently using Gauss-Laguerre quadrature. The general Gauss-Lagueere quadrature formula is:

$$\int_0^\infty dz\, F(z)\, e^{-z} = \sum_{i=0}^{n} w_i F(z_i)$$

where w_i is the Gauss-Laguerre weight factor, and z_i is the ith root of the $(n+1)$th degree Laguerre polynomial. Using this form for the $\langle \sigma v \rangle$ formula:

$$\langle \sigma v \rangle \approx \sqrt{\frac{8\pi}{m_r}} \frac{1}{T_{eff}^{\frac{3}{2}}} \sum_{i=1}^{N} w_i \sigma_i E_i$$

Appendix E

D_α Photodiode Calibration

The D_α photodiodes are calibrated using the bright Labsphere. This will document the calibration procedure, including assumptions made.

E.1 D_α Signal

The D_α voltage signal is given by:

$$V_{D_\alpha} = \int T_{peri}\, T_{relay}\, T_{collimator}\, T_{filter}(\lambda)\, S_k\, R_f\, G\, I^{\lambda}_{D_\alpha}(\lambda)\, d\lambda$$

where:

T_{peri}	Periscope transmission	
T_{relay}	Relay fiber transmission	
$T_{collimator}$	Collimator transmission	
$T_{filter}(\lambda)$	Filter transmission	
S_k	Cathode Radiant Sensitivity	$\left[\frac{A}{W}\right]$
R_f	Feedback resistor	$\left[\frac{V}{A}\right]$
G	Constant etendue factor	$[m^2 \cdot ster]$
$I^{\lambda}_{D_\alpha}(\lambda)$	Input D_α Spectral Radiance	$\left[\frac{W}{m^2 \cdot ster \cdot \mathring{A}}\right]$
λ	Wavelength	$[\mathring{A}]$

E.2 D_α Calibration

The calibration of the D_α photodiodes is done with the bright Labsphere, the URS-6000. At the wavelength of interest, $\lambda_{D_\alpha} = 656.099\,[nm]$, the spectral radiance is $0.1959\left[\frac{W}{m^2 \cdot ster \cdot A}\right]$. As this is input into a fiber directly into the collimator (bypassing the periscope and relay fiber), the output voltage is:

$$\begin{aligned} V_{cal} &= \int T_{collimator}\, T_{filter}(\lambda)\, S_k\, R_{f,cal}\, G\, I^{\lambda}_{cal}(\lambda)\, d\lambda \\ &= T_{collimator}\, S_k\, R_{f,cal}\, G \int T_{filter}(\lambda)\, I^{\lambda}_{cal}(\lambda)\, d\lambda \end{aligned}$$

The output voltage during a plasma shot is:

$$\begin{aligned} V_{plasma} &= \int T_{peri}\, T_{relay}\, T_{collimator}\, T_{filter}(\lambda)\, S_k\, R_{f,plasma}\, G\, I^{\lambda}_{plasma}(\lambda)\, d\lambda \\ &= T_{peri}\, T_{relay}\, T_{collimator}\, S_k\, R_{f,plasma}\, G \int T_{filter}(\lambda)\, I^{\lambda}_{plasma}(\lambda)\, d\lambda \end{aligned}$$

The factors that stay constant between the calibration and the plasma signals are $T_{collimator}$, S_k, and G. Inserting the calibration factors in place of these we have:

$$V_{plasma} = \frac{V_{cal}}{\int T_{filter}(\lambda)\, R_{cal}(\lambda)\, d\lambda} \frac{R_{f,plasma}}{R_{f,cal}}\, T_{peri}\, T_{relay} \int T_{filter}(\lambda)\, I^{\lambda}_{plasma}(\lambda)\, d\lambda$$

If we assume the width of the plasma D_α line is much smaller than the filter function width ($\Delta_{R_{plasma}} \ll \Delta_{T_{filter}}$), then the filter function can be taken out of the integral, and evaluated at the D_α center wavlength (this errors associated with this assumption are evaluated in Appendix A). The D_α radiance can then be written:

$$I_{D_\alpha} = \int I^{\lambda}_{plasma}(\lambda)\, d\lambda = \frac{1}{T_{peri}\, T_{relay}} \frac{R_{f,cal}}{R_{f,plasma}} \frac{\int T_{filter}(\lambda)\, I^{\lambda}_{cal}(\lambda)\, d\lambda}{T_{filter}(\lambda_0)} \frac{V_{plasma}}{V_{cal}}$$

The portion that won't change between the calibration and the plasma shot can be rewritten as a calibration factor, C_{cal}:

$$C_{cal} = \frac{R_{f,cal}}{V_{cal}} \frac{\int T_{filter}(\lambda)\, I^{\lambda}_{cal}(\lambda)\, d\lambda}{T_{filter}(\lambda_0)} \qquad \left[\frac{M\Omega}{V} \cdot \frac{W}{m^2 \cdot ster}\right]$$

which produces the final equation for the D_α radiance:

$$I_{D_\alpha} = \int I^{\lambda}_{plasma}(\lambda)\, d\lambda = \frac{C_{cal}}{T_{peri}\, T_{relay}\, R_{f,plasma}} V_{plasma}$$

Error Analysis of D_α Signal

The error associated with the five entities are as follows: T_{peri} and T_{relay} errors are estimated at about 5%. C_{cal} error is calculated to be about 1%. The feedback resistors used give an error for $R_{f,plasma}$ to be 1.412%, as there are two resistors in parallel.

The remaining error bar to calculate is $\sigma_{V_{plasma}}$. Normally this would be calculated as a combination of "dark" noises (i.e. all noises associated present when no light is shining on the photodiode) and the "shot" noise (photon statistics noise):

$$\begin{aligned} \sigma_{V_{plasma}} &= \sqrt{v^2_{shot} + v^2_{dark}} = \sqrt{R^2_f 2eS_k P_i \Delta f + v^2_{dark}} \\ &= \sqrt{2eR_f V_{plasma} \Delta f + v^2_{dark}} = \sqrt{\frac{eV_{plasma}}{\pi C_f} + v^2_{dark}} \end{aligned} \tag{E.1}$$

where we have made use of $S_k P_i = \frac{V_{plasma}}{R_f}$ and $\Delta f = \frac{1}{2\pi R_f C_f}$. The dark noise can be calculated from the photodiode datasheet, or better yet measured during a completely dark time. From measurement for the photodiodes, this dark noise is typically $v_{dark} \sim 4e-4\,V_{rms}$, which is larger than quoted on the datasheet, and may have to do with additional noise added in by the digitizer or Lemo break-out panels. Considering our normal setting is $R_f = 24.390\,M\Omega$, $C_f = 5\,pF$ and the maximum voltage $V_{plasma} = +12\,V$ due to op-amp railing, the maximum shot noise is $v_{shot,max} \sim 3.5e-4\,V_{rms}$, so that we are always dark noise limited.

Bibliography

[1] R. Hazeltine. Research needs for magnetic fusion energy sciences, Report of the Research needs Workshop (ReNeW). Tech. rep., DOE/OFES Report, 2009.

[2] E. Doyle, W. Houlberg, Y. Kamada, V. Mukhovatov, et al. *Nuclear Fusion*, **47**(6), p. S18, 2007. ISSN 0029-5515. doi:10.1088/0029-5515/47/6/S02.

[3] R. Groebner, C. Chang, J. Hughes, R. Maingi, et al. *Nuclear Fusion*, **53**(9), p. 093024, 2013. ISSN 0029-5515. doi:10.1088/0029-5515/53/9/093024.

[4] S. Krivit, J. Lehr, and T. Kingery. *Nuclear energy encyclopedia: science, technology, and applications*. 2011.

[5] F. Wagner, G. Fussmann, T. Grave, M. Keilhacker, et al. *Physical Review Letters*, **53**(15), pp. 1453, 1984. ISSN 0031-9007. doi:10.1103/PhysRevLett.53.1453.

[6] F. Wagner, G. Becker, K. Behringer, D. Campbell, et al. *Physical Review Letters*, **49**(19), pp. 1408, 1982. doi:10.1103/PhysRevLett.49.1408.

[7] C. S. Chang, S. Ku, and H. Weitzner. *Physics of Plasmas*, **11**(5), pp. 2649, 2004. doi:10.1063/1.1707024.

[8] K. Burrell. *Physics of Plasmas*, **6**(12), pp. 4418, 1999. doi:10.1063/1.873728.

[9] H. Biglari, P. H. Diamond, and P. W. Terry. *Physics of Fluids B: Plasma Physics*, **2**(1), p. 1, 1990. ISSN 08998221. doi:10.1063/1.859529.

[10] P. Terry. *Reviews of Modern Physics*, **72**(1), pp. 109, 2000. ISSN 0034-6861. doi:10.1103/RevModPhys.72.109.

[11] K. C. Shaing and E. C. Crume. *Physical Review Letters*, **63**(21), pp. 2369, 1989. doi:10.1103/PhysRevLett.63.2369.

[12] F. L. Hinton and Y.-B. Kim. *Physics of Plasmas*, **2**(1), p. 159, 1995. ISSN 1070664X. doi:10.1063/1.871105.

[13] E.-j. Kim and P. Diamond. *Physical Review Letters*, **90**(18), p. 185006, 2003. ISSN 0031-9007. doi:10.1103/PhysRevLett.90.185006.

[14] L. Schmitz, L. Zeng, T. L. Rhodes, J. C. Hillesheim, et al. *Physical Review Letters*, **108**(15), p. 155002, 2012. ISSN 0031-9007. doi:10.1103/PhysRevLett.108.155002.

[15] D. Whyte, A. Hubbard, J. Hughes, B. Lipschultz, et al. *Nuclear Fusion*, **50**(10), p. 105005, 2010. ISSN 0029-5515. doi:10.1088/0029-5515/50/10/105005.

[16] A. E. Hubbard. *Plasma Physics and Controlled Fusion*, **42**(5A), 2000. ISSN 0741-3335. doi:10.1088/0741-3335/42/5A/302.

[17] G. Kagan and P. J. Catto. *Plasma Physics and Controlled Fusion*, **50**(8), 2008. ISSN 0741-3335. doi:10.1088/0741-3335/50/8/085010.

[18] M. Kočan, J. Gunn, S. Carpentier-Chouchana, A. Herrmann, et al. *Journal of Nuclear Materials*, **415**(1), pp. S1133, 2011. ISSN 00223115. doi:10.1016/j.jnucmat.2010.08.036.

[19] J. W. Hughes, B. LaBombard, D. A. Mossessian, A. E. Hubbard, et al. *Physics of Plasmas*, **13**(5), 2006. doi:10.1063/1.2180748.

[20] R. J. Groebner, M. A. Mahdavi, A. W. Leonard, T. H. Osborne, et al. *Physics of Plasmas*, **9**(5), pp. 2134, 2002. doi:10.1063/1.1462032.

[21] P. Snyder, R. Groebner, J. Hughes, T. Osborne, et al. *Nuclear Fusion*, **51**(10), p. 103016, 2011.

[22] M. Landreman and D. Ernst. *Plasma Physics and Controlled Fusion*, **54**(11), p. 115006, 2012.

[23] G. Kagan and P. J. Catto. *Plasma Physics and Controlled Fusion*, **52**(5), 2010. ISSN 0741-3335. doi:10.1088/0741-3335/52/5/055004.

[24] B. Lipschultz, D. Pappas, B. LaBombard, J. Rice, et al. *Nuclear Fusion*, **41**(5), pp. 585, 2001. ISSN 0029-5515. doi:10.1088/0029-5515/41/5/311.

[25] R. Ochoukov, D. Whyte, D. Brunner, I. Cziegler, et al. *Journal of Nuclear Materials*, **438**, pp. S875, 2013. ISSN 00223115. doi:10.1016/j.jnucmat.2013.01.189.

[26] B. LaBombard, J. E. Rice, A. E. Hubbard, J. W. Hughes, et al. *Physics of Plasmas*, **12**(5), p. 056111, 2005. ISSN 1070664X. doi:10.1063/1.1876294.

[27] J. Hughes, P. Snyder, J. Walk, E. Davis, et al. *Nuclear Fusion*, **53**(4), p. 043016, 2013. ISSN 0029-5515. doi:10.1088/0029-5515/53/4/043016.

[28] J. Walk, P. Snyder, J. Hughes, J. Terry, et al. *Nuclear Fusion*, **52**(6), p. 063011, 2012. ISSN 0029-5515. doi:10.1088/0029-5515/52/6/063011.

[29] A. Diallo, J. Hughes, M. Greenwald, B. LaBombard, et al. *Physical Review Letters*, **112**(11), p. 115001, 2014. ISSN 0031-9007. doi:10.1103/PhysRevLett.112.115001.

[30] A. Dominguez. *Study of density fluctuations and particle transport at the edge of I-mode plasmas.* Ph.d thesis, Massachusetts Institute of Technology, 2012.

[31] P. Helander and D. Sigmar. *Collisional transport in magnetized plasmas.* Cambridge University Press, 2005.

[32] F. L. Hinton and R. D. Hazeltine. *Reviews of Modern Physics*, **48**(2), pp. 239, 1976. doi:10.1103/RevModPhys.48.239.

[33] K. Wenzel and D. Sigmar. *Nuclear Fusion*, **30**(6), pp. 1117, 1990. ISSN 0029-5515. doi:10.1088/0029-5515/30/6/013.

[34] R. Dux. STRAHL User Manual, 2006.

[35] K. D. Marr, B. Lipschultz, P. J. Catto, R. M. McDermott, et al. *Plasma Physics and Controlled Fusion*, **52**(5), p. 055010, 2010. ISSN 0741-3335. doi:10.1088/0741-3335/52/5/055010.

[36] M. Reinke. *Experimental Tests of Parallel Impurity Transport Theory in Tokamak Plasmas.* Ph.d thesis, Massachusetts Institute of Technology, 2011.

[37] T. Pütterich, R. Dux, M. Janzer, and R. McDermott. *Journal of Nuclear Materials*, **415**(1), pp. S334, 2011. ISSN 00223115. doi:10.1016/j.jnucmat.2010.09.052.

[38] R. J. Fonck, D. S. Darrow, and K. P. Jaehnig. *Physical Review A*, **29**(6), pp. 3288, 1984. doi:10.1103/PhysRevA.29.3288.

[39] R. C. Isler. *Plasma Physics and Controlled Fusion*, **36**(2), pp. 171, 1994. ISSN 0741-3335. doi:10.1088/0741-3335/36/2/001.

[40] R. M. Churchill, C. Theiler, B. Lipschultz, R. Dux, et al. *Review of Scientific Instruments*, **84**(9), p. 093505, 2013. ISSN 00346748. doi:10.1063/1.4821084.

[41] T. Pütterich, E. Viezzer, R. Dux, R. McDermott, et al. *Nuclear Fusion*, **52**(8), p. 083013, 2012. ISSN 0029-5515. doi:10.1088/0029-5515/52/8/083013.

[42] R. Churchill, B. Lipschultz, C. Theiler, and J. Hughes. In *Bulletin of the American Physical Society*, vol. 57. 2012.

[43] R. J. Groebner and T. H. Osborne. *Physics of Plasmas*, **5**(5), p. 1800, 1998. ISSN 1070664X. doi:10.1063/1.872849.

[44] K. Burrell. *Physics of Plasmas*, **4**(5), pp. 1499, 1997. doi:10.1063/1.872367.

[45] R. Groebner, C. Chang, P. Diamond, J. Hughes, et al. Final report of the FES 2011 Joint Facilities and Theory Research Target. Technical report, Fusion Energy Sciences, 2011.

[46] H. Meyer, M. De Bock, N. Conway, S. Freethy, et al. *Nuclear Fusion*, **51**(11), p. 113011, 2011.

[47] B. Lipschultz, D. Whyte, and B. LaBombard. *Plasma Physics and Controlled Fusion*, **47**(10), pp. 1559, 2005. ISSN 0741-3335. doi:10.1088/0741-3335/47/10/001.

[48] M. Tendler and D. Heifetz. *Fusion Technology*, **11**(2), pp. 289, 1987.

[49] R. J. Goldston. *Introduction to Plasma Physics*. CRC Press, 1995.

[50] R. L. Boivin, J. A. Goetz, A. E. Hubbard, J. W. Hughes, et al. *Physics of Plasmas*, **7**(5), pp. 1919, 2000. doi:10.1063/1.874016.

[51] K. Burrell. *Physics of Plasmas*, **10**(6), pp. 2616, 2003. doi:10.1063/1.1574811.

[52] H. Summers. ADAS User Manual. Tech. rep., University of Strathclyde, 2004.

[53] D. Stotler and C. Karney. *Contrib. Plasma Phys.*, **34**(2-3), pp. 392, 1994. doi:10.1002/ctpp.2150340246.

[54] D. Reiter, M. Baelmans, and P. Börner. *Fusion Science and Technology*, **47**(2), p. 172, 2005.

[55] B. LaBombard. KN1D: A 1-D Space, 2-D Velocity, Kinetic Transport Algorithm for Atomic and Molecular Hydrogen in an Ionizing Plasma. Technical report, MIT Plasma Science and Fusion Center, 2000.

[56] T. Fülöp, P. J. Catto, and P. Helander. *Physics of Plasmas*, **8**(12), pp. 5214, 2001. doi:10.1063/1.1418241.

[57] W. Wan, S. E. Parker, Y. Chen, G. Y. Park, et al. *Physics of Plasmas*, **18**(5), p. 056116, 2011. doi:10.1063/1.3589467.

[58] R. E. Olson. *Physical Review A*, **24**(4), pp. 1726, 1981. doi:10.1103/PhysRevA.24.1726.

[59] R. Janev and H. Winter. *Physics Reports*, **117**(5-6), pp. 265, 1985. ISSN 03701573. doi:10.1016/0370-1573(85)90118-8.

[60] I. Hutchinson. *Principles of Plasma Diagnostics*. Cambridge University press, 2002.

[61] F. Guzmán, L. F. Errea, C. Illescas, L. Méndez, et al. *Journal of Physics B: Atomic, Molecular and Optical Physics*, **43**(14), p. 144007, 2010. ISSN 0953-4075. doi:10.1088/0953-4075/43/14/144007.

[62] J. P. Freidberg. *Plasma Physics And Fusion Energy.* Cambridge University press, 2007.

[63] J. Ghosh, H. R. Griem, R. C. Elton, J. L. Terry, et al. *Physics of Plasmas*, **11**(3), pp. 1033, 2004. doi:10.1063/1.1646394.

[64] E. Viezzer, T. Pütterich, R. Dux, R. M. McDermott, et al. *Review of Scientific Instruments*, **83**(10), p. 103501, 2012. doi:10.1063/1.4755810.

[65] K. Burrell and J. M. Muñoz Burgos. *Physics of Plasmas*, **19**(7), p. 072507, 2012. doi:10.1063/1.4736732.

[66] B. J. Ding, Y. Sakamoto, and Y. Miura. *Plasma Physics and Controlled Fusion*, **47**(6), pp. 789, 2005. ISSN 0741-3335. doi:10.1088/0741-3335/47/6/005.

[67] M. Tunklev, P. Breger, K. Günther, M. von Hellermann, et al. *Plasma Physics and Controlled Fusion*, **41**(8), p. 985, 1999. ISSN 0741-3335. doi:10.1088/0741-3335/41/8/305.

[68] E. Viezzer, T. Pütterich, R. Dux, and A. Kallenbach. *Plasma Physics and Controlled Fusion*, **53**(3), p. 035002, 2011. ISSN 0741-3335. doi:10.1088/0741-3335/53/3/035002.

[69] T. S. Pedersen, R. Granetz, A. Hubbard, I. Hutchinson, et al. *Nuclear Fusion*, **40**(10), pp. 1795, 2000. ISSN 0029-5515. doi:10.1088/0029-5515/40/10/310.

[70] K. Marr, B. Lipschultz, B. LaBombard, and J. Terry. *Journal of Nuclear Materials*, **337-339**, pp. 286, 2005. ISSN 00223115. doi:10.1016/j.jnucmat.2004.10.029.

[71] R. M. McDermott, B. Lipschultz, J. W. Hughes, P. J. Catto, et al. *Physics of Plasmas*, **16**(5), p. 056103, 2009. ISSN 1070664X. doi:10.1063/1.3080721.

[72] D. Jablonski. *Local Gas Injection as a Scrape-off Layer Diagnostic on the Alcator C-Mod Tokamak.* Phd, Massachusetts Institute of Technology, 1996.

[73] B. Lipschultz, Y. Lin, E. Marmar, D. Whyte, et al. *Journal of Nuclear Materials*, **363-365**, pp. 1110, 2007. ISSN 00223115. doi:10.1016/j.jnucmat.2007.01.227.

[74] R. M. McDermott. *Edge Radial Electric Field Studies Via Charge Exchange Recombination Spectroscopy on the Alcator C-Mod Tokamak.* Ph.d. thesis, Massachusetts Institute of Technology, 2009.

[75] K. D. Marr. *Comparison of Charge-Exchange Recombination Spectroscopy Measurements of the Pedestal Region of Alcator C-Mod with Neoclassical Flow Predictions by.* Ph.D. thesis, Massachusetts Institute of Technology, 2010.

[76] R. E. Bell. *Review of Scientific Instruments*, **75**(10), pp. 4158, 2004. doi:10.1063/1.1787601.

[77] R. E. Bell, L. E. Dudek, B. Grek, D. W. Johnson, et al. *Review of Scientific Instruments*, **70**(1), pp. 821, 1999. doi:10.1063/1.1149460.

[78] A. Blom and C. Jupen. *Plasma Physics and Controlled Fusion*, **44**(7), pp. 1229, 2002. ISSN 07413335. doi:10.1088/0741-3335/44/7/312.

[79] R. S. Freund, J. A. Schiavone, and H. M. Crosswhite. *Journal of Physical and Chemical Reference Data*, **14**(1), pp. 235, 1985. doi:10.1063/1.555750.

[80] B. Cao, D. P. Stotler, S. J. Zweben, M. Bell, et al. *Fusion Science and Technology*, **64**(1), p. 29, 2013.

[81] A. Blom. *Physica Scripta*, **T120**, pp. 90, 2005. ISSN 0031-8949. doi:10.1088/0031-8949/2005/T120/014.

[82] C. Theiler. *Nuclear Fusion*, **TBD**(TBD), p. TBD, 2014.

[83] R. C. Isler, R. W. Wood, C. C. Klepper, N. H. Brooks, et al. *Physics of Plasmas*, **4**(2), p. 355, 1997. ISSN 1070664X. doi:10.1063/1.872095.

[84] M. Greenwald, R. Boivin, P. Bonoli, R. Budny, et al. *Physics of Plasmas*, **6**(5), pp. 1943, 1999. doi:10.1063/1.873451.

[85] I. H. Hutchinson. *Plasma Physics and Controlled Fusion*, **44**(1), 2002. ISSN 0741-3335. doi:10.1088/0741-3335/44/1/307.

[86] E. Delabie, M. Brix, C. Giroud, R. J. E. Jaspers, et al. *Plasma Physics and Controlled Fusion*, **52**(12), 2010. ISSN 0741-3335. doi:10.1088/0741-3335/52/12/125008.

[87] L. Lao, H. St. John, R. Stambaugh, A. Kellman, et al. *Nuclear Fusion*, **25**(11), pp. 1611, 1985. ISSN 0029-5515. doi:10.1088/0029-5515/25/11/007.

[88] S. Wolfe. MIT Plasma Science and Fusion Center, private communication, 2013.

[89] R. S. Granetz, I. H. Hutchinson, J. Gerolamo, W. Pina, et al. *Review of Scientific Instruments*, **61**(10), pp. 2967, 1990. doi:10.1063/1.1141741.

[90] J. Neuhauser, D. Coster, H. U. Fahrbach, J. C. Fuchs, et al. *Plasma Physics and Controlled Fusion*, **44**(6), p. 855, 2002. ISSN 0741-3335. doi:10.1088/0741-3335/44/6/316.

[91] J. Callen, R. Groebner, T. Osborne, J. Canik, et al. *Nuclear Fusion*, **50**(6), p. 064004, 2010. ISSN 0029-5515. doi:10.1088/0029-5515/50/6/064004.

[92] A. N. Simakov and P. J. Catto. *Physics of Plasmas*, **10**(12), p. 4744, 2003. ISSN 1070664X. doi:10.1063/1.1623492.

[93] S. Hirshman and D. Sigmar. *Nuclear Fusion*, **21**(9), 1981. ISSN 0029-5515. doi:10.1088/0029-5515/21/9/003.

[94] B. LaBombard. Te at the Separatrix in C-Mod. Tech. rep., MIT PSFC, 2003.

[95] J. Kim, K. Burrell, P. Gohil, R. Groebner, et al. *Physical Review Letters*, **72**(14), pp. 2199, 1994. ISSN 0031-9007. doi:10.1103/PhysRevLett.72.2199.

[96] E. Viezzer, T. Pütterich, C. Angioni, A. Bergmann, et al. *Nuclear Fusion*, **54**(1), p. 012003, 2014. ISSN 0029-5515. doi:10.1088/0029-5515/54/1/012003.

[97] K. H. Burrell, W. P. West, E. J. Doyle, M. E. Austin, et al. *Plasma Physics and Controlled Fusion*, **46**(5A), pp. A165, 2004. ISSN 0741-3335. doi:10.1088/0741-3335/46/5A/018.

[98] B. LaBombard. *Physics of Plasmas*, **Submitted**, 2014.

[99] Y. Lin. *Experimental application and numerical study of reflectometry in the Alcator C-Mod tokamak*. Ph.D. thesis, 2001.

[100] R. Churchill, B. Lipschultz, and C. Theiler. *Nuclear Fusion*, **53**(12), p. 122002, 2013. ISSN 0029-5515. doi:10.1088/0029-5515/53/12/122002.

[101] H. Chen, N. C. Hawkes, L. C. Ingesson, M. von Hellermann, et al. *Physics of Plasmas*, **7**(11), pp. 4567, 2000. doi:10.1063/1.1311806.

[102] G. Kagan, K. D. Marr, P. J. Catto, M. Landreman, et al. *Plasma Physics and Controlled Fusion*, **53**(2), p. 025008, 2011. ISSN 0741-3335. doi:10.1088/0741-3335/53/2/025008.

[103] I. Pusztai and P. J. Catto. *Plasma Physics and Controlled Fusion*, **52**(7), p. 075016, 2010. ISSN 0741-3335. doi:10.1088/0741-3335/52/7/075016.

[104] M. Landreman, T. Fülöp, and D. Guszejnov. *Physics of Plasmas*, **18**(9), p. 092507, 2011. doi:10.1063/1.3631819.

[105] E. Viezzer, T. Pütterich, E. Fable, A. Bergmann, et al. *Plasma Physics and Controlled Fusion*, **55**(12), p. 124037, 2013. ISSN 0741-3335. doi:10.1088/0741-3335/55/12/124037.

[106] R. Snider. *Nuclear Fusion*, **30**(11), pp. 2400, 1990. ISSN 0029-5515. doi:10.1088/0029-5515/30/11/017.

[107] T. S. Pedersen, R. S. Granetz, E. S. Marmar, D. Mossessian, et al. *Physics of Plasmas*, **9**(10), pp. 4188, 2002. doi:10.1063/1.1506162.

[108] D. Brunner, B. LaBombard, R. M. Churchill, J. Hughes, et al. *Plasma Physics and Controlled Fusion*, **55**(9), p. 095010, 2013. ISSN 0741-3335. doi:10.1088/0741-3335/55/9/095010.

[109] A. Kirk, T. O'Gorman, S. Saarelma, R. Scannell, et al. *Plasma Physics and Controlled Fusion*, **51**(6), p. 065016, 2009. ISSN 0741-3335. doi:10.1088/0741-3335/51/6/065016.

[110] B. LaBombard and B. Lipschultz. *Nuclear Fusion*, **27**(1), pp. 81, 1987. ISSN 0029-5515. doi:10.1088/0029-5515/27/1/007.

[111] P. H. Rutherford. *Physics of Fluids*, **17**(9), p. 1782, 1974. ISSN 00319171. doi:10.1063/1.1694975.

[112] A. Samain and F. Werkoff. *Nuclear Fusion*, **17**(1), pp. 53, 1977. ISSN 0029-5515. doi:10.1088/0029-5515/17/1/006.

[113] R. Hawryluk, S. Suckewer, and S. Hirshman. *Nuclear Fusion*, **19**(5), pp. 607, 1979. ISSN 0029-5515. doi:10.1088/0029-5515/19/5/005.

[114] G. McCracken, R. Granetz, B. Lipschultz, B. Labombard, et al. *Journal of Nuclear Materials*, **241-243**, pp. 777, 1997. ISSN 00223115. doi:10.1016/S0022-3115(97)80139-0.

[115] N. Smick, B. LaBombard, and C. Pitcher. *Journal of Nuclear Materials*, **337-339**, pp. 281, 2005. ISSN 00223115. doi:10.1016/j.jnucmat.2004.09.035.

[116] K. Behringer. *Journal of Nuclear Materials*, **145-147**, pp. 145, 1987. ISSN 00223115. doi:10.1016/0022-3115(87)90319-9.

[117] B. LaBombard and L. Lyons. *The Review of scientific instruments*, **78**(7), p. 073501, 2007. ISSN 0034-6748. doi:10.1063/1.2754392.

[118] L. Lin, M. Porkolab, E. M. Edlund, J. C. Rost, et al. *Physics of Plasmas*, **16**(1), p. 012502, 2009. ISSN 1070664X. doi:10.1063/1.3057420.

[119] L. Lin, E. M. Edlund, M. Porkolab, Y. Lin, et al. *Review of Scientific Instruments*, **77**(10), p. 10E918, 2006. ISSN 00346748. doi:10.1063/1.2228623.

[120] I. Cziegler, J. L. Terry, J. W. Hughes, and B. LaBombard. *Physics of Plasmas*, **17**(5), 2010. doi:10.1063/1.3421577.

[121] K. L. Bell, H. B. Gilbody, J. G. Hughes, A. E. Kingston, et al. *Journal of Physical and Chemical Reference Data*, **12**(4), p. 891, 1983. ISSN 00472689. doi:10.1063/1.555700.

[122] V. Naulin. *Physical Review E*, 2005.

[123] N. T. Howard, M. Greenwald, and J. E. Rice. *The Review of scientific instruments*, **82**(3), p. 033512, 2011. ISSN 1089-7623. doi:10.1063/1.3565448.

[124] P. Helander. *Physics of Plasmas*, **5**(11), pp. 3999, 1998. doi:10.1063/1.873121.

[125] P. Catto, F. Parra, and G. Kagan. *Plasma Physics and Controlled Fusion*, **55**, p. 045009, 2013.

[126] F. Scotti, V. Soukhanovskii, R. Bell, S. Gerhardt, et al. *Nuclear Fusion*, **53**(8), p. 083001, 2013. ISSN 0029-5515. doi:10.1088/0029-5515/53/8/083001.

[127] A. Mikhailovskii and V. Tsypin. *Beiträge aus der Plasmaphysik*, 1984.